Code 731

INTERFEROMETER POSITION LOCATION CONCEPT

Contract No.: NAS5-21043

Federal Systems Division
International Business Machines Corporation
18100 Frederick Pike
Gaithersburg, Maryland 20760

June 1970
Final Report

Prepared for

GODDARD SPACE FLIGHT CENTER
Greenbelt, Maryland 20771

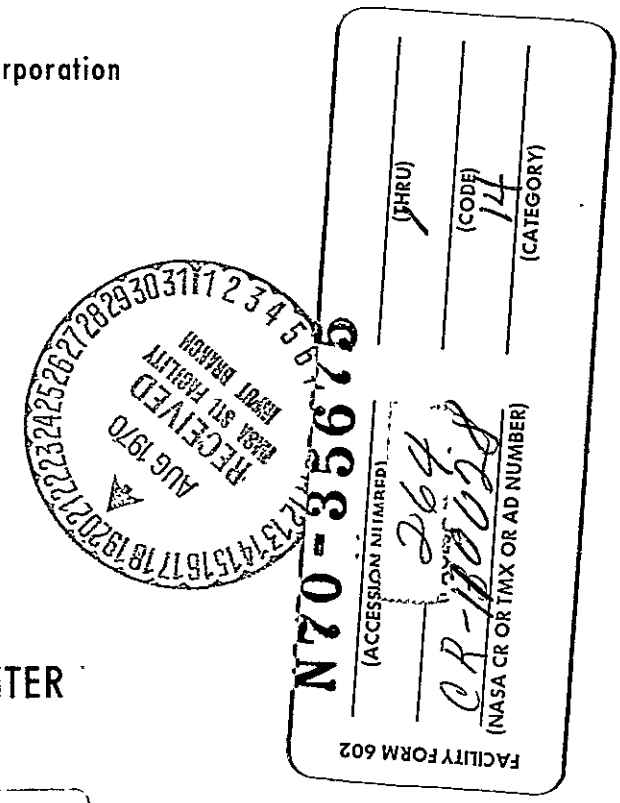

1 Report No.	2. Government Accession No.	3. Recipient's Catalog No.

4. Title and Subtitle	5. Report Date
INTERFEROMETER POSITION LOCATION CONCEPT	June 1970
	6. Performing Organization Code
7. Author(s)	8. Performing Organization Report No. FSC 70-5193
9. Performing Organization Name and Address Federal Systems Division International Business Machines Gaithersburg, Maryland 20760	10. Work Unit No.
	11. Contract or Grant No. NAS5-21043
	13. Type of Report and Period Covered
12. Sponsoring Agency Name and Address Goddard Space Flight Center Greenbelt, Maryland 20771 Tech. Monitor: M.S. Maxwell	Final Report
	14. Sponsoring Agency Code

15 Supplementary Notes

16. Abstract

The basic method studied for position location of a low power emitter at a known altitude is to determine the direction with respect to a satellite borne interferometer. The application considered is a system of 15,000 meterological balloons for determining wind velocity. The study included calibration, boom dynamics, multiple access, phase extraction, multipath and refraction.

Trade offs were made between baseline length, frequency, required phase measurement accuracy and ambiguity resolution. A frequency of 1600 MHz and a baseline length of 400 wavelengths was chosen, requiring a phase measurement accuracy of about 0.7 degrees ($1\sigma_T$) in order to obtain a position location accuracy of 1 km ($1\sigma_T$).

Four widely spaced calibration transmitters constantly illuminate the satellite to provide continuous calibration of the orientation and length of the baseline and of the system phase biases. Continuous calibration relaxes the requirements for stringent attitude stabilization. To achieve a 0.7 deg phase accuracy, one watt emitters transmit for 10 sec. Boom angular motion of the order of 10^{-5} radians per second will affect the measured phase but with continuous calibration these effects can be compensated.

17. Key Words (Selected by Author(s))	18. Distribution Statement
Position Location Interferometer Data Gathering Multiple Access	

19. Security Classif. (of this report)	20. Security Classif. (of this page)	21. No. of Pages	22. Price*
Unclassified		264	

*For sale by the Clearinghouse for Federal Scientific and Technical Information, Springfield, Virginia 22151.

TABLE OF CONTENTS

		Page
Section I-1	INTRODUCTION	I-1-1
	I-1.1 Summary and Conclusions	I-1-2
	I-1.2 Recommendations	I-1-7
Section I-2	USE OF INTERFEROMETER FOR POSITION LOCATION	I-2-1
	I-2.1 Interferometer Principle	I-2-1
	I-2.2 Long Baseline Spaceborne Interferometer	I-2-3
	I-2.3 Ambiguity Resolution	I-2-5
	I-2.4 Calibration	I-2-5
	I-2.5 Link Calculation	I-2-7
	I-2.6 Error Budget	I-2-9
	I-2.7 Accuracy — Position Location	I-2-11
	I-2.8 Accuracy — Velocity	I-2-14
	I-2.9 Error Breakdown — Position Location	I-2-14
Section I-3	PROPAGATION AND POLARIZATION EFFECTS	I-3-1
	I-3.1 Multipath	I-3-1
	I-3.2 Refraction	I-3-4
	I-3.3 Polarization Mismatch Errors	I-3-5
Section I-4	SPACECRAFT SYSTEMS	I-4-1
	I-4.1 Antenna Element	I-4-1
	I-4.2 Mechanical Systems	I-4-2
	I-4.3 Electronic Systems	I-4-6
	I-4.4 Multiple Access	I-4-10
Section I-5	BALLOON BEACON	I-5-1
	I-5.1 Data Transmission	I-5-1
	I-5.2 Identification	I-5-3

TABLE OF CONTENTS (Cont'd.)

		Page
Section I-5	BALLOON BEACON (Cont'd.)	
	I-5.3 Timer	I-5-3
	I-5.4 Balloon (dc) Power Requirements	I-5-4
Section I-6	GROUND SYSTEMS	
	I-6.1 Electronics	I-6-1
	I-6.2 Data Processing	I-6-5
Section II-1	SYSTEM CONSIDERATION AND TRADEOFF ANALYSIS	II-1-1
	II-1.1 Relationship Among Electrical Angle, Space Angle, and Position Location	II-1-2
	II-1.2 Position Location Determination and Velocity Determination Tradeoff	II-1-6
	II-1.3 Calibration	II-1-10
	II-1.4 Ambiguity Resolution	II-1-16
	II-1.5 Link Calculation	II-1-25
	II-1.6 Orbit Choices	II-1-29
	II-1.7 Multiple Access	II-1-31
	II-1.8 Boom Motion Effects	II-1-34
	II-1.9 Choice of Operating Frequency	II-1-39
Section II-2	ERROR ANALYSIS	II-2-1
	II-2.1 Position Location Error	II-2-1
	II-2.2 Expansion into Phase Errors	II-2-6
	II-2.3 Expansion in Terms of Four CT Phase Noises, CT Survey Errors, and Satellite Ephemeris Error	II-2-10
	II-2.4 Composite Error Equation	II-2-16
	II-2.5 Statistical Error Analysis	II-2-17
	II-2.6 Computer Implementation	II-2-18

TABLE OF CONTENTS (Cont'd.)

		Page
Section II-3	MULTIPATH	II-3-1
	II-3.1 The Geometrical and Mathematical Model	II-3-1
	II-3.2 Position Error Resulting from Multipath	II-3-8
	II-3.3 Bandspreading	II-3-8
	II-3.4 Effects of Filtering	II-3-26
Section II-4	REFRACTION	II-4-1
Section II-5	POLARIZATION MISMATCH ERROR	II-5-1
Section II-6	ANTENNA ELEMENT SELECTION	II-6-1
	II-6.1 Antenna Element Requirements	II-6-1
	II-6.2 Candidate Antenna Elements and Their Characteristics	II-6-4
	II-6.3 Selection of Optimum Antenna	II-6-14
	II-6.4 Mechanical/Thermal Design	II-6-14
Section II-7	MECHANICAL STUDIES	II-7-1
	II-7.1 Candidate Element Description	II-7-3
	II-7.2 Environmental Effects	II-7-6
	II-7.3 Thermal Twist	II-7-11
	II-7.4 System Frequency	II-7-17
	II-7.5 Dynamic Simulation	II-7-21
	II-7.6 Attitude Control System and Gravity-Gradient Control	II-7-31
Section II-8	SATELLITE AND GROUND ELECTRONICS	II-8-1
	II-8.1 Satellite Repeater	II-8-1
	II-8.2 Ground Station Receiver	II-8-10
	II-8.3 Acquisition Time	II-8-12
	II-8.4 Phase Measurement	II-8-14

TABLE OF CONTENTS (Cont'd.)

		Page
Section II-9	BALLOON BEACON	II-9-1
	II-9.1 Balloon Antenna	II-9-2
	II-9.2 Balloon Transmitter	II-9-6
	II-9.3 Identification	II-9-6
	II-9.4 Data Measurement and Transmission	II-9-6
	II-9.5 Timer Requirements	II-9-10
	II-9.6 Balloon (dc) Power Requirements	II-9-10
GLOSSARY		G-1
REFERENCES		R-1
BIBLIOGRAPHY		B-1

LIST OF ILLUSTRATIONS

Figure		Page
I-1-1	System Concept	I-1-3
I-2-1	Principle of Radio Interferometer	I-2-2
I-2-2	Ambiguity Resolution	I-2-2
I-2-3	Required Phase Accuracy	I-2-4
I-2-4	Baselines	I-2-6
I-2-5	Beacon Horizontal Position CEP in km (Multipath Excluded)	I-2-12
I-2-6	Beacon North-South Position Standard Deviation (1σ) in km (Multipath Excluded)	I-2-13
I-2-7	Beacon East-West Position Standard Deviation (1σ) in km (Multipath Excluded)	I-2-13
I-2-8	North-South Velocity Standard Deviation (1σ) in m/s	I-2-15
I-2-9	Beacon East-West Velocity Standard Deviation (1σ) in m/s	I-2-15
I-2-10	Beacon Horizontal Velocity CEP in m/s	I-2-16
I-2-11	Beacon Position Standard Deviation Breakdown	I-2-18
I-2-12	Error Sensitivities	I-2-19
I-3-1	Position Error Due to Multipath	I-3-2
I-3-2	Multipath Performance with Filtering	I-3-2
I-3-3	Refraction Error	I-3-5
I-4-1	Boom Deflection	I-4-4
I-4-2	Natural Frequency for Antisymmetric Mode	I-4-4
I-4-3	Time History of Baseline Angular Position	I-4-5
I-4-4	Time History of Baseline Angular Rate	I-4-5
I-4-5	Functional Diagram of Satellite Repeater	I-4-8
I-4-6	Typical Spectrum Format at Input to Repeater Upconverter	I-4-9
I-5-1	Functional Diagram, Balloon Electronics	I-5-2

LIST OF ILLUSTRATIONS (Cont'd.)

Figure		Page
I-5-2	Balloon Transmission Format	I-5-3
I-6-1	Signal Acquisition and Filtering	I-6-2
I-6-2	Ground Station Receiver Configuration	I-6-4
I-6-3	Data Processing Functional Flow Diagram	I-6-7
II-1-1	Principle of a Radio Interferometer	II-1-4
II-1-2	Position Location Geometry	II-1-4
II-1-3	Space Angle Accuracy as Function of Elevation Angle	II-1-5
II-1-4	Electrical Angle Accuracy as Function of Elevation Angle	II-1-5
II-1-5	Standard Deviation of Phase Measurement	II-1-7
II-1-6	Standard Deviation of Phase Angle Measurement Versus Equivalent Noise Filter Bandwidth	II-1-9
II-1-7	Velocity Errors (rms)	II-1-11
II-1-8	Baseline Calibration, 2-Dimensional Presentation	II-1-12
II-1-9	Baselines for Ambiguity Resolution	II-1-17
II-1-10	Baselines	II-1-20
II-1-11	Ambiguity Resolution with Offset Baselines	II-1-20
II-1-12	Non-Integer Solution for k_2 as Function of Error Made in Estimating k_2, Unsymmetrical CT Illumination	II-1-23
II-1-13	Non-Integer Solution for k_2 as Function of Error Made in Estimating k_2, Symmetrical CT Illumination	II-1-24
II-1-14	SNR and Standard Deviation of Electrical Phase Measurement Versus Elevation Angle E	II-1-28
II-1-15	Coverage with Position Location Error less than 2 km	II-1-30
II-1-16	Effect of Boom Motion on Electrical Phase	II-1-35
II-2-1	Beacon-Satellite Geometry	II-2-2
II-2-2	Coordinate Frame	II-2-20
II-3-1	Beacon-Earth-Satellite Multipath Geometry	II-3-3
II-3-2	Angle Difference Between Direct Ray and Multipath Ray	II-3-3
II-3-3	Geometry at the Interferometer	II-3-5

LIST OF ILLUSTRATIONS (Cont'd.)

Figure		Page
II-3-4	Multipath Electrical Angle	II-3-5
II-3-5	Maximum Position Error Resulting from Multipath as Function of Elevation Angle	II-3-9
II-3-6	Maximum Position Error Resulting from Multipath	II-3-10
II-3-7	Scattering Geometry and Explanations	II-3-14
II-3-8	Three-Dimensional Geometry of Reflection	II-3-15
II-3-9	Spectrum of Multipath Signal	II-3-22
II-3-10	Bandspread	II-3-23
II-3-11	Geometry for Approximate Determination of ξ_1	II-3-24
II-3-12	Multipath-to-Signal Ratio with Filtering	II-3-29
II-3-13	Multipath Performance Using Filters	II-3-29
II-4-1	Refraction	II-4-2
II-4-2	Ray Tracing	II-4-2
II-4-3	Refraction Error	II-4-4
II-5-1	Geometrical Relationship of Polarization Ellipses	II-5-2
II-5-2	Elliptically Polarized Plane Wave	II-5-2
II-6-1	Backfire Antenna with Flat Reflector	II-6-5
II-6-2	Backfire Antenna with Stepped Reflector	II-6-5
II-6-3	Short Backfire Antenna Characteristics	II-6-7
II-6-4	Angular Dependence of Helix Antenna Axial Ratio	II-6-11
II-6-5	Backfire Antenna	II-6-15
II-7-1	Baseline Definition	II-7-2
II-7-2	Boom Configuration	II-7-5
II-7-3	Satellite Dynamics	II-7-7
II-7-4	Thermal Deflections	II-7-9
II-7-5	Thermal Defections of Beryllium-Copper Boom with $\frac{D}{t} = 250L$	II-7-10
II-7-6	Logarithm of Twist Angle at Length L	II-7-16
II-7-7	Cantilever Frequency for a 1.0 in. diam Hiagelock TEE	II-7-19
II-7-8	Cantilever Frequency for a 0.5 in. diam Edgelock TEE	II-7-19

LIST OF ILLUSTRATIONS (Cont'd.)

Figure		Page
II-7-9	Antisymmetric System Natural Frequency for 1.0 in. diam TEE	II-7-20
II-7-10	Antisymmetric System Natural Frequency for 0.5 in. diam TEE	II-7-20
II-7-11	Gravity-Gradient Rod as Function of Boom Length	II-7-21
II-7-12	Antisymmetric Natural Frequency with Gravity-Gradient Rod, 0.5 in. TEE	II-7-22
II-7-13	Antisymmetric Natural Frequency with Gravity-Gradient Rod, 1.0 in. TEE	II-7-22
II-7-14	Simulation Model	II-7-23
II-7-15	Coordinate Frame for Dynamic Simulation	II-7-24
II-7-16	Absolute Maximum Baseline Rate	II-7-27
II-7-17	Hub Rotation (Φ)	II-7-29
II-7-18	Tip Deflection Relative to Body Axis (η)	II-7-29
II-7-19	Baseline Rate of Motion	II-7-30
II-7-20	Angular Baseline Position (α)	II-7-30
II-7-21	Attitude Rate Uncertainty	II-7-32
II-7-22	Disturbance and Correction Torques	II-7-32
II-7-23	System Behavior	II-7-34
II-8-1	Essential Elements for a Simplified Interferometer Receiver System	II-8-2
II-8-2	Functional Diagram of Satellite Repeater	II-8-3
II-8-3	Local Oscillator Synthesizer	II-8-4
II-8-4	Alternate Method of Signal Transmission from Antenna to Spacecraft	II-8-5
II-8-5	Typical Spectrum Format at Input to Repeater Upconverter	II-8-7
II-8-6	Upconverter Output Power Amplifier Configuration	II-8-9
II-8-7	Signal Acquisition and Filtering	II-8-11
II-8-8	Ground Station Receiver Configuration	II-8-13
II-8-9	Digital Phase Meter	II-8-15

LIST OF ILLUSTRATIONS (Cont'd.)

Figure		Page
II-9-1	Functional Diagram, Balloon Electronics	II-9-3
II-9-2	Radiation Pattern of Planar Spiral Mounted 0.35λ above a Ground Plane	II-9-5
II-9-3	Successive Approximation, A/D Converter	II-9-8
II-9-4	Balloon Transmission Format	II-9-9

LIST OF TABLES

Number		Page
I-1-1	System Parameters	I-1-5
I-2-1	System Concepts Using Interferometers	I-2-1
I-2-2	Link Power Budget	I-2-8
I-2-3	Error Summary	I-2-10
I-3-1	Residual Phase Error Resulting from Polarization Mismatch	I-3-6
I-5-1	Balloon Package Power Requirements	I-5-4
I-6-1	Preliminary Instruction Count per Beacon Position Calculation	I-6-5
II-1-1	Link Power Budget	II-1-27
II-3-1	Differential Doppler Shift Δf (Hz)	II-3-26
II-5-1	Polarization Errors	II-5-8
II-5-2	Residual Polarization Phase Error (worst cases)	II-5-9
II-6-1	Interferometer Antenna Element Requirements	II-6-2
II-6-2	Gain of Backfire Antenna	II-6-6
II-6-3	Three-dB Beamwidth of Broadside Half-Wave Dipole Array with Half-Wave Spacing Between Dipoles	II-6-8
II-6-4	Characteristics of the Candidate Antenna Elements	II-6-13
II-7-1	Boom Parameters	II-7-4
II-9-1	Balloon Platform Requirements	II-9-2
II-9-2	Balloon Package Power Requirements	II-9-11

FOREWORD

This study represents the combined efforts of members of the Communication and Engineering Sciences Center of IBM. Consequently, assigning credit to specific sections of the report is difficult. Dr. E. I. Muehldorf was project manager of the study and principle contributor to the studies on propagation effects. Mr. J. E. Henrich and Mr. D. P. Bedford contributed to mathematical modeling of the interferometer and error analysis. Dr. C. T. Tsitsera was concerned primarily with system considerations. Mr. S. Cost contributed to the electronic design. Mr. E. Kramer contributed to the antenna study.

This study was carried out with Fairchild-Hiller Corporation in Germantown, Maryland, as subcontractor for the mechanical portions. The principal contributor was Mr. J. Talcott.

The study team received valuable assistance and guidance from members of the Goddard Space Flight Center, including Mr. M. Maxwell, who was technical officer for the contract, and Mr. F. X. Downey and Mr. R. Shelly.

Section I-1

INTRODUCTION

Angle measuring techniques employing spaceborne interferometers have previously been considered for use in navigation, air traffic control, and wind measurement balloon systems.[1,2]

This study evaluates a system which will locate to within 1 km 15,000 meteorological balloons scattered throughout the world at known altitudes to determine wind velocity profiles. These balloon beacons must be able to transmit two data measurements, pressure and temperature for example, to an accuracy of 1 percent as they are being located. The balloon platform electronics, including solar power supply, when produced in quantity, must be frangible and inexpensive.

The most economical balloon package is merely an RF beacon uplink with no command downlink. A geosynchronous satellite with a long baseline crossed interferometer on the spacecraft is used to determine the direction to the balloon. This, together with the balloon altitude, determines position. The uplink from the balloon will be in L-band. The signals received by the interferometer antennas are multiplexed and transmitted to a ground processing center, where all phase measurements are made. Three geostationary satellites provide global coverage except in the vicinity of the poles.

The Interferometer Position Location Concept described above was analyzed and evaluated. Several implementations of the concept were considered, and the most promising was analyzed in detail. The effort was primarily on the system design, with less effort on the spacecraft and ground systems and with the least emphasis on the balloon electronic package.

The report is divided into two parts. Part I is a summary of the results of the study. Details of tradeoff studies, error analyses, and derivations are contained in Part II, which contains nine sections. The first section discusses systems considerations and tradeoff analysis, error budgets, choice of frequency and length of baseline, calibration considerations, multiple-access method, and effects of boom motion.

Section II-2 presents a derivation of position error equations in terms of beacon phase noises, calibration phase noise, ephemeris and ground station survey errors. A computer program, which simulates the geometry of moving platforms and satellites and provides a statistical error analysis is also described.

Section II-3 gives a detail derivation of multipath effects for an interferometer, and Section II-4 contains an analysis of refraction errors for the three frequencies, i.e., 400, 1000, and 1600 MHz. In Section II-5, errors caused by antenna polarization mismatch are derived and analyzed. This is followed by Section II-6 which presents the considerations for the interferometer antenna selection. Section II-7 Mechanical Studies, includes analysis of boom dynamics and thermal effects, and Section II-8 describes the satellite hardware and the signal processing and phase extraction in the ground station. The last section of Part II, Section II-9, gives the balloon beacon considerations.

I-1.1 SUMMARY AND CONCLUSIONS

Position location to an accuracy of 1 km (1 σ error) by means of an interferometer in geostationary orbit is feasible. Wind velocity is determined from successively determined positions. Thus the wind velocity (averaged over 2 hours) can be estimated to approximately 1 km/hour. For weather prediction this is considered to be excellent.

The system concept is shown in Figure I-1-1. There are four calibration transmitters, a crossed baseline interferometer with seven antennas, and a ground receiving site. The electronics in the satellite perform the function of

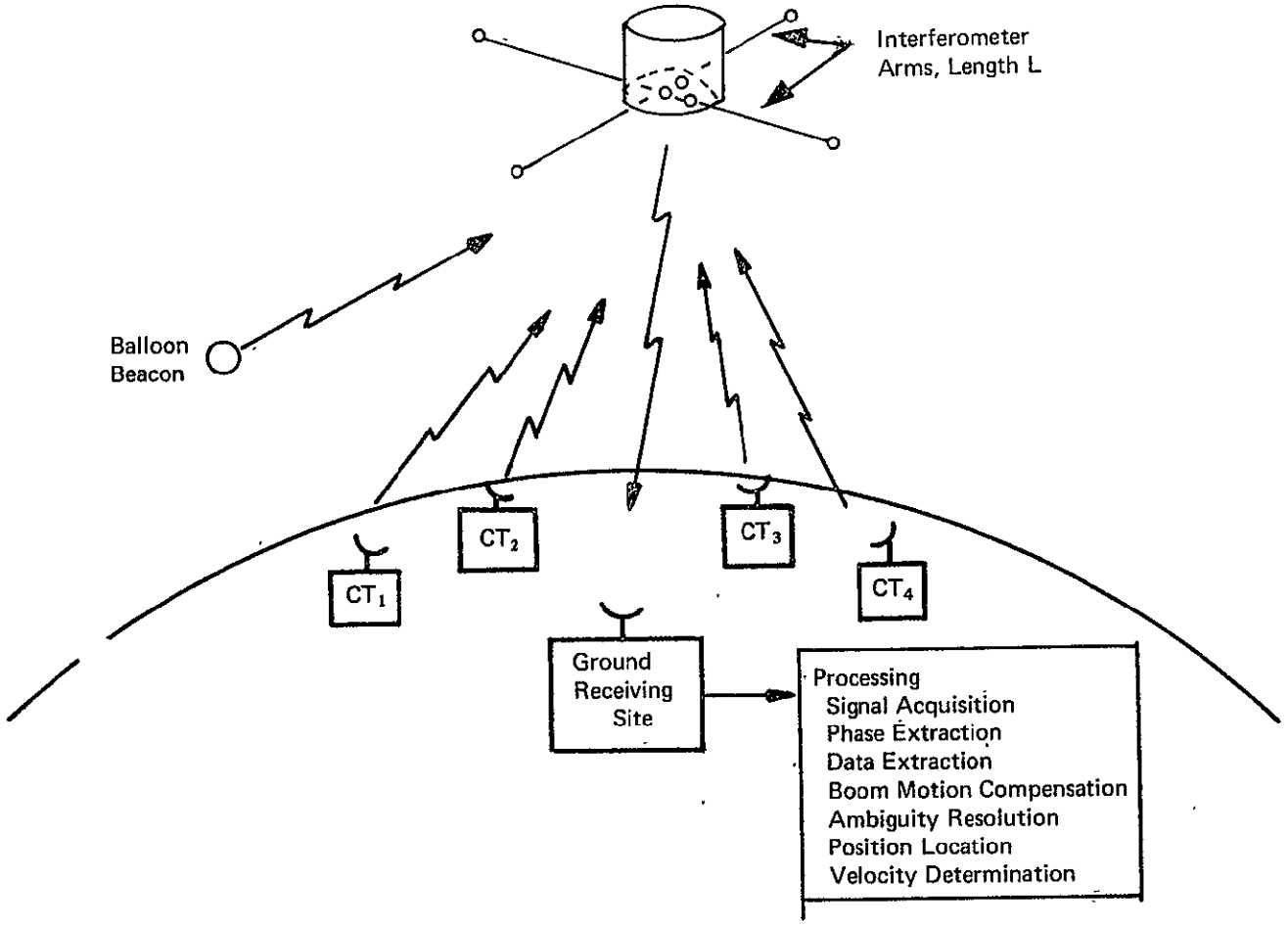

Figure I-1-1. System Concept

multiplexing the signals received by the seven antennas and transmitting the composite spectrum to the ground receiver. All acquisition functions and phase extractions are performed on the ground. The system parameters are summarized in Table I-1-1.

A nominal operating frequency of 1600 MHz was chosen as a compromise for the following reasons:

a. Multipath signal is more likely to be diffuse and bandspread than at lower frequencies

b. Ionospheric refraction is less than at lower frequencies

c. Phase accuracy requirement for a given baseline length is less than for lower frequencies

d. At higher frequencies, the decreased signal power to noise density ratio increases acquisition and phase extraction problems

e. Generating higher frequencies is more costly in terms of balloon dc power.

The baseline length of 400 wavelengths was chosen as a compromise between a smaller $\frac{L}{\lambda}$ which makes phase measurement problem more acute to meet 1 km accuracy and a larger $\frac{L}{\lambda}$ which increases the ambiguity resolution problem.

A random multiple-access scheme is recommended as it requires minimum equipment in the balloon. Separation of the balloon signals is obtained through the randomness of balloon transmissions in time and frequency. A 10 s transmission time is recommended assuming a 1 W balloon transmitter with essentially a hemispheric coverage antenna. Increasing the transmission time beyond 10 s or decreasing the 2-hour interval between transmissions would increase the multiple-access problem.

The data transmissions (9 bps) are biphase modulated. The bandwidth of the signals is thus small, and phase measurements can be made simultaneously with data extraction.

Table I-1-1

SYSTEM PARAMETERS

Operating Frequency (uplink)	1600 MHz (nominal)
Baselines (vernier)	2 orthogonal; 75 m 400 wavelengths (400 λ)
Ambiguity Resolving Baselines	3 λ, 190 λ, 400 λ (physical) 20 λ (differential)
Interferometer Arms	Extendible booms
Interferometer Antennas	Short backfire, gain 17.5 dB on axis, 22° half power beamwidth
Polarization	Circular for all antennas
Access Technique	Random (in frequency and time)
Balloon	
Beacon Power	1 W
Oscillator Stability	1 part in 10^5
Transmission Time	10 s every 2 h
Data Modulation	Phase shift keying (biphase)
Bit Rate	9 bps
Calibration Transmitter	
Number	4
ERP	20 dBw
Transmission Time	Continuous
Downlink Frequency	X-band
Bandwidth	1 MHz
Signal Processing	
Acquisition Method	Phase-locked loop aided by comb filter
Acquisition Time (frequency)	0.3 s
Beacon Phase Measurement Time	9.7 s
Filter Bandwidths (minimum)	40 Hz
Effective Noise Bandwidth	0.1 Hz
Data Processing (for each satellite)	
Average Simultaneous Balloon Transmissions	7
Position Fix Rate	0.7 s
Computer Operations (equivalent additions)	20,000 instructions/s

The baselines are formed by four extendible booms. The important requirements of the booms are:

a. They must be deployable (including coaxial cable) with an antenna at the end

b. The deployment mechanism must have provision to twist boom on initial deployment and as required

c. Boom thermal distortion must be low

d. Angular rates of baseline (or boom tip) motion must be low.

The second and third requirements are based primarily on antenna gain considerations. The design goal of maintaining antenna pointing accuracy of $\pm 1^{\circ}$ is a more stringent requirement for the booms than has been imposed in other applications. For this reason, some additional testing of booms in a thermal vacuum chamber is required and possibly some development effort will be required.

The last requirement minimizes the effect of boom motion on the phase extraction. Stiff booms have a higher natural frequency of vibration than flexible booms, but the amplitude of the vibrations is also less, so that the maximum angular rate of baseline motion tends to be independent of boom stiffness. A typical rate of phase change due to boom motion for a 400-wavelength system is 2 electrical degs maximum. Both stiff and flexible booms exhibit this property.

The phase measurement accuracies required to meet a 1 km (1σ) position location accuracy are approximately:

a. 0.7° (1σ) for the beacon

b. 0.5° (1σ) for the calibration transmitters (3.6 s smoothing time).

Phase biases common to both calibration transmitter and beacon phase measurements affect position location accuracy one or two orders of magnitude less than random phase errors.

Four calibration transmitters, emitting CW signals of 20 dBW ERP, are used to continously calibrate the system. The calibration consists of:

a. Determining the instantaneous lengths and orientation of the baselines
b. Estimating the differential phase biases.

Phase measurements of the calibration signals are made at 0.1 s intervals, which is sufficiently short that boom motion cannot appreciably degrade these phase measurements. The phase accuracy of 0.5 deg (1σ) is achieved by fitting 36 measurements to a first-order polynonimal which models the boom motion for 3.6 s.

Errors in position location due to multipath are highly geometry dependent. At an elevation angle of 20 deg and a balloon altitude of 9 km, an equivalent signal-to-multipath power ratio of 36 dB is required for an error of 1 km or less. Directly under the satellite, multipath will not cause an error, unless it is large enough to cause fading and thus decrease the signal-to-thermal noise power. The antenna on the balloon package can be designed to give a gain in the direct direction relative to the multipath direction of 10 dB or more. Attenuation due to reflection and use of circular polarization will contribute on the order of 6 dB advantage to the direct signal. Effective narrowband filtering will suppress multipath, which is due to diffuse scattering, because the relative motion of the balloon and the earth's surface produce bandspreading.

I-1.2 RECOMMENDATIONS

Studies to date have indicated that the interferometer position location concept is feasible. It is recommended, therefore, that the program be extended. The following 4-step program, culminating in a flight experiment, is suggested:

a. Laboratory Experimentation and Analysis—to verify that phase measurements can be made to the required accuracy in the multiple-access, low signal-to-noise power density environment required; to test phase center stability of circularly polarized antennas as a function of angle off boresight and of frequency; to continue the analysis efforts, especially including tradeoff among interferometer antenna gain, beacon power and allowable boom twisting and flexing.

b. Boom Development and Testing-to test samples of promising boom designs in a thermal vaccum chamber for thermal bending and thermal twisting; to develop a boom package including deployment mechanism and boom with enclosed coaxial cable; to continue the dynamic analysis of booms and interaction with spacecraft

c. Ground-Based Experiment—build a single baseline interferometer (including one movable antenna) and illuminate with three transmitters (two calibration transmitters and one beacon to be located); to demonstrate that the interferometer baseline can be calibrated and the unknown located with boom motion present

d. Flight Experiment—to demonstrate that booms can be deployed and can maintain the antennas pointed to the desired accuracy; to demonstrate that multipath effects can be kept to acceptable levels; to complete the demonstration of the concept and obtain data to allow an operational system to be designed and built.

Section I-2

USE OF INTERFEROMETER FOR POSITION LOCATION

System concepts which use spaceborne interferometers for position location are shown in Table I-2-1.

Table I-2-1

SYSTEM CONCEPTS USING INTERFEROMETERS

System Concept	Interferometer Characteristics	Comments
One Direction and Altitude	Transmitting or Receiving	Altitude of user independently determined
One Direction and Range	Transmitting or Receiving	Transponder required to obtain range
Two Directions	Transmitting or Receiving	Two satellites required

The system concept considered in detail in this report is the first one listed, implemented with a receiving interferometer. A constant pressure weather balloon drifts at an approximately constant altitude. This altitude plus the direction from the spaceborne interferometer determines the position.

I-2.1 INTERFEROMETER PRINCIPLE

A radio interferometer determines the angular position of an RF signal source by measuring the difference in radio signal path lengths from the emitting source to each of a pair of antennas (see Figure I-2-1). The phase difference (γ) is related to the angle between the baseline and arriving wavefront (φ) by the following equation:

$$\gamma = 2\pi \frac{L}{\lambda} \sin \varphi .$$

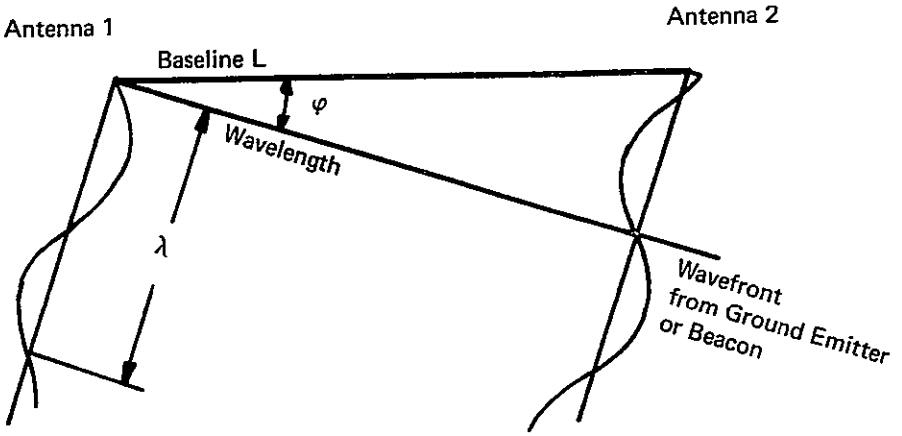

Figure I-2-1. Principle of Radio Interferometer

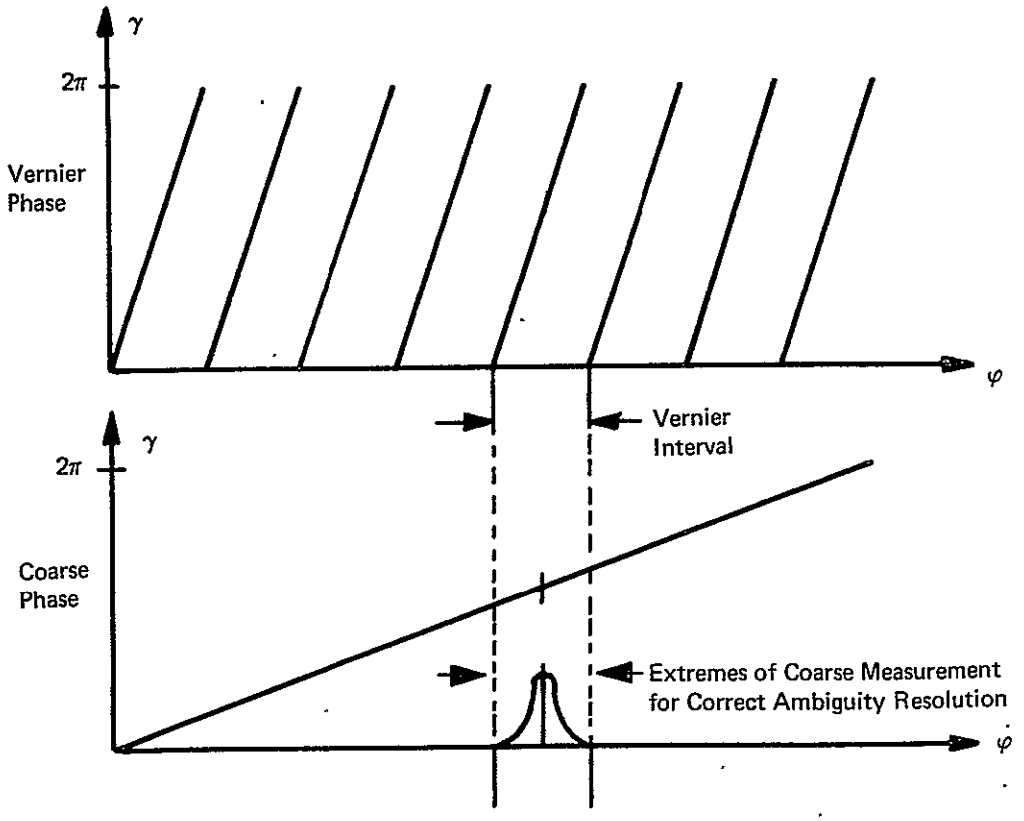

Figure I-2-2. Ambiguity Resolution

For large baselines $L >> \lambda$, a small change in φ results in a change in γ exceeding 2π, resulting in ambiguous regions (lanes) across the earth's surface. This is shown in the upper lines of Figure I-2-2. To resolve the angle completely and determine in which vernier interval the measurements falls, coarse measurements with one or more short baselines are needed. This is shown in the bottom line of Figure I-2-2, where the permissible coarse space angle measurement is shown covering one of the vernier intervals.

I-2.2 LONG BASELINE SPACEBORNE INTERFEROMETER

To locate a balloon to an accuracy of 1 km, a spaceborne interferometer must be able to resolve space angles φ to about 10^{-3} deg. It can be seen from Equation I-2-1 that, for small space angles, the electrical angle is obtained by multiplying with $\frac{2\pi L}{\lambda}$, which may be called the "magnification" of the interferometer.

Although the accuracy of the electrical phase measurement may be limited, any desired fineness of space angle resolution can be obtained by a sufficiently large ratio of baseline length to wavelength. The effect of varying $\frac{L}{\lambda}$ is illustrated in Figure I-2-3, which shows the required phase measurement accuracy for 1-km resolution as a function of elevation angle from the beacon to the interferometer with $\frac{L}{\lambda}$ as a parameter. However, increasing the baseline to gain resolution is limited by certain effects such as structural considerations and pointing accuracy of the antenna elements (hence, less usable antenna gain). For long baselines consisting of lightweight, flexible structures, relatively large boom tip motions may be encountered. From Figure I-2-3 it is apparent that, for a fixed wavefront direction, a rotating baseline will produce a time-varying phase history. Since practical considerations related to SNR necessitate measuring this phase over several seconds, the baseline rotation produces an erroneous indication of phase. There are essentially two solutions to this problem:

a. Reduce the rotation to negligible amounts

b. Reconstruct the time-varying phase during the measurement interval and remove the unwanted effect.

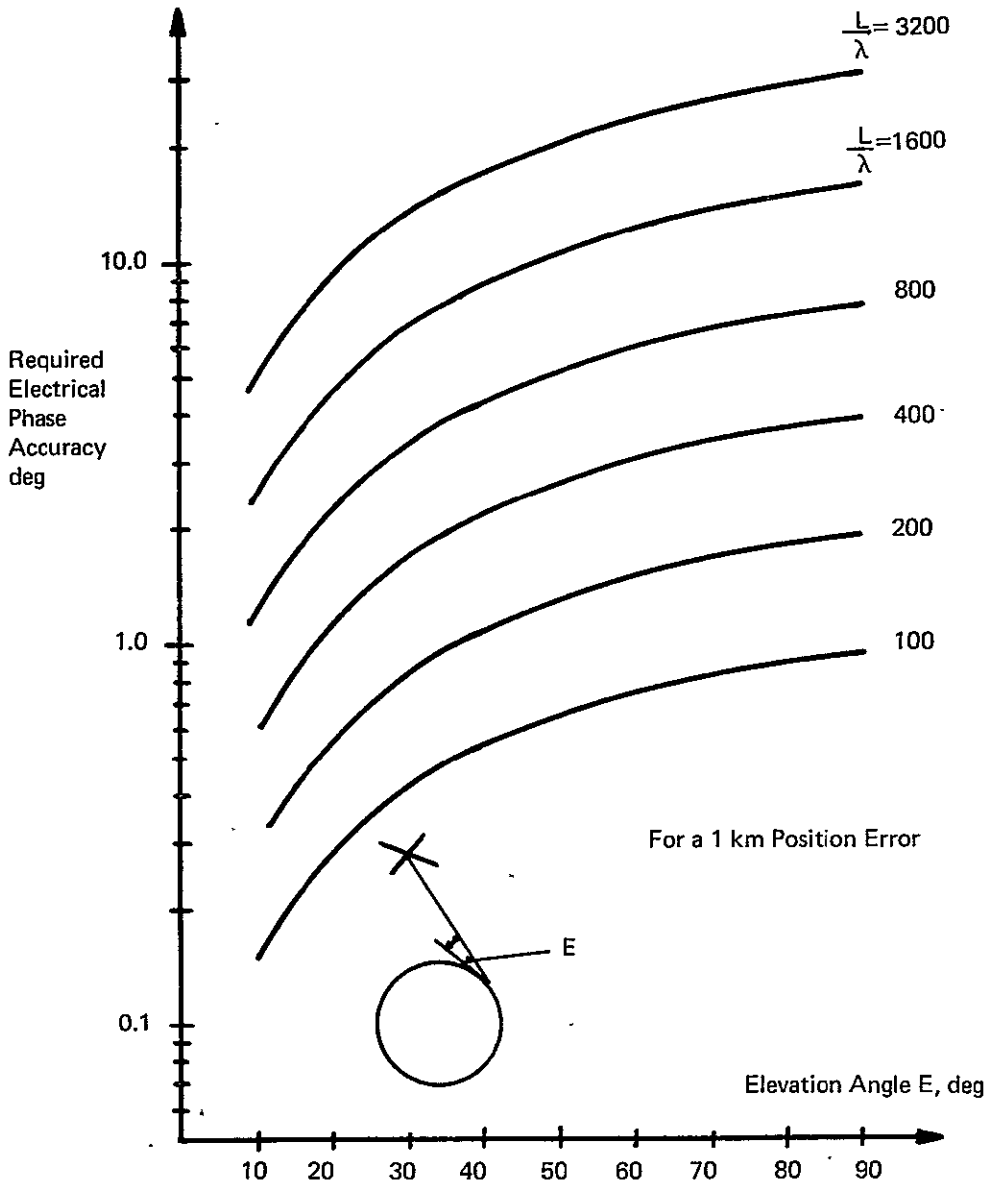

Figure I-2-3. Required Phase Accuracy

Since the former solution did not appear to be practical for the balloon signals, the latter solution was chosen. The process of reconstructing the phase and the removal of unwanted effects will be referred to as boom motion compensation.

I-2.3 AMBIGUITY RESOLUTION

There are ambiguities in the space angle measured at the interferometer every $\frac{\lambda}{L}$ rad. This corresponds to a distance of approximately 80 km on the earth's surface for a 400-wavelength system. A short baseline of 3 wavelengths is required in order to have no ambiguities on the earth's surface. The SNR available for the phase measurement for the balloons precludes resolving all the ambiguities of the 400-wavelength system in one step.

A system such as shown in Figure I-2-4 is indicated.

Seven antennas are used; one of these is common to the two crossed arms. The individual baselines used are:

a. 3 λ —formed by antennas 2 and 3

b. 20 λ —a differential baseline formed by the difference between the 210 baseline and the 190 baseline

c. 190 λ —formed by antennas 1 and 2

d. 210 λ —formed by antennas 2 and 4

e. 400 λ —formed by antennas 1 and 4.

Ambiguity resolution is performed in two steps. The 3 λ baseline resolves the ambiguities in the 20 λ baseline. The 20 λ baseline is used to resolve the ambiguities in the 400 λ baseline.

There is no necessity for the baselines to be colinear, since they are independently calibrated.

I-2.4 CALIBRATION

Calibration is to estimate accurately the length and orientation of two nominally orthogonal baselines. The principle of the calibration technique is perhaps best explained via Equation I-2-1. The unknowns in this equation,

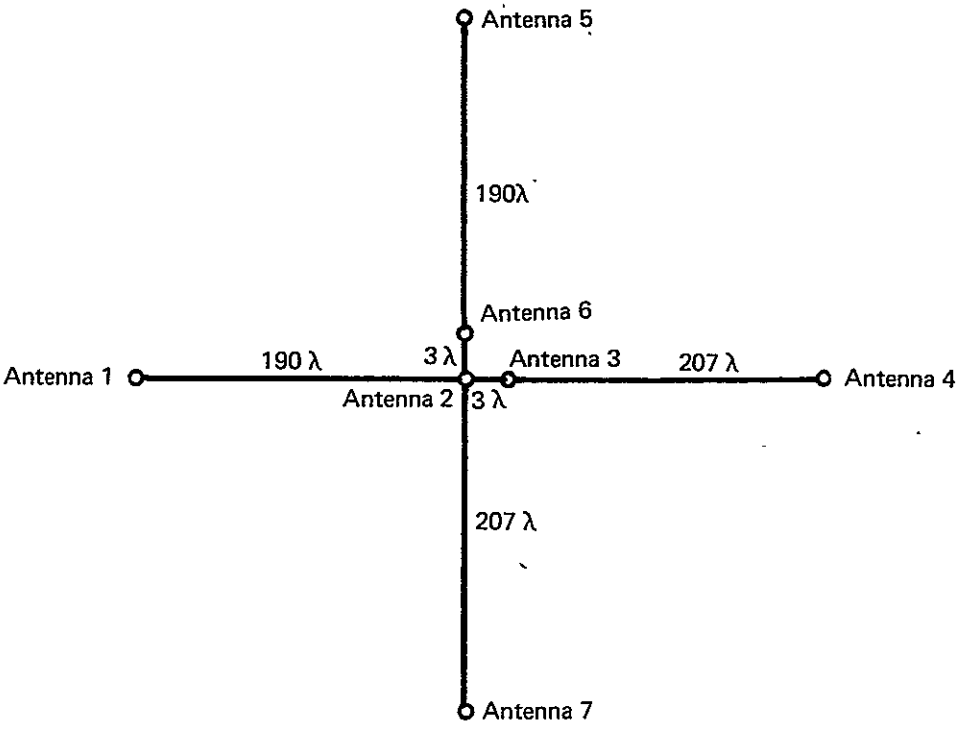

Figure I-2-4. Baselines

sofar as the calibration is concerned, are L and φ. If two γ's are measured from two different illuminators such that the relative angle between the wavefronts is known, there are now two equations in two unknowns. Solving these equations simultaneously yields L and φ.

In three dimensions the baselines are described by a length and two angles. A third equation is therefore required, and it is obtained by incorporating a third phase measurement from a third illuminator. These illuminators are called calibration transmitters (CTs).

Figure I-1-1, System Concept, shows four CTs instead of the three referred to above. The fourth CT is included to provide a fourth phase measurement which accommodates a fourth unknown, the phase bias caused by phase shifts in the satellite and in the ground equipment, e.g., unequal cable lengths.

The fact that there are multiple baselines has no impact on the number of CTs. Each baseline is illuminated from four CTs and the length, orientation, and phase bias are determined independently of all other baselines. Thus four CTs. will calibrate any number of baselines. This is used to advantage in calibrating the coarse as well as the vernier baselines.

The compound motion of the spacecraft and the booms causes the baseline orientations to change continuously and fairly rapidly. This is the primary reason for performing continuous calibration.

I-2.5 LINK CALCULATION

The link calculations are presented for the calibration transmitters (ground stations) and the balloon beacons in Table I-2-2. The link budget for the calibration transmitter is shown only at the lowest elevation angle, or worst case in this respect. The calibration transmitter effective radiated power (ERP) of 20 dBW requires only a 1 W transmitter and a 3 ft dish, for example, and can be easily increased to provide additional margin.

The link power budget for the balloon beacon is much more critical, so that it is shown for three elevation angles. A power of 1 W is assumed for

Table I-2-2.

LINK POWER BUDGET

(Emitter through Spacecraft-to-Ground Receiver)

Emitter	Calibration Transmitter	Balloon		
		E = 20°	E = 30°	E = 90°
Transmitter Power (dBW)	-	0	0	0
Transmit Antenna Gain (dB)	-	+0.7	+3.0	+2.2
ERP (dBW)	20	+0.7	+3.0	+2.2
Path Loss (dB)	-189	-188.5	-188	187.5
Polarization Loss (dB)	-0.5	-0.5	-0.5	-0.5
Interferometer Antenna Gain (dB)	+15	+15	+15.5	+17
Received Signal Power (dBW)	-154.5	-173.1	-170.3	-168.9
Receiver Noise Figure (dB)	+4.5	+4.5	+4.5	+4.5
Receiver Noise Density (dBW/Hz))	-199.5	-199.5	-199.5	-199.5
Signal-to-Noise Density Ratio (dB-Hz)	+45	-26.4	+29.2	+30.6
Time or Bandwidth Enhancement Factor (dB)	0*	10**	10**	10**
Final Signal-to-Noise Power Ratio (dB)	+45	+36.4	+39.2	+40.6
Resultant $\sigma_{\Delta\gamma}$ of Phase Measurement, (electrical deg, due to thermal noise)	0.33°	0.9°	0.6°	0.5

σ = standard deviation = $57.3\ (SNR)^{-1/2}$
SNR = power signal-to-noise ratio

* 1 s effective integration time.
** 10 s effective integration time.

the balloon beacon. If a nominal 3 dB is included in the link for margin, a modest increase in the standard deviation of the phase measurement due to thermal noise results. For example, at an elevation angle of 30 deg, the standard deviation would be 0.85 deg instead of 0.6 deg.

I-2.6 ERROR BUDGET

Table I-2-3 shows the error budget for an elevation angle of 30 deg. The position location error is a function of the 3-dimensional system geometry, so that the results presented are for a typical 30 deg elevation angle. Details of position fix errors as a function of longitude and latitude, which were obtained from a simulation program, are shown in subsection I-2.7.

As can be seen, the major sources of error are the phase measurements of the beacon and calibration signals and the multipath error. Each phase measurement error is a result of both thermal noise and instrumentation errors. The latter includes effects which are not eliminated by using the calibration transmitter signals. Systematic errors, such as phase biases, are eliminated from affecting the position location determination.

The multipath error is a function of balloon altitude, velocity, and location, as well as antenna pattern, polarization, and surface reflection coefficient. The 0.8 km error assumes an altitude of 9 km and a velocity of 30 km/hr. The antenna gain in the direction of the satellite, compared to the gain in the multipath direction, is taken to be 10 dB.

The position location error due to calibration transmitter location errors is less than for the satellite ephemeris error because there are four calibration transmitters and the resulting position location error is reduced somewhat.

The altitude error of 100 m results in a 0.2-km position error at this elevation angle. If the altitude of the balloon does not change between position fixes, the velocity determined from these fixes will be negligibly affected by the altitude error.

Table I-2-3

ERROR SUMMARY

Error Source	Phase Error	Error (in km) (1 σ, absolute)
1. Beacon Phase Measurement* Thermal Noise 0.6° Instrumentation Errors 0.3°	0.67°	0.45
2. Calibration Transmitter Phase Measurement* Thermal Noise 0.33° Instrumentation Errors 0.3°	0.45	0.30
3. Multipath (9 km Altitude, vel = 30 km/h)		0.80
4. Satellite Ephemeris Error (60 m)		0.10
5. Calibration Transmitter Location Error (60 m)		0.03
6. Altitude Error (100 m)		0.20
7. Antenna Phase Center	0.20°	0.10
8. Refraction Error		0.01
9. Polarization Error	0.10°	0.05
TOTAL ERROR (Root Sum Square)		1.0 km

Elevation Angle = 30°

*Root sum square of thermal noise and instrumentation errors.

Errors due to antenna phase center changes, refraction errors, and errors due to polarization effects are relatively small.

The resulting total error depends upon the statistics of the individual errors. To a first approximation we can assume the errors add in a root sum square manner, so that the resulting position location error is 1 km.

The thermal noise errors shown are 1σ, so that the measurements will be within the accuracy shown 68 percent of the time. If, as a first approximation, we assume that all errors have Gaussian statistics, the errors will be less than a 3σ value, or the position location error will be less than 3 km more than 99 percent of the time.

I-2.7 ACCURACY - POSITION LOCATION

Figures I-2-5, I-2-6, and I-2-7 summarize the accuracy of the system based on the error model and CT locations specified in the legend. Circular error probable (CEP) is defined as the radius R such that there is a 50 percent probability that the position location error will be less than R. For example, a CEP = 1.5 km means that the probability of making a 1.5-km position location error in any direction from the true location is less than 50 percent.

Figures I-2-6 and I-2-7 give the 1σ North-South and East-West components of position error. The error ellipses are, for the most part, nearly circular as the correlations between East-West and North-South components are small (less than 0.3) and the standard deviations are about equal. Exceptions were noted in the northern latitudes (e.g., above 50 deg) where the correlations exceeded 0.7, causing a noticeable degree of ellipticity.

The contours are almost completely dependent on the beacon and CT phase noise and much less dependent on the survey errors, the satellite ephemeris, and beacon altitude errors.

The orientation of the baselines is not critical. If the baselines were rotated 45 deg, the shape of the contours would change somewhat, but the range of CEPs would remain the same.

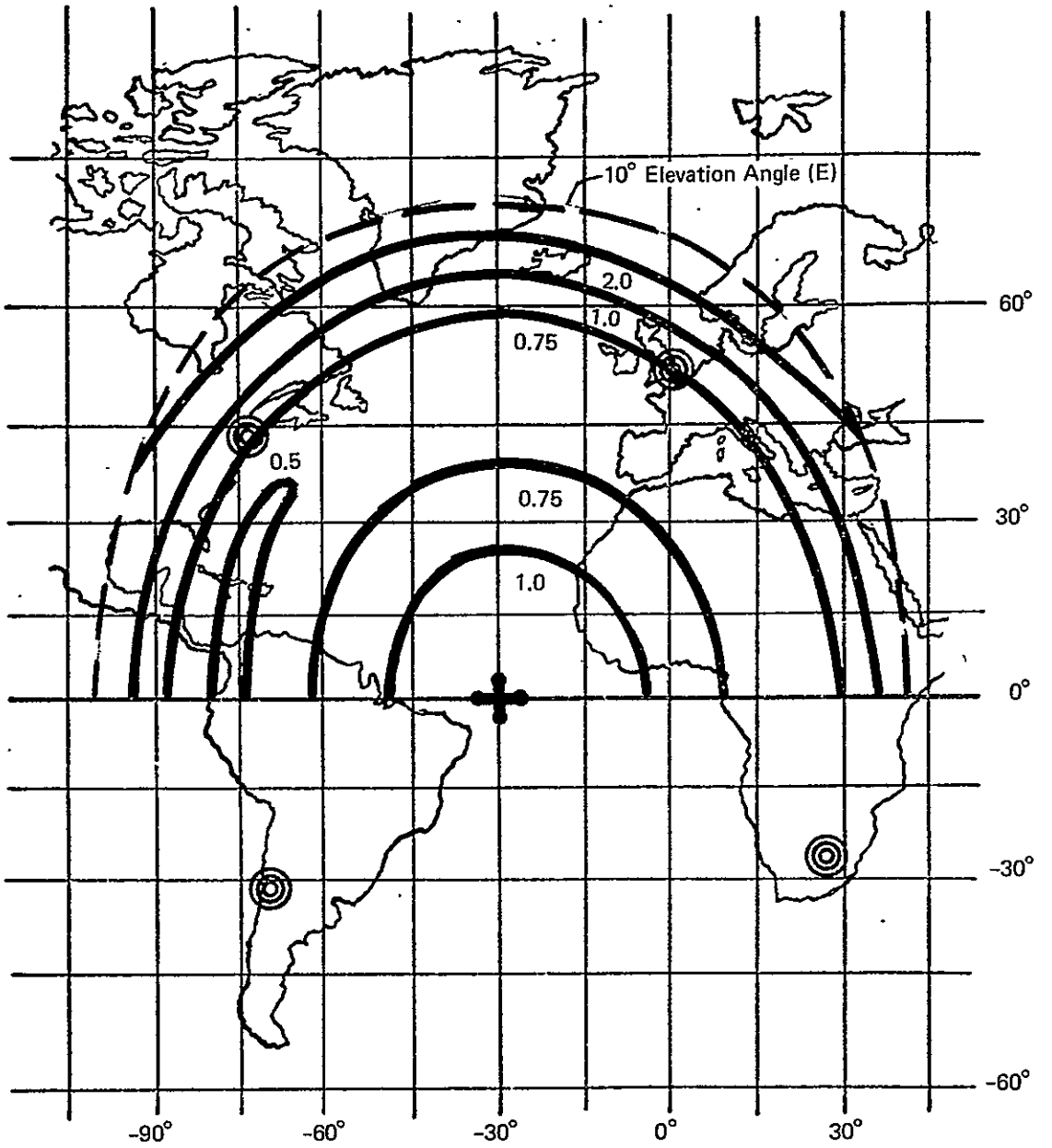

Assumptions:

Calibration Transmitters (CTs)	1 σ Errors
Rosman	CT Noise 0.45°
Santiago	CT Survey (La, Lo, h) 10, 10, 3 m
London	Satellite Ephemeris (N, T, R) 60, 60, 10 m
Johannesburg	Altitude 100 m
	Beacon Noise 0.6° @ E = 90°
	0.9° @ E = 20°

Figure I-2-5. Beacon Horizontal Position CEP in km, (Multipath Excluded)

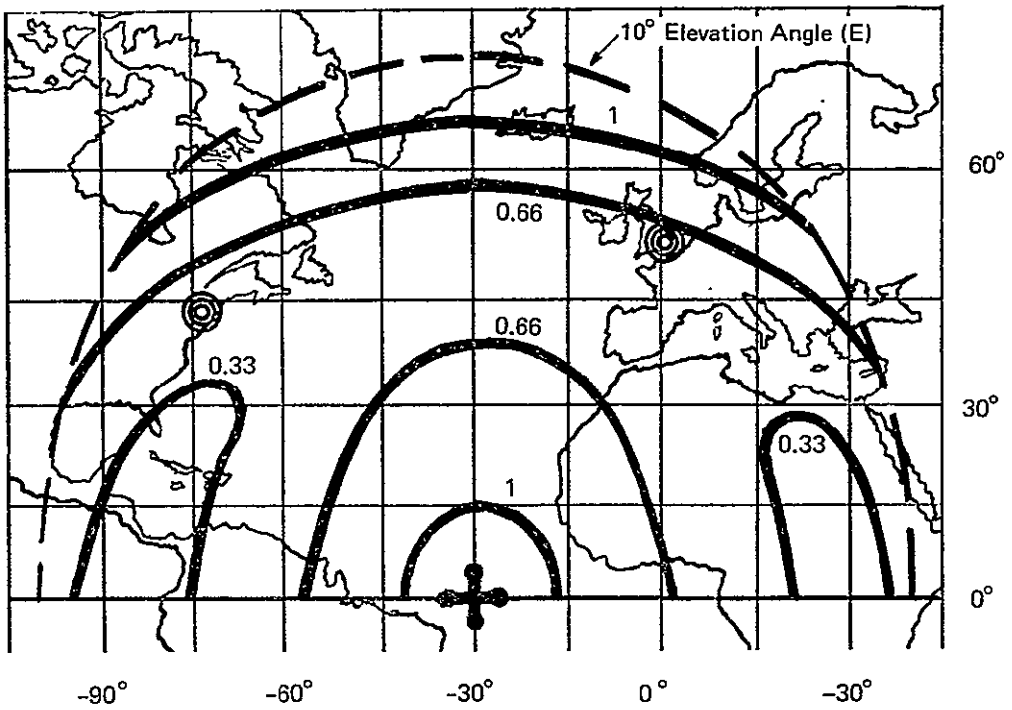

NOTE: Assumptions are the same as in Figure I-2-5.

Figure I-2-6. Beacon North-South Position Standard Deviation (1σ) in km (Multipath Excluded)

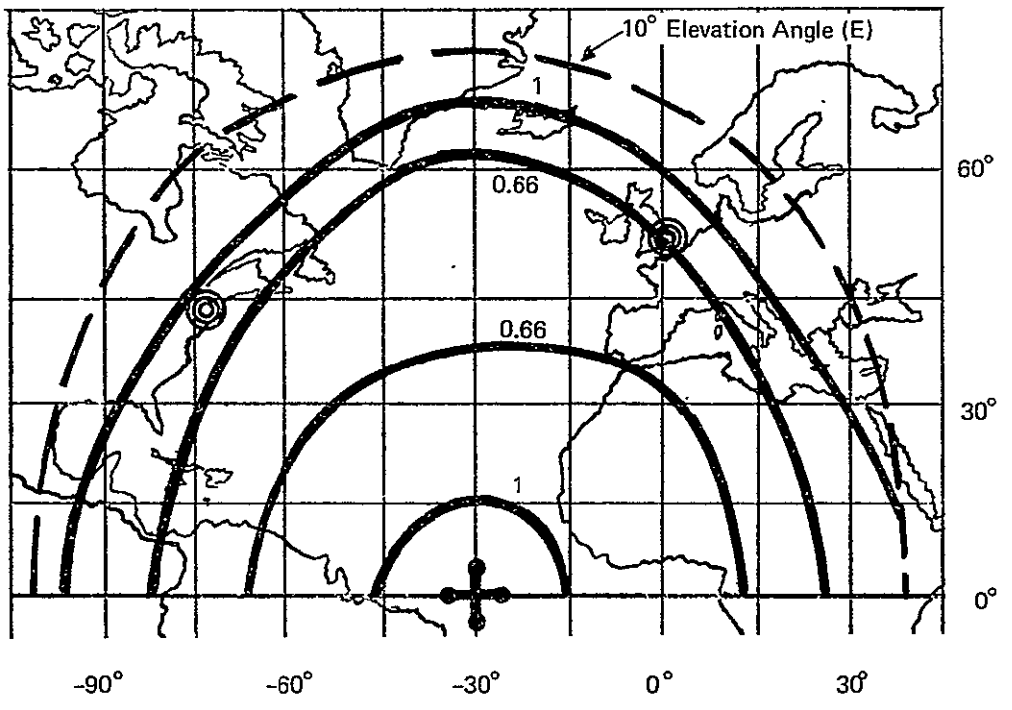

NOTE: Assumptions are the same as in Figure I-2-5.

Figure I-2-7. Beacon East-West Position Standard Deviation (1σ) in km (Multipath Excluded)

The locations of the CTs are not critical, though it is advantageous to have them spaced uniformly about the sub-satellite point with about a 20 deg to 30 deg elevation angle to the satellite.

The accuracy in the Northern and Southern hemispheres is roughly the same.

The figures do not include the error caused by multipath. The multipath error (see subsection I-3.1 and Section II-3) is included in the error budget (see subsection I-2.6). To include multipath, an error component of approximately 1 km for low elevation angles and smaller for high elevation angles must be added (root sum square) to the error shown in figures I-2-5 to I-2-7.

I-2.8 ACCURACY - VELOCITY

The velocity of the beacons is estimated by taking the difference between two successive position location fixes and dividing by the time between fixes. It is assumed that the beacons move at a constant rate, and the velocity estimate is referenced to a point halfway between fixes.

Figures I-2-8, I-2-9, and I-2-10 summarize the accuracy of the velocity estimate. The error models and CT locations are identical to those used for the position location accuracy shown in Figure I-2-5. In Figures I-2-8 and I-2-9, the contours represent the standard deviation of the velocity error components (1σ) in the North-South and East-West directions.

Figure I-2-10 gives the 50 percent error probability contours that the velocity error in any direction will not exceed the value indicated on that contour.

I-2.9 ERROR BREAKDOWN - POSITION LOCATION

Since the system uses four CTs to calibrate most of the parameters (such as baseline lengths, orthogonality, and phase biases) involved in the position location calculations, the accuracy of this calibration and hence the position location is dependent on the random CT phase errors and not on phase biases, baseline lengths, and orthogonality of baselines. However the CT surveys, the

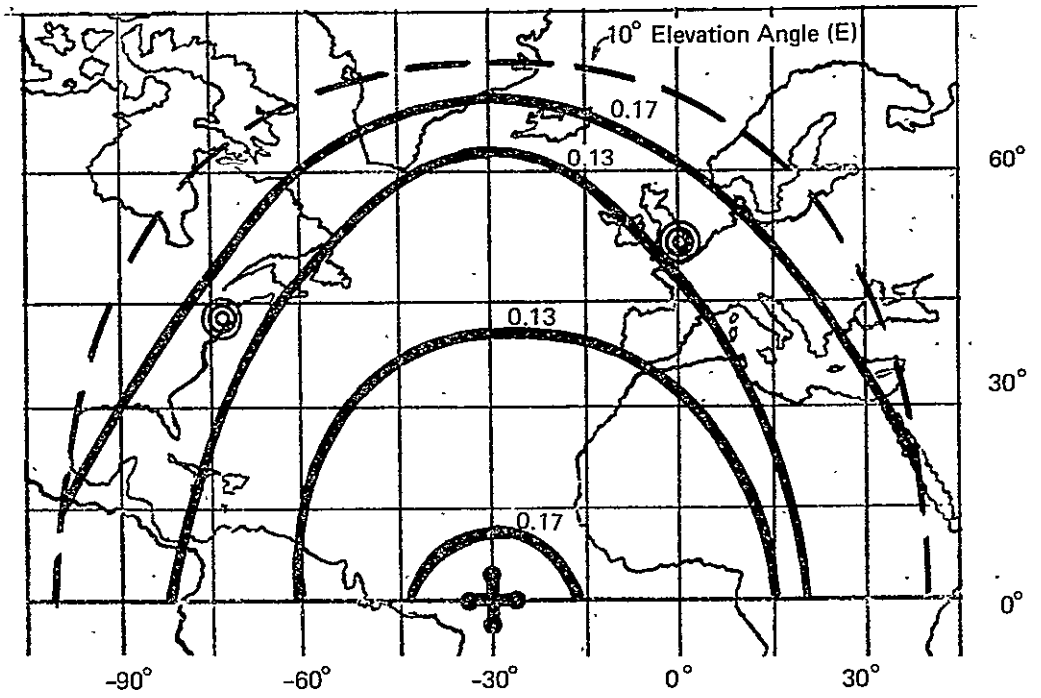

NOTE: Assumptions are the same as for Figure I-2-10.

Figure I-2-8. North-South Velocity Standard Deviation (1σ) in m/s

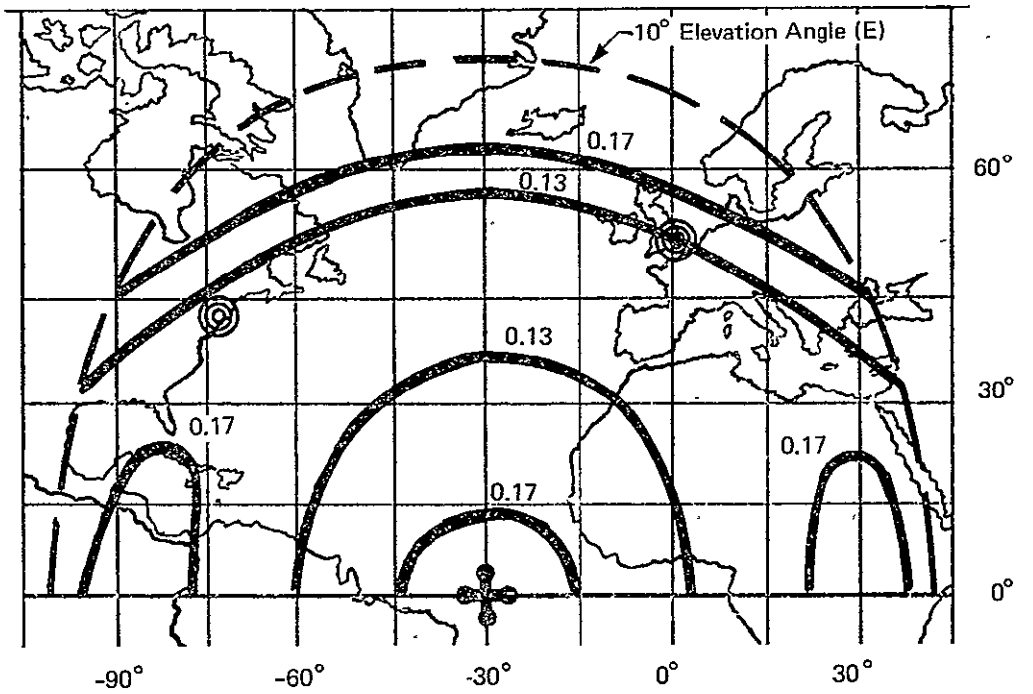

NOTE: Assumptions are the same as for Figure I-2-10.

Figure I-2-9. Beacon East-West Velocity Standard Deviation (1σ) in m/s

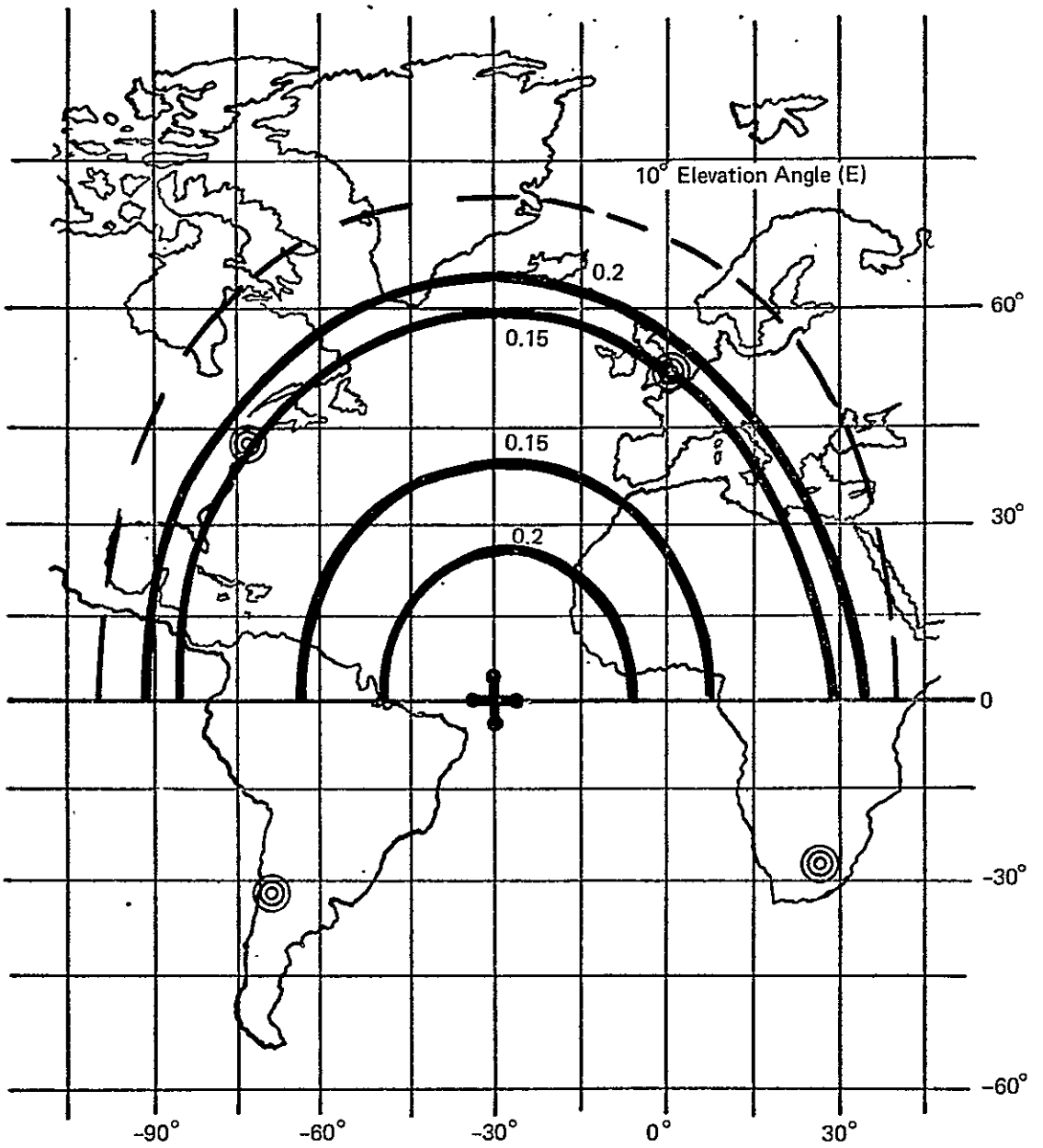

Assumptions:

Calibration Transmitters (CTs)	1 σ Errors
Rosman	CT Noise 0.45°
Santiago	CT Survey (h, La, Lo) 3, 10, 10m
London	Satellite Ephemeris (N, T, R) 60, 60, 10m
Johannesburg	Altitude 100m
	Beacon Noise 0.6° @ E = 90°
	0.9° @ = E 20°

NOTE: Two hours between position fixes.

Figure I-2-10. Beacon Horizontal Velocity CEP in m/s

satellite location, and the beacon altitude are used in the position location calculations and are not calibrated out. Thus any errors in these parameters will produce a balloon position location error.

An analysis was made to determine the position location errors due to beacon phase noise, CT phase noise, CT survey errors, satellite ephemeris errors, and beacon altitude errors. Analysis results are summarized by Figure I-2-11. The magnitude of the position errors is related to the magnitude of the error sources as specified in the legend. For example, if the satellite ephemeris errors were increased to 600 m normal error, 600 m in track error and 100 m radial error, the ordinate of the satellite ephemeris error contribution would be multiplied by 10.

The error breakdown shows that the beacon and CT phase noise dominates.

The previous results did not account for the case in which the calibration is slightly incorrect because, for example, the interferometer antenna phase centers did not track perfectly. Therefore an analysis was conducted to determine the sensitivities of position location errors due to errors not included in the simulation. Figure I-2-12 summarizes the results.

As an example of how these curves can be used, assume that the interferometer antenna phase center shifts by 10 mm axially. This shift may be caused by the difference in frequency between the balloon and CT signals. The sensitivity of position error to a change in the length of the baseline is seen to be about .125 km/cm. Thus a 10-mm shift in each antenna phase center in opposite directions (the worst case) causes a position location error of 0.25 km.

Now assume that the antenna phase center shifts normal to the baseline axis by 10 mm. This causes the baselines to be slightly nonorthogonal. The worst-case nonorthogonality error is $\frac{10 \text{ mm}}{75 \text{ m}} \times 2 = 0.26$ mrad. (The 75 m is the baseline length and the factor of 2 accounts for the two baselines.) The position location sensitivity is about 1.5 km/mrad. Thus the worst-case position error is about 0.41 km for the assumed phase center shift.

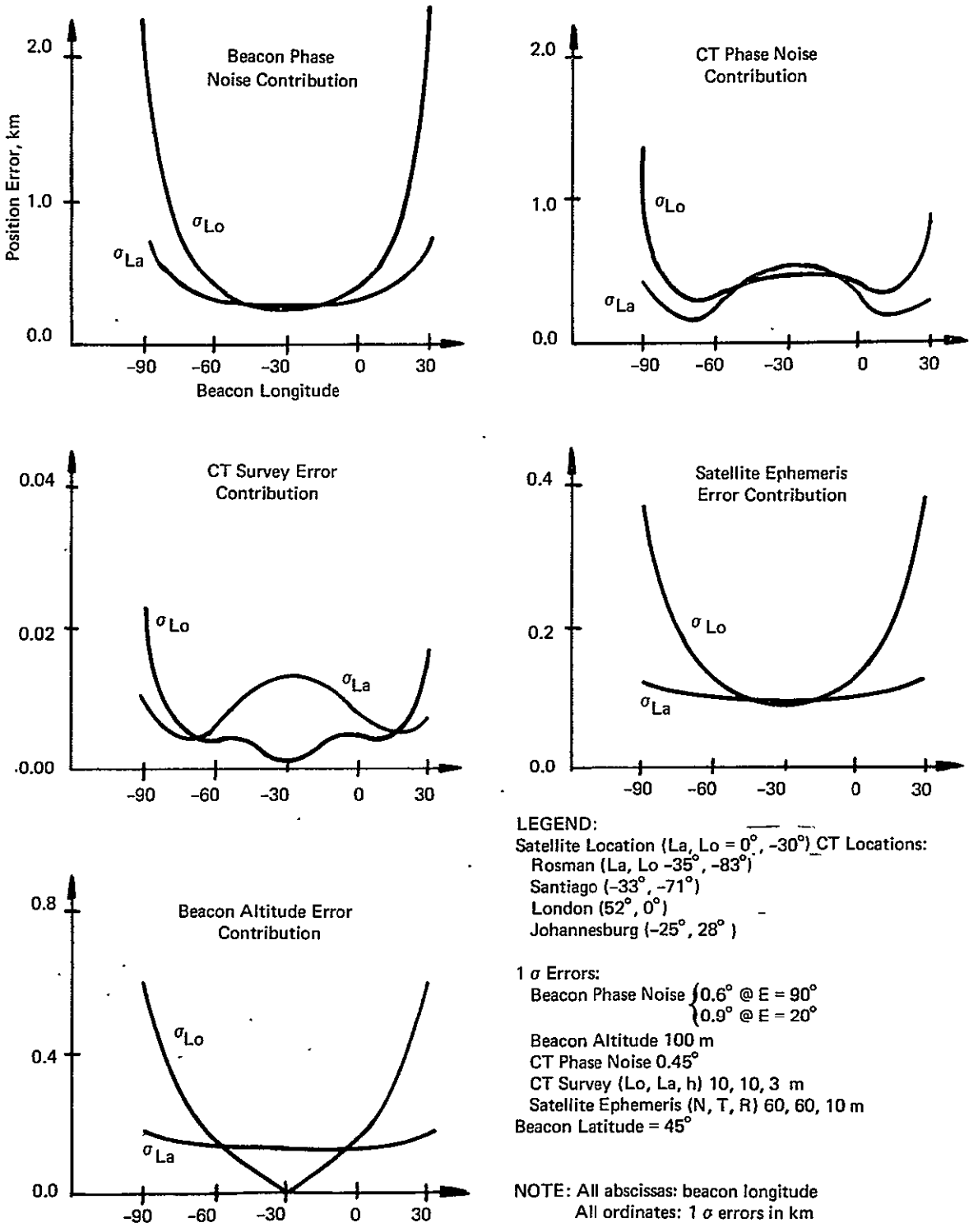

Figure I-2-11. Beacon Position Standard Deviation Breakdown

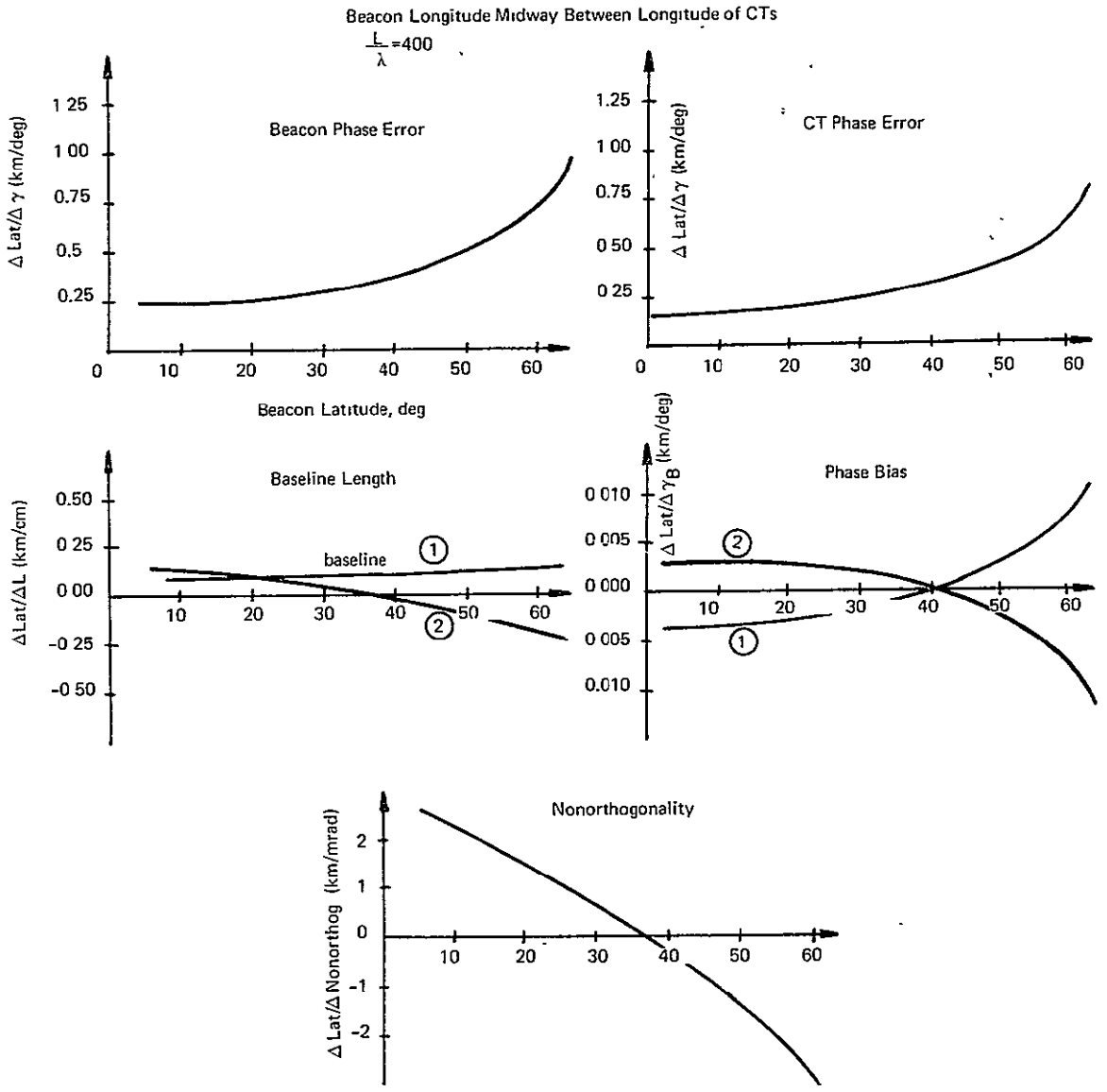

Figure I-2-12. Error Sensitivies

The effect of random and bias phase errors on position location is also shown. Highly correlated random phase errors will also have highly attenuated sensitivities relative to uncorrelated random phase errors.

The sensitivities were generated for a variety of geometries. As expected, the sensitivities are geometry dependent, but the results shown are typical.

Section I-3

PROPAGATION AND POLARIZATION EFFECTS

The major propagation effects on the signals in an interferometer system are multipath due to reflection on the earth's surface and ray bending due to refraction. Polarization of the transmitting and receiving antennas affects the multipath, but can also produce phase errors if there is a mismatch in the antennas.

I-3.1 MULTIPATH

A signal transmitted from a weather balloon and received at a satellite interferometer will be disturbed by a multipath signal reflected from the earth. This multipath disturbance will distort the phase measurement and consequently produce a position location error. The multipath error can be very significant (see Table I-2-3).

The angle error is a function of the geometry and the multipath-to-signal ratio. Figure I-3-1 shows the maximum position error resulting from multipath. The analysis is 2-dimensional, i.e., the interferometer arm is in the plane of the direct and reflected rays. The elevation angle E was chosen to be 20 deg. This figure shows that the multipath error is very strongly dependent on the signal-to-multipath ratio (SMR). At low altitudes, it is almost independent of the interferometer arm length expressed in wavelengths $(\frac{L}{\lambda})$, but at higher altitudes, the error decreases with increasing $\frac{L}{\lambda}$. For a large SMR (35 dB to 40 dB), the position error can be kept to values around 1 km.

A study was made to determine what affects the SMR and how it can be improved. In general, the reflected signal will be spread over a frequency band

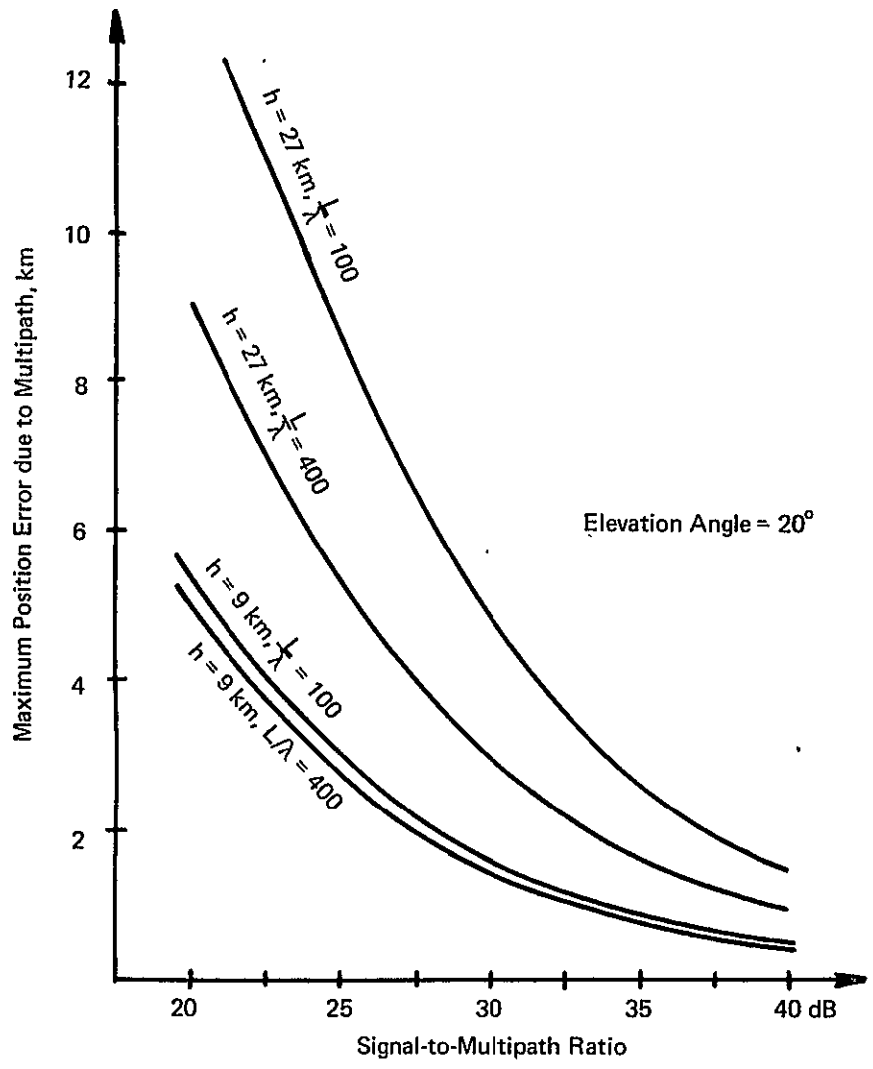

Figure I-3-1. Position Error due to Multipath

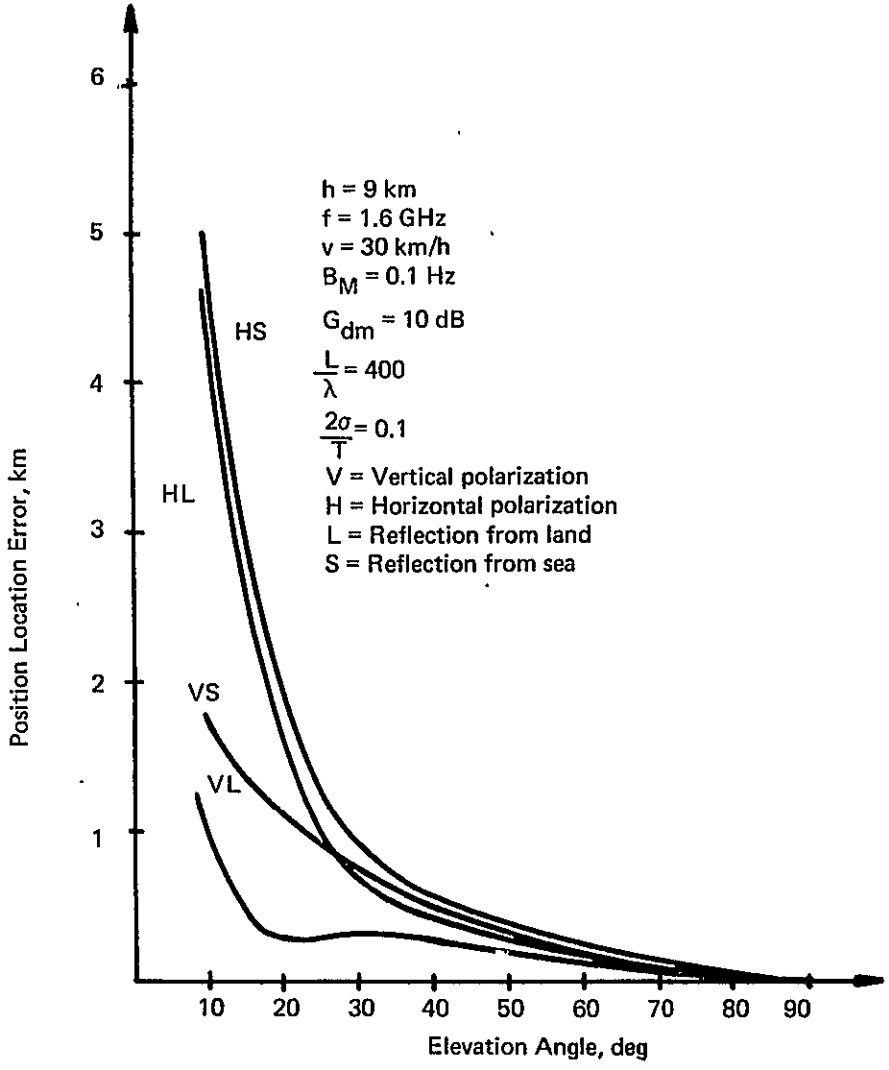

Figure I-3-2. Multipath Performance with Filtering

rather than being sinusoidal. This bandspread results from diffuse scattering and from the balloon motion or wave motion of an ocean surface. The multipath-to-signal ratio may be expressed as:

$$(\text{SMR})^{-1} = \left[\frac{P_o}{P_d}\right] [\text{filtering factor}] \left[G_{dm}\right]^{-1} . \qquad \text{(I-3-1)}$$

The balloon antenna front-to-back ratio G_{dm} can be kept to about 10 dB. The ratio of reflected power to direct power $\frac{P_o}{P_d}$ is a function of reflectivity and geometry and will differ for land, sea, horizontal, and vertical polarization. The filtering factor can be expressed as $\text{erf}\left(\frac{\pi B_M}{2\sqrt{Z}}\right)$ where B_M is the equivalent filter bandwidth. In the system under consideration, B_M is on the order of 0.1 Hz. The bandspread is a function of geometry and furthermore depends linearly on the balloon velocity and the transmission frequency. The value $2\sqrt{2Z}$ can be interpreted as the 2-sided "1σ" bandwidth of the multipath spectrum. For the balloon system under consideration, the bandspread is of the order of 10 to 100 Hz.

When all factors are considered and the multipath portion error is calculated, the curves shown in Figure I-3-2 are obtained. The parameters chosen are a relative velocity of 30 km/h, an interferometer of 400 wavelengths, and a surface characterization parameter $\frac{2\sigma}{T} = 0.1$. (σ is the mean surface bump height, while T is the correlation interval; hence $\frac{\sigma}{T}$ is the average slope inclination.) The curves are for linear horizontal and vertical polarization, and present upper and lower bounds for circular polarization, for which case the error will fall somewhere between the curves. Circularly polarized transmission signals are desirable, because on reflection the sense of polarization would be reversed and would further reduce the multipath error. From the curves it can be seen that the multipath error is zero directly under the satellite, but increases as the elevation angle decreases. With effective narrowband filtering and an

antenna front-to-back ratio of 10 dB, a position location error of less than 1 km can be achieved.

I-3.2 REFRACTION

Signals emitted from the calibration transmitters and the balloons will be subject to bending when passing through the troposphere and the ionosphere. The rays are deflected towards earth in the troposphere, follow a S-shaped path in the ionosphere, and then travel straight through the vacuum of space. This peacewise curved path of actual propagation will deviate by a small error angle from the straight path.

This error angle can be calculated by using a ray tracing program. The atmosphere and the ionosphere are assumed to consist of thin concentric spherical shells with each shell having a fixed index of refraction. By using Snell's law, the path of the ray is traced through the medium. The curved path is then compared to straight path, and the error angle determined.

Figure I-3-3 shows the resulting error angle. The model for the atmosphere is assumed to have a 100 percent relative humidity, which represents a worst case; the model for the ionosphere is assumed to have a Chapman distribution.[3] The error angle was calculated as function of the elevation angle, with the signal frequency as parameter. All curves go to zero for an elevation angle of 90 deg. It can be seen that, for elevations above 20 deg, the error for 1600 MHz will be less than 10^{-5} deg, which corresponds to a position error of 2×10^{-2} km. For a frequency of 400 MHz, a 30 times larger error occurs at low elevation angles.

The frequency-dependent part of the error is produced by the ionosphere. Partial correction of the refraction error is possible by prediction of the ionospheric bending. However, since the resulting position error is relatively small, no correction is necessary.

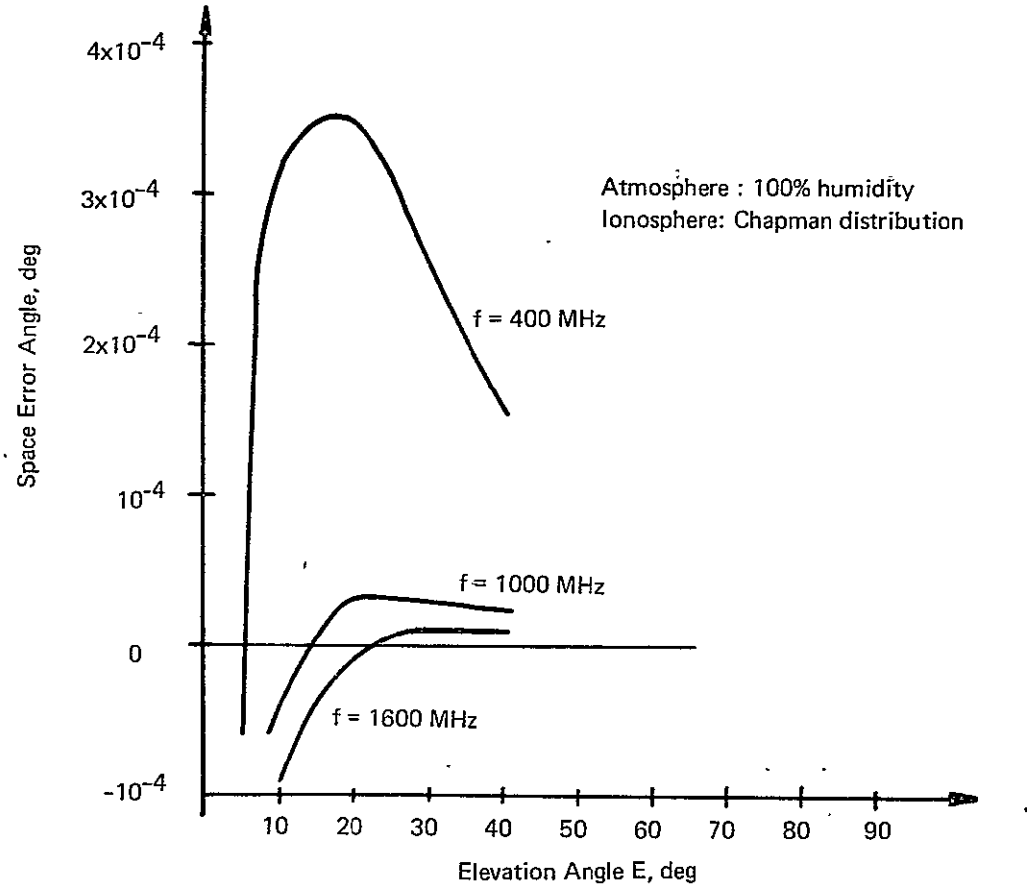

Figure I-3-3. Refraction Error

I-3.3 POLARIZATION MISMATCH ERRORS

In the balloon-interferometer transmission link, the antenna polarization must be chosen appropriately. The best performance, i.e., least loss and least error, would result in the case in which linearly polarized signals were used and polarization would be matched.*[4] For the balloon-interferometer link, this case is impractical, because no capability exists to mechanically align the interferometer antennas and the balloon antenna to produce the polarization match. Furthermore, a Faraday rotation of the polarization can be expected. Consequently, one of the link ends – transmitter or receiver — must be circularly polarized.

---

*This approach was used for the ATSF&G altitude reference interferometer, see Reference 4.

The alignment of the polarization characteristics of the two antenna elements constituting an interferometer arm is limited by imperfection of technology. This imperfection in alignment, particularly in angular orientation of the polarization ellipses, will appear in the measurement as an error component. This error component can be calibrated out, and the residual error generally has the nature of a phase bias. A case exists, however, in which the error becomes dependent on the geometry, i.e., orientation of the arriving beam with respect to the plane in which the interferometer elements lie. This orientation varies for the different ground stations and the balloons, and it would be difficult to remove the residual error by calibration.

The polarization error has been analyzed for different combinations of polarization. In this analysis, it was assumed that the maximum angle of signal arrival with respect to the plane formed by the interferometer antennas does not exceed 10 deg. Furthermore, it was assumed that the axial ratio of the interferometer antennas is no more than 0.5 dB and relative major axes of two polarization ellipses can be kept within 2 deg of each other. The results are shown in Table I-3-1.

Table I-3-1

RESIDUAL PHASE ERROR RESULTING FROM POLARIZATION MISMATCH

Satellite	Calibration Transmitter	Beacon	Approximate Residual Electrical Angle Error	Combinations
LP	LP	LP	0.0	(1)
	LP	CP	5.0	(2)
	CP	CP	0.0	(3)
CP	LP	LP	0.0	(4)
	LP	CP	0.9	(5)
	CP	CP	0.1 (max)	(6)

In the table, cases are shown for which the polarization of the calibration transmitter differs from the beacon polarization. It is noted that in these cases the errors are prohibitively large. The choice of signal polarization is between three possible combinations, i.e., (3), (4), and (6). Although (3) and (4) show no error, there will be a 3 dB polarization loss, which is undesirable, since this would increase the electrical phase error due to thermal noise. Consequently, it is recommended that circular polarization be used throughout the system. This will also be beneficial in suppressing multipath errors. The resulting maximal polarization error of 0.1 deg will cause, at most, a 0.08 km position error component.

Section I-4

SPACECRAFT SYSTEMS

The interferometer position location system consists of spacecraft systems, a ground system, and balloon beacons. This section concentrates on the essential interferometer system elements carried aboard the spacecraft.

I-4.1 ANTENNA ELEMENT

Investigation of the requirements for the interferometer antenna element showed that a circularly polarized antenna with a 22 deg beamwidth and 17.5 dB gain is necessary. To limit phase error effects, the antenna must also have high degree of polarization circularity (± 0.5 dB axial ratio tracking and ± 2 deg polarization ellipse tilt angle tracking). The overall spacecraft design and environment also limit the antenna size, weight, and construction materials.

The antenna candidates studied fell into two classes: aperture types and endfire types. The aperture types were the backfire, corner reflector, turnstile array, and planar spiral or conical spiral. The endfire types were the helix and the Yagi-Uda.

The tradeoff analysis showed that all the candidates except the backfire antenna would require arraying to achieve the desired beamwidth with the concomitant penalty of increased weight. Since the backfire antenna also has excellent polarization and phase center characteristics, it was chosen as the optimum antenna element.

The backfire antenna consists of an axial surface wave structure made up of crossed dipoles (Yagi) with a large flat reflector with a rim at one end of the structure and a small flat reflector at the other end. The phase center was

measured on a simple model of this antenna. The stability of the phase center over the 22 deg beamwidth is 0.2 deg. It was observed that the phase centers of two antennas tend to track each other, which further reduces the effect phase center shifts.

I-4.2 MECHANICAL SYSTEMS

This subsection presents the significant conclusions of that portion of the study dealing with the mechanical subsystems. These studies include a preliminary definition of the spacecraft attitude control system (ACS), a study of the dynamic coupling between the interferometer booms (baseline) and the spacecraft, and the environmental effects on the baseline. The baseline is defined as the line connecting the phase centers of the antennas. The antennas are mounted on support plates which are at the tips of a set of flexible booms. The motion of the booms, and therefore the apparent motion of the baseline, are affected by ACS perturbations, boom configuration characteristics, weights of the antenna element (boom tip weight), and the forces associated with thermal gradients. In the study, two boom configurations were considered: Astro Research Corporation's Astrocolumn and Fairchild Hiller's TEE (Tabular Extendible Element).

In the space environment, the interferometer booms will deflect either symmetrically or antisymmetrically (see Figure I-4-1), with the experiment affected primarily by the antisymmetric bending mode. The symmetric bending mode, which merely translates the baseline, is excited by stationkeeping. Gravity gradient and orientation controls perturb the antisymmetric mode, which rotates the baseline. Finally, thermal deflections are primarily symmetric, with an antisymmetric component of less than 10 percent of the total thermal deflection.

A linear analysis of the disturbance torques, which included gravity gradient, solar torque, and lateral thrust misalignment, shows that an ACS torque level of 10^{-4} foot pounds is required to maintain orientation. A nonlinear dynamic analysis of the interaction between the ACS and the motion of the baseline indicates

that a torque level as high as 10^{-3} foot-pounds would result in acceptably small deflections and rates of baseline deflection. The ACS logic used therein is a worst case on-off system which could be implemented with either reaction wheels or micro-thrusters.

The boom configuration characteristics thought to have the greatest effect on the baseline motion are its stiffness and weight. These parameters, along with the satellite body's inertia, define the system's natural frequency and, given equal boom deflections, the higher the frequency the higher the baseline rates will be. As shown in Figure I-4-2, the tip weight has little effect on the system frequency in the antisymmetric mode. Hence, it should have little effect on the baseline rates as well.

However, dynamic simulations of the equations of motion indicate that the average baseline rate is essentially independent of both the boom characteristics and the tip weight for tip weights between 2.0 and 15.0 lbs. The dynamic simulation leading to these conclusions is characterized by the on-off ACS discussed above with a dead band of ± 1 deg baseline rotation. Only local dynamics were considered in the simulation. Neither disturbance torques from external sources nor damping of any type were included. The initial conditions for each case are a "rigid body" roll rate of 10^{-5} rad/s and a roll angle of 1.0 deg. Figures I-4-3 and I-4-4 show the time histories of the baseline angular position and the baseline angular rate, respectively, for a typical simulation. It should be noted that the oscillations shown on the time history of the rate would also show up on the curve of position; however, the position change due to these oscillations is three orders of magnitude less than the scale used.

Figure I-4-4 yields the approximate baseline rate formula.

$$\dot{\alpha} = -1.05 \times 10^{-5} + 2.5 \times 10^{-6} \sin 0.095t \text{ rad/s}.$$

The first term in this equation reflects the initial roll rate and would be -1.0×10^{-5} for a rigid body. The amplitude of the second term reflects both the tip deflection, in this case 0.1 ft, the system frequency, and the angular rate of

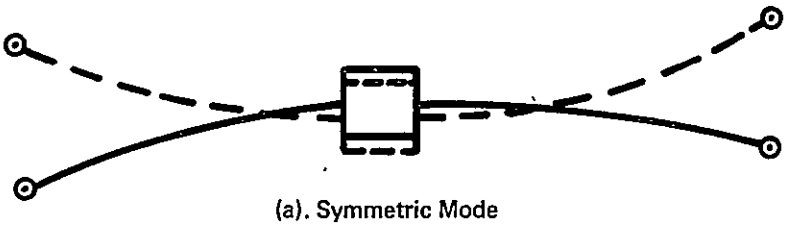

(a). Symmetric Mode

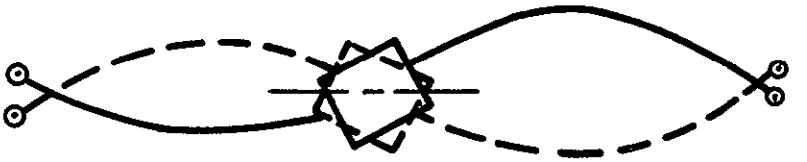

(b). Antisymmetric Mode

Figure I-4-1. Boom Deflection

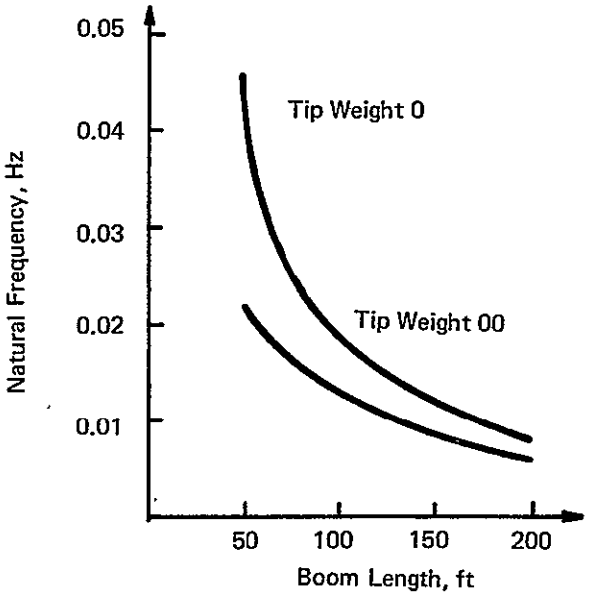

Figure I-4-2. Natural Frequency for Antisymmetric Mode

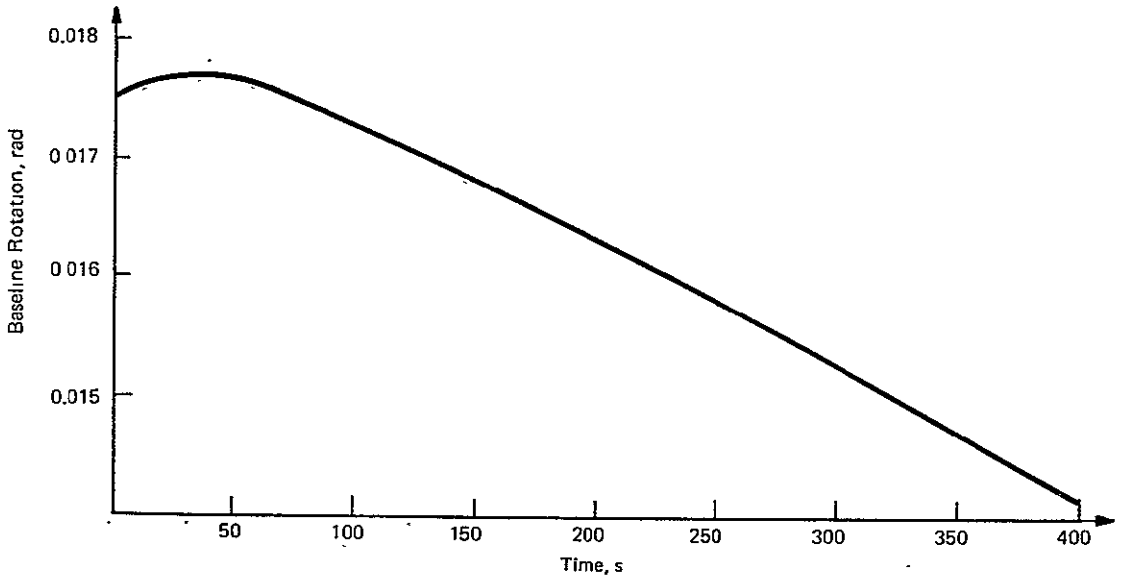

Figure I-4-3. Time History of Baseline Angular Position

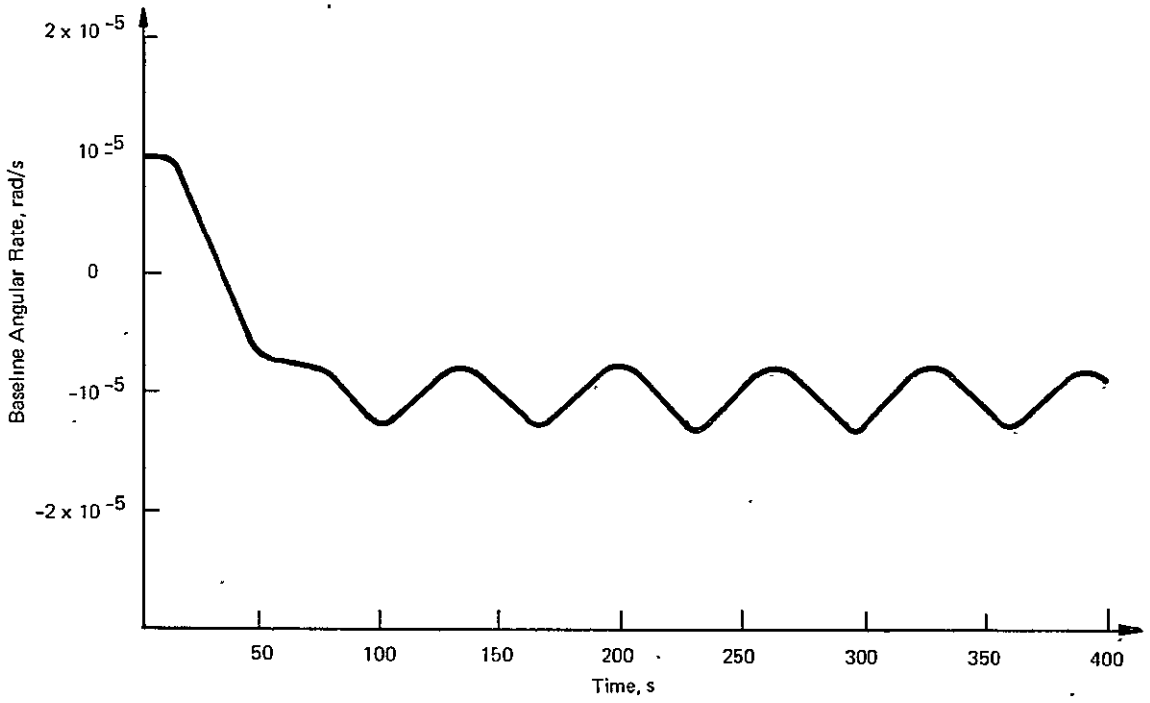

Figure I-4-4. Time History of Baseline Angular Rate

the hub. The argument of the sine term defines the system natural frequency. As stated previously, very little difference is found in the amplitude of either term regardless of the boom configuration or tip weight being simulated and in spite of large deviations in system frequency.

Worst-case calculations show that solar pressure, aerodynamic drag, and gravity-gradient deflections are negligible for all configurations.

The environmental effect which can cause the greatest deflection is the thermal gradient across the boom. Fortunately, state-of-the-art techniques make it possible to virtually eliminate thermal gradients and thermal bending in an interlocked TEE with perforations and proper coatings. Thermal bending and twisting of an Astrocolumn should likewise be small because of the open type of construction resulting in uniform heating.

Twisting of the boom tip will occur as the boom is extended. This would cause the antennas at the boom tips to point away from earth. This twisting is different from boom-to-boom and may be caused by an unpredictable imbalance of the stress distributions inherent in the tapes used to form the booms. The twisting is essentially a reproducible function of the length to which a particular boom is extended.

The recommended method to circumvent problems caused by this effect is to include a rotary joint at the root of the boom, through which the boom is rotated after extension. The calibration transmitter signals can be used to determine the antenna pointing.

I-4.3 ELECTRONIC SYSTEMS

The satellite electronics combines the CT and beacon signals received by the interferometer antennas in a frequency multiplex, and transmits these to a central ground station. Frequency multiplexing is used to transmit each signal from the various interferometer antennas separately, allowing simultaneous reception and phase measurements at the central ground station.

Figure I-4-5 illustrates the suggested implementation of the multiplexing repeater. The frequency offsets among the signals from the different antennas is achieved by use of offset local oscillator frequencies. The local oscillator synthesizer is provided with a 60-kHz reference signal, which is used within the synthesizer to produce a set of seven local oscillator frequencies related by the 60 kHz and its second and third harmonics. In this manner, the phase relationships among the appropriate antenna pairs with respect to the spacecraft-generated 60 kHz and its harmonics are maintained. This reference frequency must be continuously transmitted to the central ground station, where it and its harmonics are used as the references for phase measurement. The continuous transmission is provided by the modulation of a subcarrier and the addition of this 60 kHz-modulated subcarrier to the received signal just prior to upconversion to X-band, as shown in Figure I-4-5.

Generation of fourth-order intermodulation products in the upconverter or third-order intermodulation products in the output amplifier would result in unwanted inband components which would interfere with the tracking loops and phase measurement. For this reason, the frequency translation device of the IF signal spectrum to X-band must be carefully designed to ensure low intermodulation products. For the output amplifier, a TWT operating far below (about 20 dB) its output capacity is recommended, since operation in this region will ensure satisfactory linearity. These topics are discussed further in subsection II-8.1.

Figure I-4-6 shows the typical spectrum format of the input to the repeater upconverter. Each block contains the signals received at one antenna. The expanded signal block shows the CT signals along both edges of the band. Most of the frequency spectrum is used for the balloon signals. On the average, there will be seven balloon transmissions received at any given time by a ground station, assuming 15,000 balloons worldwide.

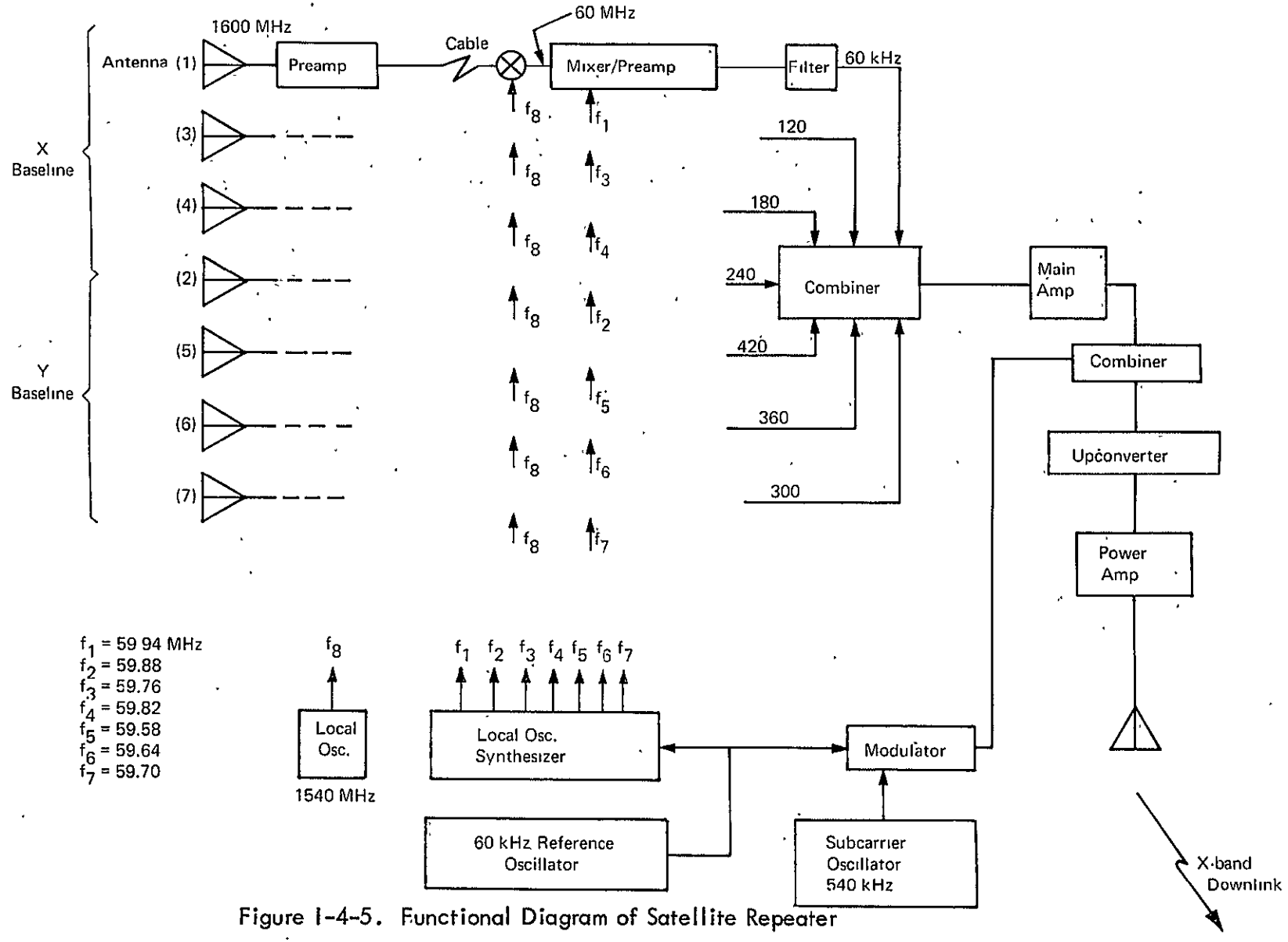

Figure I-4-5. Functional Diagram of Satellite Repeater

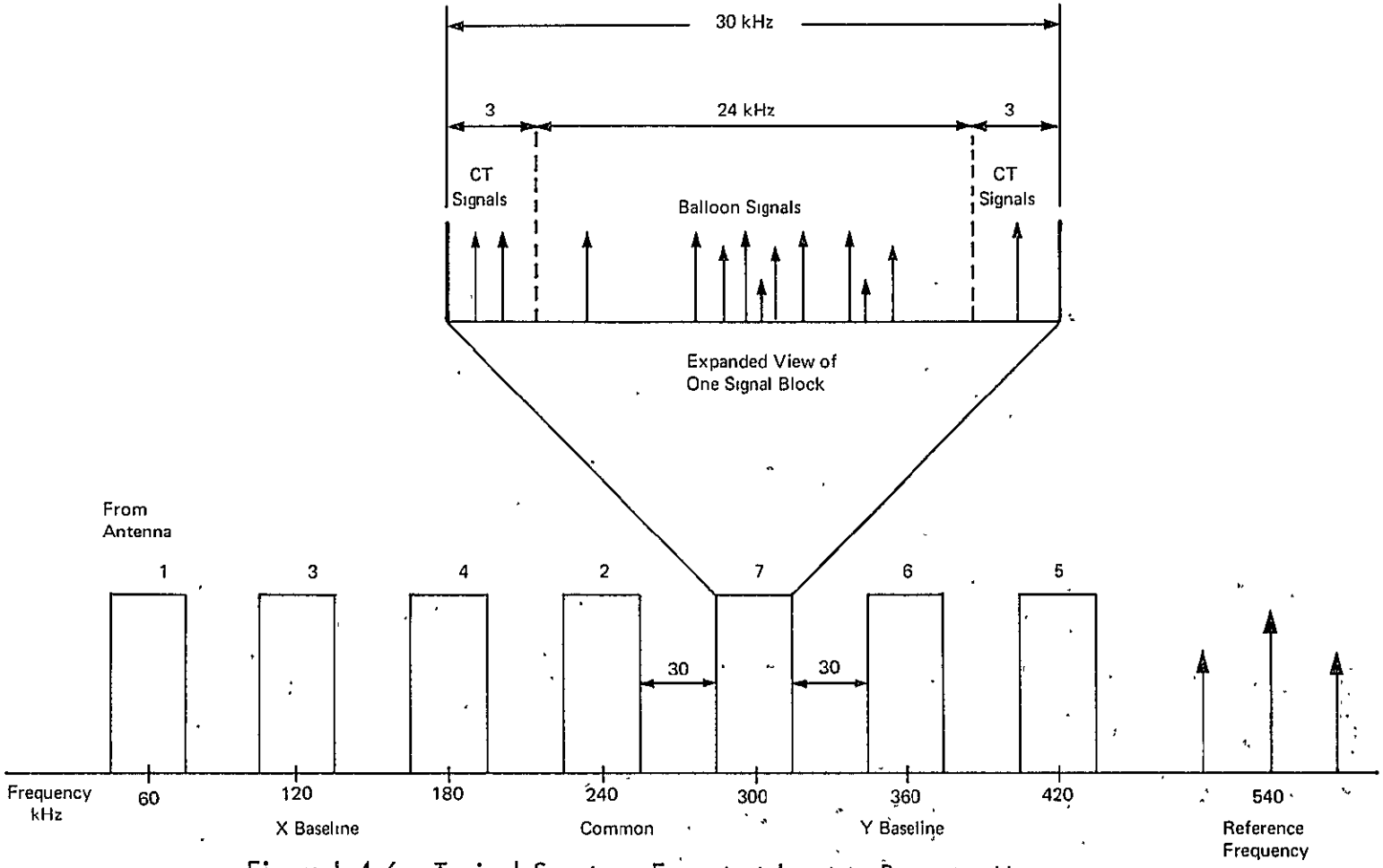

Figure I-4-6. Typical Spectrum Format at Input to Repeater Upconverter

1.4.4 MULTIPLE ACCESS

Since the balloons will be transmitting essentially at random times with respect to each other and will use oscillators with low frequency stability, a combination of frequency division and time division can be used as the multiple-access technique. A large number of balloons can be operated in the system because of the low transmission time (10 s every 2 h) required of the balloons and because the bandwidth of the signals is low (20 Hz).

The probability of obtaining a position fix given that a balloon transmits depends upon how close in frequency transmissions two balloons can be and not interfere with signal acquisition and the phase measurements. The probability of no interference from other signals given that a balloon transmits, P_{no}, can be shown to be

$$P_{no} = \exp. \left[-\frac{N}{10800} \frac{\Delta t}{T} \frac{\Delta f}{W} \right] \qquad \text{(I-4-1)}$$

where

- N = number of balloons worldwide
- Δt = transmission time in s
- T = time between balloon transmissions in h
- Δf = frequency band within which another transmission would interfere with acquisition or phase measurements
- W = bandwidth over which balloon transmissions are spread.

For $N = 15,000$, $\Delta t = 10$ s, $T = 2$ h, $\Delta f = 100$ Hz, and $W = 24$ kHz, this probability is 0.97. Since two separate position fixes are required to obtain velocity, the probability of obtaining a velocity fix from two given transmissions is 0.94. The probability of obtaining any two successive position fixes out of three (which would be a 6 h period) is greater than 0.99.

Section I-5

BALLOON BEACON

The primary components of the balloon electronic package are the timer, the encoder (data formatter and identification word generator), the transmitter, the antenna, and the power system.

I-5.1 DATA TRANSMISSION

In Figure I-5-1, which is diagram of the balloon electronics package, the meteorological data points appear as analog voltages across some nominal impedance. These data points are sampled sequentially under timer control along with some additional fixed voltages for calibration which will be required to attain the requisite accuracy of 1 percent. The analog voltage is then converted to a digital form in an A/D converter.

The format of the 10 s signal transmitted from each beacon is headed by 2 s of CW to facilitate acquisition at the ground receiver. This is followed by the necessary digital information. The digital format consists of the sequential transmission of the following blocks of bits:

- 10 bits for bit timing*
- 18 bits for frame synchronization*
- 16 bits for ID word (including 1-bit parity check)
- 9 bits for sensor calibration
- 18 bits for meteorological data samples (2).

---

* Approximate requirements

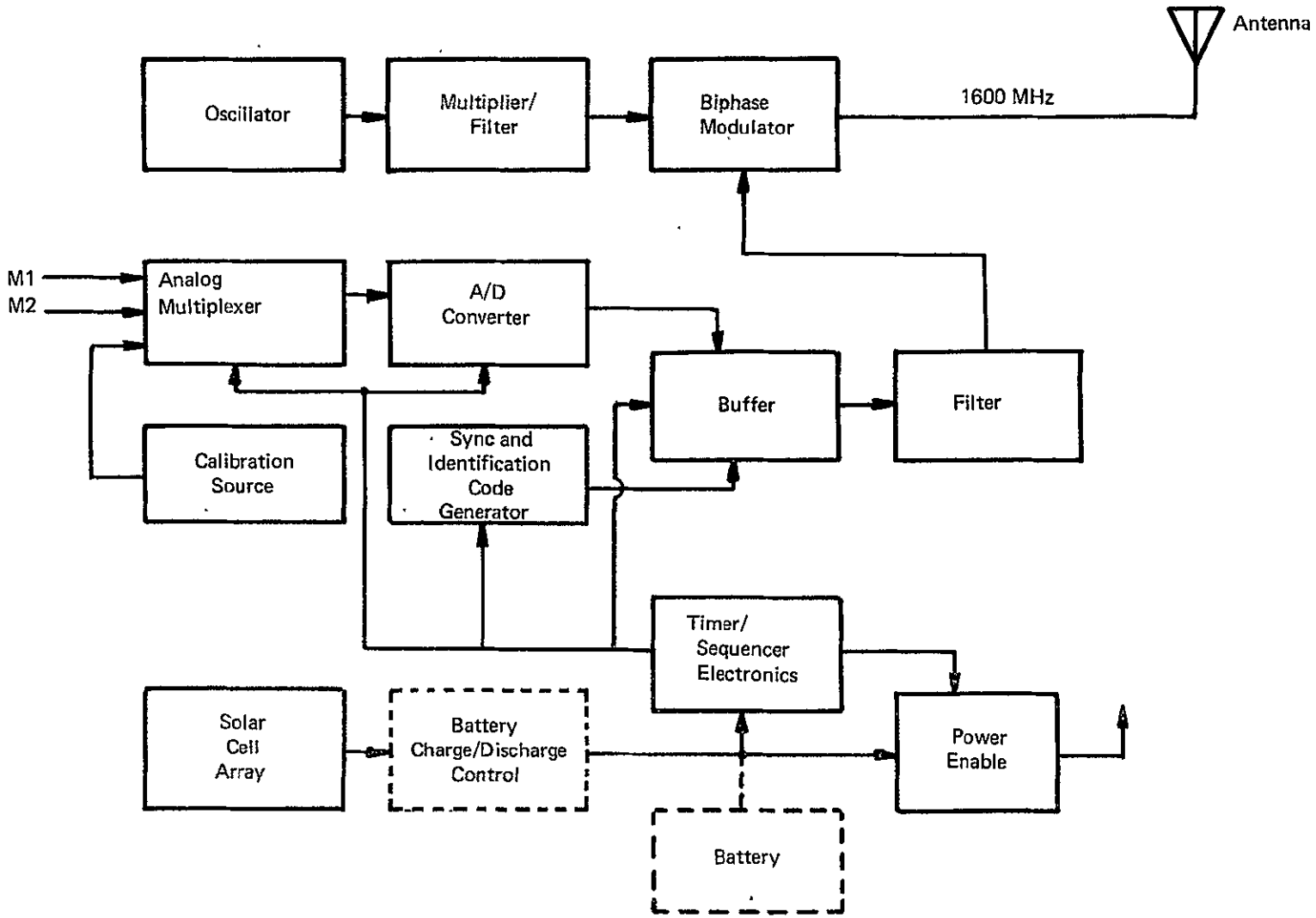

Figure I-5-1. Functional Diagram, Balloon Electronics

Figure I-5-2 is a time diagram of the transmission.

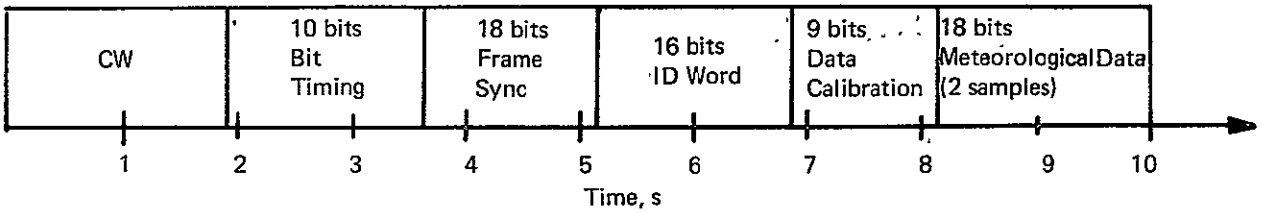

Figure I-5-2. Balloon Transmission Format

The time available for data transmission is 8 s; hence the data rate is 8.9 bps.

I-5.2 IDENTIFICATION

During the 10 s balloon transmission, a binary word of sufficient length (number of bits) must be modulated onto the carrier to identify the source of the transmission. For 15,000 possible balloons, a 14-bit word length is sufficient for this purpose.

The signal-to-noise density ratio at the ground station will be in excess of +26 dB-Hz for all cases. The bit energy-to-noise density ratio will be greater than 13.5 dB (allowing 3 dB degradation in the system) so that a bit error probability of 10^{-6} should be easily obtained with phase-shift-keyed (PSK) modulation. Thus errors in decoding the identification word will be few, and it is suggested that merely one bit be added for parity check. This enables the detection of single errors, which will be virtually the only existing errors. The identification word is shown as 16 bits in length to allow some expansion of the system.

I-5.3 TIMER

The function of the timer is to periodically activate the balloon electronics for a certain period during which the balloon transmits. The turn-on period will be every 2 h; during the 10-s active interval, the timer must provide for timing of the identification coder and the data encoder.

The timer, consisting of an oscillator and divider circuits, operates continually, enables the transmitter circuitry at the preset intervals, and controls

transmission of the identification code (gating and bit timing). The timer operates as a free running clock during the lifetime of the system. The bit timing pattern, synchronizing pattern, and identification code are generated in a preset register under control of the timer.

An accurate timer for controlling the 2 h period is neither required nor desired. By having a low accuracy timer, the transmission timer of the balloon packages will be random with respect to each other, as desired for multiple-access reasons.

I-5.4 BALLOON (DC) POWER REQUIREMENTS

An estimate of the power requirements is tabulated in Table I-5-1. The necessary solar cell array area is 2800 sq cm. The weight of the array would be approximately 1 lb.

Table I-5-1

BALLOON PACKAGE POWER REQUIREMENTS

	Mode 1 (ON) (in W)	Mode 2 (STANDBY) (in W)
Transmitter	4.0	0
Transducer Bias Circuits	0.3	0
A/D Converter	0.5	0
Code Generator	0.2	0
Timer Circuits	0.5	0.1
TOTALS	5.5	0.1

Section I-6

GROUND SYSTEMS

I-6.1 ELECTRONICS

The functions of the ground station receiver are to measure the phases between appropriate signals received at the interferometer antennas, and to demodulate the data sent from the balloons. As shown in Section II-8, the signals received by a particular interferometer antenna occupy a predetermined portion of the received spectrum. The first function of the ground receiver after the baseband signal is recovered is to filter the incoming signal spectrum into those portions corresponding to particular antennas and the reference frequency subcarrier.

Next, due to large uncertainties in balloon transmission frequencies, a technique for acquisition and narrowband filtering is required. Figure I-6-1 illustrates the essence of this acquisition and filtering technique. A bank of narrowband filters and detectors is used for acquisition. Each filter will have a bandwidth of about 50 Hz, so that about 480 filters are required to cover the 24 kHz within which balloon transmissions will occur. These filters are used solely to make the initial settings of the voltage-controlled oscillators of the phase-locked loops for acquisition.

In the steady state, the output of the filter due to the signal input at antenna 1 will be at the frequency ω_0, which is the frequency of a fixed stable offset oscillator used as part of the phase-locked loop. The output of the filter due to the signal input at antenna 2 will be at the frequency $\omega_0 + \omega_r$, where ω_r is the reference oscillator frequency in the satellite. This signal will be at phase $\theta_r + \theta$ with respect to that signal from antenna 1. When the signal from antenna

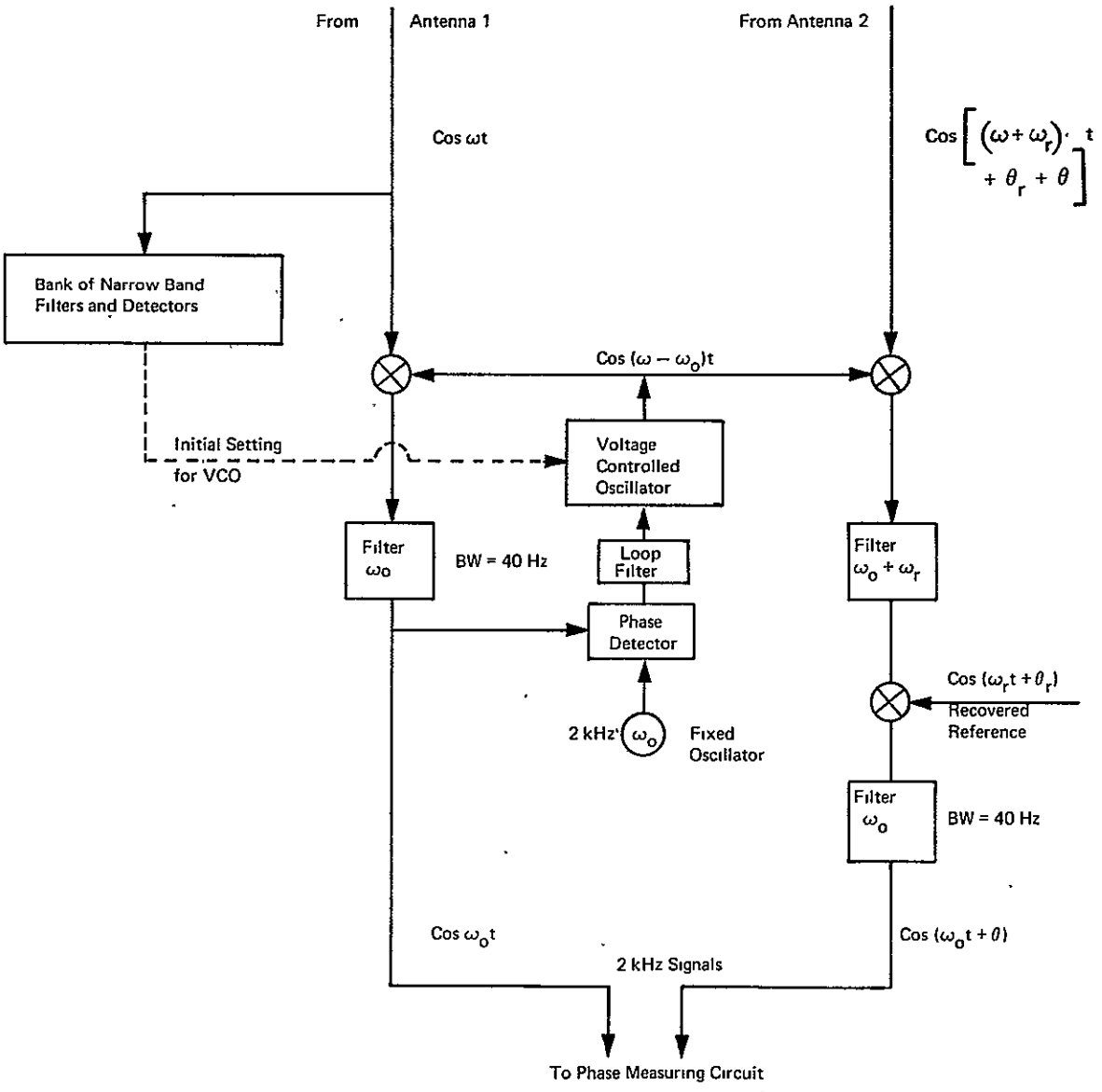

Figure I-6-1. Signal Acquisition and Filtering

2 is mixed with the recovered reference and filtered, the output will be at the offset oscillator frequency ω_o. The 2 signals at frequency ω_o are introduced to a phase measuring circuit to obtain the desired phase θ.

It should be noted that, while it is necessary for the phase-locked loop to reach frequency lock so that there is cycle slippage, it is not necessary for complete phase lock to have occurred before phase is measured. Any residual phase error of the loop is transferred to both signals and will cancel out when the phase is measured.

Figure I-6-2 is a diagram of the essential parts of the ground receiver configuration. The bank of filters across the top of the diagram accomplished the separation of signal blocks, after which the acquisition and filtering of Figure I-6-1 is implemented with a bank of phase-locked loops and mixers. Each phase-locked loop is designed to be capable of being set to track a signal anywhere in the 24-kHz band when the presence of a signal is detected. Also shown at the phase-locked loops are the data demodulators.

The bandwidth of the phase-locked loops will be approximately 25 Hz. This will give a loop SNR of about 12 dB for the balloons at elevation angles of 20 deg. This gives an adequate margin for the loop to be able to acquire the signal. Since the filters used to locate the signals are 50 Hz apart, the initial setting of the VCOs will be within 25 Hz of the correct value.

The time for a second-order loop to pull into lock under these conditions is about 0.1 s. Thus, essentially all of the 10-s transmission time is available for phase measurements.

The actual phase measurement can be made using a digital phase meter. To decrease the standard deviation of the phase measurements, many phase measurements are made during the 10 s transmission time, so that effectively an average over the 10 s is obtained. This gives an equivalent noise filtering bandwidth of 0.1 Hz for the balloon signals.

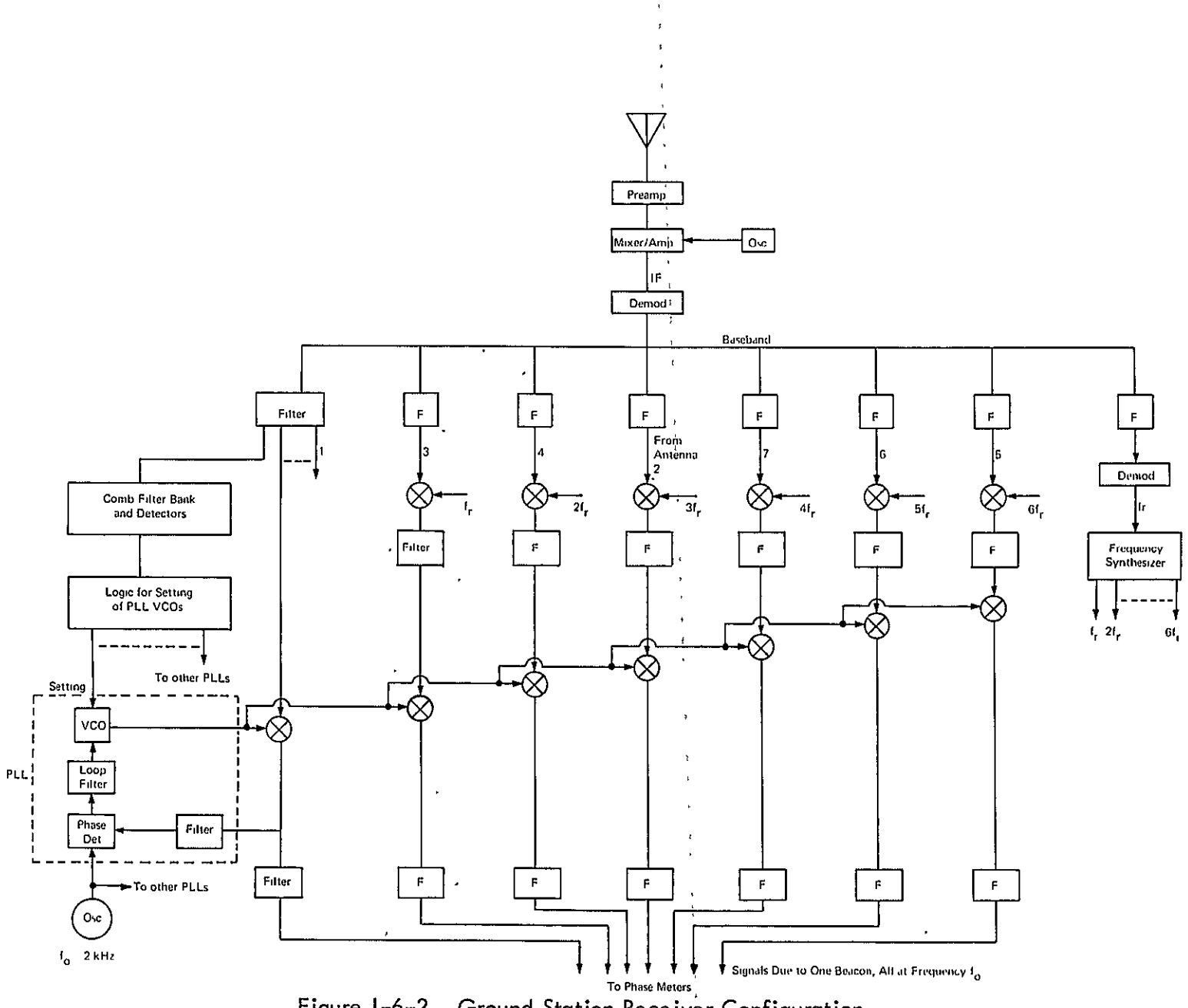

Figure I-6-2. Ground Station Receiver Configuration

I-6.2 DATA PROCESSING

Preliminary computer sizing estimates indicate no inordinate data processing problems associated with the position location algorithm. The throughput, or equivalently the number of simultaneous solutions that must be generated in a given interval of time, is limited more by the phase extraction design than by the computational load. The phase extraction requires 10 s of averaging and can process 15 beacons' signals simultaneously (including ambiguity resolution and baseline survey).

The worst-case situation for the data processor entails 15 position fixes every 10 s, or equivalently, an average of 0.67 s between position fixes.

Table I-6-1 gives a cursory count of the instructions involved in the position fix calculations excluding such things as data editing, data formatting, displays, and other auxillary functions.

Table I-6-1

PRELIMINARY INSTRUCTION COUNT PER BEACON POSITION CALCULATION

Function	Quantity	Equivalent Additions	Total Equivalent Additions per Beacon Solution plus 10 x Baseline Calibration Computations
Add	40(140)	40 (140)	1440
Multiply	100(250)	500 (1250)	13000
Divide	11(4)	220 (80)	1020
Square Root	4 (4)	80 (80)	880
Trigonometry	2	40	40
Shift, Logical, Read	200(300)	200 (300)	3200
Totals	357(698).	1080 (1850)	19580

( ) indicates baseline calibration computations

The baseline calibration must be treated separately as its nominal solution rate is 0.1 s whereas the beacon solution rate is 0.67 s. Table I-6-1 indicates that the computer must perform about 20,000 operations per second. This is certainly well within the state-of-the-art of many commercially available computers. Preliminary numerical analyses indicate that an accuracy (round-of error) of about 10^{-6} is required throughout the calculations. This translates into a 21-bit word.

Figure I-6-3 is a functional flow diagram of the data processing. The left hand column describes the steps of the baseline calibration. Actually several simultaneous baseline calibrations are being conducted. In subsection I-1.4 it was shown that the beacon signal ambiguity must be resolved in four steps which, in effect, establish eight separate coarse baselines plus two vernier baselines. The algorithms for each baseline calibration are identical, however. Data editing is achieved by comparing the actual phase measurement with the predicted. This approach makes maximum use of the small time interval between measurements and the near deterministic physical motion of the booms.

The curve fit to determine boom motion is envisioned as a low-order polynominal least squares fit. The least squares fit provides estimates of each baseline's orientation and length as well as the derivatives of its motion. The fit also provides some additional CT noise suppression.

The right hand column of Figure I-6-3 is concerned with the beacon's location. The beacon's ambiguity is resolved in the classic manner; an unambiguous fix is computed, with no provision for boom motion compensation, followed by the second and third levels of lane resolution. Finally, the vernier case (the final position fix) is computed, complete with boom motion compensation.

The logic given in the lower right hand corner sets up the calculation and display of the beacon's velocity.

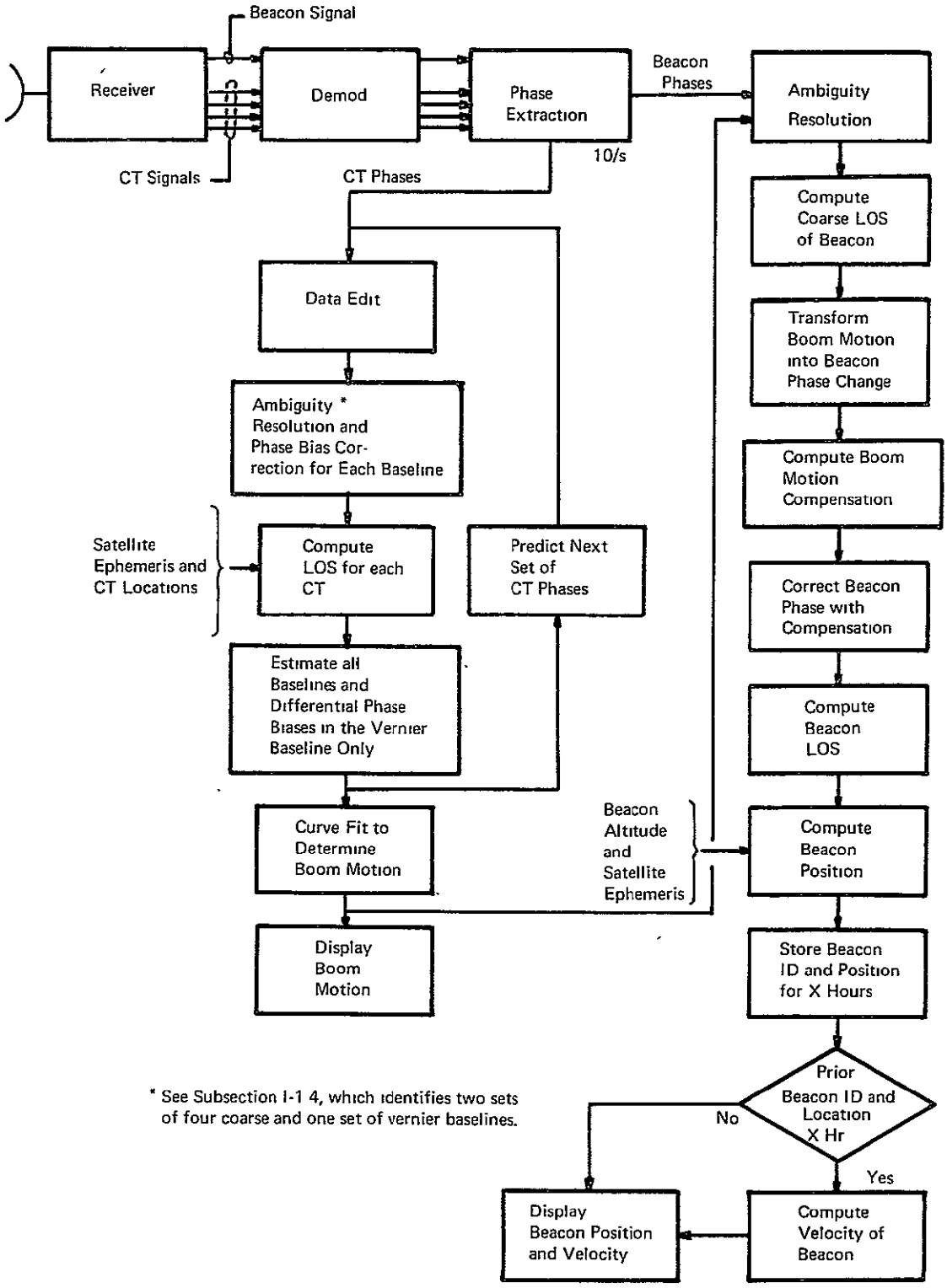

Figure I-6-3. Data Processing Functional Flow Diagram

Section II-1

SYSTEM CONSIDERATION AND TRADEOFF ANALYSIS

The study plan called for study of an interferometer system for determining constant pressure weather balloon locations to an accuracy of 1 km. By periodically determining the balloon locations, the velocity of the balloons and hence the wind velocity could be derived and used for weather prediction on a global basis.

Many of the system parameters, such as the interferometer baseline length, the operating frequency, and the type of 24^h orbit into which the satellite would be placed, were subject to tradeoff. In fact, the position accuracy requirement appeared so stringent that it was also made a parameter, and methods were studied to obtain a velocity accuracy of 1 m/s (3.6 km/h), which could be obtained from less precise position data but which may be sufficient as an input to the computerized weather prediction model. However, during the study it was found that 1-km position accuracy could be achieved.

This section presents the tradeoff studies and the rationale for system parameter choices.

II-1.1 RELATIONSHIP AMONG ELECTRICAL ANGLE, SPACE ANGLE, AND POSITION LOCATION

A radio interferometer is used to determine the angular position of an RF signal source by measuring the difference in radio signal path length from the emitting source to a pair of antennas. Figure II-1-1 shows the wavefront going through antenna element 1, but still at a distance d from antenna 2. This distance, expressed in terms of the baseline L, corresponds to the electrical angle γ of the wave traveling between the wavefront and antenna 2. This results in the interferometer equation

$$\gamma = 2\pi \frac{L}{\lambda} \sin \varphi . \qquad \text{(II-1-1)}$$

The angle γ, which is the phase difference between signals arriving at antennas A_1 and A_2, will be measured, and from it φ can be derived. If the attitude of the baseline is known in a reference frame, then the direction to the emitter can be determined. Although this is generally a complicated 3-dimensional problem which will be treated in Section II-2, 2-dimensional considerations provide insight into the possible tradeoff between measurement accuracies and position location.

The accuracy $\Delta\gamma$ with which γ can be determined is limited by precision of instrumentation, system noise, and other interferences. The angular accuracy $\Delta\varphi$ as a function of $\Delta\gamma$ becomes

$$\Delta\gamma = \Delta\varphi \; 2\pi \frac{L}{\lambda} \cos \varphi . \qquad \text{(II-1-2a)}$$

Since $0 < \varphi < 9^\circ$,

$$\cos \varphi \doteq 1$$

and

$$\Delta\gamma \doteq 2\pi \frac{L}{\lambda} \Delta\varphi . \qquad \text{(II-1-2b)}$$

The space angle uncertainty $\Delta\varphi$ equals the electrical angle difference uncertainty $\Delta\gamma$ multiplied by the magnification of the interferometer, which is $2\pi\frac{L}{\lambda}$.

Knowledge of the space angle to an accuracy $\Delta\varphi$ permits calculation of the balloon position to an accuracy ΔX, where it is assumed that ΔX is along the shell in which the balloon moves. For an explanation consider Figure II-1-2. The angle between the direction of propagation (which is a line normal to the wavefront) and the local normal at the interferometer is β. The uncertainty in determining φ, i.e., $\Delta\varphi$, equals an uncertainty in β, i.e., $\Delta\beta$. For simplicity, the figure shows the interferometer in its nominal position, i.e., parallel to a plane tangential to earth's surface. Since $\Delta\beta = \Delta\varphi$, one can write, applying the law of sines to the cross-hatched triangle,

$$\sin \Delta\varphi \doteq \Delta\varphi \doteq \Delta X \frac{\sin E}{r} . \qquad \text{(II-1-3)}$$

The relationship given by Equation II-1-3 is shown in Figure II-1-3, which displays the required space angle as a function of elevation angle with position error ΔX as parameter. It is important to note that the required accuracy drops by one half order of magnitude ($\sqrt{10}$) between elevation angle values of E = 10 deg to 30 deg. This steep drop points out that a lower limit of the elevation angle E must be chosen for system design purposes. It will be seen later (subsections II-1-5 and II-9-4) that the system can be made to work quite well between elevation angles of 20 deg $\leq$ E $\leq$ 90 deg.

A relationship between the electrical angle accuracy $\Delta\gamma$ and the position location can be established by combining equations II-1-2a and II-1-3. This yields

$$\Delta\gamma = 2\pi\frac{L}{\lambda} \frac{\sin E}{r} \Delta X. \qquad \text{(II-1-4)}$$

Figure II-1-4 shows the relationship given by Equation II-1-4 as a function of elevation angle with $\frac{L}{\lambda}\Delta X$ as parameter. Figure II-1-4 also illustrates the same effect of a rapid increase in required accuracy for very low elevation angles. Furthermore, it can be seen that, as $\frac{L}{\lambda}$ is increased for a given ΔX, the electrical angle accuracy requirement drops.

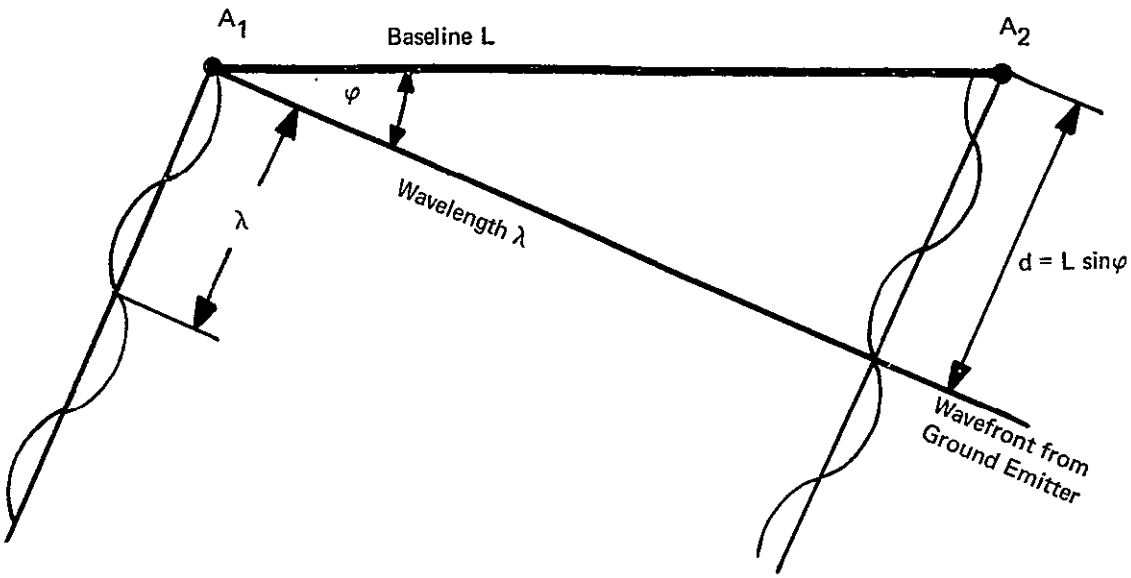

Figure II-1-1. Principle of a Radio Interferometer

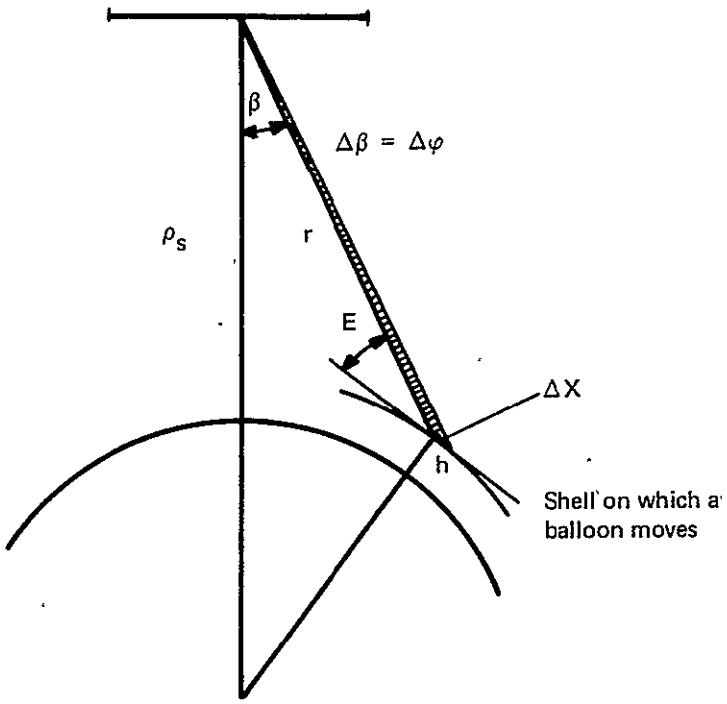

Figure II-1-2. Position Location Geometry

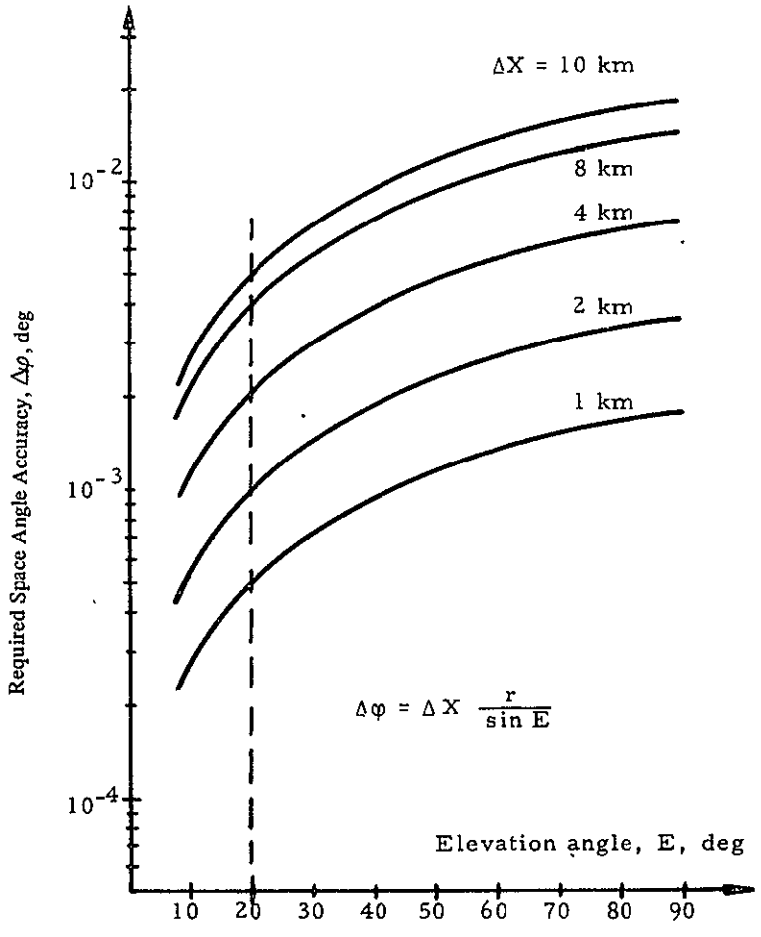

Figure II-1-3. Space Angle Accuracy as Function of Elevation Angle

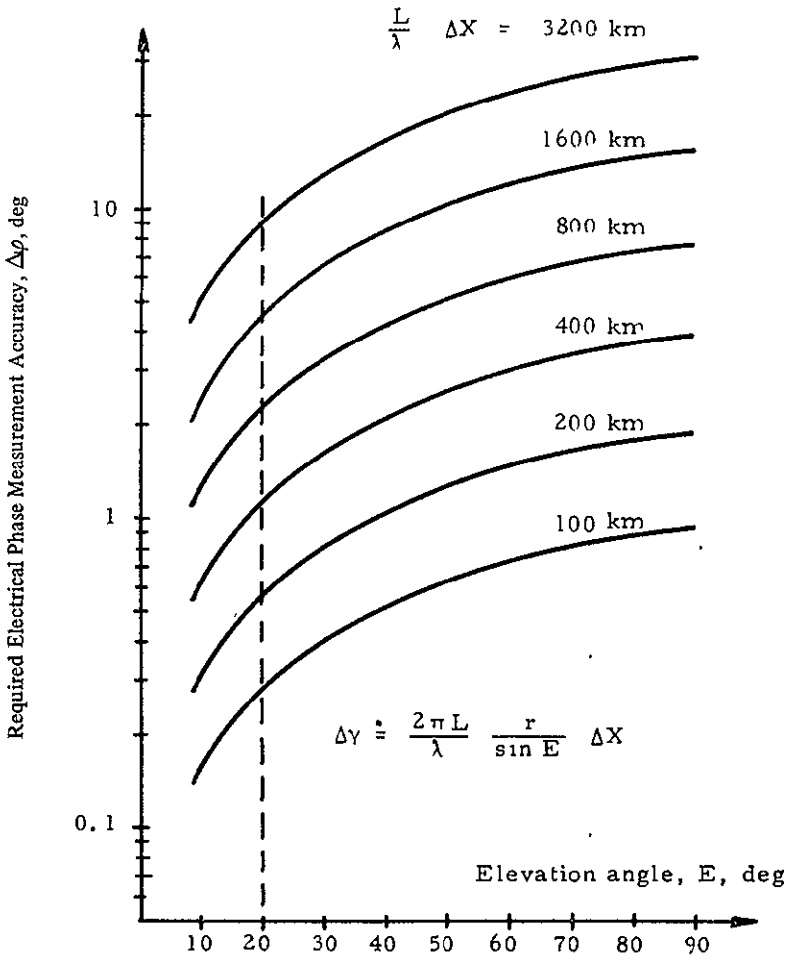

Figure II-1-4. Electrical Angle Accuracy as Function of Elevation Angle

If the small angle approximation for the angle φ is not made, Equation (II-1-4) would be

$$\Delta\gamma = 2\pi \frac{L}{\lambda} \frac{\Delta X}{r} \sin E \left[1 - \left(\frac{\rho_e}{\rho_s}\right)^2 \cos^2 E\right]^{1/2} \qquad \text{(II-1-5)}$$

where we have used the relation

$$\sin \varphi = \frac{\rho_e + h}{\rho_s} \cos E \doteq \frac{\rho_e}{\rho_s} \cos E. \qquad \text{(II-1-6)}$$

II-1.2 POSITION LOCATION DETERMINATION AND VELOCITY DETERMINATION TRADEOFF

In subsection II-1.1 the position location accuracy ΔX was derived as a function of the electrical angle accuracy $\Delta\gamma$. From Equation II-1-6 follows

$$\Delta X = \Delta\gamma \frac{\lambda}{2\pi L} \frac{r}{\sin E} \left[1 - \left(\frac{\rho_e}{\rho_s}\right)^2 \cos^2 E\right]^{-1/2}. \qquad \text{(II-1-7)}$$

The standard deviation σ of the phase of a sinusoidal signal corrupted by Gaussian noise[5] is given by

$$\sigma = \frac{1}{\sqrt{2\ \text{SNR}}} \qquad \text{(II-1-8a)}$$

where SNR is the signal-to-noise power ratio. This equation applies when the phase of a noisy signal is measured with respect to a clean reference. If the phase difference γ is measured between two noisy sine waves, each with the same SNR (and with independent noises), the standard deviation of error $\Delta\gamma$ (or of the phase) would be

$$\sigma_{\Delta\gamma} = \frac{1}{\sqrt{\text{SNR}}}. \qquad \text{(II-1-8b)}$$

Figure II-1-5 graphically represents equations II-1-8a and II-1-8b.

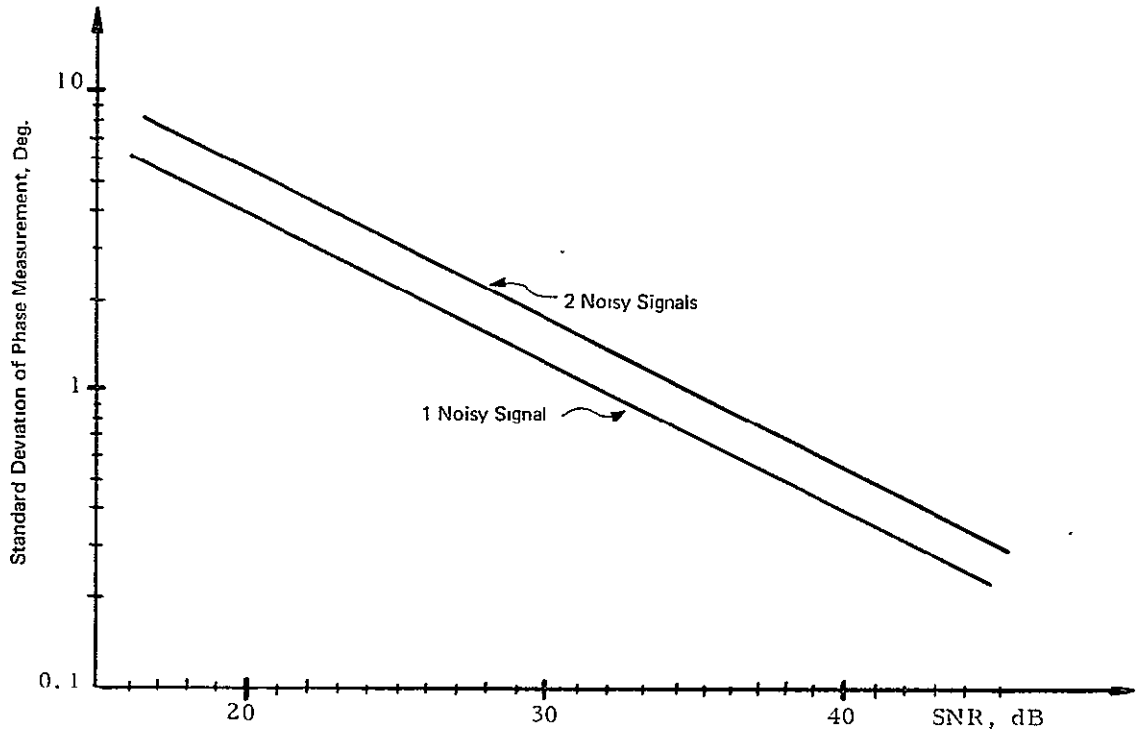

Figure II-1-5. Standard Deviation of Phase Measurement

The SNR of each signal can be expressed as

$$\text{SNR} = \frac{G_s P_B G_B}{N_o B_n L_p} \qquad \text{(II-1-9)}$$

with

$$L_p = \left(\frac{4\pi r}{\lambda}\right)^2$$

where L_P is the space loss, G_s is the satellite antenna gain, G_B is the antenna gain of the balloon beacon, P_B the effective radiated power produced by the balloon beacon, N_o is the noise density, and B_n is the receiver noise bandwidth.

Combining equations II-1-8 and II-1-9 yields

$$\sigma_{\Delta\gamma} = \sqrt{\frac{N_o B_n}{P_B G_s G_B}} \left(\frac{4\pi r}{\lambda}\right) \quad . \tag{II-1-10}$$

This relationship is shown in Figure II-1-6, which presents the required equivalent noise bandwidth for a given electrical phase measurement error with the balloon beacon power and the frequency as parameters. From the knowledge of the value of $\sigma_{\Delta\gamma}$, the standard deviation of ΔX can be determined using Figure II-1-4.

It is of interest to investigate how the position accuracy $\sigma_{\Delta X}$ depends on the other system parameters. Combining equations II-1-7 and II-1-10 yields

$$\sigma_{\Delta X} = 2\sqrt{\frac{N_o B_n}{G_s P_B G_B}} \left[\frac{r^2}{L \sin E}\right] \left[1 - \left(\frac{\rho_e}{\rho_s}\right)^2 \cos^2 E\right]^{-1/2} . \tag{II-1-11}$$

This shows that the position accuracy is independent of the operating frequency for a given B_n, L, G_s, and P_B, except for slightly increased noise figures at higher frequencies. The increase in the standard deviation of the phase measurement due to increased space loss at higher frequencies is offset by the increased resolution capabilities at the higher frequency due to a higher $\frac{L}{\lambda}$. However, more dc power will be required to produce the RF balloon power at the higher frequency, and the beacon cost may increase owing to the increased cost of higher frequency components. This result is important when it comes to choosing an operating frequency for the system.

Next, the impact of the position accuracy on the velocity accuracy is examined. This tradeoff is discussed here using a 1-dimensional model and considering only the component of the position error caused by random noise errors. This approach simplifies the explanation and brings out the pertinent points. For the 3-dimensional calculation, the reader is referred to Section II-2 of this report.

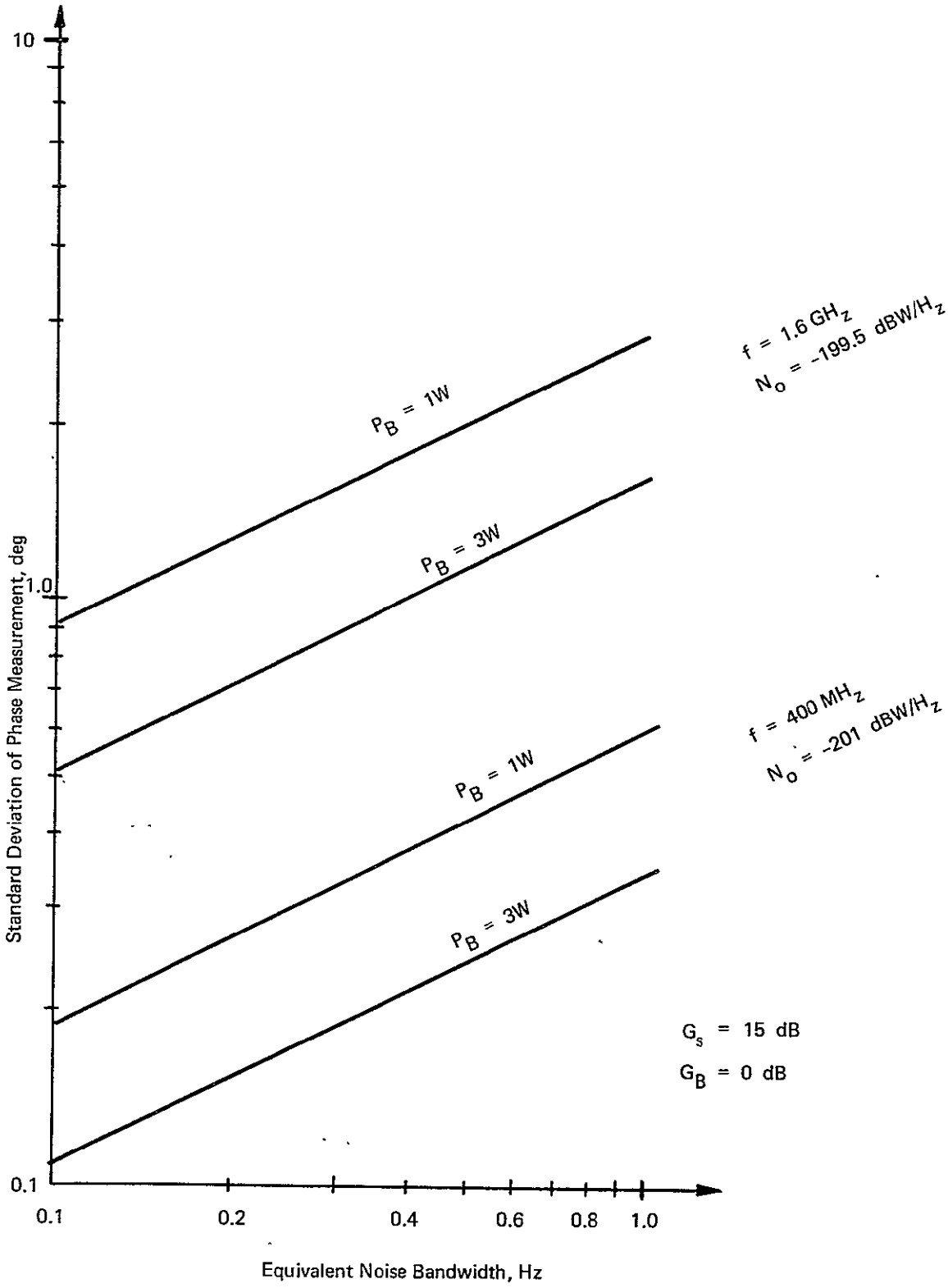

Figure II-1-6. Standard Deviation of Phase Angle Measurement Versus Equivalent Noise Filter Bandwidth.

The standard deviation of the velocity can be expressed as

$$\sigma_{\Delta v} = \frac{\sqrt{2}\sigma_{\Delta X}}{T} \qquad \text{(II-1-12)}$$

where T is the time between two position fixes and independence of the two fixes is assumed.

This relationship is shown in Figure II-1-7. For a given position location error, the average velocity measurement-can be determined to a higher accuracy as the interval between measurements increases. For example, since the wind velocity may be needed to an accuracy of 1 to 2 m/s for weather prediction, for an interval T between measurements of 2 hours the position need only be determined accurately to 5 to 10 km to meet the requirements. This indicates that if wind velocity determination alone is the purpose of the system, the position accuracy requirement of 1 km might be considerably relaxed.

II-1-3 CALIBRATION

The interferometer baseline is defined by a line joining the two antenna phase centers and not by the shape of the booms. The baseline calibration (both length and orientation), therefore, involves determining the relative location of the antenna phase centers at the tips of the booms. Changes in orientation of the satellite's hub, thermal distortion of the booms, and transient fluttering of the booms all cause changes in the baseline orientation and length. Therefore, the calibration must be carried out sufficiently often to follow these baseline changes. The boom analysis shows that the resonance period of the booms is on the order of 60 s. The data link analysis indicates that, for 20 dBW ground transmitters, an acceptably low phase error can be achieved with only a 0.1 s integration. These two results indicate that phase measurements can be made often enough that the phase will not be smeared due to averaging in the presence of boom motion.

A simplified explanation for one baseline calibration in the 2-dimensional case is shown in Figure II-1-8. The simplified explanation is realistic, because in the 3-dimensional case the baselines are calibrated independently.

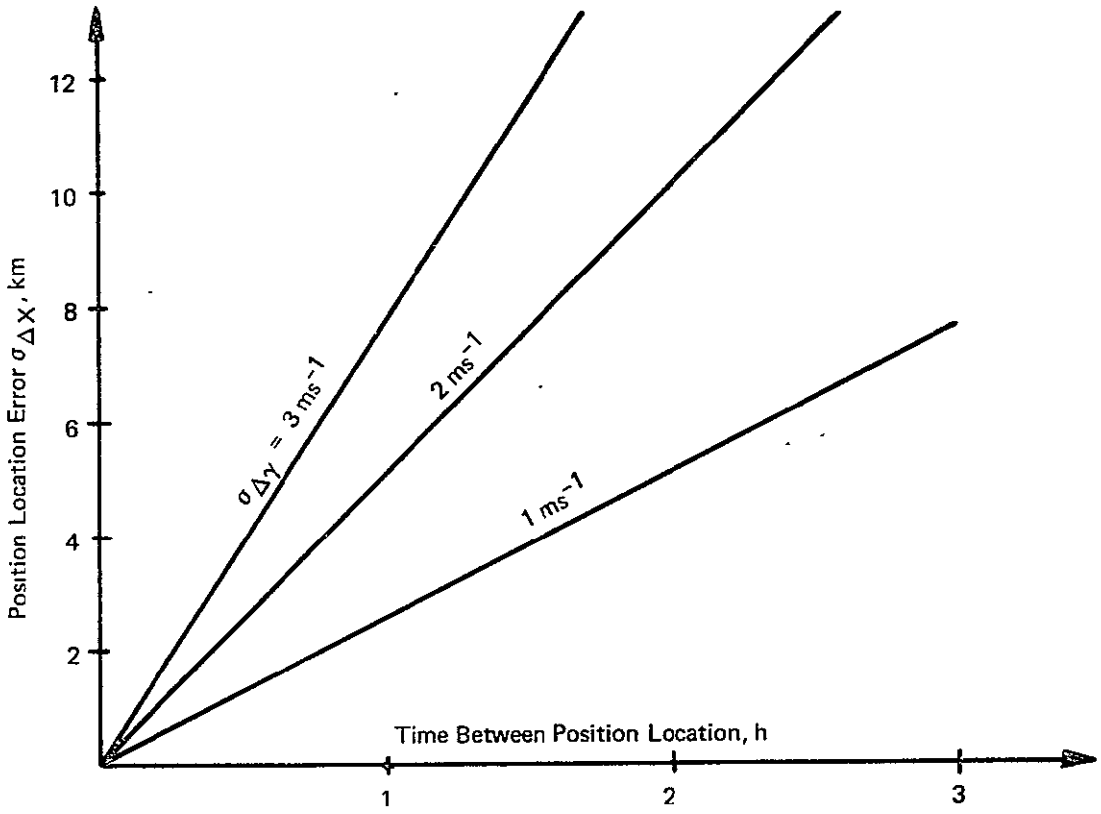

Figure II-1-7. Velocity Errors (rms)

The phase measurements γ_1 and γ_2 across the baseline from ground transmitters 1 and 2 are given by equations II-1-13 and II-1-14, as follows:

$$\gamma_1 = \frac{2\pi L}{\lambda} \cos(\alpha + 90 - \beta_1) \qquad \text{(II-1-13)}$$

$$\gamma_2 = \frac{2\pi L}{\lambda} \cos(\alpha + 90 - \beta_2) \; . \qquad \text{(II-1-14)}$$

The unknown quantities of these equations are α and L.

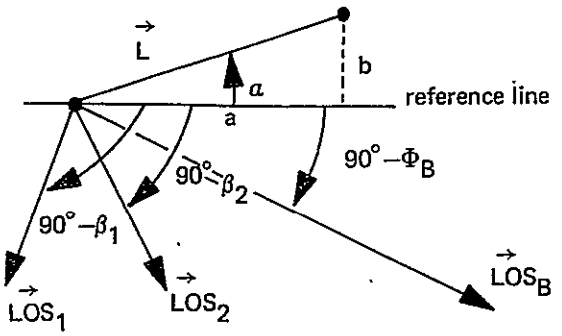

$\vec{LOS}_1$ and $\vec{LOS}_2$ are the lines-of-sight to two known ground transmitters, hence β_1 and β_2 are known.

α is the unknown orientation, and L is the unknown length.

$\vec{LOS}_B$ is the line-of-sight to the beacon to be located.

Figure II-1-8. Baseline Calibration, 2-Dimensional Presentation

Expanding the cosine terms and noting that $a = L \cos \alpha$ and $b = L \sin \alpha$, these two equations may be written as

$$\gamma_1 = \frac{2\pi}{\lambda} \left[a \sin \beta_1 - b \cos \beta_1 \right] \qquad \text{(II-1-15)}$$

and

$$\gamma_2 = \frac{2\pi}{\lambda} \left[a \sin \beta_2 - b \cos \beta_2 \right] . \qquad \text{(II-1-16)}$$

If L were presumed known, then only α remains unknown. Thus either Equations II-1-15 or Equation II-1-16 may be used, and the other equation is simple redundant. When L is not known, these two linear algebraic equations may be solved as follows:

$$a = \frac{\lambda}{2\pi \sin(\beta_2 - \beta_1)} \left[-\gamma_1 \cos \beta_2 + \gamma_2 \cos \beta_1 \right] \qquad \text{(II-1-17)}$$

$$b = \frac{\lambda}{2\pi \sin(\beta_2 - \beta_1)} \left[-\gamma_1 \sin \beta_2 + \gamma_2 \sin \beta_1 \right] . \qquad \text{(II-1-18)}$$

The solution for a and b constitutes the baseline calibration.

In the analysis of the 3-dimensional case, $\vec{L}$ has a third component. For determination of $\vec{L}$, a third phase measurement from a third ground station is used to completely determine the vector $\vec{L}$.

The line-of-sight to the balloon is given by

$$\gamma_B = \frac{2\pi}{\lambda}\left[a \sin \Phi_B - b \cos \Phi_B\right]$$

with (II-1-19)

$$\Phi_B \doteq 90^\circ .$$

Substituting II-1-17 and II-1-18 into II-1-19 and simplifying by approximating sin Φ with Φ and cos Φ with 1 yields

$$\Phi_B = \frac{(\beta_2 - \beta_1)}{(\gamma_2 - \gamma_1)}\ \gamma_B + \frac{\gamma_2\beta_1 - \gamma_1\beta_2}{\gamma_2 - \gamma_1} \quad . \tag{II-1-20}$$

Note that all references to the length and orientation of the baseline have been eliminated. Only the known angles β_1 amd β_2 and the measured values γ_1 and γ_2 are found. The significance of Equation II-1-20 is that the critical parameter in the position location, i.e., $\overrightarrow{LOS}_B$ (or in the 2-dimensional case, Φ_B) is not an explicit function of baseline length or orientation but rather a function of measured quantities and known angles.

In a static environment, Equation II-1-20 is corrected stated. However, in a realistic environment, where the baselines move about, all measurements must be time averaged in order to obtain the requisite phase accuracy. Thus, Equation II-1-20 should be written as

$$\Phi_B\,(t+\tau) = \frac{\beta_2 - \beta_1}{\wwave{\gamma_1}(t) - \wwave{\gamma_2}(t)}\ \wwave{\gamma_B}\,(t+\tau) + \frac{\wwave{\gamma_1}(t)(90-\beta_1) - \wwave{\gamma_2}(t)\,(90-\beta_2)}{\wwave{\gamma_1}(t) - \wwave{\gamma_2}(t)} \tag{II-1-21}$$

where $\wwave{\ }$ indicates time averaging. Hence the measured value of γ will be the mean of the variable, and if the time averaging is long, a problem may exist with respect to the time to which the mean value refers. From Figure II-1-8, β_1 and β_2 are seen to be independent of α and, therefore, not dependent on the boom motion.

Since $\tilde{\gamma}_1$ and $\tilde{\gamma}_2$ are measured 10 times a second, the maximum time skew between the calibration signals and the beacon signals is $\frac{\tau}{2}$ or 0.5 s. Thus asynchroneity of calibration and balloon signals is small and effect the position location only negligibly.

Potentially, the greatest source of error which might be embedded in Equation II-1-21 is that γ_1, γ_2 and, γ_B are mean values without, as yet, a clear understanding of the time to which the mean refers.

A correct formulation for these measured phases is

$$\gamma_k = \frac{1}{\tau} \int_t^{t+\tau} \left[\dot{\gamma}_k \, t + \gamma_k^* \right] \, dt \qquad \text{(II-1-22)}$$

where γ_k^* is the value of γ_k if there is no boom motion.

In Section II-1.8, a derivative for $\gamma_{k\ max}$ is given, (see Equation II-1-62). This derivative is

$$\dot{\gamma}_{max} = \frac{2\pi L}{\lambda} \left[\omega_1 + A_m \, \omega_2 \right] . \qquad \text{(II-1-23)}$$

As pointed out in Section II-1.8, $\omega_1 \gg A_m \, \omega_2$, and $\dot{\gamma}_{max} \doteq 2$ deg/s for $\frac{L}{\lambda} = 400$. Assume $\dot{\gamma}$ is a constant over the integration time. The worst effect $\dot{\gamma}_2$ can have on $\tilde{\gamma}_h$ is given by

$$\frac{1}{\tau} \int_t^{t+\tau} 2t \, dt = \tau \text{ (deg)} . \qquad \text{(II-1-24)}$$

On the other hand, if the averaging interval straddled the time of maximum $\dot{\gamma}$ (this is equally likely as the worst case),

$$\frac{1}{\tau} \int_{t-\frac{\tau}{2}}^{t+\frac{\tau}{2}} 2t \, dt = 0 . \qquad \text{(II-1-25)}$$

The CT signals with their higher ERPs require $\tau = 0.1$ s. Thus a worst case γ for the CT phases due to boom motion is $0.1°$, and on the average, the error will be much less than the random part ($0.4°$). Consequently, with the CT phases measured 10 times a second, the effect of boom motion on the calibration is small. Thus, the time of the mean value is of minor importance, and the mean value is assumed to apply to the end of the integration interval.

Unfortunately, this conclusion cannot be extended to the balloon signals because their ERP is much less, and to achieve the required phase accuracy, τ must be greater than 0.1 s. For the low ERP balloons, τ has been calculated to be 10 s.

Reconsider Equation II-1-19 in the sense that γ_B is a time averaged variable, i.e.,

$$\gamma_B(t) = \frac{1}{\tau} \int_{t}^{t+\tau} \frac{2\pi}{\lambda} \left[a(t) \cos \Phi_B - b(t) \sin \Phi_B \right] dt \qquad \text{(II-1-26)}$$

and a(t) and b(t) indicate that the baselines (booms) are moving. With the assistance of Figure II-1-8 it is seen that Φ_B is a constant in Equation II-1-26. Hence

$$\gamma_B(t) = \frac{2\pi}{\tau\lambda} \left[\cos \Phi_B \int_{t}^{t+\tau} a(t)\, at - \sin \Phi_B \int_{t}^{t+\tau} b(t)\, dt \right] . \qquad \text{(II-1-27)}$$

The significance of Equation II-1-27 is that its integrands are known, and for practical purposes, they are known on a continual basis by virtue of their determination 10 times a second. For example, with $\tau = 10$ s, a(t) and b(t) would be computed 100 times. Coupled with the low period of oscillation of the booms ($\frac{1}{\omega_1}$ = 1 cycle/60 s), the truncation error associated with the numerical integration is less than 0.001 deg.

We now treat a(t) as $a(t_s) + \Delta a(t)$ and $b(t_s) + \Delta b(t)$ where $a(t_s)$ and $b(t_s)$ refer to the baselines at an instant of time t_s and $\Delta a(t)$ and $\Delta b(t)$ are the changes in the baselines after the time t_s has passed. The time t_s physically would be the start of the balloon integration interval.

Equation II-1-27 may be rewritten as

$$\gamma_B = \frac{2\pi}{\tau\lambda}\left[\cos\Phi_B\, a(t_s) - \sin\Phi_B\, b(t_s)\right] + \frac{2\pi}{\tau\lambda}\left[\cos\Phi_B \int_{t_s}^{t_s+\tau} \Delta a(t)\,dt - \sin\Phi_B \int_{t_s}^{t_s+t} \Delta b(t)\,dt\right]. \qquad \text{(II-1-28)}$$

The second term on the right hand side of II-1-28 is the boom motion compensation, and $\tilde{\gamma}$ is the measured phase; the first term on the right-hand side is the phase measurement corrected for the boom motion.

The net result is that, with $\tilde{\gamma}_B$ corrected for boom motion via Equation II-1-28, Equation II-1-21 has no significant errors other than the randomness in the measurements of $\tilde{\gamma}_1$, $\tilde{\gamma}_2$ and $\tilde{\gamma}_B$.

II-1.4 AMBIGUITY RESOLUTION

Since the baseline will be many wavelengths long, many ambiguities will exist in the phase measurements, space angle, and resulting position location; these, of course, must be resolved. A short baseline can be added to the system or a differential baseline can be used. Figure II-1-9 illustrates these two methods. The short baseline method has a physically short baseline L_3. The differential baseline is formed by the difference of the two lengths or

$$L_1 - L_2 = L_3 \qquad \text{(II-1-29)}$$

if we want the same equivalent length.

For the long baseline, we measure the electrical phases γ_{11} and γ_{13}. Because the phase measurements are modulo 2π, we have

$$\gamma_{11} - \gamma_{13} \pm n2\pi = \frac{2\pi L}{\lambda} \sin\varphi; n = 0, 1, 2, \ldots \qquad \text{(II-1-30)}$$

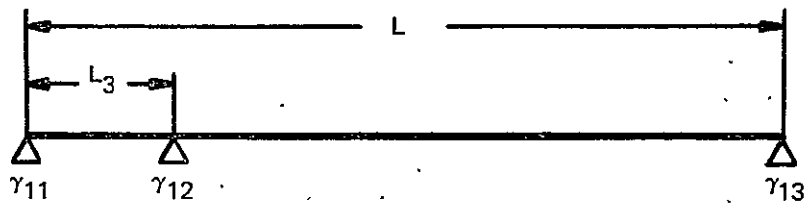

(a). Short and Long Baseline

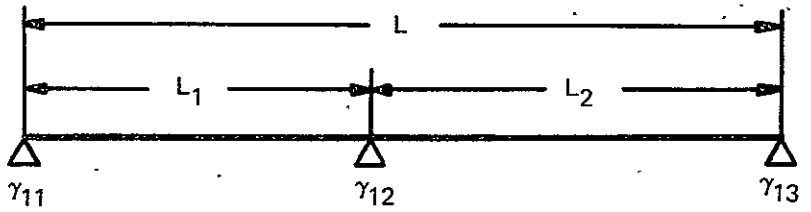

(b). Differential Baseline

Figure II-1-9. Baselines for Ambiguity Resolution

where φ is the space angle. Use of the small angle approximation yields

$$\varphi = \left(\gamma_{11} - \gamma_{13}\right) \frac{\lambda}{2\pi L} \pm n\left(\frac{\lambda}{L}\right) \text{ rad} \qquad \text{(II-1-31)}$$

so that ambiguities occur in space every $\frac{\lambda}{L}$ rad. Since the short baseline L_3, no ambiguities are wanted, L_3 will be restricted so that

$$-\pi \leq \frac{2\pi L_3}{\lambda} \sin\varphi \leq +\pi \,. \qquad \text{(II-1-32)}$$

For a satellite at snychronous orbit, the space angle can vary from about -9.6 deg to +9.6 deg (allowing some satellite attitude error) so that we must be able to resolve the space angle in this range. Any other space angle is physically impossible for a balloon. This gives a maximum value of 3 for $\frac{L_3}{\lambda}$.

If the standard deviation of each phase difference measurement is $\sigma_{\Delta\gamma}$, the standard deviation of the space angle measurement for the short baseline is

$$\sigma_\varphi = \sigma_{\Delta\gamma}\left(\frac{\lambda}{2\pi L_3}\right). \qquad \text{(II-1-33)}$$

Thus the standard deviation of the space angle measurement by the short baseline compared to one half of the ambiguity interval is

$$\frac{\sigma_\varphi}{\frac{1}{2}\text{ ambiguity interval}} = \frac{\sigma_{\Delta\gamma}\, L}{2\pi L_3} \text{ (short baseline)} . \qquad \text{(II-1-34)}$$

We would normally want this to be one-third or less so that an error in ambiguity resolution occurs less than 1% of the time. For a $\sigma_{\Delta\gamma}$ of 1 deg and $L_3=3\lambda$, for example, we would be limited to a long baseline of about 350 wavelengths.

For the differential baseline measurement, we form the quantity

$$\gamma_{11} - 2\gamma_{12} + \gamma_{13} = \frac{2\pi\,(L_1 - L_2)}{\lambda} \sin\varphi$$

$$\doteq \frac{2\pi\, L_3}{\lambda}\ \varphi \ . \qquad \text{(II-1-35)}$$

Since the standard deviation of each phase is $\frac{\sigma_{\Delta\gamma}}{\sqrt{2}}$ (since for a phase difference it is $\sigma_{\Delta\gamma}$), the standard deviation of the space angle is now

$$\sigma_\varphi = \sqrt{3}\ \sigma_{\Delta\gamma}\left(\frac{\lambda}{2\pi L_3}\right). \qquad \text{(II-1-36)}$$

The ambiguity interval to be resolved is approximately $\frac{2\lambda}{L}$, since each of the baselines $\left(L_1 \text{ and } L_2\right)$ is approximately $\frac{L}{2}$. Therefore

$$\frac{\sigma_\varphi}{\frac{1}{2}\text{ ambiguity interval}} = \frac{\sqrt{3}\ \sigma_{\Delta\gamma}\, L}{4\pi\, L_3} \text{ (differential baseline)} . \qquad \text{(II-1-37)}$$

The performance is, therefore, comparable to that of the short baseline.

Figure II-1-10 shows the system proposed to resolve ambiguities for the balloons. The ambiguity resolution steps for the balloons would be as follows:

a. 3λ baseline - no ambiguities
b. 20λ baseline - resolved by 3λ baseline
c. 190λ baseline - resolved by 20λ baseline
d. 400λ baseline - resolved by 190λ baseline.

The 20λ baseline is a differential baseline (210λ minus 190λ). If, in the final system design, the links have sufficient margin, resolution from the 20λ baseline to the 400λ baseline in one step may be possible.

It should be noted that no necessity exists for the baselines to be colinear in order to be able to resolve ambiguities, as illustrated in Figure II-1-11, in which the short baseline L_1 is used to resolve ambiguities in the long baseline L_2. The location of the baselines is known through the calibration signals, so that the angle φ_1 is known. It remains to find the angle φ of the incoming signal with respect to a reference, say the normal to the baseline L_2. The phase difference γ across the short baseline L_1 is

$$\gamma = \frac{2\pi L}{\lambda} \sin (\varphi - \varphi_1) \qquad \text{(II-1-38)}$$

and since φ_1 is known, φ can be solved for directly.

The discussion of the problem up to this point assumed that the baselines are known from the calibration process, where the angles between the baselines are known. The techniques analyzed above will, therefore, work for the balloon signals but not for the CT signals, where the calibration process is used to determine the lengths of the baselines and angles between them.

During the study, this problem was addressed in sufficient depth that it is now believed that a viable solution can be postulated. However, additional work is required to complete the logic of the solution in three dimensions. The 2-dimensional solution is discussed below, augmented by the results of the analysis and simulation.

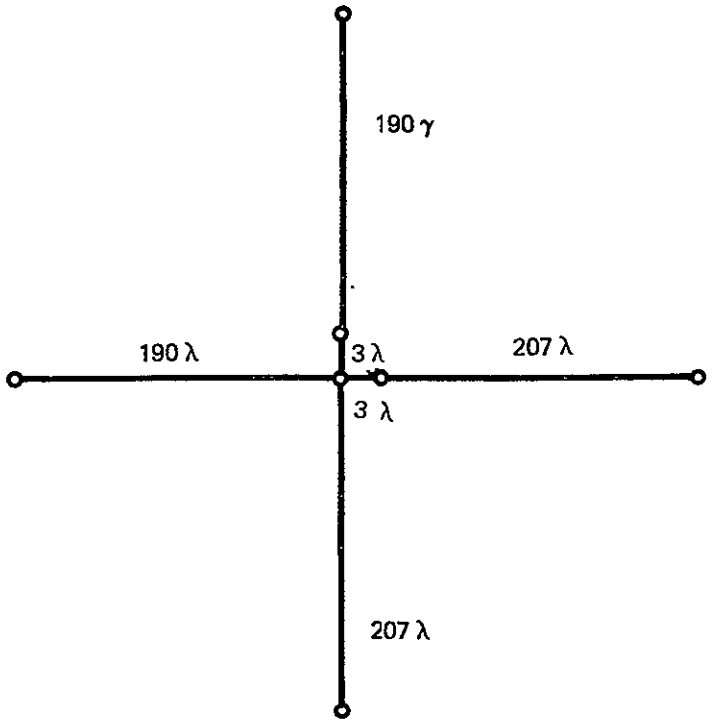

Figure II-1-10. Baselines

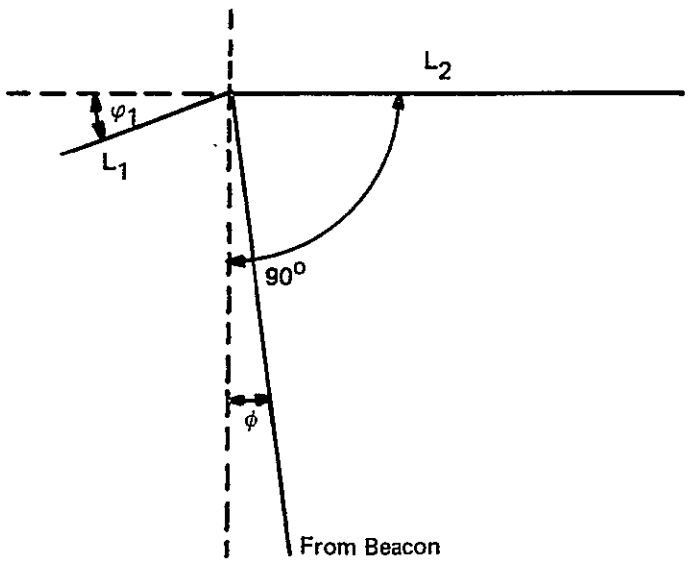

Figure II-1-11. Ambiguity Resolution with Offset Baselines

The basic idea is again based on the fundamental equations II-1-13 and II-1-14. These have been repeated here for convenience, with modification made to the left hand side to introduce the ambiguities.

$$\gamma_1^m + 2\pi k_1 = \frac{2\pi L}{\lambda} \cos(\alpha + 90 - \beta_1) \qquad \text{(II-1-39)}$$

$$\gamma_2^m + 2\pi k_2 = \frac{2\pi L}{\lambda} \cos(\alpha + 90 - \beta_2) \qquad \text{(II-1-40)}$$

where k_1 and k_2 are integers and constitute the missing wavelengths in the measurements (denoted here by γ_1^m and γ_2^m). The unknowns in these equations are k_1, k_2, and α. For the present, it is assumed the L is known. An additional very important constraint is that k_1 and k_2 must be integers.

From the error analysis it was learned that the error in γ_1 or γ_2 must be less than 0.4 deg to maintain a satisfactory calibration accuracy. However, an error in k_1 and k_2 causes an error of 360 x n deg, where n is the number of missing wavelengths. Thus one missing wavelength causes 900 times more error than the random error and will, therefore, amplify the error in α by 900 times.

The approach to determining k_1 and k_2, then, is to determine the integers k_1 and k_2 which minimize the disagreement of α obtained via equations II-1-39 and II-1-40.

Preliminary analyses indicated that, for an arbitrary α, this approach was unfeasible from a logical viewpoint; the combinations of k_1 and k_2 for $\frac{L}{\lambda} = 400$ caused inordinate computational problems. However, the boom flexure analysis indicated that the non-colinearity was small or, equivalently, k_1 and k_2 could only assume a small range of integers. Thus, the approach appears practical.

An analysis of the technique was conducted. Figures II-1-12 and II-1-13 show the results. The logic used to generate the curves is as follows:

Give $\frac{L}{\lambda}$, β_1, β_2, γ_1^m, γ_2^m, an upper and lower bound on k_1 and k_2, a value for k_1 is selected. An α which satisfies Equation II-1-39 is then computed. The same α is entered into Equation II-1-40, yielding a value for k_2. However k_2 must be an integer, and if it is not, the value for k_1 cannot be correct. Thus k_1 is changed by one integer, and the entire process is repeated until the computed k_2 is an integer.

The confusion factors which could lead to erroneous solutions for k_1 and k_2 are the error in γ_1^m, γ_2^m, and L.

From Figure II-1-12, an error in the calculation of k_2 of one integer causes the computed value of k_2 to have a noninteger solution of $\Delta k_B \doteq 0.015$. The equivalent phase error is 0.015 times 360 or 5.5 deg. In other words, if $\Delta\gamma_1^m$ or $\Delta\gamma_2^m$ where 5.5^o, a false solution for the ambiguity could be made. The probability of a phase error that large for the CT signals is negligibly small (about 10σ).

The other possibility is that L is incorrect. The variation of γ with respect to L is $\frac{2\pi}{\lambda} \cos(\alpha + 90 - \beta_1) \doteq \frac{1}{\lambda}(\alpha + 90 + \beta_2)$ cycles/m. Since $\lambda \doteq 0.2$ m and $\alpha + 90 - \beta_1 < 10^o$ it follows that $\frac{\Delta\gamma}{\Delta L} \doteq 1/2$ cyckes/m. Therefore, to avoid an error in k due to an error in L, $\Delta L < 0.015/0.5 = 3.0$ cm (about 1-1/4 in.). Again, a baseline length error of this magnitude is considered very unlikely. Thermal effects are well below this magnitude, and initial deployment can easily be measured to considerably better than 1 in. by monitoring the mechanical reel.

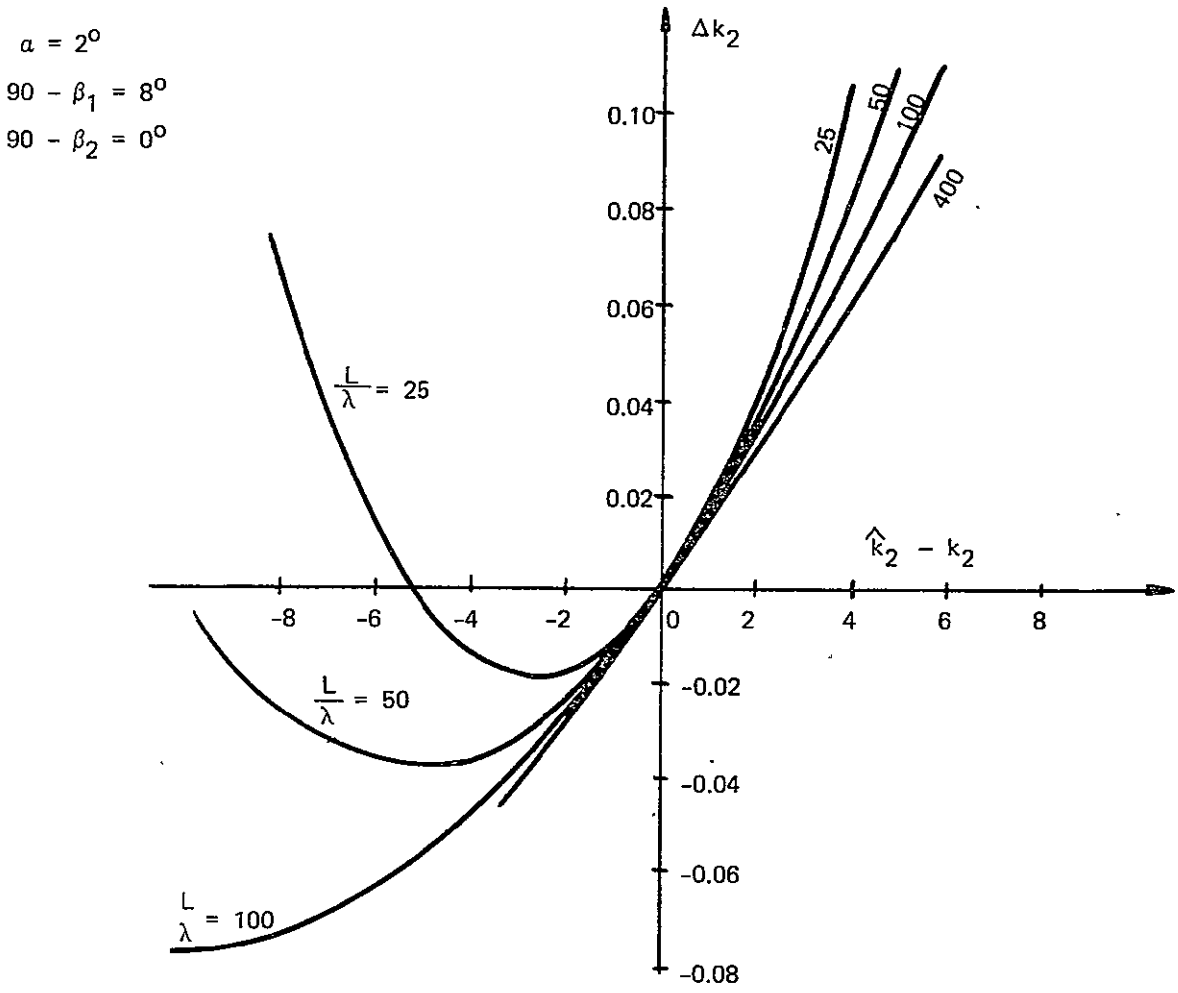

Figure II-1-12. Non-Integer Solution for k_2 as Function of Error Made in Estimating k_2, Unsymmetrical CT Illumination

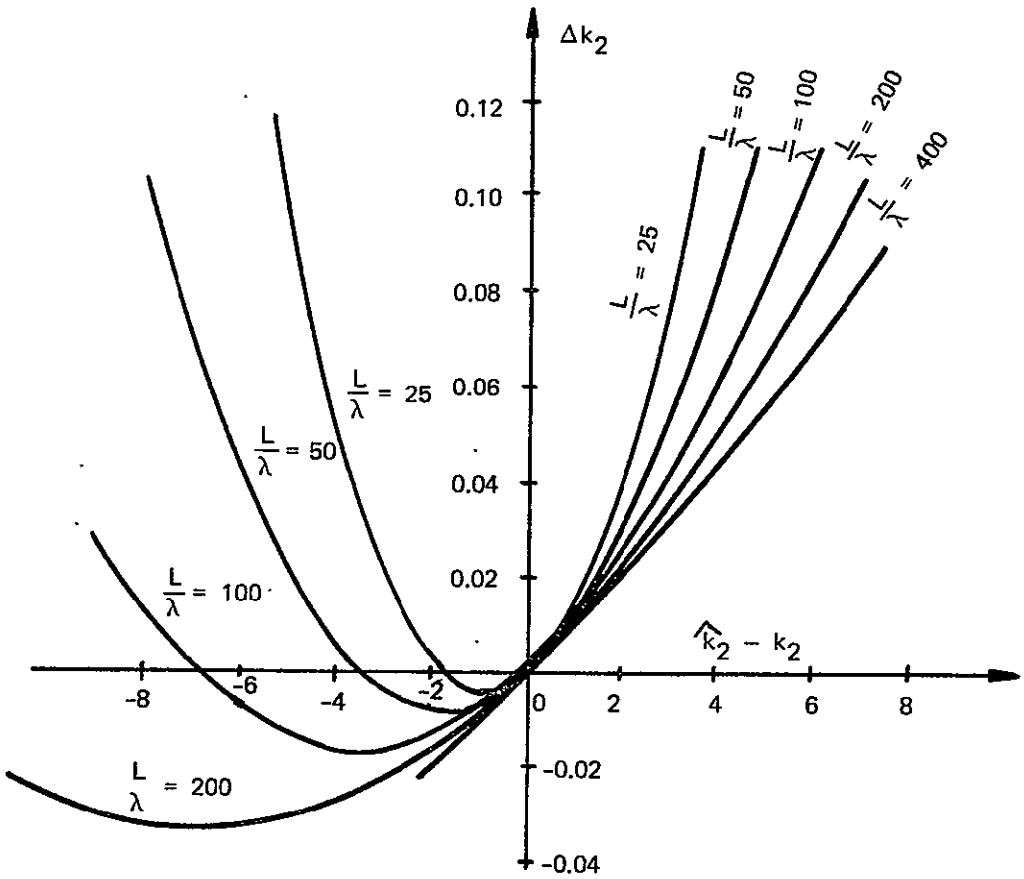

Figure II-1-13. Non-Integer Solution for k_2 as Function of Error Made in Estimating k_2, Symmetrical CT Illumination.

The ambiguity resolution begins with the shortest baseline which has no ambiguities. The orientation of this baseline is computed. An estimate of the phase to be measured by the next larger baseline is made to limit the range of k_1 and k_2. The phase measurements are then made for this baseline, and the true values of k_1 and k_2 determined. This enables one to compute the length and orientation of this baseline, which is used to provide an estimate of the next larger baseline, and so on until all baselines have been calibrated.

Since the baseline motions are relatively slow and the solution rate high, it is very probable that all eight baselines would not have to be calibrated 10 times a second. Only the vernier baseline must be calibrated that often. However, the computational loading analyses have assumed that all eight baselines are calibrated 10 times per second.

II-1.5 LINK CALCULATION

Link calculations are presented for the following emitters: calibration transmitter (ground station), and balloon platform. The link budget for the calibration transmitter exhibits a reasonable margin, and therefore the link budget is calculated only at the worst case for this emitter. The link budget for the balloon platform, however, becomes marginal at low balloon elevation angles; therefore this particular link budget is calculated over a range of elevation angles (20 deg to 90 deg).

The power received at the terminals of any particular interferometer antenna from a balloon emitter is given by

$$P_R = \frac{P_B G_B G_R}{L_p} \qquad \text{(II-1-41)}$$

where

P_R = signal power received

P_B = emitter output power $\equiv 1$ W

G_B = gain of emitter antenna = $G_B(E)$

G_R = gain of receiving antenna = $G_R(\Phi)$

L_p = path loss = $L_p(r)$.

To perform the link calculation as a function of the elevation angle E, the above quantities (G_B, G_R, and L_p) are expressed as functions of E. For the balloon antenna pattern, the values of gain (G_B) versus E may be taken from the radiation pattern shown in Figure II-9-3. The satellite antenna gain G_R is approximated by

$$G_R = 50 \ (\sin x/x)^2 \qquad \text{(II-1-42)}$$

with $x = 7.3 \sin \varphi$. This was chosen for a fit to the gain and -3 dB beamwidth of the interferometer antenna given in Section II-6. The angle φ is related to the angle E by the following relationship (see Figure II-1-2 and Equation II-1-6):

$$\sin \varphi = \frac{\rho_e + h}{\rho_s} \cos E \ . \qquad \text{(II-1-43)}$$

Using the law of sines, one finds that the range r is directly related to E by the equation

$$r = \frac{\rho_s}{\cos E} \cos \left[E + \arcsin \left(\frac{\rho_e + h}{\rho_s} \cos E \right) \right] . \qquad \text{(II-1-44)}$$

The 1-way path loss L_p is directly dependent upon r^2; and in turn upon E by Equation II-1-44.

Table II-1-1

LINK POWER BUDGET

(Emitter through Spacecraft-to-Ground Receiver)

Emitter	Calibration Transmitter	Balloon		
		E = 20°	E = 30°	E = 90°
Transmitter Power (dBW)	-	0	0	0
Transmit Antenna Gain (dB)	-	+0.7	+3.0	+2.2
ERP (dBW)	20	+0.7	+3.0	+2.2
Path Loss (dB)	-189	-188.5	-188	187.5
Polarization Loss (dB)	-0.5	-0.5	-0.5	-0.5
Interferometer Antenna Gain (dB)	+15	+15	+15.5	+17
Received Signal Power (dBW)	-154.5	-173.1	-170.3	-168.9
Receiver Noise Figure (dB)	+4.5	+4.5	+4.5	+4.5
Receiver Noise Density (dBW/Hz))	-199.5	-199.5	-199.5	-199.5
Signal-to-Noise Density Ratio (dB-Hz)	+45	-26.4	+29.2	+30.6
Time or Bandwidth Enhancement Factor (dB)	0 *	10 **	10 **	10 **
Final Signal-to-Noise Power Ratio (dB)	+45	+36.4	+39.2	+40.6
Resultant $\sigma_{\Delta\gamma}$ of Phase Measurement, (electrical deg, due to thermal noise)	0.33°	0.9°	0.6°	0.5

σ = standard deviation = $57.3\ (SNR)^{-1/2}$
SNR = power signal-to-noise ratio

* 1 s effective integration time.
** 10 s effective integration time.

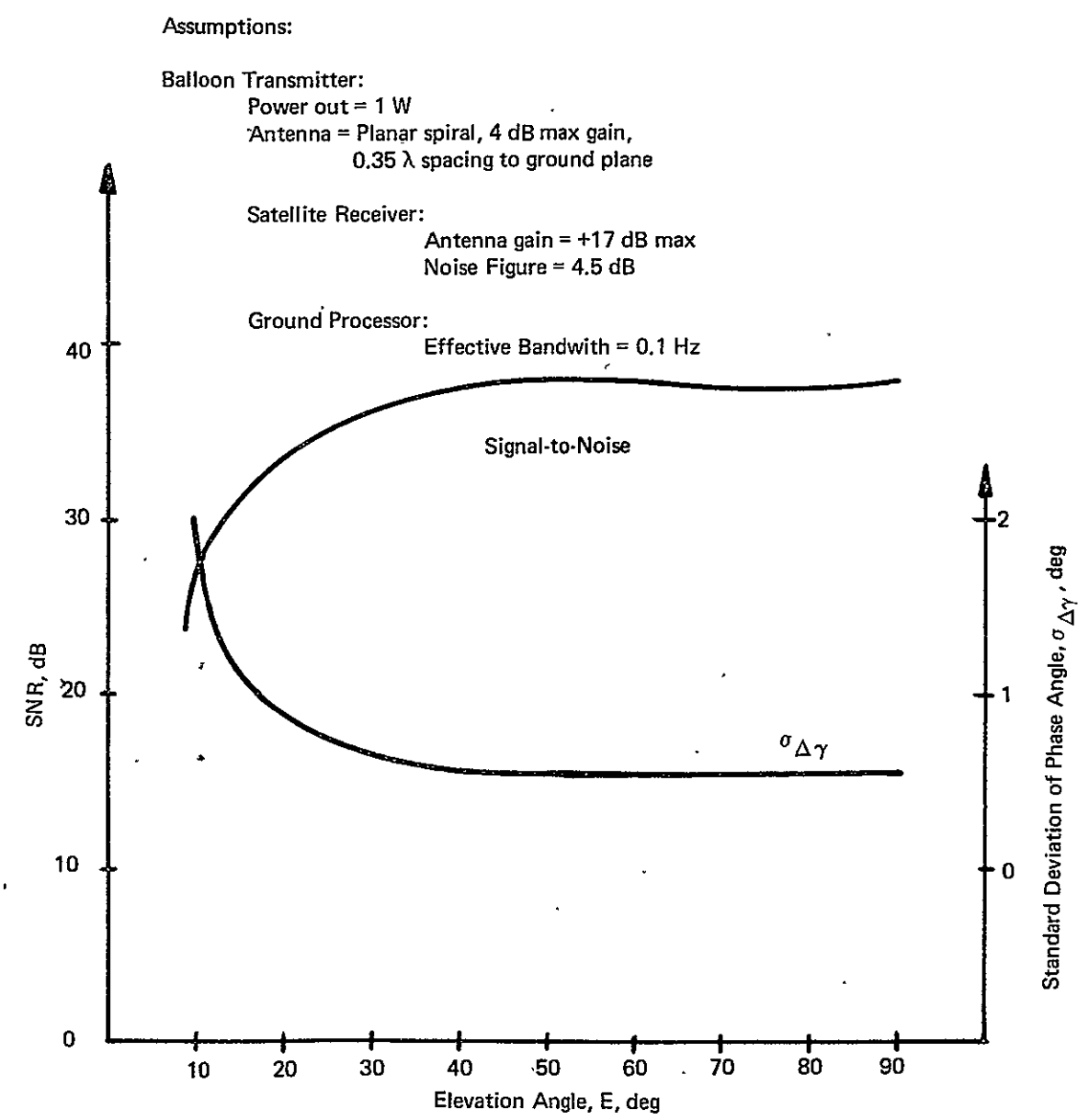

Figure II-1-14. SNR and Standard Deviation of Electrical Phase Measurement Versus Elevation Angle E

Using the above equations to evaluate the received signal from the balloon emitters, the link power budget and resultant standard deviation of the phase measurement is given for 3 values of elevation angle in Table II-1-1. Also given in this table are the link budgets for the ground calibration transmitters (CTs) with an ERP of 20 dBW. Then in Figure II-1-14 the SNR and phase measurement standard deviation $\sigma_{\Delta\gamma}$ for the balloon emitter are plotted over an elevation angle range from 10 deg to 90 deg. It is evident from Figure II-1-14 that the judicious choice of a balloon antenna pattern has provided a relatively flat curve of σ_{γ} for E greater than 20 deg.

II-1.6 ORBIT CHOICES

Two classes of orbits were investigated during the study: geostationary and zero eccentricity inclined. The later class of orbits was investigated because, at the outset of the study, it was believed that coverage in the extreme latitudes with the required accuracy could only be achieved with inclined orbits. This belief was verified during the study. The error analysis shows that the 1 km accuracy is achieved using geostationary satellites for latitudes less than 60 deg.

Another concern at the study outset was the extent of the detrimental effect of the satellite motion apparent with inclined orbits on the velocity estimate. The error study showed this effect to be small compared to the geostationary orbit case. Thus the choice of inclined or geostationary orbit becomes primarily dependent on the coverage requirements. Such factors as orbit perturbations and booster payload tradeoffs were not considered.

Polar coverage can only be achieved with inclined orbits. As seen from Figure II-1-15, three or four geostationary satellites will provide full world coverage for less than 60 deg. A tractable compromise between the number of satellites and the accuracy coverage requirement may be to incline one of the satellites about 30 deg. This inclination would provide between 5 and 7 hours of polar coverage each day at the expense of mid-latitude coverage for an equal period of time, e.g., when the satellite is at its maximum northern latitude, 30 deg south latitude is the limit of coverage.

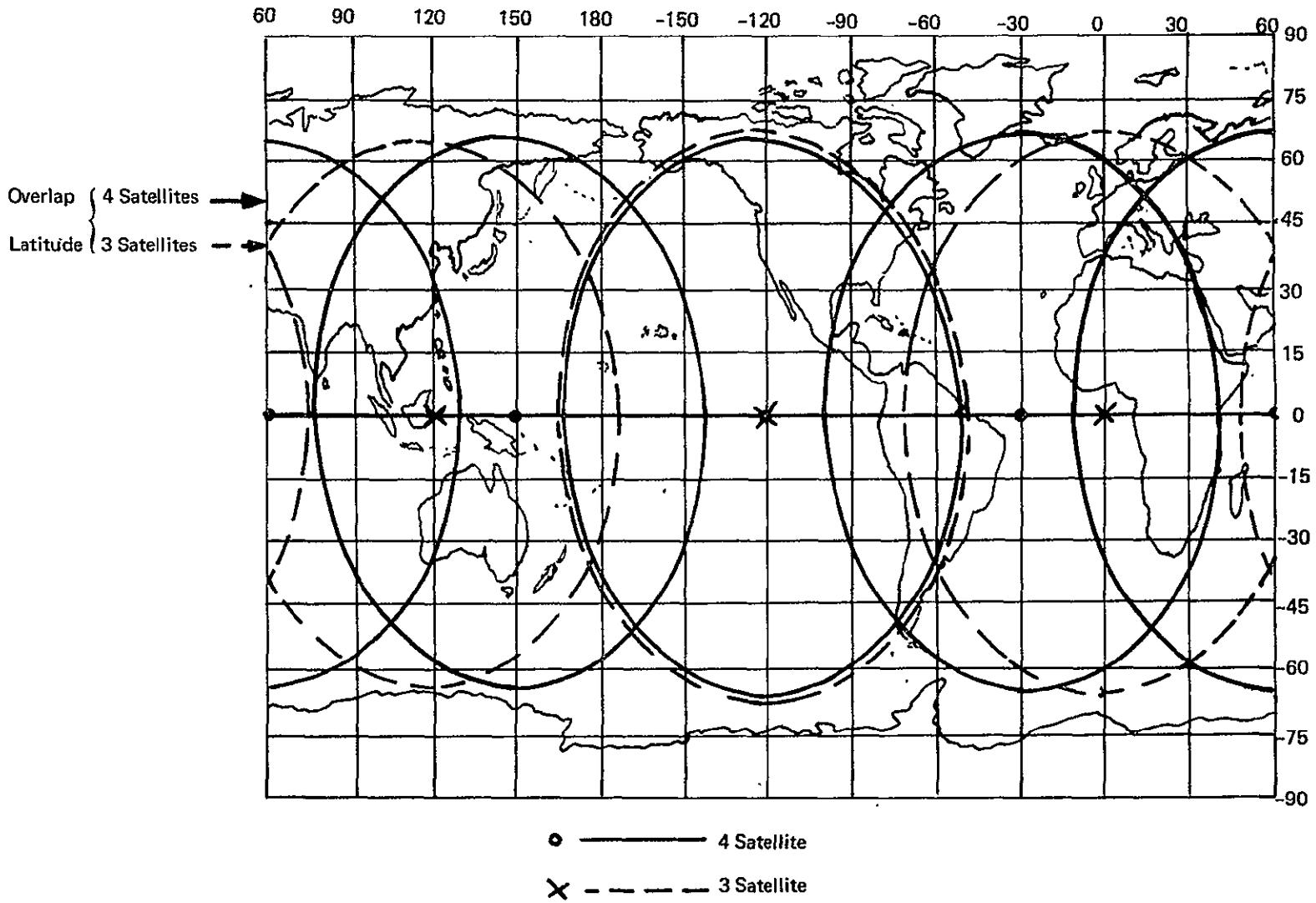

Figure II-1-15. Coverage with Position Location Error less than 2 km

II-1.7 MULTIPLE ACCESS

Two types of multiple access were considered for this application:

a. Time division using interrogation of the balloons

b. A combination frequency and time division system using randomly transmitting balloons.

The time division system requires a decoder and receiver in each balloon, whereas the randomly transmitting balloon system requires a timer. The time division system would simplify the ground station and possibly save a small amount of bandwidth. Since there may be 15,000 balloons in an operational system versus three ground stations, cost considerations dictate using the simplest balloon package. Therefore, a random system wherein each balloon is controlled by a preset timer was chosen. The timers are set at random starting times and are of low accuracy, so that the balloons essentially transmit randomly with respect to each other.

Frequency division comes about because of the low stability of the oscillator in in the balloon. With a frequency stability of one part in 10^5, there will be a frequency uncertainty of 16,000 Hz at 1600 MHz. Because of the low data rate (less than 10 bits/s) and biphase modulation, the bandwidth of the signals is low.

Since two position fixes are required to obtain the velocity, two important requirements of the meteorological models which are used to predict weather impact the transmission patterns, namely:

a. The time between position fixes used to determine velocity

b. The time between successive velocity determinations.

Indications are that a 2-hour velocity average is satisfactory, and a velocity determination every 6 hours is adequate. Two transmission patterns are suggested. One pattern is for the balloon to transmit pulses in a group, with the pulses separated by, say, 1 h, and the group of pulses repeated every 6 h. The second transmission pattern is to transmit a pulse every 2 h. Because it requires the simplest timer, the second method is considered in the analysis below.

To determine the performance of the randomly transmitting balloon system from a multiple-access point-of-view, we must determine the probability of interference between signals. Let

P_{tr} = probability that a given balloon transmits in Δt s in the frequency interval Δf within the field-of-view of the satellite considered.

Assuming randomness in transmission times, this probability can be expressed as

$$P_{tr} = \frac{1}{3}\left(\frac{\Delta t}{3600T}\right)\left(\frac{\Delta f}{W}\right) \qquad \text{(II-1-45)}$$

where

Δt = pulse length in s

T = time interval between transmissions in h

W = bandwidth over which balloon transmission frequencies are spread (assumed uniform distribution in this calculation)

Δf = frequency band within which another transmission would interfere with acquisition or phase measurement

Let

P_{no} = probability that no other balloon transmission interferes given that a particular balloon transmits.

This last expression is given by

$$P_{no} = \left[1 - P_{tr}\right]^{N_B - 1} \qquad \text{(II-1-46)}$$

where N_B = total number of balloons in the worldwide system. The balloons are assumed to be distributed randomly worldwide, so that each balloon has a probability of approximately one-third of being within the field-of-view of a particular geostationary satellite with earth coverage. On the average, there will be a $\frac{N_B}{3}$ balloons in view of a given satellite, and this is, of course, included in the formulation above.

For $P_{tr} \ll 1$ and $N_B \gg 1$, we have

$$P_{no} \cong \exp\left[-N_B P_{tr}\right] \tag{II-1-47}$$

so that

$$P_{no} = \exp\left[\frac{-N_B}{10800} \frac{\Delta t}{T} \frac{\Delta f}{W}\right]. \tag{II-1-48}$$

The exponent is given by $1.45 \times 10^{-6} N_B$ for the following values of parameters:

$\Delta t = 10$ s
$T = 2$ h
$\Delta f = 100$ Hz
$W = 24,000$ Hz.

Thus, for 15,000 balloons worldwide, the probability of no interference for a given transmission is 0.97. However, the important consideration is the probability of obtaining a useful pair measurement so that a velocity determination can be made.

The probability of no interference for two successive transmissions from a balloon is $\left(P_{no}\right)^2$ or 0.94. The probability of no interference for at least two successive transmissions out of three transmissions (which would be 6 h) is $P_{no}^2 \left[3-2 P_{no}\right]$ which, for this condition, is greater than 0.99.

The next factor to be determined is the number of sets of phase measuring circuits required for the balloon signals. The average number of transmissions initiated per second by the balloons is $\frac{N_B}{3600T}$ or 2.1/s. For each station, it would be 0.7 transmissions/s average. If there are M sets of phase measuring circuits, the probability that a given transmission is not lost because of a lack of phase measuring circuits is equal to the probability that, in the proceeding

10 s, fewer than M balloons initiated transmission within the satellite's field-of-view. This is given by

$$\sum_{k=0}^{M-1} \binom{N_B-1}{k} p^k \quad (1-p)^{N_B-1-k} \qquad \text{(II-1-49)}$$

where

$$p = \frac{\Delta t}{10800T} = 4.63 \times 10^{-4} .$$

This probability, because of small p and large N_B, can be approximated by

$$\sum_{k=0}^{M-1} \frac{e^{-N_B p}}{k!} (N_B p) \quad . \qquad \text{(II-1-50)}$$

For N_B = 15,000 balloons, this probability will be greater than 0.99 if M, the number of sets of phase measuring circuits per station, is 13 or more.

II-1.8 BOOM MOTION EFFECTS

Assume that the motion of the apparent baseline, i.e., the line connecting the two antennas (as shown in Figure II-1-16), has a motion consisting of a constant angular velocity plus a sinusoidal component. The space angle between the normal to the baseline and the local vertical can be approximated by

$$\alpha(t) = \alpha_c + \omega_1 t + A_m \sin \omega_2 t. \qquad \text{(II-1-51)}$$

Consider the point in space where antenna 1 is located at the time t = 0. Let the signal at that point in space be

$$S_1(t) = \cos\left(\omega t + \theta_o\right). \qquad \text{(II-1-52)}$$

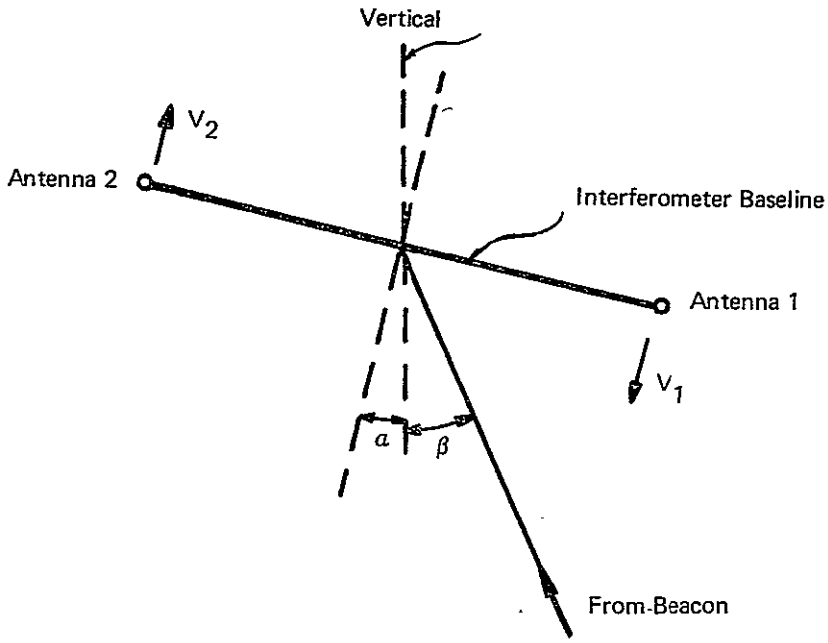

Figure II-1-16. Effect of Boom Motion on Electrical Phase

Because of the boom motion, antenna 1 has a velocity given by

$$V_1(t)\ \frac{L}{2}\ \frac{d\alpha}{dt} = \frac{L}{2}\ \left[\omega_1 + A_m\ \omega_2\ \cos\ \omega_2 t\right]\ . \qquad \text{(II-1-53)}$$

The portion of this velocity normal to the wavefront is

$$V_1\ \cos\ (\alpha + \beta) \cong V_1$$

where β is the space angle between the beacon line-of-sight and the local vertical. The approximation holds since the angle will not exceed 10°.

The single voltage induced in antenna 1, including the effect of its motion, is

$$V_1 = \cos\left[\omega\left(1 - \frac{L\omega_1}{2c}\right)t + \theta_o - \frac{\omega L}{2c}\ A_m \sin\ \omega_2 t\right]. \qquad \text{(II-1-54)}$$

The signal voltage induced in antenna 2 is given by

$$V_2 = \cos\left[\omega\left(1+\frac{L\omega_1}{2c}\right)t+\theta_o+\frac{\omega L}{2c}\ A_m \sin\omega_2 t+\frac{2\pi L}{\lambda}\sin(\alpha+\beta)\right]. \quad \text{(II-1-55)}$$

One of these two signals is translated in frequency by the reference oscillator aboard the spacecraft so that it becomes

$$V_2' = \cos\left\{\left[\omega\left(1+\frac{L\omega_1}{2c}\right)+\omega_r\right]t+\theta_o+\theta_r+\frac{\omega L}{2c}\ A_m \sin\omega_2 t + \frac{2\pi L}{\lambda}\sin(\alpha+\beta)\right\} \quad \text{(II-1-56)}$$

where the reference signal is given by

$$V_r = \cos\left[\omega_r t+\theta_r\right]. \quad \text{(II-1-57)}$$

On the ground, these two signals are mixed so that we recover the signal

$$V'' = \cos\left[\left(\omega\frac{L\omega_1}{c}+\omega_r\right)t+\theta_r+\frac{\omega L}{c}\ A_m \sin\omega_2 t+\frac{2\pi L}{\lambda}\sin(\alpha+\beta)\right]. \quad \text{(II-1-58)}$$

The phase difference of this signal and the reference signal (measured on the ground) is given by

$$\gamma(t) = \left(\frac{2\pi L}{\lambda}\ \omega_1\right)t + \frac{2\pi L}{\lambda}A_m \sin\omega_2 t+\frac{2\pi L}{\lambda}\sin(\alpha+\beta). \quad \text{(II-1-59)}$$

The time dependence of this phase is due to the boom motion. If the boom were stationary, ω_1 and A_m would be zero so that we would have

$$\gamma = \frac{2\pi L}{\lambda}\sin(\alpha+\beta). \quad \text{(II-1-60)}$$

The actual phase measurement is an average phase, γ_m, obtained over the time interval τ or

$$\gamma_m = \frac{1}{\tau} \int_t^{t+\tau} \gamma(t)\, dt .$$

Use of the model yields

$$\gamma_m = \frac{2\pi L}{\lambda}\, \omega_1 \left(t + \frac{\tau}{2}\right) + \frac{4\pi L A_m}{\tau \lambda \omega_2} \sin\left(\omega_2 \frac{\tau}{2}\right) \sin \omega_2 \left(t + \frac{\tau}{2}\right)$$

$$+ \frac{2\pi L}{\lambda} \sin(\alpha + \varphi) . \qquad \text{(II-1-61)}$$

The three characteristics of the time dependence of the phase and the measurement which are of interest are:

a. Maximum rate of change of phase

b. Total phase change over the measuring interval

c. Average phase over the measuring interval compared to phase at (say) center of measuring interval.

The maximum rate of change of phase is given by

$$\dot{\gamma}_{max} = \frac{2\pi L}{\lambda} \left(\omega_1 + A_m \omega_2\right) . \qquad \text{(II-1-62)}$$

The values for the constants for the flexible boom considered herein are (see Section II-7):

$$\omega_1 = 1.05 \times 10^{-5} \text{ rad/s}$$
$$\omega_2 = 0.095 \text{ rad/s}$$
$$A_m = 2.6 \times 10^{-5} \text{ rad} .$$

For this example, with a 400-wavelength system, the maximum rate is 1.9 deg/s. This will determine the maximum measuring time interval allowed to accurately follow the boom motion. For a time interval of 0.1 s, the maximum phase change

is 0.2 deg or $\pm$ 0.1 deg if considering the phase at the center of the interval. Most of this change is due to the constant angular rate ω_1, rather than the oscillation.

The total phase change over the measuring interval τ is

$$\gamma(t+\tau) - \gamma(t) = \frac{2\pi L}{\lambda}\,\omega_1\,\tau + \frac{2\pi LA_m}{\lambda}\left[\sin\omega_2(t+\tau) - \sin(\omega_2 t)\right]$$

$$= \frac{2\pi L}{\lambda}\left[\omega_1\,\tau + 2A_m \cos\omega_2\left(t+\frac{\tau}{2}\right)\sin\frac{\omega_2\tau}{2}\right]. \quad \text{(II-1-63)}$$

The maximum value of this phase change for the same values of the parameters and for a measuring time interval τ of 1 and 10 s is 1.87 deg and 18.4 deg, respectively.

The phase in the middle of the measuring interval T is given by

$$\gamma\left(t+\frac{\tau}{2}\right) = \frac{2\pi L}{\lambda}\left[\omega_1\left(t+\frac{\tau}{2}\right) + A_m \sin\omega_2\left(t+\frac{\tau}{2}\right) + \sin(\alpha+\beta)\right]. \quad \text{(II-1-64)}$$

Comparing the measured value Φ_m with this yields

$$\gamma_m - \gamma\left(t+\frac{\tau}{2}\right) = \frac{2\pi L}{\lambda}\,A_m\left[\frac{\sin\frac{\omega_2\tau}{2}}{\frac{\omega_2\tau}{2}} - 1\right]\sin\left(\omega_2 t + \frac{\tau}{2}\right). \quad \text{(II-1-65)}$$

Note that the constant angular rate ω_1 does not appear in this expression because we are making the comparison with the phase value at the middle of the measuring interval.

The maximum value of the above expression for the same value of parameters used before is 0.001 deg for τ = 1 s and 0.066 deg for τ = 10 s.

From the above, it is obvious that calibration must be performed continuously. When an average phase measurement is used, the compensation term can be calculated as an average over the same measurement interval, or the term can be calculated as the value at the center of the interval.

II-1.9 CHOICE OF OPERATING FREQUENCY

The original frequency considered for the transmission link from the balloon to the interferometer was 400 MHz. However, it soon became apparent that there are important advantages to using a higher frequency, and 1600 MHz was selected. All considerations were based on using a fixed physical baseline length so that, at a higher frequency, the length increases in terms of wavelengths.

The advantages are:

a. Error in position location due to thermal noise is independent of frequency for same ERP

b. Electrical phase accuracy requirement is less for given position location error

c. Multipath errors are smaller

d. Refraction errors are smaller

e. Antennas are smaller and lighter.

The disadvantages of using a higher frequency are:

a. More dc power is required in balloon for same ERP

b. There are more ambiguities to resolve

c. SNR is smaller and data transmission capability decreases.

d. Higher frequency uncertainty increases the acquisition problem.

The first advantage is the reason that an increase in frequency can be realistically considered. The space loss is proportional to the square of the frequency. However, the accuracy of the electrical angle measurement is proportional to the square root of the signal-to-noise power ratio or inversely proportional to the frequency (for given ERP, etc.). Since the required electrical phase measurement accuracy for a given baseline length is inversely proportional to frequency, the location accuracy of the system due to thermal noise is independent of the frequency.

The higher operating frequency would then mean that relatively fixed electrical phase errors become less important. Instrumentation problems would be less severe since larger electrical phase errors are permissible.

At higher frequencies, errors in position location resulting from multipath will be smaller because:

a. Reflection coefficients are lower at higher frequencies

b. Multipath signal tends to be more diffuse

c. Spectral broadening of reflected signal due to motion of balloon is greater.

These effects are discussed in detail in the multipath section of the report.

Another advantage of higher frequencies is that refraction errors are smaller. In addition, the antennas in both the balloon and satellite are smaller and lighter.

The major disadvantage of a higher frequency is that more dc power will be required in the balloons. This requires more solar cells, of course, and a larger battery, if one is used. The batteries are the most difficult items to make frangible and are the most susceptible to the extreme temperature variations. In addition, the higher frequency components would be somewhat more expensive.

Since the signal power-to-noise density ratio is less at the higher frequencies, the possible data transmission rate decreases. However, because of the low data rates required, the SNR is sufficient at 1600 MHz.

The ambiguity resolution becomes more difficult, but at most it would require an additional antenna and associated equipment in the satellite, plus some additional processing in the ground stations.

The higher frequency, for a given oscillator stability, increases the frequency uncertainty in transmitted signals. This eases the multiple-access problem, but increases the acquisition problem.

An L-band frequency would also make the equipment compatible with the equipment planned for other satellite applications for location and communication with aircraft.

The overriding considerations in choosing 1600 MHz instead of 400 MHz for the operating frequency were the advantages from a multipath standpoint and the fact that the required phase accuracy is less for a given length baseline.

Section II-2

ERROR ANALYSIS

This section is divided into four parts to facilitate the derivation of the combined error equation. Figure II-2-1 shows the geometric relationships of the problem. First, the errors in the position location are given as functions of the line-of-sight vector $\overrightarrow{LOS}_B$, the satellite radius vector the $\vec{\rho}_s$, and the balloon position $|\vec{\rho}_e + h|$. Second, the errors in $\overrightarrow{LOS}_B$ are given in terms of the baselines $\vec{L}_1$, $\vec{L}_2$, the phase biases, and the beacon phase noises. But since $\vec{L}_1$, $\vec{L}_2$, and the phase biases are constantly being estimated (calibrated) from the CT signals, the third step consists of expressing the errors in these terms as functions of CT phase noise, phase biases, CT survey errors, and $\vec{\rho}_s$. The final step combines all expressions to yield one composite error equation. The resulting matrix equation is much too complex to investigate analytically, hence a computer program was developed. This program, discussed in subsection II-2.6, was used to derive the numerical results shown in Part I of this report.

II-2.1 POSITION LOCATION ERROR

The position location solution, given $\overrightarrow{LOS}_B$, $\vec{\rho}_s$, and $|\vec{\rho}_e + h|$, is obtained by solving the following four vector equations in sequence:

$$\cos\beta = \overrightarrow{LOS}_B \cdot \frac{\vec{\rho}_s}{|\vec{\rho}_s|} \qquad \text{(II-2-1)}$$

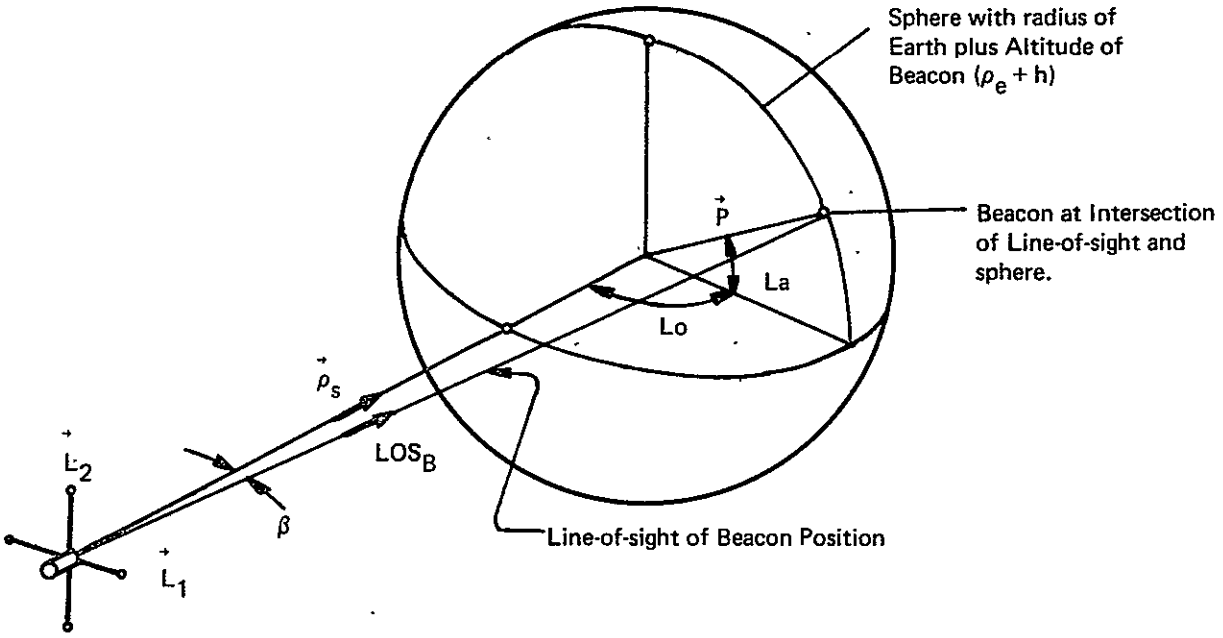

Figure II-2-1. Beacon-Satellite Geometry

$$r = \rho_s \cos\beta - \left[(\rho_e + h)^2 - \rho_s^2 \sin^2\beta\right]^{1/2} \qquad \text{(II-2-2)}$$

$$\vec{r} = r\,\overrightarrow{LOS}_B \qquad \text{(II-2-3)}$$

$$\vec{P} = \vec{\rho_s} - \vec{r}\ . \qquad \text{(II-2-4)}$$

The analysis to follow is simplified by using matrix notation in lieu of vector notation. Equations II-2-1 through II-2-4 become

$$\underset{(3x1)}{[P_B]} = \underset{(3x1)}{[\rho_s]} - \underset{(3x1)}{[r]} \qquad \text{(II-2-5)}$$

$$\underset{(3x1)}{[r]} = \underset{(3x1)}{[LOS_B]}\ \underset{(1x1)}{r} \qquad \text{(II-2-6)}$$

$$\underset{(1x1)}{r} = \underset{(1x1)}{\rho_s}\ \underset{(1x1)}{\cos\beta} - \left[(\rho_e + h)^2 - \rho_s^2 \underset{(1x1)}{\sin^2\beta}\right]^{1/2} \qquad \text{(II-2-7)}$$

$$\underset{(1x1)}{\cos\beta} = \frac{\underset{(1x3)}{[\rho_s]^T}}{\rho_s}\ \underset{(3x1)}{[LOS_B]} \qquad \text{(II-2-8)}$$

where

$$[P_B] = \begin{bmatrix} x_B \\ y_B \\ z_B \end{bmatrix} = \text{location of beacon in earth-centered, fixed Cartesian coordinates}$$

$$[\rho_s] = \begin{bmatrix} x_s \\ y_s \\ z_s \end{bmatrix} = \text{location of satellite at time of beacon transmissions}$$

$$[r] = \begin{bmatrix} x_R \\ y_R \\ z_R \end{bmatrix} = \begin{bmatrix} d_{xB} \\ d_{yB} \\ d_{zB} \end{bmatrix} r; \quad \overrightarrow{LOS}_B \equiv [LOS_B] = \begin{bmatrix} d_{Bx} \\ d_{By} \\ d_{Bz} \end{bmatrix}$$

$$\rho_s = \left(x_s^{\,2} + y_s^{\,2} + z_s^{\,2}\right)^{1/2} \quad \text{(satellite geocentric radius).}$$

The error equations for equations II-2-5, II-2-6, and II-2-7 are

$$\underset{(3x1)}{[\Delta P]} = \underset{(3x1)}{[\Delta \rho_s]} - \underset{(3x1)}{[\Delta r]} \tag{II-2-9}$$

$$\underset{(3x1)}{[\Delta r]} = \underset{(3x1)}{[LOS_B]}\,\underset{(1x1)}{\Delta r} + \Delta\underset{(3x1)}{[LOS_B]}\,\underset{(1x1)}{r} \tag{II-2-10}$$

$$\Delta r = \frac{\partial r}{\partial \rho_s}\,\Delta\rho_s + \frac{\partial r}{\partial h}\,\Delta h + \frac{\partial r}{\partial \beta}\,\Delta\beta \quad \text{(all scalars).} \tag{II-2-11a}$$

But since

$$\Delta\rho_s = \left[\frac{x_s}{\rho_s} \;\vdots\; \frac{y_s}{\rho_s} \;\vdots\; \frac{z_s}{\rho_s}\right] \begin{bmatrix}\Delta x_s \\ \Delta y_s \\ \Delta z_s\end{bmatrix} \equiv [A] \quad \Delta\rho_s\Big] \tag{II-2-11b}$$

Equation II-2-11a can be rewritten as

$$\Delta r = \frac{\partial r}{\partial \rho_s}\,[A]\left[\Delta\rho_s\right] + \frac{\partial r}{\partial h}\,\Delta h + \frac{\partial r}{\partial \beta}\,\Delta\beta. \tag{II-2-11c}$$

The expression for $\Delta\beta$ is obtained from Equation II-2-8, which is expanded into scalar form as follows:

$$\cos\beta = \frac{x_s}{\rho_s}\,d_{Bx} + \frac{y_s}{\rho_s}\,d_{By} + \frac{z_s}{\rho_s}\,d_{Bz}\,. \tag{II-2-12}$$

Then

$$\begin{aligned}-\sin\beta\,\Delta\beta = {} & \frac{x_s}{\rho_s}\,\Delta d_{Bx} + \frac{y_s}{\rho_s}\,\Delta d_{By} + \frac{z_s}{\rho_s}\,\Delta d_{Bz} + \\ & + \frac{\Delta x_s}{\rho_s}\,d_{Bx} + \frac{\Delta y_s}{\rho_s}\,d_{By} + \frac{\Delta z_s}{\rho_s}\,d_{Bz} \\ & - \left(\frac{x_s d_{Bx} + y_s d_{By} + z_s d_{Bz}}{\rho_s^2}\right)\left[\frac{x\,\Delta x_s}{\rho_s} + \frac{y\,\Delta y_s}{\rho_s} + \frac{z\Delta z_s}{\rho_s}\right]\end{aligned} \tag{II-2-13}$$

which, after rearrangement of terms, becomes

$$\Delta\beta = -\frac{1}{\sin\beta}\left\{ \underset{(1x3)}{[A]} \underset{(3x1)}{[LOS_B]} + \frac{1}{|\rho_s|}\underset{(1x3)}{[LOS_B]}\underset{T}{[}\underset{(3x1)}{\Delta\rho_s]} - \frac{\cos\beta}{|\rho_s|^2}\underset{(1x3)}{[A]}\underset{(3x1)}{[\Delta\rho_s]}\right\}$$

$$= -\frac{1}{\sin\beta}[A][\Delta LOS_B] - \left\{\frac{1}{|\rho_s|\sin\beta}[LOS_B]^T - \frac{\cos\beta}{|\rho_s|^2}[A]\right\}[\Delta\rho_s] \qquad \text{(II-2-14)}$$

Substituting equations II-2-14, II-2-11b, and II-2-10 into II-2-9 yields

$$\underset{(3x1)}{[\Delta P]} = \left\{ \underset{(3x3)}{[I]} + \underset{(3x1)}{[LOS_B]}\frac{\partial r}{\partial\rho_s}\underset{(1x1)}{[A]} - \underset{(3x1)}{[LOS_B]}\frac{\partial r}{\partial\beta}\underset{(1x3)}{\frac{1}{\rho_s\sin\beta}[LOS_B]^T} + \underset{(3x1)}{[LOS_B]}\right.$$

$$\left.\underset{(1x1)}{\frac{\cot\beta}{\rho_s^2}}\underset{(1x3)}{[A]}\right\}\underset{(3x1)}{[\Delta\rho_s]}$$

$$+\left\{\underset{(3x1)}{[LOS_B]}\frac{\partial r}{\partial h}\right\}\underset{(1x1)}{\Delta h} + \left\{-\underset{(3x1)}{[LOS_B]}\frac{\partial r}{\partial\beta}\underset{(1x1)}{\frac{1}{\sin\beta}[A]} + \underset{(1x3)}{[I]}\underset{(3x3)}{r}\right\}\underset{(3x1)}{[\Delta LOS_B]} \qquad \text{(II-2-15)}$$

where [I] is the identity matrix.

For simplicity, let

$$\underset{(3x3)}{\frac{\partial P}{\partial\rho_s}} = \left\{\underset{(3x3)}{[I]} + \underset{(3x1)}{[LOS_B]}\frac{\partial r}{\partial\rho_s}\underset{(1x1)}{[A]} - \underset{(3x1)}{[LOS_B]}\frac{\partial r}{\partial\beta}\cdot\underset{(1x3)}{\frac{1}{\rho_s\sin\beta}[LOS_B]^T} + \underset{(3x1)}{[LOS_B]}\right.$$

$$\left.\underset{(1x1)}{\frac{\cos\beta}{\rho_s^2}}\underset{(1x3)}{[A]}\right\} \qquad \text{(II-2-16)}$$

This nomenclature suggest that the $\left[\frac{\partial P}{\partial \rho_s}\right]$ is the variation in the position location due to a satellite ephemeris error. The several terms arise from the fact that $\vec{\rho}_s$ appears in equations I-2-1 to I-2-3. Furthermore, it can be seen that

$$\underset{(3x1)}{\frac{\partial P}{\partial h}} = \underset{(3x1)}{\left[LOS_B\right]} \underset{(1x1)}{\frac{\partial r}{\partial h}} \qquad \text{(II-2-17)}$$

which is the sensitivity of the position location to the altitude error.
Also,

$$\underset{(3x1)}{\frac{\partial P}{\partial LOS_B}} = \left\{ \underset{(3x3)}{[I]}\, r - \underset{(3x1)}{\left[LOS_B\right]} \underset{(1x1)}{\frac{\partial r}{\partial \beta}} \underset{(1x1)}{\frac{1}{\sin \beta}} \underset{(1x3)}{[A]} \right\} \qquad \text{(II-2-18)}$$

represents the sensitivity of the position location to an error in computing the LOS to the beacon. The two terms are due to the presence of LOS_B in equations II-2-1 and II-2-3.

Rewriting Equation II-2-15 in the abbreviated notation yields

$$[\Delta P] = \frac{\partial P}{\partial \rho_s} [\Delta \rho_s] + \frac{\partial P}{\partial h} [\Delta h] + \frac{\partial P}{\partial LOS_B} \left[\Delta LOS_B\right] . \qquad \text{(II-2-19)}$$

II-2.2 EXPANSION INTO PHASE ERRORS

The vector LOS_B is derived from the beacon phase measurements by solving equations II-2-20, II-2-21, and II-2-22 simultaneously.

$$\begin{aligned} \vec{LOS}_B \cdot \vec{L}_1 &= \frac{\lambda}{2\pi} \left(\gamma_{B1} - \hat{\gamma}_{BB1}\right) \\ \vec{LOS}_B \cdot \vec{L}_2 &= \frac{\lambda}{2\pi} \left(\gamma_{B2} - \hat{\gamma}_{BB2}\right) \end{aligned} \qquad \text{(II-2-20)}$$

where $|\vec{LOS}_B| = 1.$
In the equation above, the symbol "$\wedge$" on γ denotes "estimate of."

In matrix notation these equations become

$$\frac{1}{F}\begin{bmatrix} a_1 & b_1 & c_1 \\ a_2 & b_2 & b_2 \end{bmatrix}\begin{bmatrix} d_{Bx} \\ d_{Bx} \end{bmatrix} = \begin{bmatrix} \gamma_{B1} - \hat{\gamma}_{BB1} \\ \gamma_{B2} - \hat{\gamma}_{BB2} \end{bmatrix} \qquad \text{(II-2-21)}$$

and

$$d_{Bz} = \sqrt{1 - d_{Bx}^2 - d_{By}^2}$$

where F is a scalar and equal to $\frac{\lambda}{2\pi}$. Equation II-2-21 may be solved for d_{Bx} and d_{By} by classical iteration; the iteration equation is given by

$$\begin{bmatrix} \delta d_{Bx} \\ \delta d_{By} \end{bmatrix} = F\begin{bmatrix} \left(a_1 - c_1\frac{d_{Bx}}{d_{Bz}}\right) & b_1 - c_1\frac{d_{By}}{d_{Bz}} \\ \left(a_2 - c_2\frac{d_{Bx}}{d_{Bx}}\right) & b_2 - c_2\frac{d_{By}}{d_{Bx}} \end{bmatrix}^{-1}\begin{bmatrix} (\gamma_{B1} - \gamma_{BB1}) - \gamma^P_{B1} \\ (\gamma_{B2} - \gamma_{BB2}) - \gamma^P_{B2} \end{bmatrix} \qquad \text{(II-2-22)}$$

where

$$\gamma^P_{B1} = \hat{d}_{Bx}a_1 + \hat{d}_{By}b_1 + c\sqrt{1 - \hat{d}_{Bx}^2 - \hat{d}_{By}^2}$$

$$\gamma^P_{B2} = \hat{d}_{Bx}a_2 + \hat{d}_{By}b_2 + c\sqrt{1 - \hat{d}_{By}^2 - \hat{d}_{By}^2}\,.$$

Equation II-2-22 is iterated until the left hand side is negligibly small. At that point, the residual error in $\hat{d}_{Bx}$ and $\hat{d}_{By}$ is due to phase noise in γ_{B1} and γ_{B2} and to errors in the estimated phase biases $\hat{\gamma}_{BB1}$ and $\hat{\gamma}_{BB2}$ and to errors in a_1, b_1, c_1, a_2, b_2, and c_2.

It may be shown that the residual error is given by (dropping the "hat" indicating the estimated values for simplicity of notation)

$$\begin{bmatrix} \Delta d_{Bx} \\ \Delta d_{By} \end{bmatrix} = F \; [W]^{-1} \begin{bmatrix} \Delta \gamma_{B1} \\ \Delta \gamma_{B2} \end{bmatrix} - F \left[\begin{array}{c|c} a_1 & b_1 \\ \hline a_2 & b_2 \end{array}\right]^{-1} \begin{bmatrix} \Delta \nu_{BB1} \\ \Delta \nu_{BB2} \end{bmatrix}$$

$$- F \; [W]^{-1} \left[\begin{array}{c|c|c} d_{Bx} & d_{By} & d_{Bz} \\ \hline 0 & 0 & 0 \end{array}\right] \begin{bmatrix} \Delta a_1 \\ \Delta b_1 \\ \Delta c_1 \end{bmatrix}$$

$$-F \; [W]^{-1} \left[\begin{array}{c|c|c} 0 & 0 & 0 \\ \hline d_{Bx} & d_{By} & d_{Bz} \end{array}\right] \begin{bmatrix} \Delta a_2 \\ \Delta b_2 \\ \Delta c_2 \end{bmatrix} \qquad \text{(II-2-23)}$$

where

$$W = \begin{bmatrix} \left(a_1 - c_1 \frac{d_{Bx}}{d_{Bz}}\right)\left(b_1 - c_1 \frac{d_{By}}{d_{Bz}}\right) \\ \left(a_2 - c_2 \frac{d_{Bx}}{d_{Bz}}\right)\left(b_2 - c_2 \frac{d_{By}}{d_{Bz}}\right) \end{bmatrix}. \qquad \text{(II-2-24a)}$$

We now let

$$\left[\begin{array}{c|c|c} d_{Bx} & d_{By} & d_{Bz} \\ \hline 0 & 0 & 0 \end{array}\right]_{(2x3)} = [E_{L1}]$$

and

$$\left[\begin{array}{c|c|c} 0 & 0 & 0 \\ \hline d_{Bx} & d_{By} & d_{Bz} \end{array}\right]_{(2x3)} = [E_{L2}] \qquad \text{(II-2-24b)}$$

such that Equation (II-2-23) may be written more concisely as

$$\underset{(2x1)}{\begin{bmatrix} \Delta d_{Bx} \\ \Delta d_{By} \end{bmatrix}} = \underset{(2x2)}{[W]^{-1}} \underset{(2x1)}{[\Delta \gamma_B]} - \underset{(2x2)}{[W]^{-1}} \underset{(2x1)}{[\Delta \gamma_{BB}]} - \underset{(2x2)}{[W]^{-1}} \underset{(2x3)}{[E_{L1}]} \underset{(3x1)}{[\Delta L_1]} - \underset{(2x2)}{[W]^{-1}} \underset{(2x3)}{[E_{L2}]} \underset{(3x1)}{[\Delta L_2]} . \qquad \text{(II-2-25)}$$

By virtue of the constraint equation, i.e., $\overrightarrow{LOS}_B = 1$, we have

$$\underset{(3x1)}{\left[\Delta LOS_B\right]} = \underset{(3x1)}{\begin{bmatrix} \Delta d_{Bx} \\ \Delta d_{By} \\ \Delta d_{Bz} \end{bmatrix}} = \underset{(3x2)}{\begin{bmatrix} 1 & 0 \\ 0 & 1 \\ -\frac{d_{Bx}}{d_{Bz}} & -\frac{d_{By}}{d_{Bz}} \end{bmatrix}} \underset{(2x1)}{\begin{bmatrix} \Delta d_{Bx} \\ \Delta d_{By} \end{bmatrix}} \equiv \underset{(3x2)}{D_B} \underset{(2x1)}{\begin{bmatrix} \Delta d_{Bx} \\ \Delta d_{By} \end{bmatrix}} . \quad \text{(II-2-26)}$$

Substituting Equation (II-2-25) into Equation II-2-26 yields the LOS_B error equation in terms of beacon phase errors, phase biases, and baseline errors follows:

$$\begin{aligned} \left[\Delta LOS_B\right] &= \left[D_B\right]\left[W\right]^{-1}\left[\Delta\gamma_B\right] \text{ (contribution from beacon phase noise)} \\ &- \left[D_B\right]\left[W\right]^{-1}\left[\Delta\gamma_{BB}\right] \text{ (contribution from phase biases)} \\ &+ \left[D_B\right]\left[W\right]^{-1}\left[E_{L1}\right]\left[\Delta L_1\right] \text{ (contribution from baseline 1 errors)} \\ &- \left[D_B\right]\left[W\right]^{-1}\left[E_{L2}\right]\left[\Delta L_2\right] \text{ (contribution from baseline 2 errors).} \end{aligned} \quad \text{(II-2-27)}$$

To simplify the notation and still retain a functional meaning, let

$$\frac{\partial LOS_B}{\partial \Gamma_B} \equiv \left[D_B\right]\left[W\right]^{-1}$$

$$\frac{\partial LOS_B}{\partial \gamma_{BB}} \equiv \left[D_B\right]\left[W\right]^{-1}$$

$$\frac{\partial LOS_B}{\partial L_1} \equiv \left[D_B\right]\left[W\right]^{-1}\left[E_{L1}\right]$$

$$\frac{\partial LOS_B}{\partial L_2} \equiv \left[D_B\right]\left[W\right]^{-1}\left[E_{L2}\right] .$$

6

Then, substituting Equation II-2-26 into Equation II-2-19 yields

$$\Delta P = \frac{\partial P}{\partial \rho_s}\Delta\rho_s + \frac{\partial P}{\partial h}\Delta h + \frac{\partial P}{\partial LOS_B}\frac{\partial LOS_B}{\partial \Gamma_B}\Delta\Gamma_B - \frac{\partial P}{\partial LOS_B}\frac{\partial LOS_B}{\partial \gamma_{BB}}\Delta\gamma_{BB} - \frac{\partial P}{\partial LOS_B}\frac{\partial LOS_B}{\partial L_1}\Delta L_1 - \frac{\partial P}{\partial LOS_B}\frac{\partial LOS_B}{\partial L_2}\Delta L_2 \quad . \tag{II-2-28}$$

At this point in the derivation there are several possible approaches, each of which corresponds to a particular way of determining how L_1, L_2, and the phase biases are estimated. For example, $\overrightarrow{L_1}$ and $\overrightarrow{L_2}$ could be computed by monitoring the spacecraft attitude (assuming infinitely rigid booms), without assuming expansions or contractions of the booms and orthogonality of the baselines. This approach leads to severe problems in system specifications; e.g., the altitude control specifications are inordinate.

As pointed out in Section I, a better approach is to use additional ground illuminators which serve to calibrate $\overrightarrow{L_1}$, $\overrightarrow{L_2}$, and γ_{BB}. The error analysis will consider only this approach.

II-2.3 EXPANSION IN TERMS OF FOUR CT PHASE NOISES, CT SURVEY ERRORS, AND SATELLITE EPHEMERIS ERROR

The equations which relate the CT phases to $\overrightarrow{L_1}$, $\overrightarrow{L_2}$, and γ_{BB} are:

$$L_1^* = D^{-1}\Gamma_1 F \tag{II-2-29a}$$

and

$$L_2^* = D^{-1}\Gamma_2 F \tag{II-2-29b}$$

where

$$D = \begin{bmatrix} d_{1x} & d_{1y} & d_{1z} & 1 \\ d_{2x} & d_{2y} & d_{2z} & 1 \\ d_{3x} & d_{3y} & d_{3z} & 1 \\ d_{4x} & d_{4y} & d_{4z} & 1 \end{bmatrix} \tag{II-2-30}$$

The error equation for II-2-29a is derived as follows: Rewrite II-2-29a as

$$DL_1^* = \Gamma_1 F. \tag{II-2-31}$$

Expanding II-2-31 in a first-order Taylor series yields

$$\underset{(4x4)}{D}\ \underset{(4x1)}{\Delta L_1^*} + \underset{(4x12)}{\begin{bmatrix} L_1^T & & & \\ & L_1^T & 0 & \\ & & L_1^T & \\ 0 & & & L_1^T \end{bmatrix}} \underset{(12x1)}{\begin{bmatrix} \Delta D_1 \\ \Delta D_2 \\ \Delta D_3 \\ \Delta D_4 \end{bmatrix}} = \underset{(4x1)}{\Gamma_1} \underset{(1x1)}{F} \tag{II-2-32}$$

where

$$L = \begin{bmatrix} a_1 \\ b_1 \\ c_1 \end{bmatrix}, \Delta L_1 = \begin{bmatrix} \Delta a_1 \\ \Delta b_1 \\ \Delta c_1 \end{bmatrix}, \text{ and } \Delta D_j = \begin{bmatrix} \Delta d_{jx} \\ \Delta d_{jy} \\ \Delta d_{jz} \end{bmatrix}; j = 1,2,3,4$$

Solving for ΔL_1^* gives

$$\underset{(4x1)}{\Delta L_1^*} = \underset{(4x4)}{[D]^{-1}}\ \underset{(4x1)}{[\Delta\Gamma_1]}\ F - \underset{(4x4)}{[D]^{-1}} \underset{(4x12)}{\begin{bmatrix} L_1^T & 0 & 0 & 0 \\ 0 & L_1^T & 0 & 0 \\ 0 & 0 & L_1^T & 0 \\ 0 & 0 & 0 & L_1^T \end{bmatrix}} \underset{(12x1)}{\begin{bmatrix} \Delta D_1 \\ \Delta D_2 \\ \Delta D_3 \\ \Delta D_4 \end{bmatrix}} \tag{II-2-33}$$

The expression $\Delta\Gamma_1$ denotes a (4x1) column vector of the phase noise on the CT signals, and ΔD_j is a (3x1) column vector of the error in the LOS to the j^{th} CT. Note that $\Delta\Gamma_1$ does not include the phase bias estimate by virtue of the formulation of L_1^*.

The line-of-sight to the j^{th} CT is given by

$$\begin{bmatrix} d_{jx} \\ d_{jy} \\ d_{jz} \end{bmatrix} = \frac{1}{r_j} \begin{bmatrix} x_s \\ y_s \\ z_s \end{bmatrix} - \frac{1}{r_j} \begin{bmatrix} x_{uj} \\ y_{uj} \\ z_{uj} \end{bmatrix} \qquad \text{(II-2-34)}$$

where

$$r_j = \left[(x_s - x_{uj})^2 + (y_s - y_{uj})^2 + (z_s - z_{uj})^2 \right]^{1/2}$$

$x_{uj} = \rho_{uj} \cos La_j \cos Lo_j$ $\qquad La_j$ = latitude of j^{th} CT

$y_{uj} = \rho_{uj} \cos La_j \sin Lo_j$ $\qquad Lo_j$ = longitude of j^{th} CT

$z_{uj} = \rho_{uj} \sin La_j$ $\qquad \rho_{uj}$ = geocentric radius of j^{th} CT

Using the condensed notation introduced earlier, Equation II-2-34 may be rewritten as shown by Equation II-2-35 i.e.,

$$\left[D_j\right] = \frac{1}{rj} \left[\rho_s\right] - \frac{1}{rj} \left[\rho_{uj}\right] . \qquad \text{(II-2-35)}$$

The error equation for II-2-35 becomes

$$\underset{(3x1)}{\left[\Delta D_j\right]} = \underset{(3x1)}{\frac{1}{r_j} \left(\Delta \rho_s\right)} - \underset{(3x1)}{\frac{1}{r_j} \left[\Delta \tilde{\rho}_{uj}\right]} - \underset{(3x1)}{\frac{1}{r_j^2} \left[\rho_s - \rho_{uj}\right]} \underset{(1x3)}{\frac{\partial r_j}{\partial \rho_s}} \underset{(3x1)}{\left[\Delta \rho_s\right]}$$

$$+ \frac{1}{r_j^2} \left[\rho_s - \rho_{uj}\right] \frac{\partial r_j}{\partial \rho_{uj}} \left[\Delta \tilde{\rho}_{uj}\right] \qquad \text{(II-2-36)}$$

where

$$\underset{(1x3)}{\frac{\partial r_j}{\partial \rho_s}} = \left[\frac{(x_s - x_{uj})}{r_j} \;\vdots\; \frac{(y_s - y_{uj})}{r_j} \;\vdots\; \frac{(z_s - z_{uj})}{r_j} \right]$$

and

$$\frac{\partial r_j}{\partial \rho_{uj}} = - \frac{\partial r_j}{\partial \rho_s} .$$

Collecting like terms and letting

$$\underset{(3x1)}{\frac{1}{r_j}\left[\rho_s - \rho_{uj}\right]} \underset{(1x3)}{\frac{\partial r_j}{\partial \rho_s}} \equiv \underset{(3x3)}{\left[B_j\right]} \qquad \text{(II-2-37)}$$

Produces

$$\underset{(3x1)}{\Delta D_j} = \frac{1}{r_j}\left\{\underset{(3x3)}{[I] - \left[B_j\right]}\right\}\underset{(3x1)}{\left[\Delta\rho_s\right]} - \frac{1}{r_j}\left\{\underset{(3x3)}{[I] - \left[B_j\right]}\right\}\underset{(3x1)}{\left[\Delta\rho_{uj}\right]} \; . \qquad \text{(II-2-38)}$$

However $\Delta\rho_{uj}$ is commonly given in the geocentric rather than the Cartesian frame. The relationship between $\Delta\rho_{uj}$ in Cartesian and $\Delta\rho_{uj}$ in geocentric is

$$\underset{(3x1)}{\left[\Delta\rho_{uj}\right]} = \underset{(3x3)}{\left[M_j\right]}\underset{(3x1)}{\left[\Delta\rho_{uj}\right]} \; ; j = 1, 2, 3, 4 \qquad \text{(II-2-39a)}$$

where

$$M_j = \begin{bmatrix} \cos La_j \cos Lo_j & -\rho_{uj} \cos La_j \sin Lo_j & -\rho_{uj} \sin La_j \cos Lo_j \\ \cos La_j \sin La_j & \rho_{uj} \cos La_j \cos Lo_j & -\rho_{uj} \sin La_j \sin Lo_j \\ \sin La_j & 0 & \rho_{uj} \cos La_j \end{bmatrix} . \qquad \text{(II-2-39b)}$$

Substituting Equation II-2-39a) into II-2-38 and II-2-36 into II-2-33 yields

$$\underset{(4x1)}{\left[\Delta L_1^*\right]} = \underset{(4x4)}{[D]^{-1}}\underset{(4x3)}{\left[\Delta r_1\right]} F - \underset{(4x4)}{[D]^{-1}}\underset{(4x3)}{\begin{bmatrix} L_1^T \\ 0 \\ 0 \\ 0 \end{bmatrix}}\frac{1}{r_j}\left\{\underset{(3x3)}{[I] - \left[B_1\right]}\right\}\underset{(3x1)}{\left[\Delta\rho_s\right]} - \underset{(4x4)}{[D]^{-1}}\underset{(4x3)}{\begin{bmatrix} L_1^T \\ 0 \\ 0 \\ 0 \end{bmatrix}}\frac{1}{r_2}\left\{\underset{(3x3)}{[I] - \left[B_1\right]}\right\}\underset{(3x3)}{\left[M_1\right]}\underset{(3x1)}{\left[\Delta\rho_{u1}\right]} \quad + \text{(continued next page)}$$

$$
- [D]^{-1} \begin{bmatrix} 0 \\ L_1^T \\ 0 \\ 0 \end{bmatrix} \frac{1}{r_2} \left\{ [I] - [B_2] \right\} [\Delta\rho_s] - [D]^{-1} \begin{bmatrix} 0 \\ L_1^T \\ 0 \\ 0 \end{bmatrix} \frac{1}{r_2} \left\{ [I] - [B2] \right\} [M_2] \; [\Delta\rho_{u2}]
$$

$$
- [D^{-1}] \begin{bmatrix} 0 \\ 0 \\ L_1^T \\ 0 \end{bmatrix} \frac{1}{r_3} \left\{ [I] - [B_3] \right\} [\Delta\rho_s] - [D]^{-1} \begin{bmatrix} 0 \\ 0 \\ L_1^T \\ 0 \end{bmatrix} \frac{1}{r_2} \left\{ [I] - [B_3] \right\} [M_3] \left[\Delta\rho_{u_3} \right]
$$

$$
- [D]^{-1} \begin{bmatrix} 0 \\ 0 \\ 0 \\ L_1^T \end{bmatrix} \frac{1}{r_4} \left\{ [I] - [B_4] \right\} [\Delta\rho_s] - [D]^{-1} \begin{bmatrix} 0 \\ 0 \\ 0 \\ L_1^T \end{bmatrix} \frac{1}{r_4} \left\{ [I] - [B_4] \right\} [M_4] \left[\Delta\rho_{u_4} \right] . \tag{II-2-40}
$$

Once again, for reasons of clarity and brevity, the following nomenclature is introduced into Equation II-2-40:

$$
[\Delta L_1^*] = \frac{\partial L_1^*}{\partial \Gamma_1} [\Delta\Gamma_1] - \frac{\partial L_1^*}{\partial \rho_s} [\Delta\rho_s] - \frac{L_1^*}{\partial \rho_{u_1}} \left[\Delta\rho_{u_1} \right] - \frac{\partial L_1^*}{\partial \rho_{u_2}} \left[\Delta\rho_{u_2} \right] -
$$

$$
\frac{\partial L_1^*}{\partial \rho_{u_3}} \left[\Delta\rho_{u_3} \right] - \frac{\partial L_1^*}{\partial \rho_{u_4}} \left[\Delta\rho_{u_4} \right] \tag{II-2-41}
$$

where

$$
\frac{\partial L_1^*}{\partial \Gamma_1} \equiv D_F^{-1} = \text{sensitivity of } L_1^* \text{ to CT phase errors}
$$

$$\frac{\partial L_1^*}{\partial \rho_s} = [D]^{-1} \begin{bmatrix} L_1^T \\ 0 \\ 0 \\ 0 \end{bmatrix} \frac{1}{r_1} \left\{[I] - [B_1]\right\} + [D]^{-1} \begin{bmatrix} 0 \\ L_1^T \\ 0 \\ 0 \end{bmatrix} \frac{1}{r_2} \left\{[I] - [B_2]\right\}$$

$$+[D]^{-1} \begin{bmatrix} 0 \\ 0 \\ L_1^T \\ 0 \end{bmatrix} \frac{1}{r_3} \left\{[I] - [B_3]\right\} + [D]^{-1} \begin{bmatrix} 0 \\ 0 \\ 0 \\ L_1^T \end{bmatrix} \frac{1}{r_4} \left\{[I] - [B_4]\right\}$$

= sensitivity of L_1^* to satellite ephemeris errors

$$\frac{\partial L_1^*}{\partial \rho_{uj}} = [D]^{-1} \begin{bmatrix} L_1^T \\ 0 \\ 0 \\ 0 \end{bmatrix} \frac{1}{r_j} \left\{[I] - [B_j]\right\} M_j \; ; j = 1, 2, 3, 4$$

= sensitivity of L_1^* to the j^{th} CT survey error.

The error equation for L_2^* is identical to Equation II-2-41 that L_1^T becomes L_2^T and Γ_1 becomes Γ_2 as follows:

$$\Delta L_2^* = \frac{\partial L_2^*}{\partial \Gamma_2} [\Delta \Gamma_2] - \frac{\partial L_2^*}{\partial \rho_s} [\Delta \rho_s] - \frac{\partial L_2^*}{\partial \rho_{u_1}} [\Delta \rho_{u_1}] - \frac{\partial L_2^*}{\partial \rho_{u_2}} [\Delta \rho_{u_2}]$$

$$- \frac{\partial L_2^*}{\partial \rho_{u_3}} [\Delta \rho_{u_3}] - \frac{\partial L_2^*}{\partial \rho_{u_4}} [\Delta \rho_{u_4}] .$$

(II-2-42)

II-2.4 COMPOSITE ERROR EQUATION

Begin by modifying Equation II-2-28 to fit Equation II-2-42, This simply consists of combining in matrix notation ΔL_1 and ΔL_2 with $\Delta\gamma_{BB1}$ and $\Delta\gamma_{BB2}$ respectively, as follows:

$$[\Delta P] = \frac{\partial P}{\partial \rho_s} [\Delta \rho_s] + \frac{\partial P}{\partial h} [\Delta h] - \frac{\partial P}{\partial LOS_B} \begin{bmatrix} \overbrace{\frac{\partial LOS_B}{\partial L_1}}^{\frac{\partial LOS_B}{\partial L^*_1}} & 0 \\ 0 & \frac{\partial LOS_B}{\partial \gamma_{B_1}} \end{bmatrix} \begin{bmatrix} \Delta L_1 \\ \Delta \gamma_{B_1} \end{bmatrix}$$

$$- \frac{\partial P}{\partial LOS_B} \begin{bmatrix} \overbrace{\frac{\partial LOS_B}{\partial L_2}}^{\frac{\partial LOS_B}{\partial L^*_2}} & 0 \\ 0 & \frac{\partial LOS_B}{\partial \gamma_{B_2}} \end{bmatrix} \begin{bmatrix} \Delta L_2 \\ \Delta \gamma_{B_2} \end{bmatrix} + \frac{\partial P}{\partial LOS_B} \frac{\partial LOS_B}{\partial \Gamma_B} [\Delta \Gamma_B] \cdot \quad \text{(II-2-43)}$$

Equations II-2-41 and II-2-42 may now be substituted directly into Equation II-2-43 to give

$$[\Delta P] = \frac{\partial P}{\partial \rho_s} [\Delta \rho_s] + \frac{\partial P}{\partial h} [\Delta h] + \frac{\partial P}{\partial LOS_B} \frac{\partial LOS_B}{\partial L^*_1} \left\{ \frac{\partial L^*_1}{\partial \Gamma_1} [\Delta \Gamma_1] - \frac{\partial L^*_1}{\partial \rho_s} [\Delta \rho_s] \right.$$

$$\left. - \frac{\partial L^*_1}{\partial \rho_{u_1}} [\Delta \rho_{u_1}] - \frac{\partial L^*_1}{\partial \rho_{u_2}} [\Delta \rho_{u_2}] - \frac{\partial L^*_1}{\partial \rho_{u_3}} [\Delta \rho_{u_3}] - \frac{\partial L^*_1}{\partial \rho_{u_4}} [\Delta \rho_{u_4}] \right\}$$

$$+ \frac{\partial P}{\partial LOS} \frac{\partial LOS}{\partial \Gamma_B} [\Delta \Gamma_B] + \frac{\partial P}{\partial LOS_B} \frac{\partial LOS_B}{\partial L^*_2} \left\{ \frac{\partial L^*_2}{\partial \Gamma_2} [\Delta \Gamma_2] - \frac{\partial L^*_2}{\partial \rho_s} [\Delta \rho_s] - \right.$$

$$\left. \frac{\partial L^*_2}{\partial \rho_{u_1}} [\Delta \rho_{u_1}] - \frac{\partial L^*_2}{\partial \rho_{u_2}} [\Delta \rho_{u_2}] \frac{\partial L^*_2}{\partial \rho_{u_3}} [\Delta \rho_{u_3}] - \frac{\partial L^*_2}{\partial \rho_{u_4}} [\Delta \rho_{u_4}] \right\}.$$

(II-2-44)

Combining sensitivities of common error sources and regrouping yields

$$
\begin{aligned}
[\Delta P] = {} & \left\{ \frac{\partial P}{\partial \rho_s} - \frac{\partial P}{\partial LOS_B} \frac{\partial LOS_B}{\partial L_1^*} \frac{\partial L_1^*}{\partial \rho_s} - \frac{\partial P}{\partial LOS_B} \frac{\partial LOS_B}{\partial L_2^*} \frac{\partial L_2^*}{\partial \rho_s} \right\} [\Delta \rho_s] \\
& + \frac{\partial P}{\partial LOS_B} \frac{\partial LOS_B}{\partial L_1^*} \frac{\partial L_1^*}{\partial \Gamma_1} [\Delta \Gamma_1] + \frac{\partial P}{\partial LOS_B} \frac{\partial LOS_B}{\partial L_2^*} \frac{\partial L_2^*}{\partial \Gamma_2} [\Delta \Gamma_2] \\
& - \frac{\partial P}{\partial LOS_B} \left\{ \frac{\partial LOS_B}{\partial L_1^*} \frac{\partial L_1^*}{\partial \rho_{u_1}} + \frac{\partial LOS_B}{\partial L_2^*} \frac{\partial L_2^*}{\partial \rho_{u_1}} \right\} \left[\Delta \rho_{u_1} \right] \\
& - \frac{\partial P}{\partial LOS_B} \left\{ \frac{\partial LOS_B}{\partial L_1^*} \frac{\partial L_1^*}{\partial \rho_{u_2}} + \frac{\partial LOS_B}{\partial L_2^*} \frac{\partial L_2^*}{\partial \rho_{u_2}} \right\} \left[\Delta \rho_{u_2} \right] \\
& - \frac{\partial P}{\partial LOS_B} \left\{ \frac{\partial LOS_B}{\partial L_1^*} \frac{\partial L_1^*}{\partial \rho_{u_3}} + \frac{\partial LOS_B}{\partial L_2^*} \frac{\partial L_3^*}{\partial \rho_{u_3}} \right\} \left[\Delta \rho_{u_3} \right] \\
& - \frac{\partial P}{\partial LOS_B} \left\{ \frac{\partial LOS_B}{\partial L_1^*} \frac{\partial L_1^*}{\partial \rho_{u_4}} + \frac{\partial LOS_B}{\partial L_2^*} \frac{\partial L_2^*}{\partial \rho_{u_4}} \right\} \left[\Delta \rho_{u_4} \right] \\
& + \frac{\partial P}{\partial h} [\Delta h] + \frac{\partial P}{\partial LOS_B} \frac{\partial LOS_B}{\partial \Gamma_B} [\Delta \Gamma_B] \quad . \qquad \text{(II-2-45)}
\end{aligned}
$$

Equation II-2-45 is the complete error equation which relates the errors in the individual sources of error to errors in the position fix. The partial derivative matrices (they are not truly partial derivatives in a strict mathematical sense) provide the error sensitivities.

II-2.5 STATISTICAL ERROR ANALYSIS

Equation II-2-45 through fundamental to the error analysis, is not generally useful because of the proliferation of terms. It contains 18 distinct error sensitivities relating 26 error sources to the 3 components of position error. To reduce this to more manageable terms, a statistical approach is used.

The covariance matrix S_p of ΔP is defined as the expectation of ΔP times ΔP^T. Since all sources of errors are independent, the expectation of all mixed products is zero. Thus

$$S_p = E(\Delta P \Delta P^T) = N_\rho S_{\rho_s} N_\rho^T + N_{\Gamma_1} S_{\Gamma_1} N_{\Gamma_1}^T + N_{\Gamma_2} S_{\Gamma_2} N_{\Gamma_2}^T$$

$$+ N_h S_h N_h^T + N_{\Gamma_B} S_{\Gamma_B} N_{\Gamma_B}^T + N_{u1} S_{u1} N_{u1}^T + N_{u2} S_{u2} N_{u2}^T$$

$$+ N_{u3} S_{u3} N_{u3}^T + N_{u4} S_{u4} N_{u4}^T \qquad \text{(II-2-46)}$$

where

$$N_{\rho s} = \frac{\partial P}{\partial \rho_s} - \frac{\partial P}{\partial LOS_B} \frac{\partial LOS_B}{\partial L_1^*} \frac{\partial L_1^*}{\partial \rho_s} - \frac{\partial P}{\partial LOS_B} \frac{\partial LOS_B}{\partial L_2^*} \frac{\partial L_2^*}{\partial \rho_s}$$

$$N_{\Gamma_1} = \frac{\partial P}{\partial LOS_B} \frac{\partial LOS_B}{\partial L_1^*} \frac{\partial L_1^*}{\partial \Gamma_1}$$

$$N_{\Gamma_2} = \frac{\partial P}{\partial LOS_B} \frac{\partial LOS_B}{\partial L_2^*} \frac{\partial L_2^*}{\partial \Gamma_2}$$

$$N_{\Gamma_B} = \frac{\partial P}{\partial LOS_B} \frac{\partial LOS_B}{\partial \Gamma_B}$$

$$N_h = \frac{\partial P}{\partial h}$$

$$N_{uj} = \frac{\partial P}{\partial LOS_B} \left\{ \frac{\partial LOS_B}{\partial L_1^*} \frac{\partial L_1^*}{\partial \rho_{uj}} + \frac{\partial LOS_B}{\partial L_2^*} \frac{\partial L_2^*}{\partial \rho_{uj}} \right\}; \quad j = 1, 2, 3, 4$$

$S_k \equiv E[\Delta k \ \Delta k^T]$, k = column vector consisting of k error sources.

II-2.6 COMPUTER IMPLEMENTATION

The computer program has four subroutines, each of which is discussed below.

The first subroutine generates the nominal geometry. It computes the satellite's orbit in earth-centered inertial coordinates, then transfers this into

an earth-centered fixed coordinate frame. The CT sites are entered in earth-centered spherical coordinates (i.e., latitude, longitude, and geocentric altitude) which are transformed into earth-centered fixed Cartesian coordinates. The LOS of each CT is then computed per Equation II-2-34.

The interferometer baselines are entered in a local Cartesian satellite frame for convenience and then transformed into the earth-centered fixed Cartesian frame. The local spherical frame has one axis along the instantaneous geocentric radius, another along the instantaneous direction of motion, and a third forming an orthogonal triad, as shown in Figure II-2-2.

The last part of this subroutine computes the nominal beacon LOS given the beacon's location. Again, for convenience, the beacon's location is entered in an earth-centered fixed spherical frame and then transformed into an earth-centered fixed Cartesian frame.

The second subroutine computes all N matrices given by Equation II-2-46. However, since the earth-centered fixed Cartesian frame is not a convenient frame for expression of the results, the program transforms the sensitivity matrices into a local earth surface fixed Cartesian frame. Thus the sensitivities of position are given in terms of north, east, and vertical components at the nominal beacon location. The program will, at the users option, print out the entire set of sensitivities (some 78 terms).

The third subroutine evaluates Equation II-2-46 term-by-term and then performs the matrix summations. By this term-by-term evaluation an error breakdown is generated. The breakdown is most usefully expressed in the following way:

$$\text{Beacon Phase Noise} = N_{\Gamma_B} S_{\Gamma_B} N_{\Gamma_B}^T$$

$$\text{CT Phase Noise} = N_{\Gamma_1} S_{\Gamma_1} N_{\Gamma_1}^T + N_{\Gamma_2} S_{\Gamma_2} N_{\Gamma_2}^T$$

$$\text{Ephemeric Errors} = N_\rho S_{\rho s} N_\rho^T$$

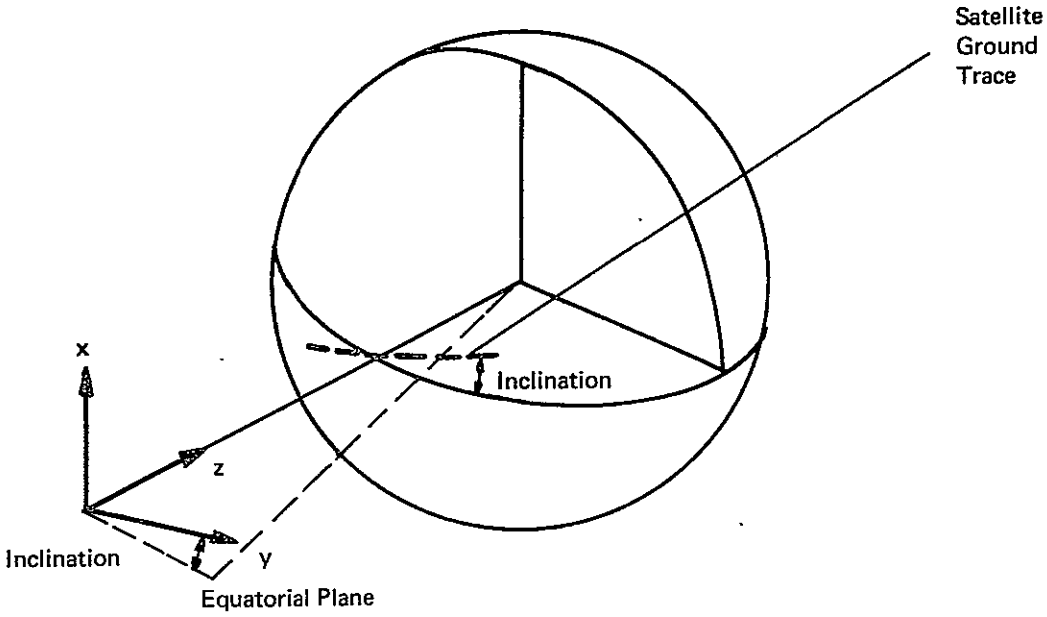

a. Satellite Local Cartesian Frame

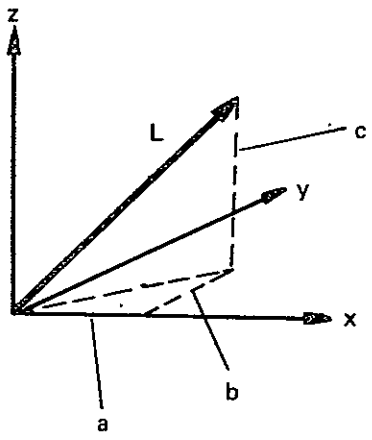

b. Interferometer Baseline Components in Satellite Local Cartesian Frame

Figure II-2-2. Coordinate Frame

$$\text{Beacon Altitude Error} = N_h \; S_h \; N_h^T$$

$$\text{CT Survey Errors} = \sum_{j=1}^{4} N_{u_j} \; S_{u_j} \; N_{u_j}^T \; .$$

The subroutine performs a useful step by converting the covariance matrices into a standard deviation matrix and a correlation matrix.

The subroutine computes S_p, its standard deviation and correlation matrices, and its eigen values and eigen vectors. This last step provides the user with the axes of the error elipsoid as well as the orientation of the ellipsoid relative to worth, east and vertical. If the ratio of the major to the minor axes of the ellipse generated by a horizontal out is less than 3, the CEP (circular error probable = 50%) is computed from the well known approximation

$$\text{CEP} = 0.588 \; (\sigma \text{ major} + \sigma \text{ minor}). \qquad \text{(II-2-47)}$$

The fourth subroutine computes the velocity error ellipsoid. The computation is straightforward. S_v, the covariance matrix of velocity errors, is obtained by computing the expectation of ΔV times ΔV^T where

$$\Delta V\left(t + \frac{T}{2}\right) = \frac{[\Delta P \; (t + T) \; - \; \Delta P \; (t)]}{T} \; . \qquad \text{(II-2-48)}$$

and T is the interval between position fixes. The value of ΔP and hence ΔV are computed in the earth-centered fixed Cartesian reference frame.

The subroutine computes the sensitivities of ΔP (t) and ΔP (t + T) from Equation II-2-45 separately. This is necessary because the N matrices can be strong functions of the relative geometry. However, errors such as the CT survey errors and the satellite ephemeris errors (for an hour or so) are the same at both time t and time t + T. On the other hand, such errors as the CT and beacon phase noises are not the same. Therefore,

$$\Delta P \; (t) = N_{\Gamma B} \; (t) \; \Delta\Gamma_B \; (t) + N_{\Gamma_1} \; (t) \; \Delta\Gamma_1 \; (t)$$
$$+ N_{\Gamma_2} \; (t) \; \Delta\Gamma_2 \; (t) + N_h \; (t) \; \Delta h \; (t) + \text{ (continued on next page)}$$

$$+ N_{\rho s}(t)\,\Delta\rho_s + \sum_{j=1}^{4} N_{u_j}(t)\,\Delta\rho_{uj} \qquad \text{(II-2-49)}$$

From the above it follows directly that

$$\begin{aligned} T\,S_v\left(t+\frac{T}{2}\right) = {} & N_{\Gamma B}(t)\,S_{\Gamma B}\,N_{\Gamma_B}^T(t) + N_{\Gamma B}(t+T)\,S_{\Gamma B}\,N_{\Gamma B}^T(t+T) \\ & + N_{\Gamma_1}(t)\,S_{\Gamma_1}\,N_{\Gamma_1}^T(t) + N_{\Gamma_1}(t+T)\,S_{\Gamma_1}\,N_{\Gamma_1}^T(t+T) \\ & + N_{\Gamma_2}(t)\,S_{\Gamma_2}\,N_{\Gamma_2}^T(t) + N_{\Gamma_2}(t+T)\,S_{\Gamma_2}\,N_{\Gamma_2}^T(t+T) \\ & + N_h(t)\,S_h\,N_h^T(t) + N_h(t+T)\,S_h\,N_h^T(t+T) \\ & + \left[N_{\rho s}(t+T) - N_{\rho s}(t)\right] S_{\rho s}\left[N_{\rho s}(t+T) - N_{\rho s}(t)\right]^T \\ & + \sum_{j=1}^{4}\left[N_{uj}(t+T) - N_{uj}(t)\right] S_{uj}\left[N_{uj}(t+T) - N_{uj}(t)\right]^T \end{aligned}$$

and it is assumed that S_{Γ_B}, S_{Γ_1}, S_{Γ_2} and, S_h are stationary.

The subroutine converts S_v from the earth-centered fixed Cartesian frame to the earth surface fixed local frame prior to printing the result.

Section II-3

MULTIPATH

The signals transmitted from a balloon beacon will propagate along two paths to the satellite. One is the direct path and the other is reflected from the ground. Both signals arriving at the satellite are superimposed, and will produce an erroneous phase reading when compared to a reading produced by a signal coming in along the direct path only.

II-3.1 THE GEOMETRICAL AND MATHEMATICAL MODEL

Figure I-3-1 shows the multipath geometry. The direct ray is along the distance r between the balloon and satellite, and the indirect ray is reflected at the earth's surface.

For the moment, it is assumed that the geometry is ideal and that the earth is an ideal specular reflector. At the reflection point, the grazing angle θ is the same for the incoming and reflected rays.

The mathematical description of this geometry for the calculation of the angle ϵ can be simplified by assuming θ as the independent variable. Then

$$\cos\left(\theta+\zeta_1\right) = \frac{\rho_e}{\rho_e+h}\cos\theta \qquad \text{(II-3-1a)}$$

and

$$\cos\left(\theta+\zeta_2\right) = \frac{\rho_e}{\rho_s}\cos\theta\ . \qquad \text{(II-3-1b)}$$

From this

$$\xi = -2\theta + \arccos\left[\frac{\rho_e}{\rho_e+h}\cos\theta\right] + \arccos\left[\frac{\rho_e}{\rho_s}\cos\theta\right]. \quad \text{(II-3-2)}$$

To calculate the multipath, the angle ϵ shown in Figure II-3-1 is important. To obtain ϵ, β_1 and β_2 must be determined. Thus

$$\sin\beta_2 = \frac{\rho_e}{\rho_s}\cos\theta \quad \text{(II-3-3)}$$

$$\sin\beta_1 = \frac{\rho_e+h}{\rho_s}\cos E \quad \text{(II-3-4)}$$

and

$$E = 90-\beta_1-\zeta. \quad \text{(II-3-5)}$$

Introducing Equation II-3-5 into Equation II-3-4 and calculating β_1 yields

$$\tan\beta_1 = \frac{\frac{\rho_e+h}{\rho_s}\sin\zeta}{1-\frac{\rho_e+h}{\rho_s}\cos\zeta}. \quad \text{(II-3-6)}$$

Then

$$\epsilon = \beta_1-\beta_2. \quad \text{(II-3-7)}$$

It is desirable to have ϵ as a function of ζ or E. For this, the following procedure is used:

a. Assume a value for θ

b. Calculate ξ from Equation II-3-2

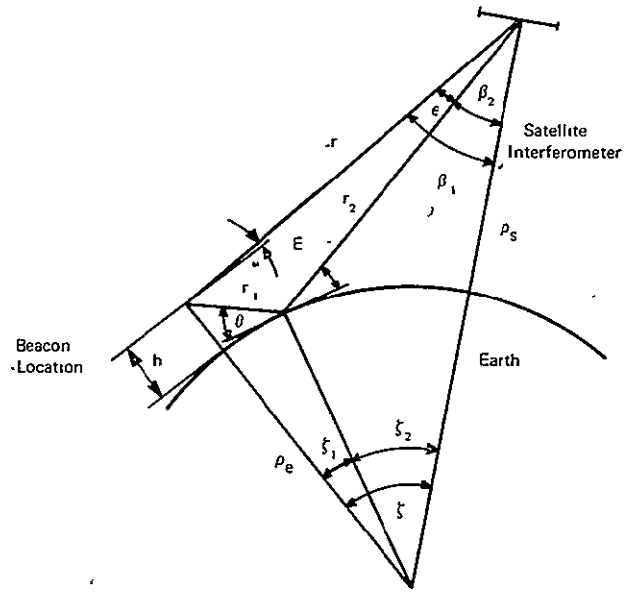

Figure II-3-1. Beacon-Earth-Satellite Multipayh Geometry

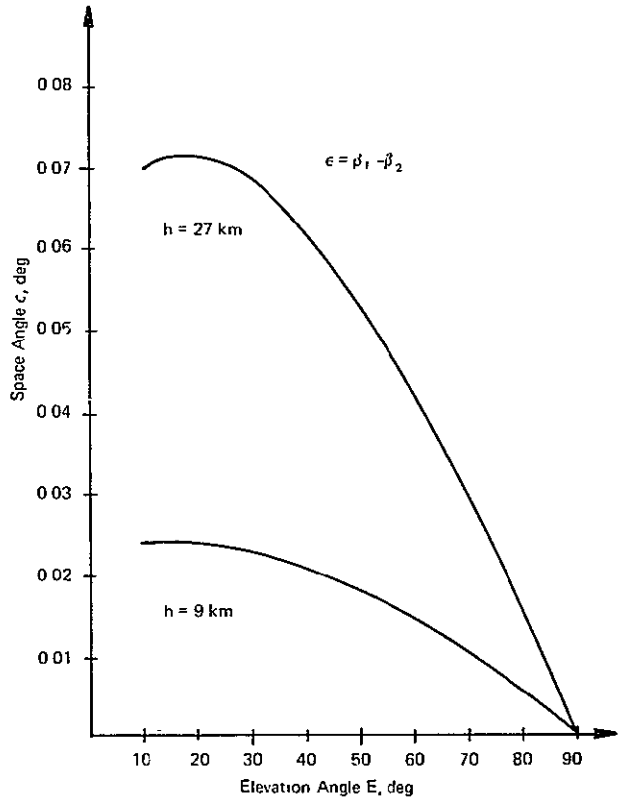

Figure II-3-2. Angle Difference Between Direct Ray and Multipath Ray

c. Calculate β_2 from Equation II-3-3

d. Calculate β_1 from Equation II-3-6

e. Calculate ϵ from Equation II-3-7

f. Calculate E from Equation II-3-5.

Figure II-3-2 shows the angle difference between the multipath ray and the direct ray. This angle difference is a strong function of the balloon altitude h and that it diminishes for increasing elevation angle.

Figure II-3-3 shows the importance of ϵ, which is the angle between the direct ray and the multipath ray. The wavefront of the balloon signal is assumed to arrive at an angle φ, and the wavefront of the multipath signal is assumed to arrive at an angle φ'. The amplitude of the sinusoidal direct signal is A, and the amplitude of the sinusoidal multipath signal is B. The multipath signal is assumed to have an arbitrary phase Φ with respect to the direct signal. The following abbreviations are introduced:

$$\frac{\omega}{c} d = p \quad \frac{\omega}{c} d' = q \quad \frac{B}{A} = \alpha \quad q-p = \chi \; . \tag{II-3-8}$$

The angle χ describes the error. It can be expressed in terms of angles φ and φ' as follows:

$$-\chi = p-q = \frac{d}{c}\omega - \frac{d'}{c}\omega = \omega\frac{L}{c}\sin\varphi - \omega\frac{L}{c}\sin\varphi' \; . \tag{II-3-9a}$$

From this

$$-\chi = \omega\frac{L}{c}(\sin\varphi - \sin\varphi') = \frac{4\pi L}{\lambda}\cos\frac{\varphi+\varphi'}{2}\sin\frac{\varphi'-\varphi}{2} \; . \tag{II-3-9b}$$

From Figure II-3-3 it can be seen that the $\varphi - \varphi'$ equals ϵ. Since ϵ is small and $\frac{\varphi+\varphi'}{2} \leq 10$, it is appropriate to use the approximation

$$-\chi \doteq 2\pi\frac{L}{\lambda}\epsilon \; . \tag{II-3-10}$$

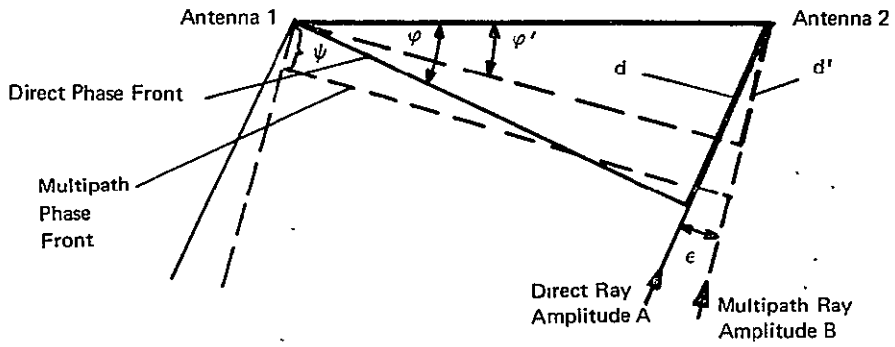

Figure II-3-3. Geometry at the Interferometer

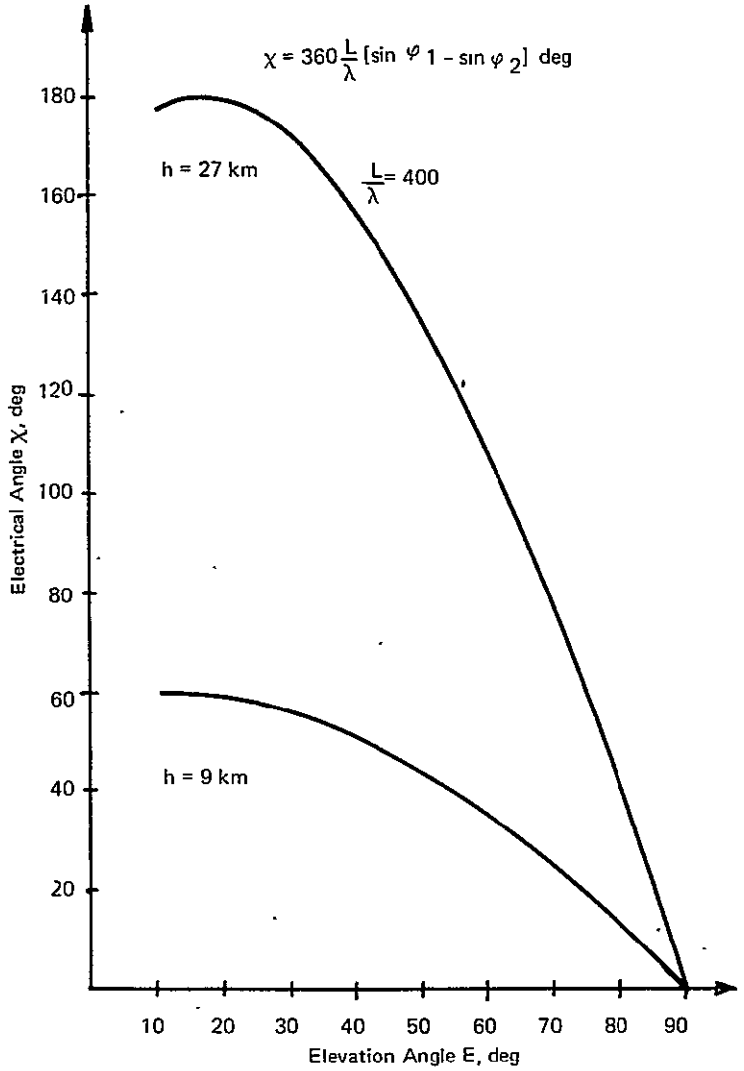

Figure II-3-4. Multipath Electrical Angle

Although the angle ϵ is quite small, as seen from Figure II-3-2, the corresponding electrical angle χ is large, because ϵ is magnified by $\frac{L}{\lambda}$. Figure II-3-4 shows angle χ as a function of the elevation angle E. As expected, χ is also a strong function of the balloon altitude h.

As the next step, the phase angle error δ resulting from multipath is calculated. To this end, the phase difference between the signals at the two antennas is determined. The signal S_1 arriving at antenna 1 is

$$S_1 = A\cos\omega t + B\cos(\omega t+\psi) = \sqrt{A^2+2AB\cos\psi+B^2}\,\cos\left(\omega t+\arctan\frac{B\sin\psi}{A+B\cos\psi}\right). \qquad \text{(II-3-11)}$$

The signal S_2 arriving at antenna 2 is

$$\begin{aligned} S_2 &= A\cos(\omega t+p) + B\cos(\omega t+q+\psi) \\ &= A\cos(\omega t+p) + B\cos(\omega t+p+\chi+\psi) \\ &= \sqrt{A^2+2AB\cos(\chi+\psi)+B^2}\,\cos\left(\omega t+p+\arctan\frac{B\sin(\chi+\psi)}{A+B\cos(\chi+\psi)}\right). \end{aligned} \qquad \text{(II-3-12)}$$

The interferometer determines the phase difference between S_1 and S_2. This phase difference can be expressed as

$$\gamma = -\arctan\frac{B\sin\psi}{A+B\cos\psi} + p+\arctan\frac{B\sin(\chi+\psi)}{A+B\cos(\chi+\psi)}.$$

The expected phase difference from the direct signal is p; hence, the error δ owing to multipath is

$$\delta = -\arctan\frac{\alpha\sin\psi}{1+\alpha\cos\psi} + \arctan\frac{\alpha\sin(\psi+\chi)}{1+\alpha\cos(\psi+\chi)}. \qquad \text{(II-3-13)}$$

The phase error δ is a function of ψ, χ and α.

The ratio α is the multipath-to-signal amplitude ratio and will later be replaced by $\sqrt{\text{MSR}}$, the root of the multipath-to-signal power ratio. The angle ψ is considered a random angle because, although the geometry shown in Figure II-3-1 is assumed ideal, any small change in the position of the balloon or the satellite will cause the paths r_1, r_2, and r to change such that the phasefronts will shift by many multiples of wavelengths. Consequently, ψ can vary over the range $0 \leq \psi \leq 2\pi$.

For assessing the largest multipath error, δ will be maximized with respect to ψ, i.e.,

$$\frac{\partial \delta}{\partial \psi} = 0.$$

From Equation II-3-13

$$\left[\alpha \cos\psi + \alpha^2\right]\left[1+2\alpha \cos(\psi + \chi) + \alpha^2\right] = \left[\alpha \cos(\psi + \chi)+\alpha^2\right]\left[1+2\alpha \cos\psi + \alpha^2\right]$$

$$\cos\psi = \cos(\psi + \chi)$$

$$\cos\psi \left[1-\cos\chi\right] = -\sin\psi \sin\chi$$

and finally

$$\tan\psi = \frac{\cos\chi - 1}{\sin\chi} \qquad \text{(II-3-14)}$$

Then

$$\sin\psi = \frac{\cos\chi - 1}{\sqrt{2\,(1-\cos\chi)}} \qquad \text{(II-3-15a)}$$

$$\cos\chi = \frac{\sin\chi}{\sqrt{2\,(1-\cos\chi)}}. \qquad \text{(II-3-15b)}$$

Inserting Equations II-3-15a) and II-3-15b into Equation II-3-12 yields

$$\delta_{max} = 2 \arctan \frac{\alpha\,(1-\cos\chi)}{\sqrt{2(1-\cos\chi) + \alpha \sin}} \qquad \text{(II-3-16)}$$

II-3.2 POSITION ERROR RESULTING FROM MULTIPATH

The electrical angle error δ_{max} as defined in Equation II-3-16 can be translated into a position error. First the electrical angle error is translated into a space angle error $\Delta\varphi$ as follows:

$$\Delta\varphi = \frac{\lambda}{2\pi L} \frac{1}{\cos\varphi} \delta_{max} . \qquad \text{(II-3-17)}$$

From this the position error is derived using Equation II-1-3. This yields

$$\Delta X = \frac{\lambda}{2\pi L} \frac{r}{\sin E} \frac{\delta_{max}}{\cos\varphi} . \qquad \text{(II-3-18)}$$

To assess the magnitude of the multipath error and its dependence on the different parameters, consider Figure II-3-5, which shows the multipath error as function of elevation angle. The magnification, $\frac{L}{\lambda}$, the balloon altitude, and the signal-to-multipath ratio (SMR) are parameters.

It can be seen that the position error drops significantly with decreasing SMR. To show this effect more clearly, the position error was replotted in Figure II-3-6 as a function of the SMR. The curves are for a fixed elevation angle of 20 deg, which can be considered as the lower limit in elevation angle for the system. This figure shows that, for large $\frac{L}{\lambda}$, the error is less than for smaller $\frac{L}{\lambda}$. This is an important reason for choosing L and λ. The figure also shows that, for an SMR of 25 dB or more, the position error can be kept below 5 km for elevation angles greater than 20 deg, which may be sufficient for velocity determination. However, as shown later, a much better SMR can be achieved and the multipath error can be reduced below 1 km.

II-3.3 BANDSPREADING

There are three types of reflection for the indirect ray: specular, mixture of specular and diffuse, and diffuse. The criterion determining which type of

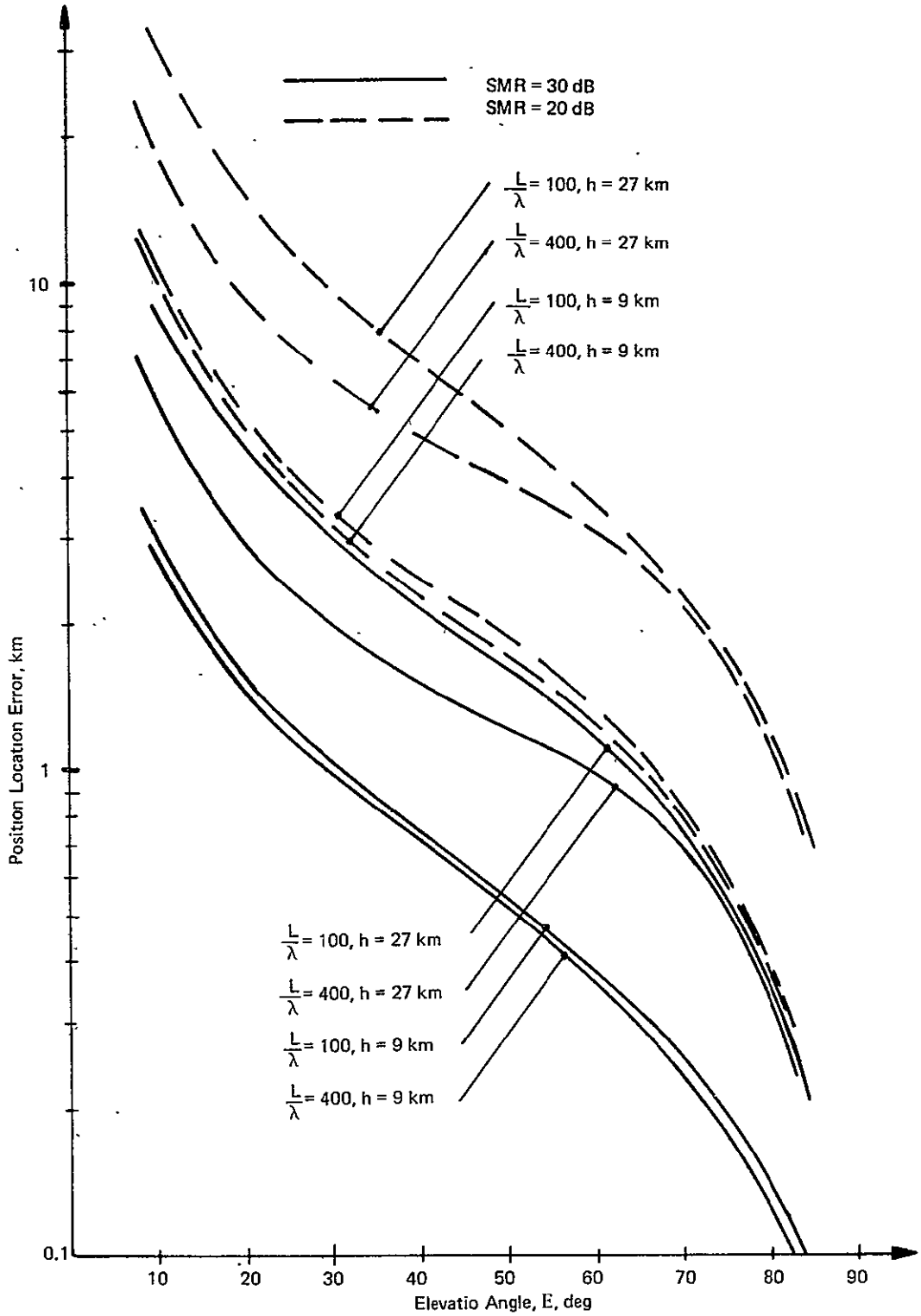

Figure II-3-5. Maximum Position Error Resulting from Multipath as Function of Elevation Angle

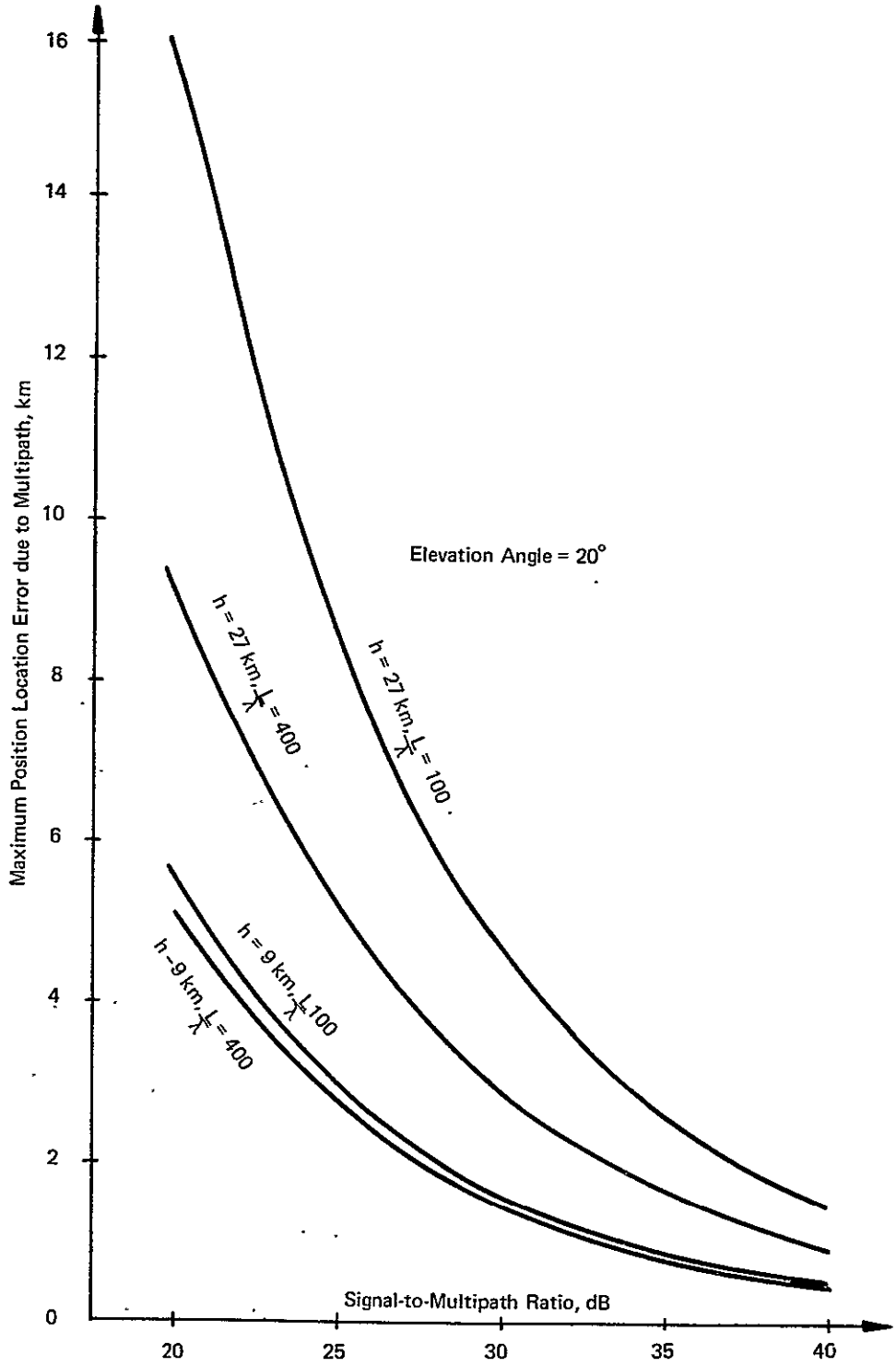

Figure II-3-6. Maximum Position Error Resulting from Multipath

reflection exists is the surface roughness, which is given by the standard deviation of the surface bumps σ.

The bump height standard deviation σ can be related to the bump maximum dimension s_{max} by [6]

$$\sigma \doteq \frac{s_{max}}{4.66} .$$

Then the different regions for the types of reflection can be considered to be at

$\frac{\sigma}{\lambda} < \frac{1}{16 \sin\theta}$	Specular reflection
$\frac{\sigma}{\lambda} > \frac{1}{16 \sin\theta}$	Mixture of diffuse and specular reflection
$\sigma >> \lambda$	Entirely diffuse scattering

(θ = grazing angle)

Examination of the interferometer position location scheme shows that for $E > 20$ deg (at the balloon beacon) $\theta > 20$ deg; hence $\frac{1}{16 \sin\theta} < 0.0182$.

Consider next the cases of 400 MHz ($\lambda = 75$ cm) and 1600 MHz ($\lambda = 18.75$ cm) for land. Since land will always exhibit roughness, it can be assumed that, for the area which contributes to the multipath signal (about 20 mi radius), there will be surface irregularities, so that $s_{max} >> \lambda$ for either 75 cm or 18.75 cm. Land will therefore always produce diffuse scattering.

Considering the sea for which a wave height exceeding one ft will exist for 98.3 percent of all times, and for which a wave height of more than 3 ft will exist for more than 60.9 percent of all times, [7] the average wave maximum can be assumed to be 2 ft most of the time. Therefore $\sigma = 0.43$ ft is a warranted assumption. Then the criterion for diffuse reflection becomes

λ	=	75 cm (2.5 ft)		λ	=	18.75 cm (0.625 ft)	
$\frac{\sigma}{\lambda}$	>	0.171		$\frac{\sigma}{\lambda}$	>	0.685	
$\frac{1}{16 \sin\theta}$	<	0.55		$\frac{1}{16 \sin\theta}$	<	0.55	($\theta > 20^\circ$)
$\frac{\sigma}{\lambda}$	$\doteq$	$\frac{1}{16 \sin\theta}$		$\frac{\sigma}{\lambda}$	>	$\frac{1}{16 \sin\theta}$	

Duncan[6] also shows that for values of the grazing angle exceeding 10 deg, diffuse reflection will exist whenever $\frac{\sigma}{\lambda} > 1.0$. In Duncan's calculation, the criterion for diffuse reflection is $\frac{\sigma}{\lambda} > \frac{0.1}{\sin\theta}$; our assumption of $\frac{\sigma}{\lambda} > \frac{1}{16 \sin\theta}$ is perhaps a little less conservative. However, it can be seen that for f = 1600 MHz (λ = 18.75 cm), reflection will be generally diffuse. Because of this, the multipath behavior for diffuse reflection must be investigated.

The results shown in Figure II-3-6 assume the idealistic model shown in Figure II-3-1, where the earth is a perfect spherical reflector, and the reflected signal is sinusoidal. Considering the earth as a rough reflector, the reflected signal will consist of a superimposition of many small contributing signals of random relative phases, each reflected by a different facet of the constantly changing reflector surface. This constant change comes about by the relative motion of the balloon with respect to the surface; furthermore, much of the reflecting surface consists of ocean surface with its moving waves.

The analysis is carried out by calculating a spectrum of the reflected signal using the model of reflection from a rough surface. In this case, the ratio of reflected power to direct power can be written as

$$\frac{P_o}{P_d} = \frac{D^2 |R|^2}{4\pi} \frac{r^2}{r_1^2 r_2^2} \frac{\cot^2\beta_o}{\cos^4\beta} \exp\left\{-\frac{\tan^2\beta}{\tan^2\beta_o}\right\} \qquad \text{(II-3-19)}$$

where

P_o	=	power in the reflected ray
P_d	=	power in the direct ray
D	=	spherical divergence factor
R	=	Fresnel reflection coefficient
r	=	range, direct ray
r_1	=	range to the area of reflection
r_2	=	range from area of reflection to satellite
$\tan \beta_o$	=	$\frac{2\sigma}{T}$
σ	=	surface bump height
T	=	correlation interval.

The angle β can be related to the angles of incidence and reflection by

$$\tan^2 \beta \quad \frac{\sin^2\theta_1 + \sin^2\theta_2 - 2\sin\theta_1 \sin\theta_2 \cos\Phi}{(\cos\theta_1 + \cos\theta_2)^2} \qquad \text{(II-3-20)}$$

where θ_1 is the angle between the ray and the point of reflection and θ_2 is the angle of the reflected ray (see Figure II-3-7).

Formula II-3-19 describes the ratio of the multipath power from one reflection element to the power in the direct ray. To obtain the SMR, the contribution of all elements must be superimposed. This can be done by computing the correlation function and the spectrum of the multipath power.

The correlation function, i.e.,

$$C(\tau) = E[S(t)\ S^*(t+\tau)] \qquad \text{(II-3-21)}$$

is expressed as the expected value of the random scattered ground signal S(t). From literature 9, 10

$$C(t) = \int P_o \exp\left[-jk(r_o - r_n)\right] d\Sigma \qquad \text{(II-3-22)}$$

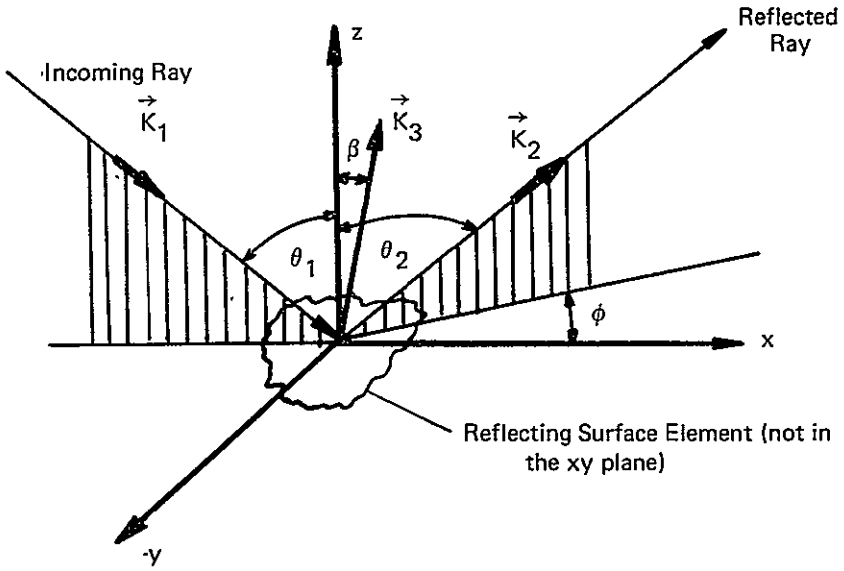

xyz is the frame of the "local" scattering geometry.

$\vec{K}_1$ is the unit vector of the incoming ray; it lies in the x-z plane.

$\vec{K}_2$ is the unit vector of the reflected ray; it lies in a plane forming

the angle ϕ with the x-z plane.

$$\vec{K}_1 - \vec{K}_2 = \vec{K}_3$$

$\vec{K}_3$ is a vector normal to the reflecting surface element.

$$\vec{K}_1 = \begin{cases} \sin\theta_1 \\ 0 \\ \cos\theta_1 \end{cases} \qquad K_2 = \begin{cases} \sin\theta_2 \cos\phi \\ \sin\theta_2 \sin\phi \\ \cos\theta_2 \end{cases}$$

β is the angle between $\vec{K}_3$ and the z axis.

$$\tan^2\beta = \frac{K_{3x}^2 + K_{3y}^2}{K_{3z}^2} .$$

Figure II-3-7. Scattering Geometry and Explanations

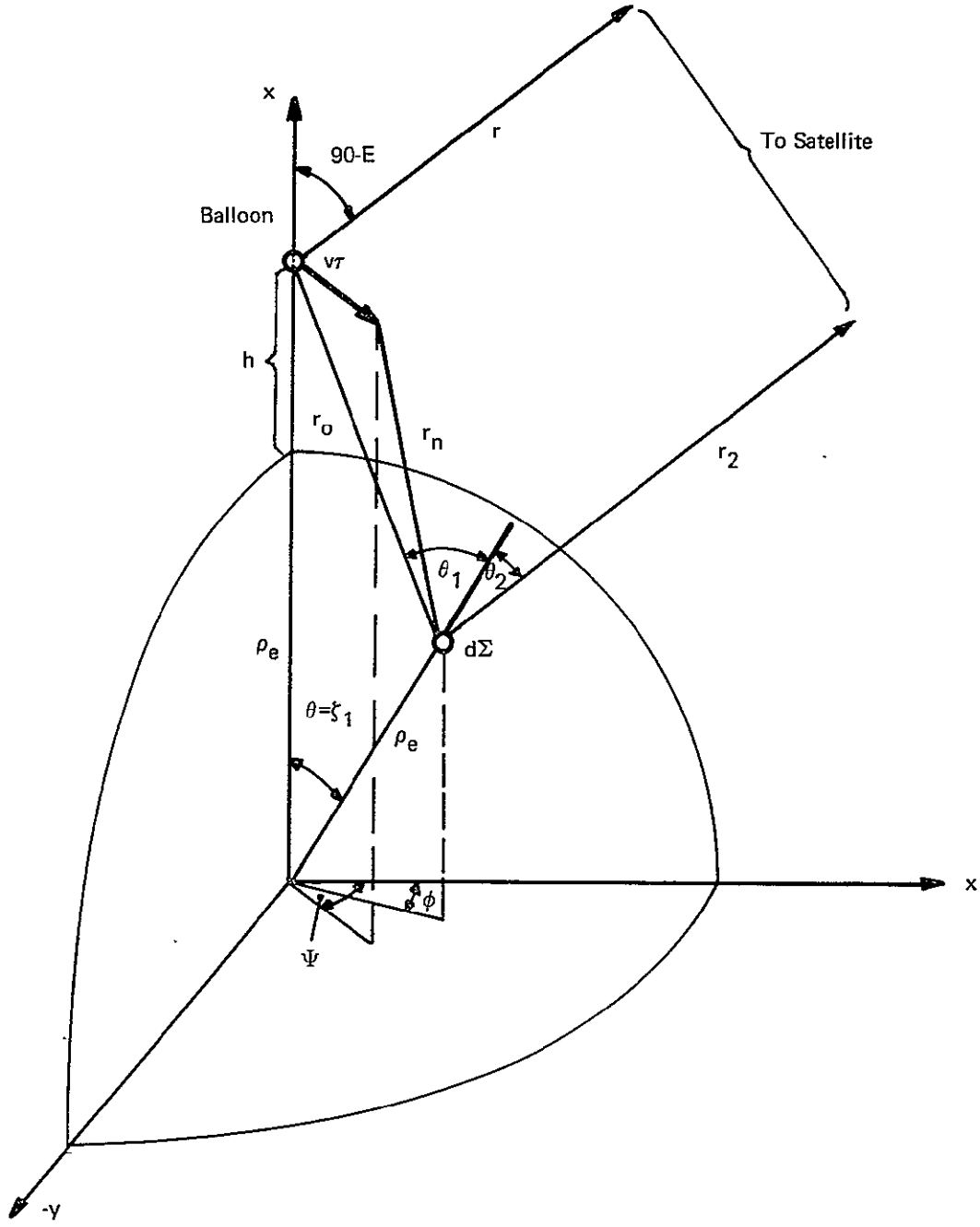

Figure II-3-8. Three-Dimensional Geometry of Reflection

where $r_o - r_n$ is the change in path length in a time internal τ, $k = \frac{2\pi}{\lambda}$, k is the wave number of the signal being reflected and $d\Sigma$ is the elements of the scattering surface. The integral must be evaluated over the area where reflection takes place.

The geometry is shown in Figure II-3-8. The balloon is assumed to be along the axis through the pole of an earth central coordinate system.. The portion of the scattering element $d\Sigma$ is characterized by a polar angle θ and a longitudinal angle Φ. The balloon height $h << \rho_e$, hence $\theta << 1$.

At the beginning of the time interval τ, the range to the scattering element is r_o; at the end of the interval, when the balloon has moved $v\tau$ units of length, the range has become r_n. Also shown are the angles of incidence and reflection, i.e., θ_1 and θ_2. The angle of the projection of $\vec{v}\,\tau$ on the "equatorial" plane in Figure II-3-8 is ψ. To a first-order approximation, the change in range will be $r_o - r_n$, which can be approximately expressed by

$$r_o - r_n \doteq v\tau \sin(\theta_1 - \theta)\cos(\Phi - \psi) \quad . \tag{II-3-23}$$

The surface element $d\Sigma$ is

$$d\Sigma = \rho_e^2 \sin\theta \, d\theta \, d\Phi \quad . \tag{II-3-24}$$

The ratio of the correlation function of the multipath to the power along the direct ray can then be written as

$$\frac{C(\tau)}{P_d} = \frac{D^2 |R|^2}{4\pi} \int \frac{r^2 \rho_e^2}{r_1^2 r_2^2} \frac{\cot^2\beta_o}{\cos^4\beta} \exp\left\{-\frac{\tan^2\beta}{\tan^2\beta_o}\right\} \exp\Big\{jkv\tau \sin(\theta_1 - \theta)$$

$$\cos(\Phi - \psi)\Big\} \sin\theta \, d\theta \, \Phi \quad . \tag{II-3-25}$$

To evaluate the integral, it is assumed that $\tan\beta_o$ is sufficiently small that the method of steepest descent can be used. This involves finding the stationary points $\tan^2\beta$, i.e., simultaneous solutions of

$$\frac{\partial \tan^2\beta}{\partial \Phi} = 0$$

and

$$\frac{\partial \tan^2\beta}{\partial \theta} = 0 \; . \qquad \text{(II-3-26)}$$

This leads to

$$\theta_1 = \theta_2 \; ; \qquad \theta = \zeta_1 \; ; \qquad \Phi << 1 \; (\Phi \doteq 0) \; . \qquad \text{(II-3-27)}$$

At this point, it may be useful to compare figures II-3-1, the 2-dimensional multipath geometry and II-3-8, the 3-dimensional geometry. What can be deduced from Equation II-3-27 is that, for the case of interest, the reflection takes place in a plane, for which $\Phi = 0$, and the angle θ from Figure II-3-8 then becomes the angle ζ_1 of Figure II-3-1.

The following approximations are also introduced:

$$\cos\beta \doteq 1 \qquad \frac{r}{r_2} \doteq 1$$

$$\tan^2\beta \doteq \frac{1}{2}\left(\frac{\partial \tan^2\beta}{\partial \Phi}\right)\Bigg|_{\substack{\theta=\zeta_1 \\ \Phi=0}} \Phi^2 + \frac{1}{2}\left(\frac{\partial \tan^2\beta}{\partial \theta}\right)\Bigg|_{\substack{\theta=\zeta_1 \\ \Phi=0}} \left(\theta - \xi_1\right)^2$$

$$\doteq \frac{1}{4} \tan^2\Gamma \, \Phi^2 + M^2 \left(\theta - \zeta_1\right)^2 \qquad \text{(II-3-28)}$$

with

$$\Gamma = 90\text{-}E\text{-}\xi_1$$

$$M = 1+\frac{1}{2}\,\frac{H^2}{\sqrt{H^2+H\,\xi_1^2}\left[H^2+(1+H)\,\zeta_1^2\right]}\quad ; \qquad H=\frac{h}{\rho_e}\,. \tag{II-3-29}$$

Also needed for computing the integral is the relationship

$$\frac{\rho_e^2}{r_1^2}\sin\theta = \frac{\sin^2(\theta_1-\theta)}{\sin\theta} \doteq \frac{\theta}{H^2+(1-H)\theta^2}\,.$$

the latter equation, when evaluated at ξ_1, produces

$$\frac{\rho_e^2}{r_1^2}\sin\theta = \frac{\zeta_1}{H^2+(1+H)\,\zeta_1^2}\,. \tag{II-3-30}$$

Next the value of $r_o - r_n$ is evaluated. Expanding from Equation II-3-23 yields

$$r_o - r_n \doteq v\tau\sin(\theta_1-\theta)\cos\Phi\cos\Psi + v\tau\sin(\theta_1-\theta)\sin\Phi\sin\Psi\,.$$

Observing that $\Phi << 1$, $\sin\Phi \doteq \Phi$, and $\cos\Phi \doteq 1$, $r_o - r_n$ becomes

$$r_o - r_n = v\tau\sin(\theta_1-\theta)\cos\Psi + v\tau\,\Phi\sin(\theta_1-\theta)\sin\Psi\,. \tag{II-3-31}$$

It is also observed that the first part of $r_o - r_n$ varies only with θ, while the second part varies strongly with Φ and weakly with θ. When $\sin(\theta_1-\theta)$ is developed around ζ_1,

$$\sin(\theta_1-\theta) \doteq \frac{\zeta_1}{\sqrt{H^2+(1+H)\,\zeta_1^2}}$$

$$\doteq \sin\Omega + J\left(\theta-\zeta_1\right) \tag{II-3-32}$$

$$\Omega = 90\text{-E-}2\,\zeta_1 \quad . \tag{II-3-33}$$

Introducing Equation II-3-32 into Equation II-3-31 yields

$$r_o - r_n \doteq v\tau \sin\Omega \cos\Psi + v\tau J(\theta - \xi_1)\cos\Psi + v\tau\Phi \sin\Omega \sin\Psi \quad . \tag{II-3-34}$$

When equations II-3-28 to II-3-30 and Equation II-3-34 are introduced into the integral II-3-25, one finally obtains

$$\frac{C(\tau)}{P_d} = \frac{D^2|R|^2}{4\pi} \frac{\cot^2\beta_o\,\zeta_1}{H^2+(1+H)\zeta_1^2} \exp(jkv\tau \sin\Omega \sin\Psi) \int \exp\left\{ -\frac{1}{4} \frac{\tan^2\Gamma}{\tan^2\beta_o}\Phi^2 + jkv\tau\,\Phi \sin\Omega \sin\Psi \right\} d\Phi$$

$$\cdot \int \exp\left\{ - \frac{M^2(\theta - \zeta_1)^2}{\tan^2\beta_o} + jkv\tau\, J(\theta - \zeta_1)\cos\Psi \right\} d(\theta - \zeta_1) \cdot \tag{II-3-35}$$

The value of the integrals is approximated by taking the integrals from $+\infty$ to $-\infty$. This is permissible, since the integrands are functions that have narrow Gaussian bell curves as envelopes. Then

$$\frac{C(\tau)}{P_d} = \frac{D^2|R|^2}{4\pi} \cot^2\beta_o \frac{\sqrt{\pi}\ 2\tan\beta_o}{\tan\Gamma} \frac{\sqrt{\pi}\ \tan\beta_o}{M} \frac{\xi_1}{H^2 + (1+H)\zeta_1^2}$$

$$\exp\left\{ - \frac{k^2v^2\tau^2\sin^2\Omega\tan^2\beta_o\sin^2\Psi}{\tan^2\Gamma} - \frac{k^2v^2\tau^2 J^2\tan^2\beta_o\cos^2\Psi}{4M^2} \right.$$

$$+ jkv\tau \sin\Omega \cos\Psi \Bigg\}$$

which is simplified to

$$\frac{C(\tau)}{P_d} = D^2 |R|^2 Q \exp\left\{-k^2 v^2 \tau^2 \tan^2\beta_o \left[\frac{\sin^2\Omega}{\tan^2\Gamma}\sin^2\Psi + \left(\frac{\left(1+H\tan^2\Omega\right)\cos\Omega}{\left|+H\tan^2\Omega+\frac{4\zeta_1}{\sin^2\Omega}\right.}\right)^2 \cos^2\Psi\right]\right.$$

$$\left. + jkv\tau \sin\Omega\cos\Psi\right\} . \qquad \text{(II-3-36)}$$

One further step of simplification leads to

$$\frac{C(\tau)}{P_d} = D^2 |R|^2 Q \exp\left(-\tau^2 Z + j\tau\mu\right) \qquad \text{(II-3-37)}$$

where

$$Q = \frac{\xi_1}{H^2+(1+H)\xi^2} \cdot \frac{|}{2M\tan\Gamma} \qquad \text{(II-3-38a)}$$

$$Z = k^2 v^2 \frac{4\sigma^2}{T^2}\left\{\frac{\sin^2\Omega}{\tan^2\Gamma}\sin^2\Psi + \left[\frac{(1+H\tan^2\Omega)\cos\Omega}{1-H\tan^2\Omega+\frac{4\zeta_1}{\sin^2\Omega}}\right]^2 \cos^2\Psi\right\} \qquad \text{(II-3-38b)}$$

$$\mu = kv\sin\Omega\cos\Psi . \qquad \text{(II-3-38c)}$$

The power spectrum of the multipath signal can now be obtained by taking the Fourier transformation

$$\frac{\Phi(\omega)}{P_d} = D^2 |R|^2 Q \frac{1}{2\pi} \int_{-\infty}^{+\infty} \exp\left[-\tau^2 Z + j(\mu - \omega)\tau\right] dt$$

$$\frac{\Phi(\omega)}{P_d} = D^2 |R|^2 Q \frac{1}{2\pi} \sqrt{\frac{\pi}{Z}} \exp \frac{(\mu - \omega)^2}{4Z} \quad . \qquad \text{(II-3-39)}$$

This spectrum which is shown in Figure II-3-9, is a Gaussian bell curve, shifted by μ from the frequency corresponding to the wave number k and having a "1 σ bandwidth" of $2\sqrt{2Z}$. Thus it is recognized that μ is the Doppler shift * owing to the balloon velocity and $\sqrt{2Z}$ is a measure of the bandspread.

Next consider the bandspread as defined by $2\sqrt{2Z}$. Figure II-3-10 shows the bandspread in Hz for v = 30 km/h, $\Psi = 0$, and the two frequencies f= 400 MHz and 1.6 GHz. The bandspread varies very little with altitude. The curves for h = 9 and h = 27 are indistinguishable on the scale shown. Similarly, the variation with Ψ is almost imperceptible.

There will be a differential Doppler shift between the signal in the direct path and the multipath ray. Consider first the change of the direct path r (see Figure II-3-7). From the geometry

$$r = \sqrt{(\rho_e+h) + \rho_s^2 - 2(\rho_e+h)\,\rho_s \cos \zeta}$$

$$\rho_s \sin \xi = r \sin(E+90) = r \cos E \qquad \text{(II-3-40)}$$

Then

$$\frac{dr}{dt} = \frac{d\zeta}{dt} \cdot \frac{(\rho_e+h)\,\rho_s \sin \zeta}{r}$$

and further

$$\frac{dr}{dt} = \frac{d\zeta}{dt}(\rho_e+h) \cos E. \qquad \text{(II-3-41)}$$

*This is well in agreement with another study of the multipath spectrum, Reference 11.

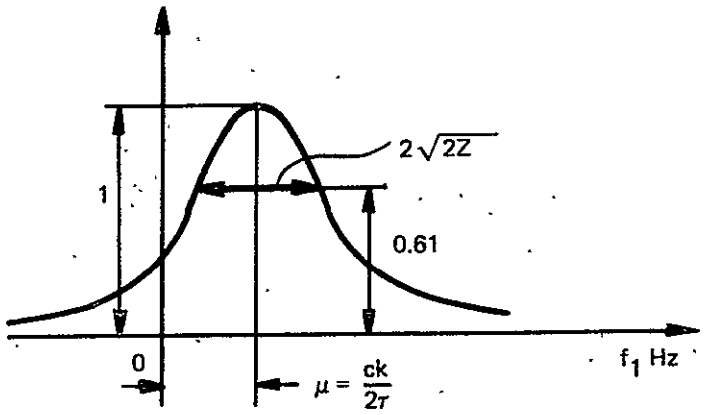

Figure II-3-9. Spectrum of Multipath Signal

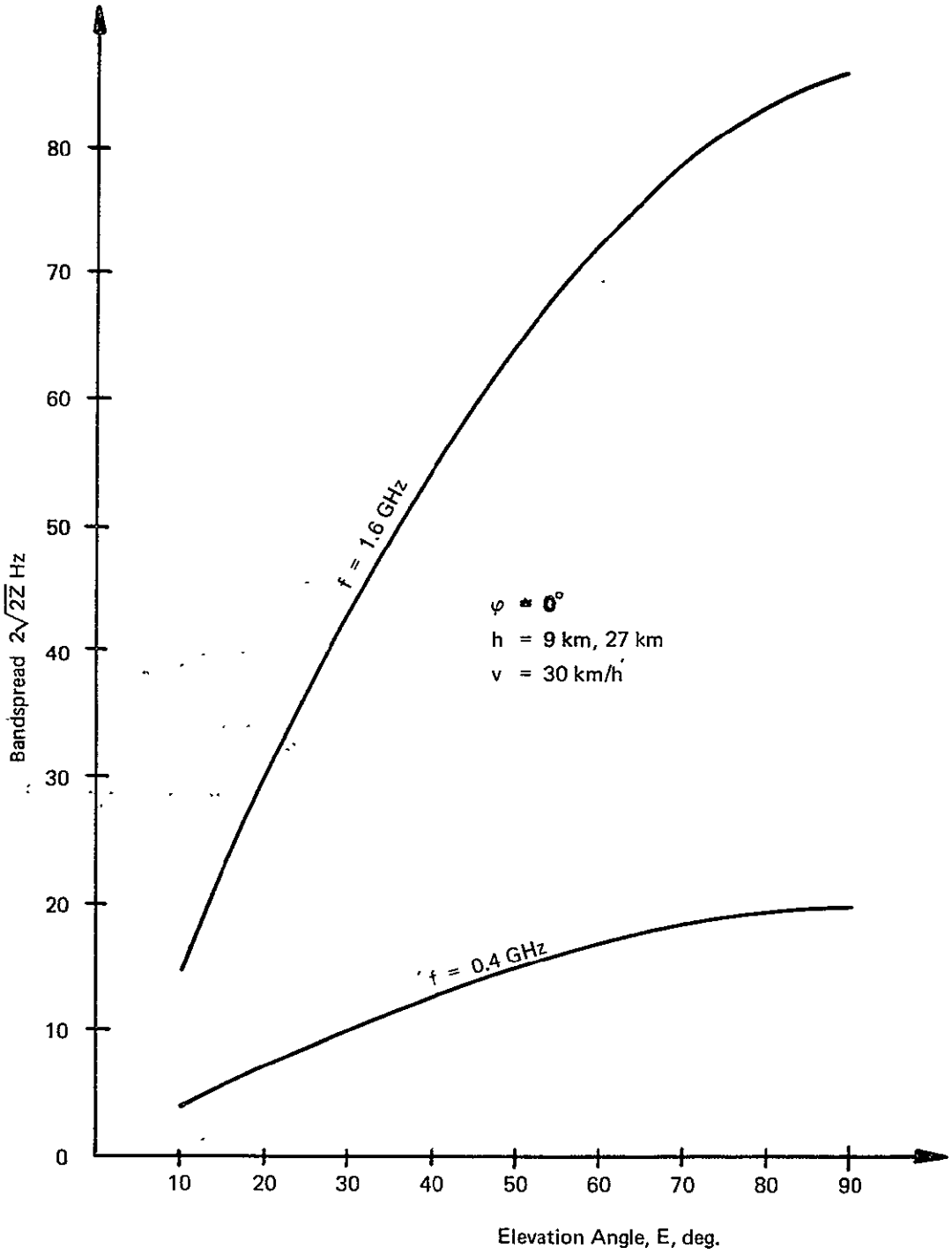

Figure II-3-10. Bandspread

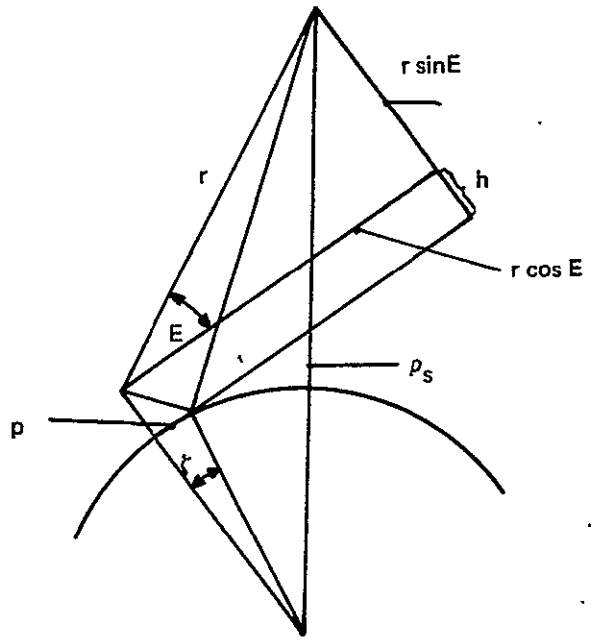

Figure II-3-11. Geometry for Approximate Determination of ζ_1.

$$p : q = h : (h + r \sin E)$$

$$p + q = r \cos E$$

$$p = \frac{rh \cos E}{2h + r \sin E}$$

$$\frac{p}{\rho_e} = \sin \zeta_1$$

$$\sin \zeta_1 = \frac{rh \cos E}{\rho_e (2h + r \sin E)} = \frac{h \cos E}{\rho_e \sin E}$$

Assuming that the balloon moves in the plane of reflection, the angle $\Psi = 0$ and the angular velocity $\frac{d\zeta}{dt}$ is expressed as

$$\frac{d\zeta}{dt} = \frac{v}{\rho_e + h} \quad . \tag{II-3-42}$$

Hence,

$$\frac{dr}{dt} = v \cos E \tag{II-3-43}$$

and

$$\omega_d = \omega \frac{v}{c} \cos E. \tag{II-3-44}$$

When the differential Doppler is calculated, the difference between equations II-3-44 and II-3-38c is formed as follows:

$$\Delta \omega_d = \omega \frac{v}{c} \left\{ \sin \Omega - \cos E \right\} \quad .$$

Inserting from Equation II-3-33 one obtains, for the difference in Doppler shift $\Delta \omega_d$,

$$\Delta \omega_d = \omega \frac{v}{c} \left\{ \cos \left(E - 2\zeta_1 \right) - \cos E \right\}$$

and

$$\Delta \omega_d = 2 \frac{\omega v}{c} \sin\left(E - \xi_1 \right) \sin \zeta_1 \quad . \tag{II-3-45}$$

An approximation for $\sin \xi_1$ can be obtained by considering that ξ_1 is a small angle. Using the geometry shown in Figure II-3-11, one finally obtains, for the differential Doppler shift,

$$\Delta \omega_d \doteq 2 \omega \frac{v}{c} \frac{h}{\rho_e} \cos E. \tag{II-3-46}$$

This approximation holds only for angles $E \gg \xi_1$ where $h \ll r \sin E$.

The magnitude of this effect is shown in Table II-3-1 for $v = 30$ km h^{-1}; the radian frequency ω has been replaced by f, the frequency of operation. The values in the table show that the differential Doppler effect is too small to be useful to discriminate against the multipath.

Table II-3-1

DIFFERENTIAL DOPPLER SHIFT Δf (Hz)

E	20°	30°	50°	70°	90°
f = 400 MHz	0.031	0.027	0.020	0.011	0
f = 1600 MHz	0.125	0.108	0.082	0.044	0

II-3.4 EFFECTS OF FILTERING

The bandspread produced by motion allows discrimination against the multipath by filtering. The MSR for filtering with a narrowband rectangular filter centered on the multipath spectrum can be computed by integrating the spectrum over the filter bandwidth. Then

$$\mathrm{MSR} = \frac{1}{P_d} \int_{-\pi B_M}^{\pi B_M} \Phi(\omega)\, d\omega = \frac{D^2 |R|^2 Q}{2\sqrt{2Z}} \int_{-\pi B_M}^{\pi B_M} \exp - \frac{\omega^2}{4Z}\, d\omega$$

and

$$\mathrm{MSR} = D^2 |R|^2 Q \, \mathrm{erf}\left(\frac{\pi B_M}{2\sqrt{Z}}\right) . \qquad \text{(II-3-47)}$$

The MSR can finally be expressed as

$$\text{MSR} = \frac{1}{G_{dm}} \left[\frac{P_o}{P_d}\right] \text{ [filtering factor]} . \qquad \text{(II-3-48)}$$

In the above expression, G_{dm} is the front-to-back ratio of the balloon antenna and $\frac{P_o}{P_d}$ the ratio of reflected power to direct power. By comparison it is seen that

$$\frac{P_o}{P_d} = D^2 |R|^2 Q \qquad \text{(II-3-49a)}$$

$$\text{[filtering factor]} = \text{erf}\left(\frac{\pi B_M}{2\sqrt{Z}}\right) . \qquad \text{(II-3-49b)}$$

For numerical evaluation, it is observed that $D \doteq 1$. The reflection coefficient varies, depending on whether the signal is horizontally or vertically polarized and whether the reflection is from land or sea. For horizontal polarization

$$R_h = \frac{\cos\theta - \sqrt{n^2 - \sin^2\theta}}{\cos\theta + \sqrt{n^2 - \sin^2\theta}} \qquad \text{(II-3-50a)}$$

while for vertical polarization

$$R_v = \frac{n^2 \cos\theta - \sqrt{n^2 - \sin^2\theta}}{n^2 \cos\theta + \sqrt{n^2 - \sin^2\theta}} . \qquad \text{(II-3-50b)}$$

In the above expression, the refractive index of the reflecting medium is

$$h^2 = \epsilon_r + j\, 60\lambda\, \sigma_e \qquad \text{(II-3-51)}$$

with

ϵ_r = relative dielectric constant

σ_e = electric conductivity

λ = wavelength

θ = angle of incidence

For land $\epsilon_r = 15$ $\sigma_e = 10^{-6}\ \Omega^{-1}m^{-1}$

For sea $\epsilon_r = 81$ $\sigma_e = 4.64 \times 10^{-3}\ \Omega^{-1}m^{-1}$

When equation (II-3-47) is evaluated, the plot shown in Figure II-3-12 results. It can be seen that an SMR in excess of 30 dB can be obtained by filtering.

If the SMR is introduced into Equation (II-3-16) and the resulting maximum electrical error angle is converted into a position location error using Equation (II-3-18), the graph shown in Figure II-3-13 is obtained. This graph shows the multipath performance, including filtering for different kinds of polarization and different reflecting surfaces. The dotted line at E = 20 deg shows the performance at the lower limiting evaluation angle of the system.

It is of interest to consider the performance for circular polarization since CP is recommended to further reduce the multipath and to eliminate polarization losses. The curves for horizontal and vertical polarization shown in Figure II-3-13 can be considered the upper and lower bounds for performance if CP is used. A CP wave will be reflected as a linearly polarized signal at the Brewster angle; above the Brewster angle, the reflected wave will be elliptically polarized and have an inverse sense of polarization. For evaluation angles E > 20 deg, the reflection will be above the Brewster angle; hence the sense of polarization will be reversed in the multipath ray. This can be used to discriminate against multipath even more than shown so far, and a multipath performance better than indicated on the curves shown in figure II-3-13 can be achieved.

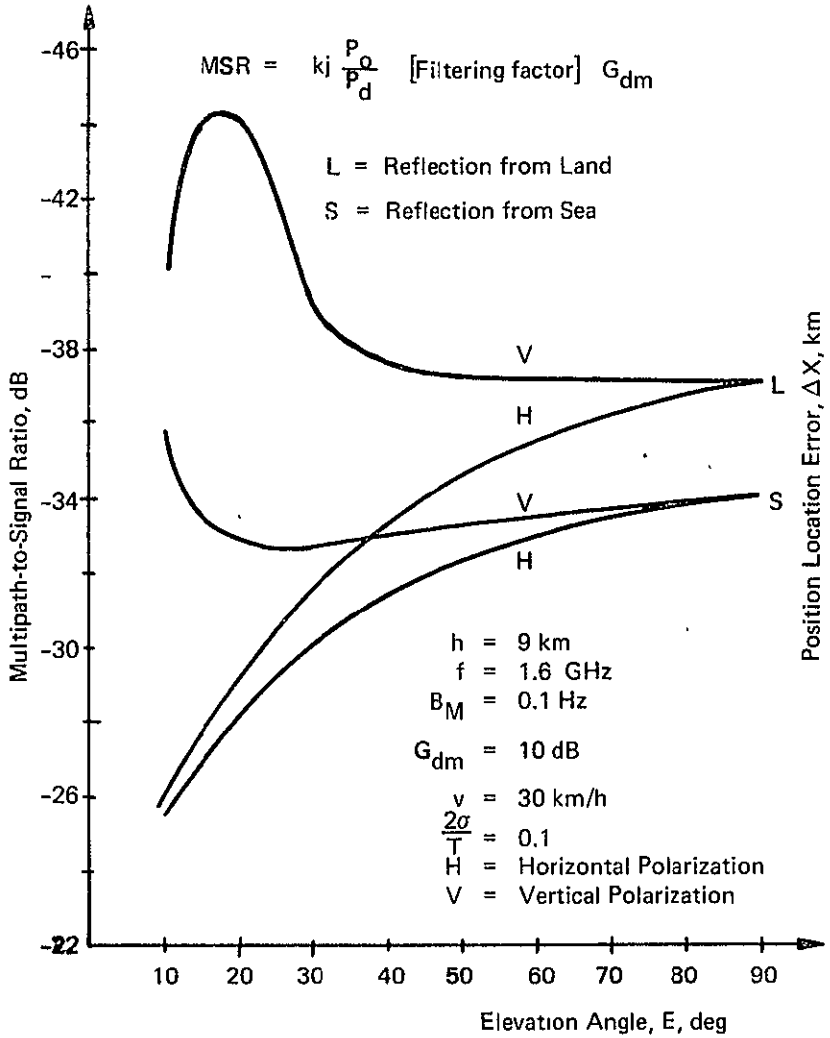

Figure II-3-12. Multipath-to-Signal Ratio with Filtering

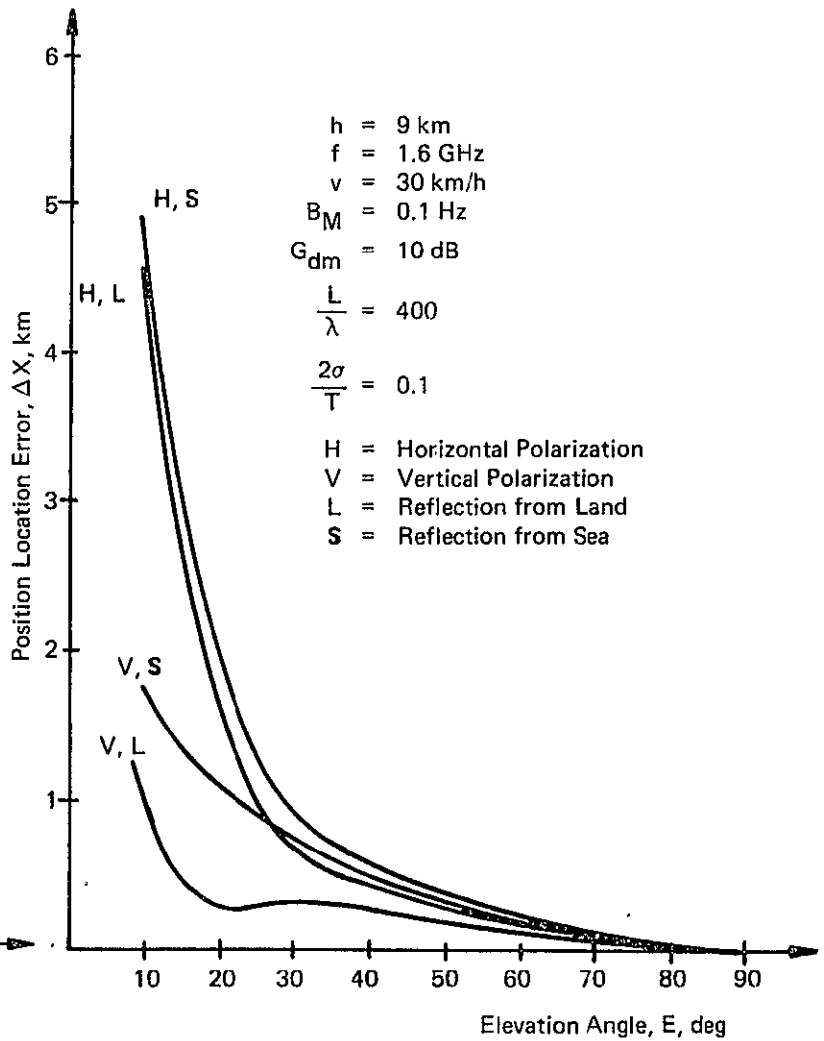

Figure II-3-13. Multipath Performance Using Filters

Section II-4

REFRACTION

The rays from the calibration ground stations or the balloons transverse the troposphere and ionosphere in curved paths. Figure II-4-1 is an exaggerated portrayal of this curve. In the troposphere (up to 30 km), the ray is bent towards Earth. Then it transverses an electrically neutral region until, at about 80 km altitude, it reaches the ionosphere. For the region of increasing electron concentration, the ray is bent towards Earth; in the region of decreasing electron concentration, the ray is bent away from Earth. From about a 2000-km altitude on, the ray is in virtually empty space and follows a straight line. The actual ray will have an elevation angle E_1 at the source, while the straight line connecting source and the satellite has an elevation angle E_d. At the satellite, the angle of arrival (with respect to Earth normal) is β_s, while β_d is the angle between Earth normal and the straight line connecting the source and the satellite. The error angle ϵ_r with respect to the model used for angle calculation is then

$$\epsilon_r = \beta_b - \beta_d \quad . \tag{II-4-1}$$

To calculate the error angle, a ray tracing program, as shown in Figure II-4-2, is required. The atmosphere is considered as consisting of concentric shells of constant refractive index. The ray is assumed to propagate along a straight line in each shell. Then

$$\cos E_i = \frac{n_1 \rho_1}{n_i \rho_i} \cos E_1 \; ; \; \rho_1 = \rho_e \tag{II-4-2}$$

$$\beta_i = \arcsin\left[\frac{\rho_1}{\rho_{i+1}} \frac{n_1}{n_i} \cos E_1\right] \tag{II-4-3}$$

and

$$\xi_i = 90 - E_{i-1} - \beta_{i-1} \quad . \tag{II-4-4}$$

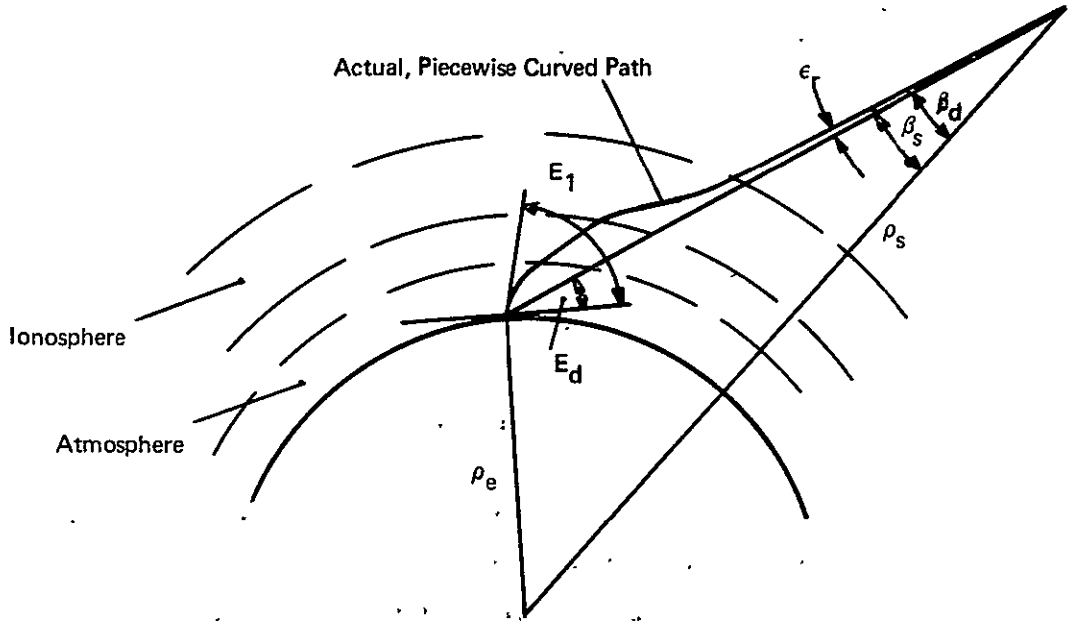

Figure II-4-1. Refraction

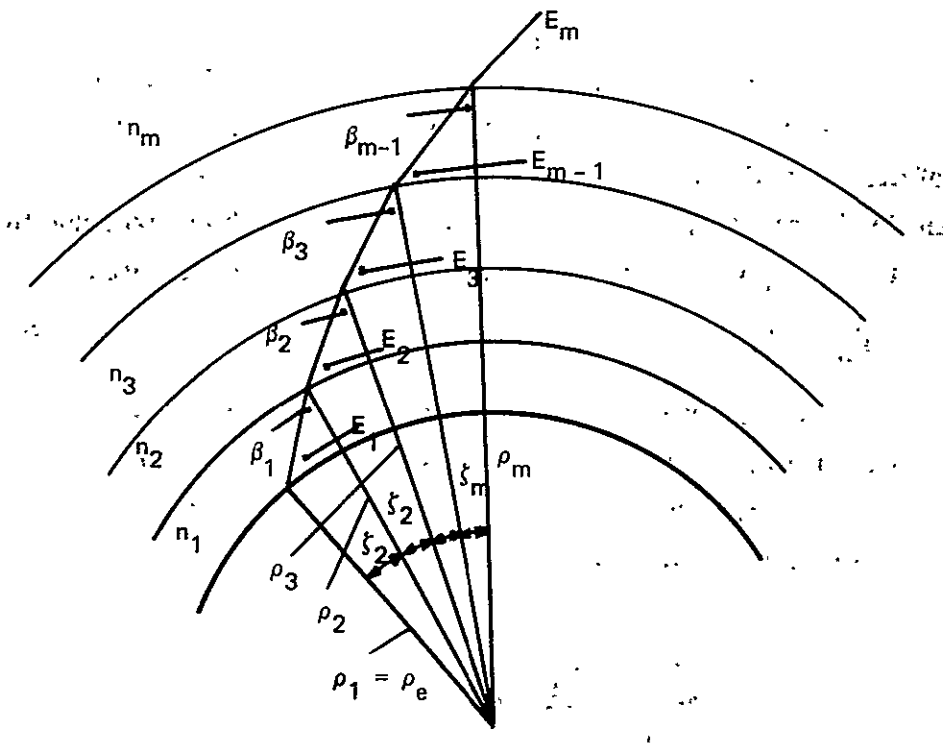

Figure II-4-2. Ray Tracing

Equations (II-4-2) to (II-4-4) are applicable to any of the triangles formed by the center of Earth and the straight path within one shell. By tracing the ray, the angles ζ_i can be calculated and accumulated. Then

$$\zeta \doteq \sum \zeta_i \qquad \text{(II-4-5)}$$

The angle β_d can then be calculated from

$$\beta_d \doteq \arctan\left[\frac{\sin \zeta}{\frac{\rho_s}{\rho_1} - \cos \zeta}\right] \qquad \text{(II-4-6)}$$

The index of refraction for the atmosphere is given by

$$n \doteq 1\text{-}N\text{x}10^{-6} \qquad \text{(II-4-7)}$$

and for the ionosphere it is given by

$$n \doteq \sqrt{1\text{-}8.06\text{x}10^{7}\frac{N_e}{f^2}} \qquad \text{(II-4-8)}$$

where N_e is the electron concentration, f is the frequency, and N is a number related to the refractive index. The electron density N_e and N can be taken from curves 3; for the tracing program, the Chapman distribution is used.

The following method for ray tracing was used:

a. A value of E_1 was selected
b. The atmosphere up to 33 km was divided into shells 1-km thick
c. The layer between 33 km and 80 km was treated as one shell
d. The ionosphere from 80 to 390 km was divided into 10-km shells
e. The ionosphere from 390 to 1990 km was divided into 100-km shells
f. Straight line propagation (one shell) from 1990 km to 35600-km altitude was used
g. The angles ζ_i for all shells were calculated and summed
h. The angle β_i at the satellite was calculated according to Equation (I-4-3)
i. The angle β_d was calculated according to Equation (II-4-6)
j. The error ϵ_r was calculated according to Equation (II-4-1).

Figure II-4-3 shows the result for an atmosphere of 100 percent humidity (which is the worst case), the ionosphere having a Chapman distribution to the maximum electron concentration, and an exponential decline to 10^3 electons/m^3 at 2000 km plotted versus the elevation angle (E_d).

The parameter is the operating frequency. The curves peak at about a 25 to 30 deg inclination angle and go to zero at an elevation angle of 90 deg. It is interesting to note that, for a frequency of 400 MHz, the maximum angle error is about 3.5×10^{-4} deg. An error of this magnitude would produce a position error of as much as 1 km. (See Figure II-1-3). For higher frequencies (1600 MHz), the refraction error for elevation angles above 20 deg appears to be negligible; the maximum position error would be between 10 and 100 m. Although it is theoretically possible to correct for refraction errors, the position error at 1600 MHz is so small that correction is not necessary.

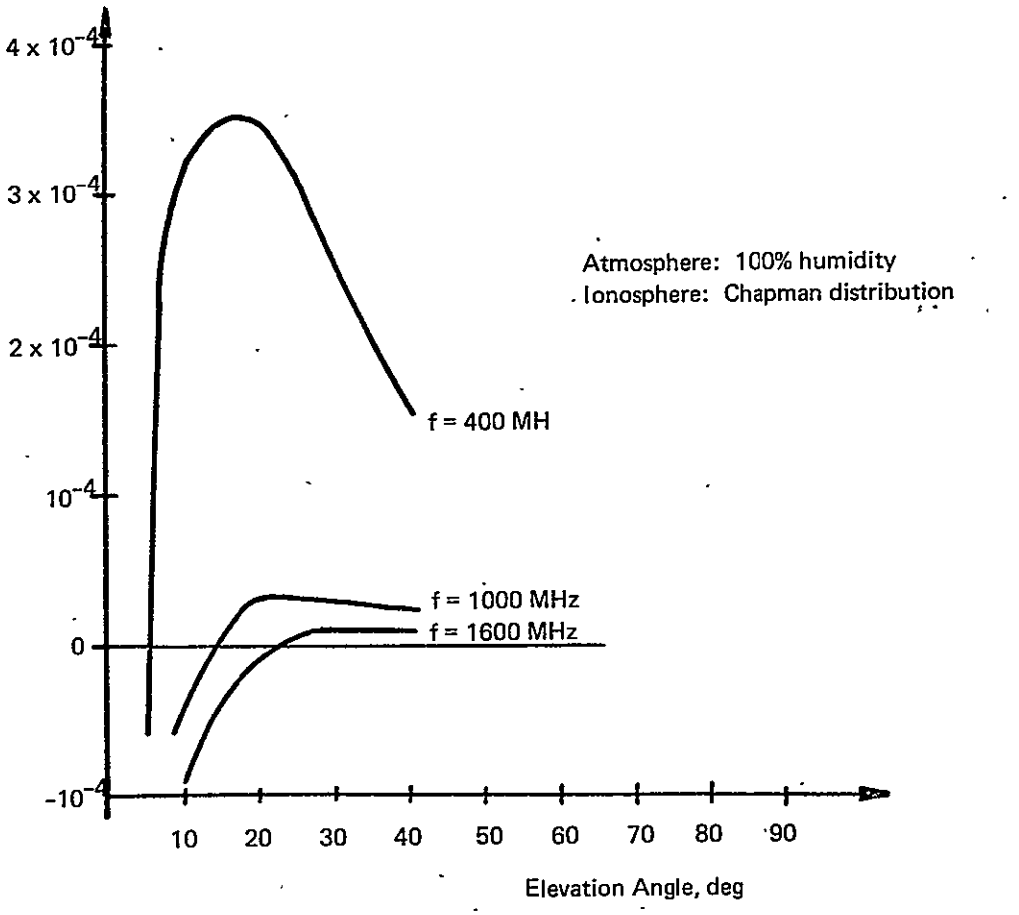

Figure II-4-3. Refraction Error

Section II-5

POLARIZATION MISMATCH ERROR

The choice of the polarization of the interferometer antenna elements, the polarization of the calibration station antennas, and the polarization of the balloon beacon antennas will influence the accuracy of the interferometer system. This section analyzes the errors resulting from antenna and signal polarization mismatch and chooses a preferred polarization.

The polarization geometry is shown in Figure II-5-1. The interferometer antennas are separated by the baseline of length L. The baseline is in the x-y plane of a coordinate system, which has its z-axis in the direction of boresight. The x-axis of the coordinate system is aligned with the major axis of the polarization ellipse of the incoming wave. The direction of propagation of the incoming wave is defined by two angles, η and ξ ; η is in the x-z plane, counted from z, while ξ is the declination from the x-z plane.

Also shown in this figure are the orientations of three polarization ellipses—two for the interferometer antennas, which lie in the x-y plane, and a third ellipse for the incoming wave which is in a plane normal to the direction of propagation. The interferometer antennas are inclined by the angles B_1 and B_2 with respect to the x-axis, and the ellipses have axial ratios of R_1 and R_2. The polarization ellipse of the incoming wave has the axial ratio R_T.

Consider an elliptically polarized plane wave traveling in the z' direction of an x'y'z' system[12] (see Figure II-5-2). Assume that the major and minor axes coincide with the x' and y' axes, respectively. Then the field of this wave can be written as

$$E = (\vec{a}_{x'} E_{x'} + j \vec{a}_{y'} E_{y'}) \exp j(\omega t - kz). \qquad \text{(II-5-1)}$$

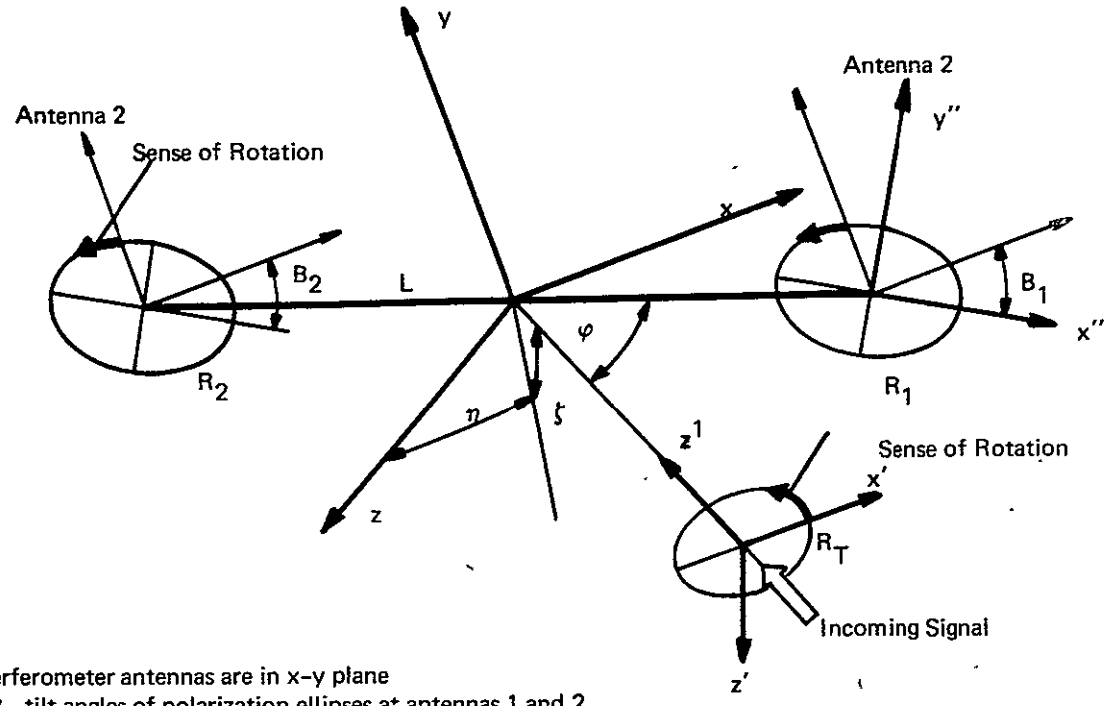

Interferometer antennas are in x-y plane
$B_1 B_2$ tilt angles of polarization ellipses at antennas 1 and 2
$R_1 R_2$ axial ratios at antennas 1 and 2
R_T axial ratio of incoming signal
ζ, η orientation of incoming signal

Figure II-5-1. Geometrical Relationship of Polarization Ellipses

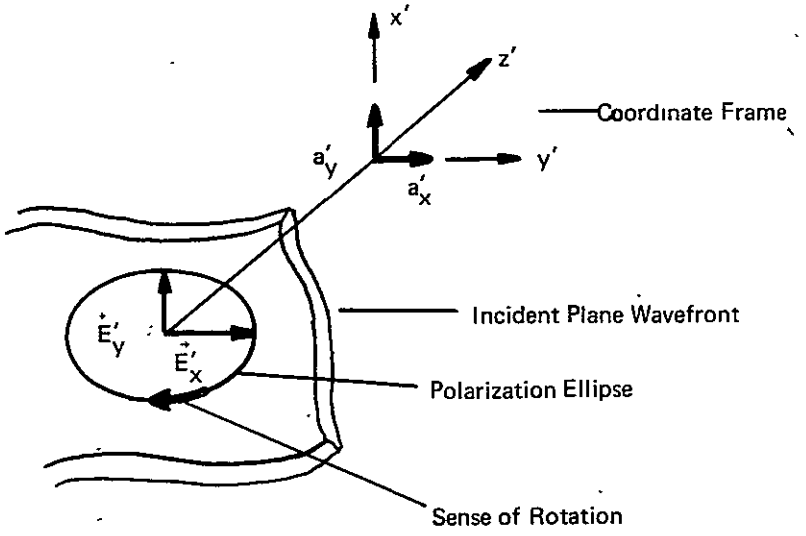

Figure II-5-2. Elliptically Polarized Plane Wave

Furthermore assume that the power carried by this wave is constant, hence

$$E_{x'}^2 + E_{y'}^2 = 1. \qquad \text{(II-5-2)}$$

Let the axial ratio R be defined as

$$R = \frac{E_{y'}}{E_{x'}} = \frac{\sqrt{1 - E_{x'}^2}}{E_{x'}} \quad . \qquad \text{(II-5-3)}$$

Then

$$E_{x'} = \frac{1}{\sqrt{1 + R^2}} \qquad E_{y'} = \frac{R}{\sqrt{1 + R^2}} \qquad \text{(II-5-4)}$$

and the field vector can be written as

$$\vec{E} = \begin{cases} \vec{E}_{x'} \\ \vec{E}_{y'} \end{cases} = \frac{1}{\sqrt{1 + R^2}} \begin{cases} \vec{a}_{x'} \\ \vec{a}_{y'} jR \end{cases} \quad . \qquad \text{(II-5-5)}$$

The rotational sense of the polarization ellipse is indicated in figures II-5-1 and II-5-2. This field is being received by antennas defined in the x y z coordinate system (see Figure II-5-1). The component vectors of $\vec{E}$ are therefore resolved in the x y z system as follows:

$$\vec{E}_x = (E_{x'} \cos\eta - E_{y'} \sin\eta \sin\xi)\, \vec{a}_x \qquad \text{(II-5-6a)}$$

and

$$\vec{E}_y = (E_{y'} \cos\xi)\, \vec{a}_y . \qquad \text{(II-5-6b)}$$

Consider this arriving field now as the transmitted field E_T. Then

$$\vec{E}_T = \frac{1}{\sqrt{1 + R_T^2}} \begin{cases} \vec{a}_x (\cos\eta - j R_T \sin\eta \sin\xi) \\ \vec{a}_y \; j R_T \cos\xi \end{cases} \qquad \text{(II-5-7)}$$

Let one of the receiving antennas, say antenna 1, be placed at the origin of the x-y-z system (x = y = z = 0) with boresight coinciding with the z-axis, but with the major axis of its polarization ellipse inclined at an angle B_1 to the x-axis (compare Figure II-5-1). The coordinate system of this ellipse is x"y".

From Equation II-5-5 it can be seen that the electric field of the receiving antenna in the x"y" frame is

$$\vec{E}_R = \begin{Bmatrix} \vec{E}_{Rx''} \\ \vec{E}_{Ry''} \end{Bmatrix} = \frac{1}{\sqrt{1+R_1^2}} \begin{Bmatrix} \vec{a}_{x''} \\ -\vec{a}_{t''} jR_1 \end{Bmatrix} \qquad \text{(II-5-8)}$$

Observe that the y" component is negative to account for the rotational sense.

This ellipse is rotated by the angle B_1 into the x-y coordinate and is then described by the following equations:

$$\vec{E}_R = \begin{Bmatrix} \vec{E}_{Rx} \\ \vec{E}_{Ry} \end{Bmatrix} = \frac{1}{\sqrt{1+R_1^2}} \begin{Bmatrix} \vec{a}_x (\cos B_1 - jR_1 \sin B_1) \\ -\vec{a}_y (\sin B_1 + jR_1 \cos B_1) \end{Bmatrix} \qquad \text{(II-5-9)}$$

With the rotational senses of both ellipses matched, the voltage U_R induced by the receiving antenna by the inclined plane wavefront is [12]

$$U_R \angle\theta_R = (\vec{E_R}) \cdot (\vec{E_R}) = E_{Tx}E_{Rx} + E_{Ty}E_{Ry} \; . \qquad \text{(II-5-10)}$$

The phase of the received voltage is

$$\theta_R = \arctan \frac{\text{Im}\left\{E_{Tx}E_{Rx} + E_{Ty}E_{Ry}\right\}}{\text{Re}\left\{E_{Tx}E_{Rx} + E_{Ty}E_{Ry}\right\}} \; . \qquad \text{(II-5-11)}$$

From equations (II-5-7) and (II-5-9)

$$\text{Im}\left\{E_{Tx}E_{Rx}\right\} = \frac{-R_1 \sin B_1 \cos\eta - R_T \sin\eta \sin\xi \cos B_1}{\sqrt{1+R_1^2}\;\sqrt{1+R_T^2}}$$

$$\text{Im}\left\{E_{Ty}E_{Ry}\right\} = \frac{-R_T \cos\xi \sin B_1}{\sqrt{1+R_1^2}\;\sqrt{1+R_T^2}}$$

$$\mathrm{Re}\left\{E_{Tx}E_{Rx}\right\} = \frac{\cos\eta\ \cos B_1 - R_T R_1 \sin\eta \sin\xi \sin B_1}{\sqrt{1+R_1^2}\quad\sqrt{1+R_T^2}}$$

$$\mathrm{Re}\left\{E_{Ty}E_{Ry}\right\} = \frac{+R_T R_1\ \cos\xi\ \cos B_1}{\sqrt{1+R_1^2}\quad\sqrt{1+R_T^2}} \quad .$$

(II-5-12)

Introducing the expression II-5-12 into II-5-11, the following phase angle of the voltage in receiving antenna number 1 is obtained:

$$\theta_{R|\text{antenna 1}} = \arctan \frac{R_1 \sin B_1 \cos\eta + R_T \cos\xi \sin B_1 + R_T \sin\eta \sin\xi \cos B_1}{-\cos\eta \cos B_1 + R_T R_1 \sin\eta \sin\xi \sin B_1 - R_T R_1 \cos\xi \cos B_1} \quad .$$

(II-5-13)

For receiving antenna number 2, the following is obtained:

$$\theta_{R|\text{antenna 2}} = \arctan \frac{R_2 \sin B_2 \cos\eta + R_T \cos\xi \sin B_2 + R_T \sin\eta \sin\xi \cos B_2}{-\cos\eta \cos B_2 + R_T R_2 \sin\eta \sin B_2 - R_T R_2 \cos\xi \cos B_2} + \frac{2\pi L}{\lambda} \sin\varphi \quad .$$

(II-5-14)

The last term is the desired angle $\frac{2\pi L}{\lambda} \sin\varphi$. The angular error δ_{pol} resulting from polarization mismatch is then

$$\delta_{pol} = \theta_{R|\text{antenna 1}} - \theta_{R|\text{antenna 2}} + \frac{2\pi L}{\lambda} \sin\varphi \quad .$$

(II-5-15)

$$\delta_{pol} = \arctan \frac{R_1 \sin B_1 \cos\eta + R_T \cos\xi \sin B_1 + R_T \sin\eta \sin\xi \cos B_1}{-\cos\eta \cos B_1 + R_T R_1 \sin\eta \sin\xi \sin B_1 - R_T R_1 \cos\xi \cos B_1}$$

$$- \arctan \frac{R_2 \sin B_2 \cos\eta + R_T \cos\xi \sin B_2 + R_T \sin\eta \sin\xi \cos B_2}{-\cos\eta \cos B_2 + R_T R_2 \sin\eta \sin\xi \sin B_2 - R_T R_2 \cos\xi \cos B_2} \quad .$$

(II-5-16a)

To simplify the expression for the phase error it is recognized that ξ and η will always be less than 10 deg, hence

$$\xi, \eta << 1; \quad \sin \xi \doteq \xi ; \sin \eta \doteq \eta ; \quad \cos \xi \doteq 1 ; \cos \eta \doteq 1 .$$

Then Equation II-5-15 becomes

$$\delta_{pol} \doteq \arctan \frac{(R_1 + R_T) \sin B_1 + R_T \xi \eta \cos B_1}{-(1 + R_1 R_T) \cos B_1 + R_1 R_T \xi \eta \sin B_1}$$

$$- \arctan \frac{(R_2 + R_T) \sin B_2 + R_T \xi \eta \cos B_2}{-(1 + R_2 R_T) \cos B_2 + R_2 R_T \xi \eta \sin B_2} . \qquad \text{(II-5-16b)}$$

From Equation II-5-16b, the four possible cases of polarization will be explored.

a. Case 1—Linear polarization at receiver and transmitter—Here

$$R_T = R_1 = R_2 = 0, \text{ and } \delta_{1\,pol} = 0 .$$

b. Case 2—The satellite receiver is linearly polarized and the ground transmitter signals are circularly (elliptically) polarized. Here $R_1 = R_2 = 0$; expressions with $(\xi \eta)^2$ are neglected; $B_2 - B_1 = \Delta B << 1$; and, since the argument is small, the arctangent is replaced by its argument. Then, from Equation I-5-16b,

$$\delta_{2\,pol} \doteq \arctan R_T \frac{\sin B_1 \cos B_2 + \xi \eta \cos B_1 \cos B_2 - \sin B_2 \cos B_1 - \cos B_1 \cos B_2}{\cos B_1 \cos B_1 + R_T^2 \sin B_1 \sin B_2 + \xi \eta \cos B_1 \sin B_2 + \xi \eta \sin B_1 \cos B_2}$$

$$\doteq \frac{R_T \Delta B}{\frac{1}{2}(1+R_T^2) + \frac{1}{2}(1-R_T^2) \cos (2B_1 + \Delta B) + R_T^2 \xi \eta \sin (2B_1 + \Delta B)} . \qquad \text{(II-5-18)}$$

The worst case of this polarization error will occur for $R_T \doteq 1$, $B_1 + \frac{\Delta B}{2} \doteq 45°$. However, because the term with B_1 in the denominator is multiplied with $\xi\eta$, the variation with B_1 is very weak; hence the term is neglected. Then

$$\delta_{2\ \text{pol max}} \doteq \frac{2R_T}{1+R_T^2}\ \Delta B.$$

c. Case 3—The signal transmitted from the ground is linearly polarized, while the satellite antennas are circularly (elliptically) polarized. Then $R_T = 0, B_2 - B_1 = \Delta B \ll 1$, and $R_2 - R_1 = \Delta R \ll 1$. Then, from Equation II-5-16b

$$\delta_{3\ \text{pol}} \doteq \arctan \frac{-R_1 \sin B_1 \cos B_2 + R_2 \cos B_1 \sin B_2}{\cos B_1 \cos B_2 + R_1 R_2 \sin B_1 \sin B_2}$$

$$\doteq \frac{R \sin (2B_1 + \Delta B) + (R_1 + R_2)\Delta B}{(1+R_1R_2) + (1-R_1R_2)\cos (2B_1 + \Delta B)} \qquad \text{(II-5-19)}$$

An estimate of a worst-case error may be obtained by letting $R_1 = R_2 = 1$ for circular polarization. Then the maximal error will occur at $B_1 + \frac{\Delta B}{2} = 45°$, and the worst-case (maximal) error will be

$$\delta_{3\ \text{pol max}} = \frac{\Delta R}{2} + \Delta B.$$

d. Case 4—The transmitted signal and the receiving antennas are circularly (elliptically) polarized. Then use is made of the fact that R_1 and R_2 are almost 1. Hence, where appropriate,

$$R_1 + R_T \doteq R_2 + R_T \doteq 1$$

$$1+R_1R_T \doteq 1 + R_2R_T \doteq 1+R_T\ .$$

Again, $R_2 - R_1 = \Delta R$ and $B_2 - B_1 = \Delta B$. Hence $\sin \Delta B \doteq \Delta B$, $\cos \Delta B \doteq 1$, and expressions with $(\xi\eta)^2$ are neglected. Then

$$\delta_{4\ \text{pol}} = \frac{(1+R_T)^2\ \Delta B + \xi\eta R_T^2\ \Delta R}{(1+R_T)^2 + \xi\eta R_T^2 (1-R_1R_2) \sin (2B_1 + \Delta B)}. \qquad \text{(II-5-20)}$$

The worst case is again occurring at $B_1 + \frac{\Delta B}{2} \doteq 45°$. Furthermore, since the term varying with B_1 is multipled by $\xi\,\eta$ and both are small, the term (in the denominator) may be neglected. Then

$$\delta_{4\ \text{pol max}} \doteq \Delta B + \xi\,\eta\,\frac{R_T^2}{(1+R_T)^2}\,\Delta R\ . \qquad \text{(II-5-21)}$$

The different cases of polarization errors are summarized in Table II-5-1.

Table II-5-1

POLARIZATION ERRORS

Polarization		Approximate Expression for an Estimate of the Maximum Error
Signal Transmitted from Ground	Satellite Antenna	
LP	LP	0
$\doteq$ CP	LP	$\frac{2R_T}{(1+R_T)^2}\,\Delta B$
LP	$\doteq$ CP	$\frac{\Delta R}{2} + \Delta B$
$\doteq$ CP	$\doteq$ CP	$\Delta B + \frac{R_T^2}{(1+R_T^2}\,\Delta R_i$

The polarization errors can be calibrated out to a large degree. If the interferometer is illuminated from a CT, this will result in a phase error $\delta_{\text{pol CT}}$. The same or a very similar error $\delta_{\text{pol B}}$ will be made when the interferometer is illuminated from a beacon. It is the difference which will not be calibrated out. This difference, called the residual phase error, is shown in Table II-5-2 for worst cases. Different cases of polarization calibration signals and beacon signals are considered.

Table II-5-2

RESIDUAL POLARIZATION PHASE ERROR (WORST CASES)

Polarization			Approximate Expression for the Residual Phase Error	Numerical Estimate	Case
Satellite	Calibration Station	Beacon			
LP	LP	LP	0	0	1
	LP	CP	$\frac{\Delta R}{2} + \Delta B$	5°	2
	CP	CP	0	0	3
CP	LP	LP	0	0	4
	LP	CP	$\frac{1-R_T}{1+R_T}\Delta B + \xi\eta\frac{R_T^2}{(1+R_T)^2}\Delta R$	0.9°	5
	CP	CP	$\frac{R_T^2}{(1-R_T)^2}\Delta R\left\{\xi_\epsilon\eta_\epsilon - \xi_B\eta_B\right\}$	0.1°	6

To obtain the numerical estimate of the error shown in the table, certain assumptions about the angle difference ΔB, the axial ratios, and the angles ξ and η were made. It was previously assumed that ξ and η are, at most, 10 deg. Consequently, when the difference between a calibration transmitter and a beacon occur, i.e., the expression $(\xi_\epsilon \eta_\epsilon - \xi_B \eta_B)$, the maximum difference will be taken. For R_T values were assumed which yielded the worst estimate; this is $R_T = 0.5$, case 5, and $R_T = 1$, case 6.

It is further assumed that the satellite antennas are turnstiles of the short backfire antenna fed by phase shifters. The phase shifter stability is ± 1.5 deg electrical phase and a maximum of 0.5 dB amplitude difference. With these assumptions, $\Delta B = 2°$ and $\Delta R = 0.1$ are reasonable values, and the numerical values shown in Table I-5-2 are obtained.

In choosing polarization for the antennas in the system, it must be observed that at least at one end of the link, the antennas must be circularly polarized. With this consideration, only cases 3, 4, and 6 of Table II-5-2 are practical

choices. Cases 3 and 4 show no error, but an undesirable 3-dB polarization loss (LP to CP) will occur. It can be seen from subsection II-1.5 that a 3-dB loss in the link would increase the rms random noise error by 0.2 deg.

Hence, case 6 for which the satellite, the ground CT, and the beacons are circularly polarized, is recommended. Total errors in the system are minimized by this choice. Furthermore, this choice may further reduce the multipath error, since the repeated multipath signals have a sense of rotation which is opposite to the direct signal. This provides additional discrimination against multipath.

Section II-6

ANTENNA ELEMENT SELECTION

An important part of the interferometer is the antenna element. This element must have suitable coverage and phase center characteristics sufficiently independent of orientation to minimize errors. Many candidate antennas were considered. This section discusses each and gives the rationale for the optimum antenna element choice.

II-6.1 ANTENNA ELEMENT REQUIREMENTS

Table II-6-1 lists requirements for the interferometer elements. Circular polarization was chosen to match reception from a variety of ground emitters and to provide for multipath suppression. How well the elements approach the ideal of exactly circular polarization is characterized by the ratio of the minor to major axis of the polarization ellipse, by the axial ratio, and by the tilt angle of the major axis of the polarization ellipse. Since the interferometer measures phase angle differences, the requirements have been placed on the tracking of the axial ratios and tilt angles of any pair of antennas over the field-of-view and frequency band. Differences in polarization which do not vary over the field-of-view can be calibrated out. The polarization tracking requirements given will limit the phase error due to polarization mismatch effects to less than 0.1 deg for the preferred approach.

The phase center of a transmitting antenna is defined as the point from which the far field spherical wavefronts appear to emanate. By reciprocity, when the antenna is used as a receiving element in a 2-element interferometer, the phase difference is measured between the two phase centers. The phase center position is a function of the antenna angle of illumination. Only in the main beam

Table II-6-1

INTERFEROMETER ANTENNA ELEMENT REQUIREMENTS

Polarization

Type: Circular

Axial Ratio Tracking: Within $\pm$0.25 dB over 22° Field-of-view (FOV) and Over the 0.001% Frequency Band

Polarization Ellipse Tilt Angle Tracking: Within $\pm$2° over FOV and over the 0.001% Frequency Band

Phase Center

Tracking of Phase Centers Over FOV: Within 0.2°

Gain and Beamwidth

Beamwidth (3dB) = 22° minimum

Gain (with Respect to a Circularly Polarized Isotrope) = 17.5dB minimum

Mutual Coupling at 3λ Spacing: -50 dB minimum

VSWR Less than 1.2:1

Configuration

Readily Integrated into System and Requiring Minimum Unfurling

Size and Weight

Size: Minimum

Weight: 2 lbs maximum

Materials

Space qualified

of the antenna is its position reasonably stationary. For the interferometer, the important requirement is that the phase centers of any pair of antenna elements track over the field-of-view and over the 0.001 percent frequency band. This tracking is facilitated if the phase center location is relatively constant over the field-of-view.

The 3-dB beamwidth of the antenna must be wide enough to give full Earth coverage from synchronous altitude (17.5 deg) plus an allowance for the motion of the boom tips. From Section I-7, the maximum tip motion is ± 1 deg. Using a margin of ± 1.25 deg, the 3-dB beamwidth was chosen as 22 deg. The optimum beamwidth is a compromise between a wide beam (low gain), which gives wide field-of-view and good phase center and polarization tracking, and a narrow beam (high gain), which gives higher received signal. In lieu of such a detailed tradeoff, the simple field-of-view method was used. Assuming an 60 percent antenna efficiency, the antenna gain requirement is

$$G = \frac{42,255}{\theta_{3dB}^{2}} (0.6) = 17.5 \text{ dB} \qquad \text{(II-6-1)}$$

with respect to a circularly polarized isotrope (θ_{3dB} is the 3dB antenna beamwidth).

Mutual coupling between antenna elements can cause a phase error that varies over the field-of-view. The maximum phase error is $\Delta\gamma_m = 2\sqrt{C}$ rad, where C is the mutual coupling factor between the antennas. To reduce the phase error due to mutual coupling to less than 0.1 deg, $C \leq -55$ dB.

The voltage standing wave ratio (VSWR) requirement guarantees that small changes in the impedance match of the antenna will not produce large phase errors. Since the mismatch will not vary over the field-of-view, mismatch phase errors can be calibrated out. The VSWR requirement is therefore not stringent.

The requirements on configuration, size and weight, and materials are determined by the general requirements of the spacecraft and its environment.

II-6.2. CANDIDATE ANTENNA ELEMENTS AND THEIR CHARACTERISTICS

A number of different antenna types were identified that conceivably could satisfy the aforementioned requirements for the interferometer antenna elements. These candidate antennas fall into two general classes: aperature antennas and end fire antennas. The following subsections analyze each candidate.

II-6.2.1 Backfire Antenna

The backfire antenna [13], as shown in Figure II-6-1, is a leaky cavity resonator formed by two circular planar reflectors of unequal diameter which are spaced $n \frac{\lambda}{2}$ apart. Energy is injected into the cavity by a dipole feed and is confined to the cavity axis by a Yagi-type surface wave structure.

The gain of this antenna is proportional to the length of the surface wave structure and, up to a limit, to the diameter of the large reflector. The gain can be increased beyond the maximum obtainable with a flat reflector by using a stepped reflector as shown in Figure II-6-2. Zucker 14 shows that the gain of the backfire antenna with the stepped reflector is

$$G = 60 \frac{L}{\lambda} . \qquad \text{(II-6-2)}$$

For a backfire antenna with a flat reflector, the gain is about 2.5 dB lower, or

$$G = 33.7 \frac{L}{\lambda} .$$

Using a 60 percent aperature efficiency, the 3-dB beamwidth is

$$\theta_{3dB} = \frac{159}{\sqrt{G}} .$$

Table II-6-2 lists the gains and beamwidths for the flat and stepped reflectors. It can be seen that the 1.5λ long flat reflector antenna comes closest to the desired 22 deg beamwidth. It has a gain of 17.1 dB.

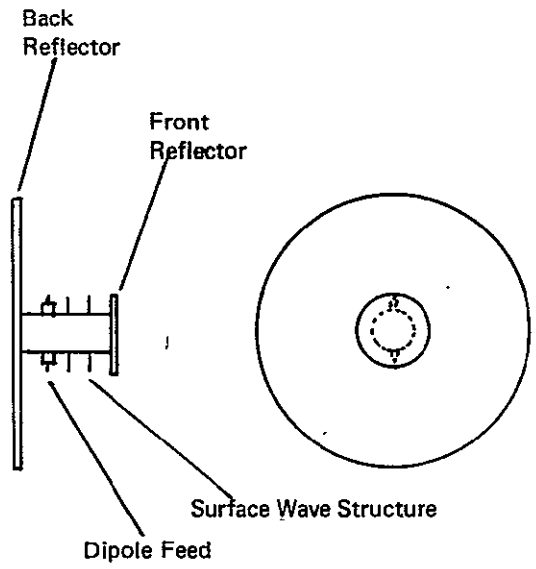

Figure II-6-1. Backfire Antenna with Flat Reflector.

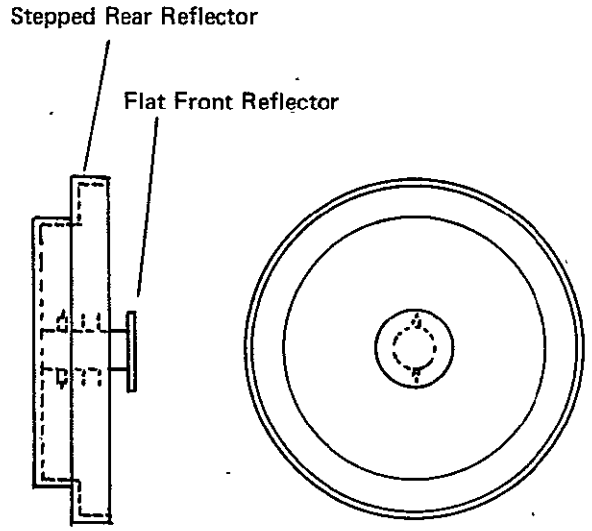

Figure II-6-2. Backfire Antenna with Stepped Reflector

Table II-6-2

GAIN OF BACKFIRE ANTENNAS

Length (wavelengths)	Backfire with Flat Reflector		Backfire with Stepped Reflector	
	Gain (dB)	Beamwidth (deg)	Gain (dB)	Beamwidth (deg)
0.5	12.3	38.8	14.9	29.1
1.0	15.3	27.5	17.8	20.6
1.5	17.1	22.4	19.6	16.8

The short backfire antenna can be circularly polarized by using a crossed dipole (turnstile) feed antenna. Since the cavity is circularly symmetrical, an excellent axial ratio is achievable.

Measurements were made on a simple model of the backfire antenna to determine its phase center and mutual coupling characteristics. This model was 0.5λ long and had a 2λ diam, with a linearly polarized dipole feed. Figure II-6-3 shows the measured E- and H-plane radiation patterns and phase patterns. It was found that the phase center is constant over the 3dB beamwidth and is in the same location in both the E- and H-planes. The measured mutual coupling between two antennas about 3λ separated on centers was -60 dB.

II-6.2.2 Corner Reflector

By tilting the dipole feed in a corner reflector, a circularly polarized beam can be generated.[15,16] The gain obtained from such an antenna is limited to about 8 dB above a CP isotrope. Therefore this antenna was not considered further.

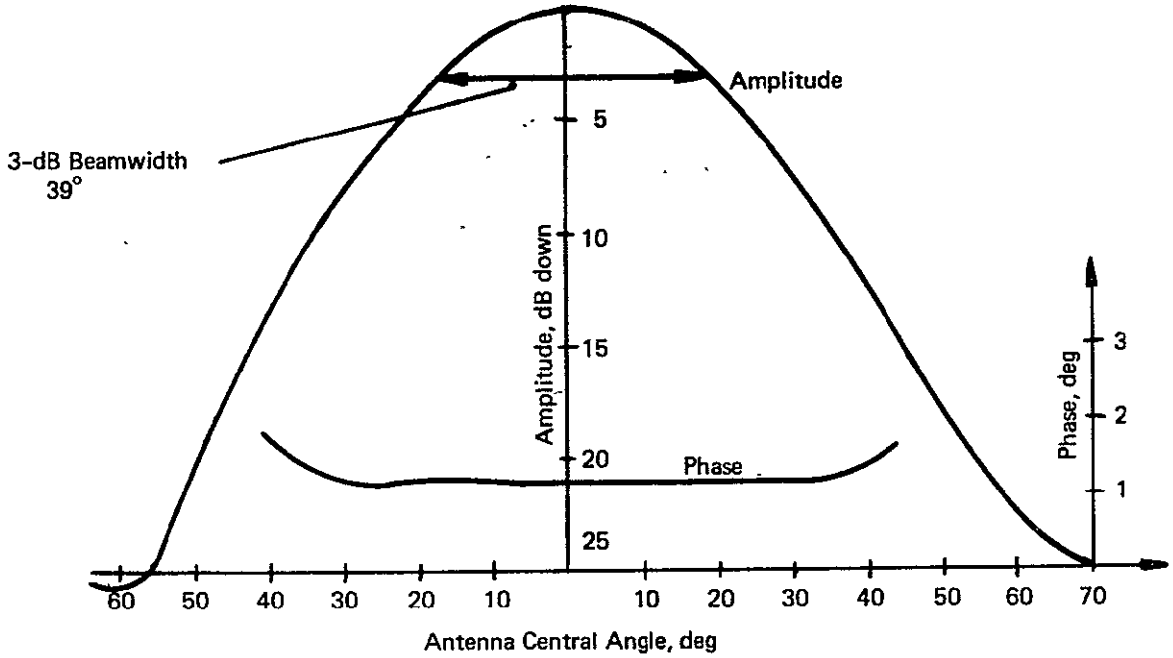

(a). E-Plane Pattern and Phase Characteristic.

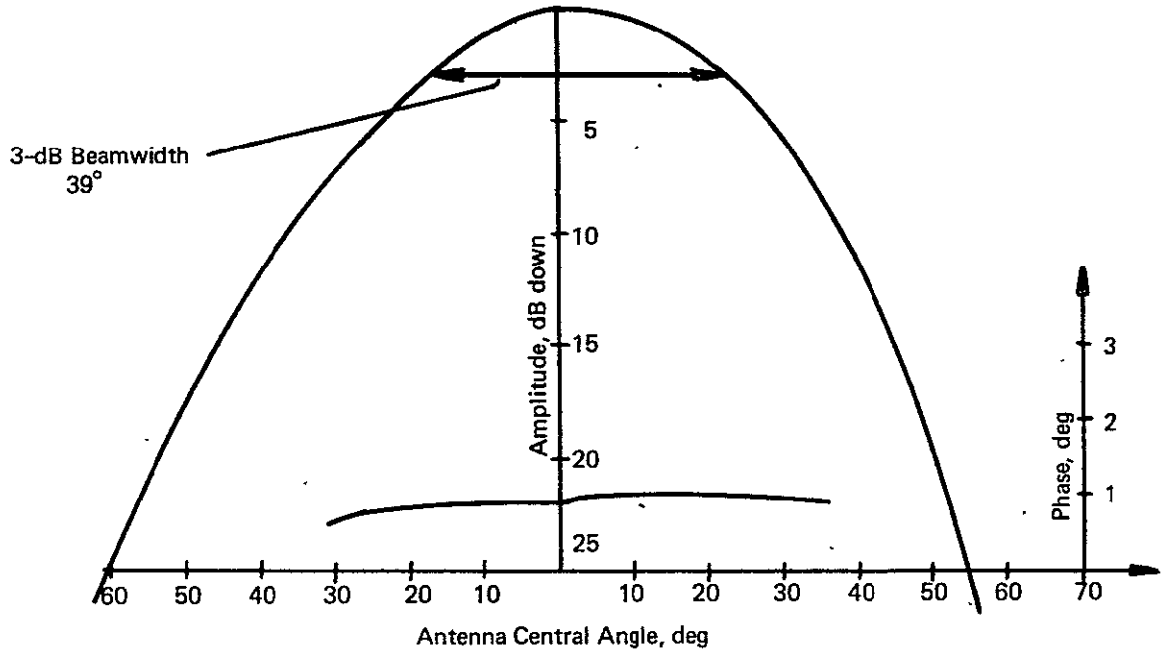

(b). H-Plane Pattern and Phase Characteristic

Figure II-6-3. Short Backfire Antenna Characteristics

II-6.2.3 Turnstile Array

The turnstile array consists of a square array of turnstile (crossed dipole) elements mounted on a ground plane. The individual elements are fed in phase by a corporate feed network.

Table II-6-3 shows the number of elements necessary to achieve a 22 deg x 22 deg beam. By using a 4 x 4 element array and making the spacing between the elements somewhat larger than 0.5λ, the desired beamwidth can be obtained. Using a 4 x 4 array also has the advantage of a fairly simple corporate feed, since it can then be implemented with hybrid-type power dividers.

Table II-6-3

THREE-dB BEAMWIDTH OF BROADSIDE HALF-WAVE DIPOLE ARRAY WITH HALF-WAVE SPACING BETWEEN DIPOLES (Ref. 17, p. 622)

No. of Elements	Beamwidth (3 dB) (deg)
2	52.5
3	34.3
4	25.6
5	20.4

An exact calculation of the array gain is difficult since the mutual impedances among all the elements must be taken into account. An estimate of the array gain can be made by using the available results for the gain of square arrays and the gain of each element as follows:

$$G = G_e G_a \qquad \text{(II-6-3)}$$

G = gain of turnstile array

G_e = gain of individual turnstile

G_a = gain of array of isotropic elements.

The gain of a half-wave dipole spaced a quarter wave above a ground plane is[18]

$G_e = 7.2.$

The gain of a broadside square array of 16 half-wave dipoles with half-wave interelement spacing is 14 dB.[19] Subtracting the dipole gain of 2.1 dB, $G_a = 11.9$ dB. Therefore

$G = 11.9 + 7.2 = 18.7$ dB.

This result is probably too high, since some of the impedance interaction between the elements has been neglected. For example, Diamond [20] shows that the gain of the center turnstile of a 7-element linear array is only 3 dB. There is also a change in the axial ratio of the turnstile element when it is arrayed. [20]

II-6.2.4 Spiral and Conical Helix

The spiral antenna consists of a pair of conductors each of which is shaped in a plane equiangular spiral. A travelling wave is excited on each conductor by the balanced feed, and radiation occurs from the conductors in the region where the circumference of each conductor is about 1 wavelength. The spiral is mounted on a $\frac{\lambda}{4}$ deep cavity to produce unidirectional radiation. The gain of the spiral is only about 5 dB, and the 3-dB beamwidth is about 60 deg. The spirals would have to be used in an array to achieve the desired gain and beamwidth. The on-axis axial ratio of the spiral remains less than 1.7 dB for angles from boresight to 70 deg-off boresight.[21] The phase center is approximately a rad behind the plane of the spiral, where a is the growth rate of the spiral. The phase center versus angle characteristic is fairly flat.[22]

The conical spiral consists of spiral conductors on the surface of a truncated cone. The gain is about 5 dB (with respect to a CP isotrope).[23] The axial ratio is less than 0.5 dB on axis, and less than 1.4 dB up to 50 deg off axis.[24] The phase center versus angle characteristic is fairly flat.[25] It has been found, however, that the phase center position is somewhat sensitive to the axial ratio of the illuminating wave.[25]

II-6.2.5 Helical Antenna

The helical antenna consists of an n turn helical conductor in front of a ground plane. If the circumference of the helix is about 1 λ, the antenna will radiate a circularly polarized beam in the direction of the axis of the helix.

The 3-dB beamwidth of the helical antenna is [26]

$$\theta_{3dB} = \frac{52}{\frac{C_a}{\lambda}\sqrt{\frac{nS}{\lambda}}}$$

$\frac{C_a}{\lambda}$ = circumference of each turn in wavelengths

$\frac{S}{\lambda}$ = pitch of each turn in wavelengths

n = number of turns.

Assuming a 1λ circumference and a 22 deg beamwidth, $\frac{nS}{\lambda} = 5.55$. Using a pitch angle of 12.5 deg, $\frac{S}{\lambda} = 0.222$ and $n = 25$. The gain of the helical antenna is

$$G = 15\left(\frac{C_a}{\lambda}\right)^2 n\frac{S}{\lambda} = 83.4 = 19.2 \text{ dB}.$$

The length of this helix for operation at 1.6 GHz is 41 in. This length would be rather difficult to support rigidly, so a 4-helix array would be preferable.

The directivity of a 4-element array of isotropes with half-wave spacing between the elements is 6 dB. Therefore the helix gain need only be 13 dB. The length of the helix element $n\frac{S}{\lambda}$ need only be 1.33 λ or 9.8 in., and the helix would have six turns.

The polarization axial ratio R of a helical antenna element is approximately

$$R = \frac{2n+1}{2n}. \qquad \text{(II-6-5)}$$

For a 6-turn helix

$$R = 1.08 = 0.4 \text{ dB}.$$

An axial ratio this low is seldom realized in an actual helical antenna due to undesirable mode currents propagating on the helix. However the axial ratio can be considerably improved by using a conical helix shape at the input and output end of the helix.[27]

The axial ratio of the helix depends critically on the circularity of each turn of the helix. By making the turns slightly elliptical, the axial ratio can be improved.

The most serious deficiency of the helical antenna is the fact that its polarization axial ratio is a function of the angle off axis. The helix axial direction is not a direction of polarization stationarity (Ref. 28, pp. 188-192). Figure II-6-4 depicts this angular dependence.

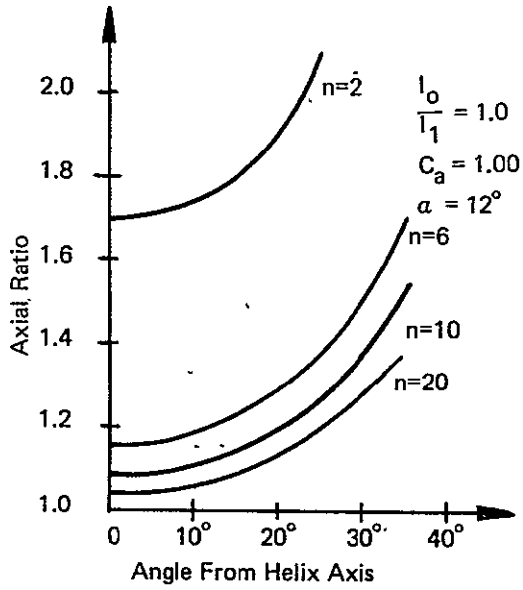

Figure II-6-4. Angular Dependence of Helix Antenna Axial Ratio

Polarization tracking between antennas will be more difficult with a helix antenna than with an antenna which has a stationary polarization versus angle, such as a spiral or turnstile antenna.

Measurements have been made on the phase center location of the helix as a function of the helix parameters,[29] but no data is available on the measured phase center as a function of angle of illumination off axis. Calculations have been made [30] which show that the phase center moves axially towards the reflector as the illumination angle increases off boresight.

II-6.2.6 Yagi-Uda Antenna

The Yagi antenna consists of a linear end fire array of dipole elements. One dipole is the driver, and the director elements are excited by the surface wave that travels along the array. A reflector element is placed about 0.25λ behind the driver half-wave dipole, so that the surface wave propagates in the end-fire direction along the director elements. The director elements are about 0.43λ long and are spaced about 0.39λ apart. To obtain circular polarization, crossed dipole elements can be used.

The gain of the Yagi is proportional to the length of the array or the number of director elements. An analysis of Wolf's directivity curve[31] shows that the gain is

$$G\,(\mathrm{dB}) = 10.2 + 4.7 \log \frac{\ell}{\lambda} . \qquad \text{(II-6-6)}$$

For 17 dB gain, $\frac{\ell}{\lambda} = 28.2$. At 1.6 GHz, the length is 209 in., which is prohibitively long. By using a square array of four Yagis, the element gain need only be 11 dB, and the Yagi is then only $1.5\ \lambda$ long or 11 in.

The beamwidths of the Yagi are nearly symmetrical (Ref. 17, Sect. VI.6), the axial ratio should be good. No information is available on the phase center.

Table II-6-4

CHARACTERISTICS OF THE CANDIDATE ANTENNA ELEMENTS

	Antenna	Axial Ratio Tracking	Phase Center Tracking	Gain and Beamwidth	Mutual Coupling	Size and Weight	Comments
Aperture Antennas	Backfire	Good	Good	Favorable	Satisfactory	Light	Chosen antenna element
	Corner Reflector	Fair	?	Low, requires arraying	Probably satisfactory	Heavy	
	Dipole Array	Fair	Poor		Probably satisfactory	Heavy	
	Spiral and Conical	Good	Good	Low, requires arraying	Probably satisfactory	Light	
Endfire Antennas	Helix	Fair	Fair	Low, requires arraying	Probably satisfactory	Light	Single element too long for required gain
	Yagi-Uda	Fair	?	Low, requires arraying	Probably satisfactory	Heavy	Single element too long for required gain

II-6.3 SELECTION OF OPTIMUM ANTENNA

Table II-6-4 summarizes the characteristics of the various antennas. Of the candidate antennas, only the backfire antenna has the desired gain without arraying. While it is possible to get the desired gain from the helix or the Yagi, the length of these antennas for high gain is prohibitive since it would be difficult to achieve the requisite mechanical stability. Array antennas, whether they be of helices, Yagis, spirals, or turnstiles, have the disadvantage of needing a feed network. This feed network increases the antenna weight, and introduces more complexity, since the feed network must provide and maintain equi-phased signals to each array element.

The backfire antenna achieves its high gain in a small size by utilizing the gain of the surface wave structure twice as well as the gain of the 2-reflector structure. Since it also has excellent axial ratio and phase center characteristics, it was chosen as the optimum antenna element.

II-6.4 MECHANICAL/THERMAL DESIGN

Figure II-6-5 illustrates a layout of the circularly polarized backfire antenna. The baluns to drive the crossed dipoles are built into the cylindrical post supporting the two reflectors. The two orthagonal baluns are driven from a hybrid network which produces a pair of 0 deg and 90 deg phased outputs. The 90 deg phase difference, when applied to the dipoles, produces the circular polarization.

The important factors in the mechanical design are to maintain both reflectors flat and parallel. This is accomplished with the ribbed support structure on both reflectors.

Since the structure is symmetrical, temperature changes should produce equal effects on the orthagonal dipoles and the baluns. Therefore no degradation in phase shift should occur. The 90 deg hybrid can maintain a ± 0.25 dB amplitude balance and ± 2 deg phase balance over a wide temperature range.

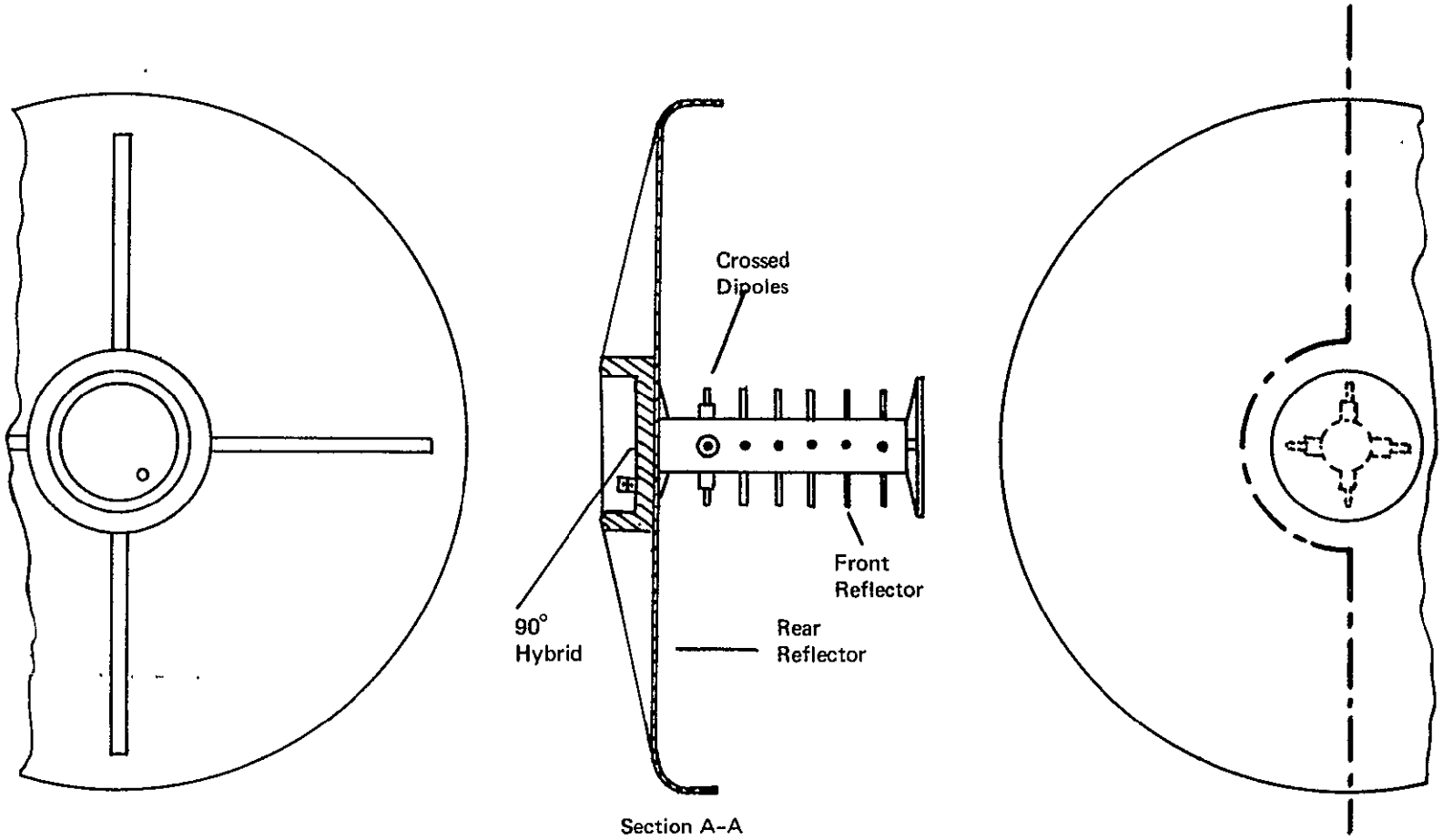

Figure II-6-5. Backfire Antenna

Section II-7

MECHANICAL STUDIES

To create a long baseline, the interferometer antennas must be mounted to an extendible structure, which is deployed to its full length once the satellite is in orbit (see Figure II-7-1). Two candidate structures, the Astrocolumn and the Fairchild Hiller TEE (tubular extendible element) were considered for this purpose.

The baseline is a line connecting the phase centers of the antennas mounted to the tips of a set of interferometer booms. In this feasibility study, it is the motion of this baseline that is of paramount importance, and factors affecting this motion, such as the environment, the Attitude Control System (ACS), boom configuration, mechanical properties, and electronic package weight (tip weight), were considered. The baseline length of 75 m or 228 ft required by the experiment precludes the use of a rigid system. Thus, the bending of the interferometer booms due to environmental factors will cause the baseline motion.

Since phase measurement requires time, it was necessary to limit the rate of baseline motion. Somewhat arbitrarily it was decided that the baseline should not rotate more than 0.001 deg in space within a tracking time interval of 1 s. This angle corresponds to a 2km position change at a 20 deg elevation angle. Furthermore, the total deviation from a nominal position was limited in that the baseline must be tangential to the earth's surface within ± 2.0 deg.

The important parameters considered in evaluating each of the two candidate structures the Astrocolumn and tubular extendible booms are:

a. Stiffness—Desire the boom to be stiff or as rigid as possible since the deflections due to the environment are a function of the product of the modulus of the material's elasticity and the configuration area moment of inertia, and it is desired that these deflections be small.

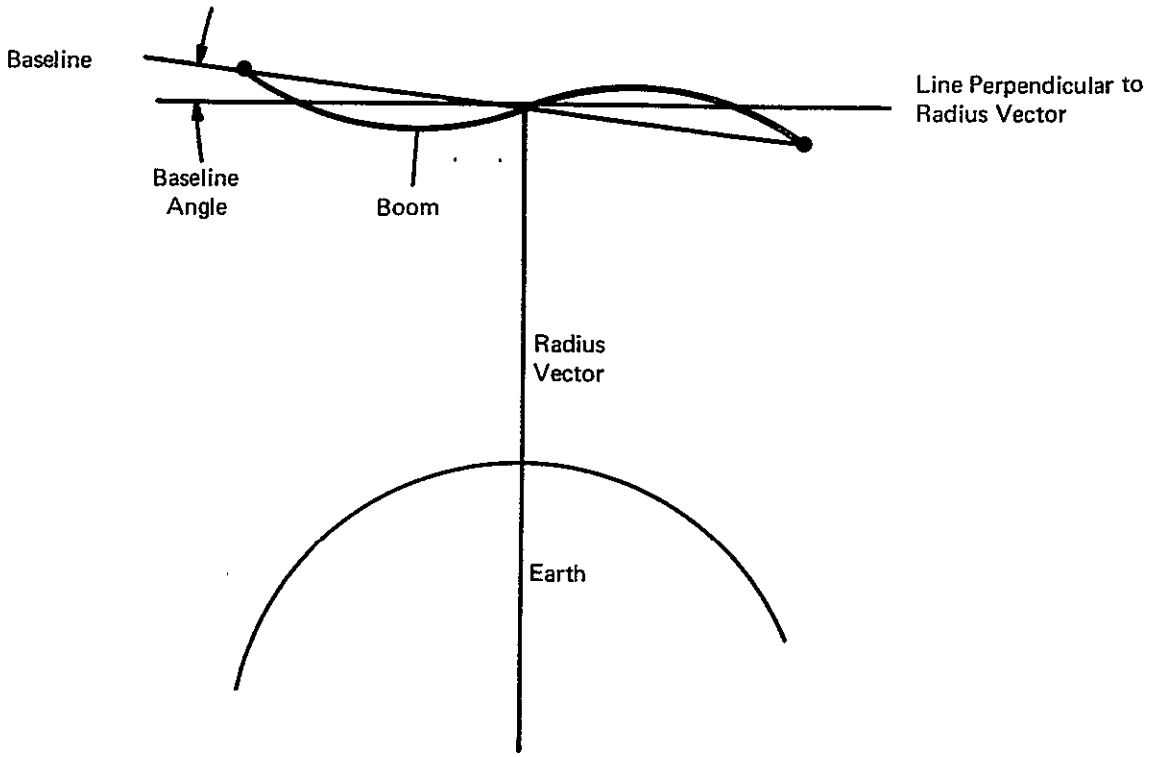

Figure II-7-1. Baseline Definition

b. Vehicle Natural Frequency—Desire the frequency of the baseline motion to to be low, for this implies a long period of oscillation with low velocities for the baseline. However, as was mentioned above, high stiffness is desired for small deflection. Unfortunately, these goals are contradictory, since frequency increases with an increase in stiffness.

c. Boom Length—The maximum interferometer antenna baseline separation was initially assumed to be on the order of 100 wavelengths at 400 MHz. This means that a tip-to-tip length of about 246 ft is required; each boom would then be approximately 120 ft. This length was not appreciably changed during the study.

d. Boom Material Characteristics—Because of weight considerations, the incentive is to have as small of a weight per unit length as possible. Frequency, however, increases as this parameter decreases. It is also important that the magnetic properties of the material not cause a moment which would adversely affect the ACS. Furthermore, the ratio of the coefficient of the thermal expansion to thermal conductivity must not be too large so as not to cause intolerably large thermal deflections.

e. Thermal Properties of the Boom—Low fluctuations in temperature are desired, especially in the case of shadowing. Also, because of baseline length changes the requirements exist to limit the longitudinal thermal expansion of the boom.

f. Boom Interferometer Antenna Package—Desire that the packaged boom have low weight, be contained in a small volume, and be within the present state-of-the-art.

II-7.1 CANDIDATE ELEMENT DESCRIPTION

The two condidate elements considered are described below.

a. Astrocolumn—The Astrocolumn is a deployable lattice structure. A typical version consists of three longitudinal members, intermittently connected by battens, and which form a triangular cross section. Small diameter steel cables diagonally connecting adjacent sets of battens provide torsional stiffness. The continuous flexible longerons are made of glass fiber. When in the packaged condition, the longerons are helically coiled, with the battens stacked on top of one another.[32]

b. Tubular Extendible Elements (TEEs)—Fairchild Hiller's Tubular Extendible Element (TEE) is a thin metal strip that is spool-wound as a tape during storage, but upon release forms automatically into tubular shape. An extendible element can be deployed by use of a simple device, such as the spool-stored self-extending TEE, or a motor, such as that utilized in the RAE spacecraft (Explorer 38) to deploy 750 ft of element.

A typical motorized mechanism consists of an element storage reel, a motor, a gear or belt drive train, element guide supports, element extend and retract limit switches, and element extended length readout instrumentation—all housed within a lightweight support structure.

Two TEE configurations were investigated: the Edgelock, which is characterized by a 1-piece tape with scalloped edges which interlock upon deployment, and the Hingelock, which is characterized by two separate tapes permanently joined along their edges in a tab-slot hinge line. Figure II-7-2 shows these two configurations and Table II-7-1 presents the properties of the various booms.

Table II-7-1

BOOM PARAMETERS

System	Material	Diameter (in.)	EI(lb. $in.^2$)	lb/ft	Estimated Size for 120 ft. Length in. x in. x in.
Edgelock TEE	BeCu	1/2	2,000	0.0151	13 x 3 x 4
Hingelock TEE	BeCu	1	26,000	0.0644	11 x 12 x 4
Astrocolumn (Flexible Longeron)	Glass Fiber	3	37,200	0.02	48 x 3 x 3
Astrocolumn (Flexible Longeron)	Glass Fiber	6	163,000	0.0636	60 x 6 x 6

The values of EI for the Astrocolumns were obtained by using a design formula received from Astro Research Corporation by telephone call.

As part of this concept study, a preliminary estimate of the package size for 120 ft boom length was made. An estimate of the package size for a 3- and 6-in, flexible longeron Astrocolumn was made based on information obtained from an Astro Research Corporation brochure.

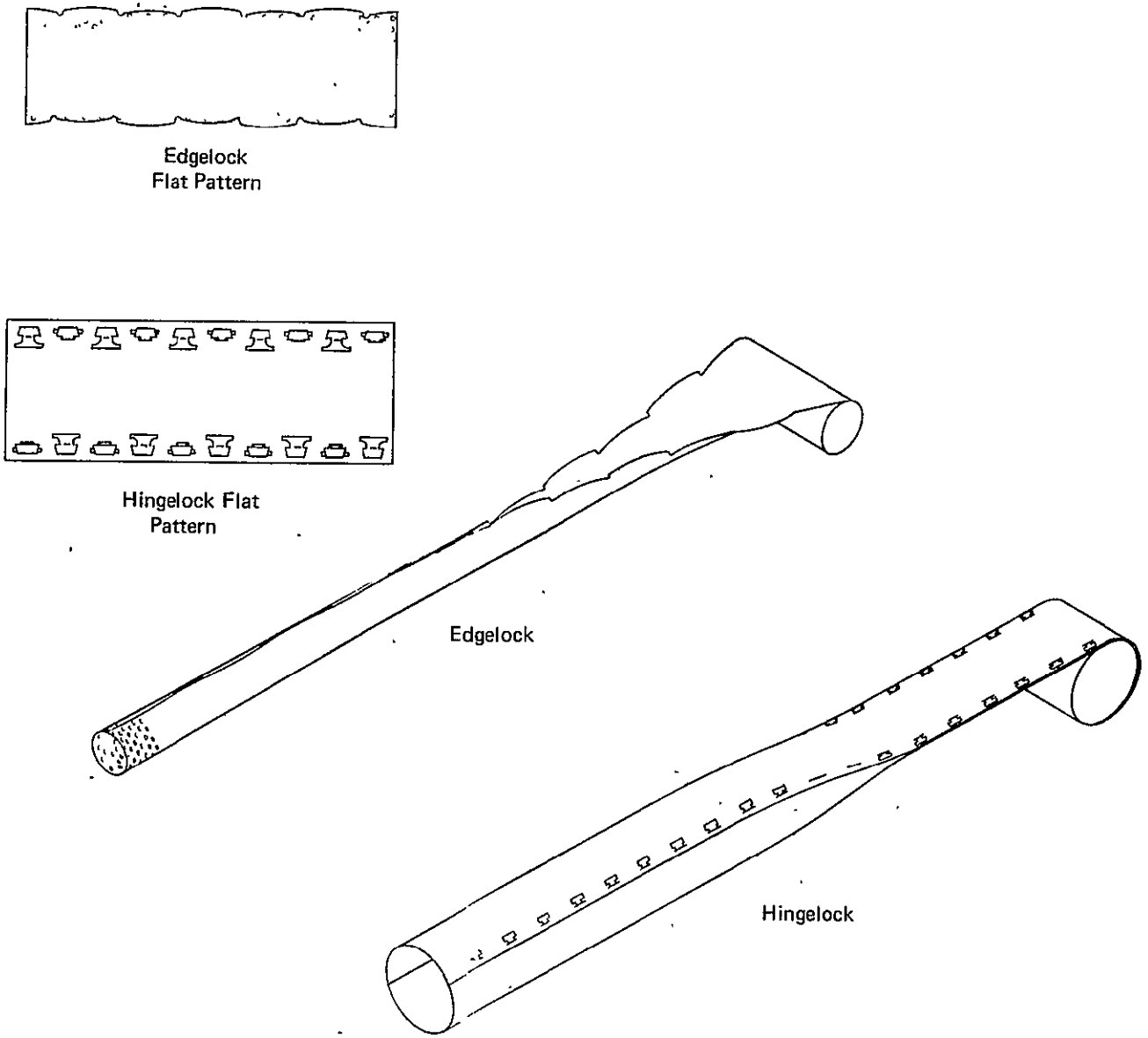

Figure II-7-2. Boom Configuration

Table II-7-1 includes the estimated package size for a 120 ft boom length. For example, for the 0.5 in. Edgelock, a volume of 156 cubic in. is required. For a 3-in. Astrocolumn, a volume of 432 cubic in. is required.

II-7.2 ENVIRONMENTAL EFFECTS

The shape of the bending modes is of greatest importance in determing the limits of the antenna baseline rotation. As it can be seen from Figure II-7-3, the antisymmetric bending mode (B) will rotate the baseline while the symmetric mode (A) merely translates the baseline and therefore, theoretically, does not affect the determination of the balloon beacon's locations.

Both the symmetric bending mode and the antisymmetric bending mode are affected by the system environment. The symmetric bending mode is affected by solar pressure and aerodynamic drag, while the antisymmetric bending mode is affected by gravity gradient. Thermal variations produce deflections mostly of a symmetric nature with the maximum "out-of-plane" bending being less than 10 percent of the "in-plane" bending. Maneuvers will produce both symmetric and antisymmetric bending. A detailed analysis of the magnitudes of these effects is given below. An extreme condition was defined to be a 200 ft long, 0.5 diam. Edgelock TEE.

II-7.1 Tip (maximum) Deflection due to Solar Pressure

$$\delta_{max} = \frac{PrL_o^4}{4\,EI}, \qquad \text{(II-7-1a)}$$

where

P = solar pressure, $4 \times 10^{-7} \frac{lb}{ft^2}$ for a reflective surface

II-7.2.2 Tip Deflection due to Aerodynamic Drag

$$\delta_{max} = \frac{PrL_o^4}{4\,EI}, \qquad \text{(II-7-1b)}$$

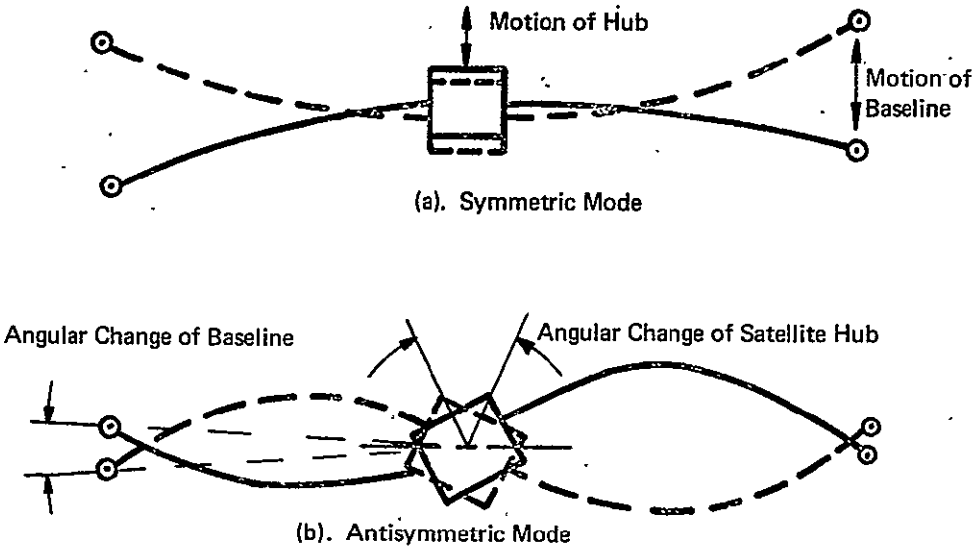

Figure II-7-3. Satellite Dynamics

where

$$P = \text{dynamic pressure, } 1/2\ \zeta_a V_a^2 C_D, \quad 1.4 \times 10^{-8} \frac{lb}{ft^2}$$

at 20,000 mile synchronous altitude.

For the case defined above, the magnitudes of the above two symmetric deflections are:

Solar pressure: 0.24 ft or 7.3 cm

Aerodynamic drag: 0.0084 ft or 2.5 mm

II-7.2.3 Tip Deflection due to the Lateral Force Induced on an Antenna due to Gravity Gradient

The gravity gradient will deflect a boom with a tip mass by

$$\delta_{max} = \frac{K_{gg}}{EI}\left\{\frac{ML_o^4}{3} + \frac{11}{120}\ mL_o^5\right\} \sin 2\theta\ . \qquad \text{(II-7-2)}$$

Calculations have been performed which indicate that, for the extreme condition defined above with a 15-lb tip weight, a gravity-gradient deflection of 0.148 ft (4.5 cm) or an angular deflection of the baseline of 0.0424 deg would occur if the baseline was rotated 45 deg out of a plane tangential to earth's surface.

II-7.2.4 Thermal Bending

The thermal deflections encountered in space will be nearly symmetric and therefore, will not affect the baseline greatly. Figure II-7-4 is a sketch of a state-of-the-art configuration of an interlocked TEE. Figure II-7-5 shows the effect of the solar windows (perforations) on thermal bending. As the area of the solar windows increase, the thermal deflections decrease. It is theoretically possible to perforate the interlocked booms to minimize thermal bending, since no diametric thermal gradient exists across the boom.

This occurs when the area of the perforations (which is equal to the exposed area of the boom side facing away from the sun) times the absorptivity of the inner surface is equal to the remaining boom area times the outer surface absorptivity.

II-7.2.5 Longitudinal Thermal Expansion

If the boom is originally heated by the sun and suddenly is plunged into the dark either by Earth shadowing or satellite shadowing, a temperature variation will occur. The boom will undergo a change of length which will affect the baseline separation. This phenomenon will occur twice a year for about 75 min maximum in the case of Earth shadow for a synchronous satellite.

The energy equation for this phenomenon is

$$\nabla^2 T + \text{N.I.} = \zeta C_p t \frac{\partial T}{\partial \tau} \qquad \text{(II-7-3)}$$

where

$\nabla^2 T = 0$, since the temperature does not depend on where any element is in space and

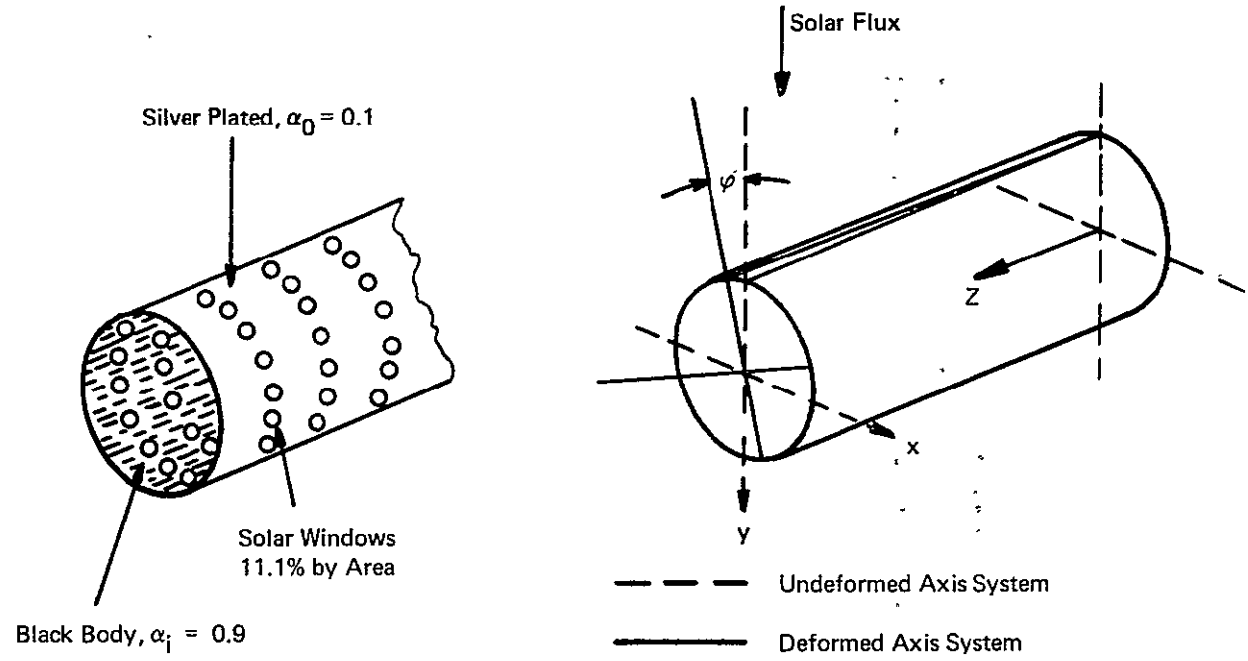

(a). Perforations for Temperature Control

(b). Coordinates for Thermal Twist Analysis

Figure II-7-4. Thermal Deflections

N.I. = Net Input, which represents all incoming energy minus all energy leaving the system and equals $-\epsilon_o A_s \sigma T^4$.

Collecting terms and realizing that the temperature depends only on time yields

$$-\epsilon_o A_s \sigma T^4 = \rho C_p \frac{t\, dT}{d\tau} \quad . \qquad \text{(II-7-4)}$$

t = wall thickness

As an example, consider that a beryllium copper 0.5 in. Edgelock TEE of 120 ft length, silver plated, with a 0.002 in wall thickness which has an initial mean temperature in the earth vicinity space environment of 234° F is suddenly thrust into darkness. The temperature variation is found as follows:

$$\frac{dT}{T^4} = \frac{\epsilon_o A_s \sigma}{\rho C_p t}\, d\tau \quad .$$

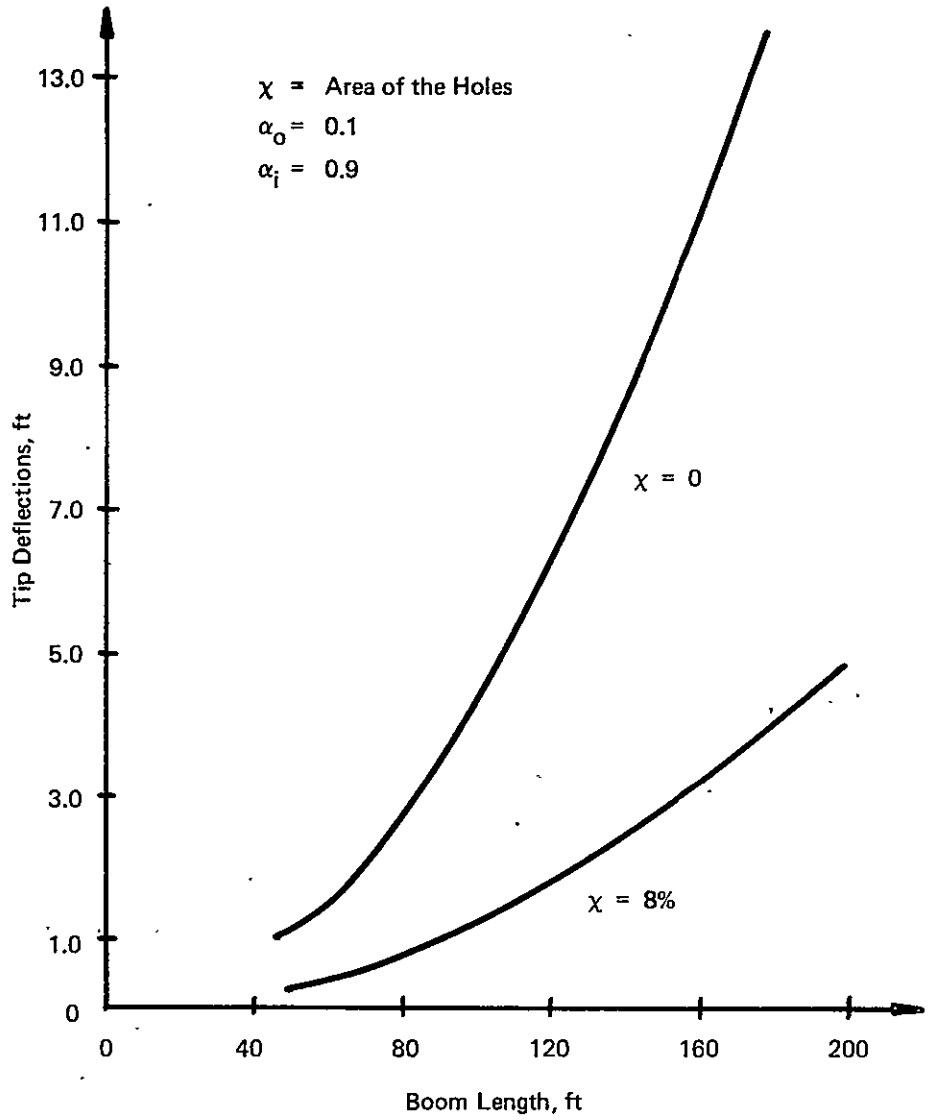

Figure II-7-5. Thermal Deflections of Beryllium-Copper Boom with $\frac{D}{t} = 250\ L$

For beryllium copper the equations are:

$$\epsilon_o = 0.02$$

$$\sigma = 0.1713 \times 10^{-8} \frac{BTU}{ft^2\ hr\ {}^oR^4}$$

$$C_P = 0.1 \frac{BTU}{lb°R}$$

$$\int_{T_i}^{T_f} \frac{dT}{T^4} = -0.6 \times 10^{-8} \tau .$$

For $T_i = 234° = 694°R$, $\tau = 1.25$ h, the final temperature was calculated to be

$$T_f = 354°R = 106°F.$$

Therefore

$$\Delta T = 340°F.$$

The change in the length of the entire baseline will be

$$\Delta L = L_o e_c \Delta T. \qquad \text{(II-7-5)}$$

The change of the length of the baseline separation was calculated to be -9.04 in. (contraction).

The maximum longitudinal velocity occurs where the temperature is the greatest, as follows:

$$\left(\frac{dL}{d\tau}\right)_{max} = - \frac{2L_o e_c \epsilon \sigma T^4 \text{ Max}}{t\zeta \quad C_p} = -2.05 \frac{ft}{h} = \frac{-0.00684 \text{ in.}}{s} . \qquad \text{(II-7-6)}$$

II-7.3 THERMAL TWIST

It has been observed from flight data from various satellites that, while in sunlight, overlapped tubular extendible elements have twisted. During the time when the boom was in the Earth's shadow, twisting was not observed. It has therefore been concluded that a solar or thermal torque must exist which twists the boom. This torque, if it existed on a Hingelock TEE, could twist the booms and move the antennas sufficiently to point them away from earth. Therefore the thermal twist on a Hingelock TEE was examined in detail. The analysis of the thermal twist phenomena is based on the coordinate system shown in Figure

II-7-4. Frisch[33] has investigated the thermal effects on unfurlable booms with respect to bending and twisting. In his work, he gave the thermal torque about the shear center as

$$T_{sc}(z) = -\Lambda t\, E e_c \frac{d\phi}{dz}\left\{ rP\left[e \sin\frac{\psi}{z} + \frac{P}{z}\right]\frac{T_m}{\phi} - \right.$$

$$\left. - \int\left[r + e\cos\left(\frac{s}{r} - \frac{\psi}{2}\right)\right]\int \frac{\partial T(\epsilon, z)}{\partial \phi(z)}\, deds \right. \qquad \text{(II-7-7)}$$

Where Λ is a factor indicating the sense of overlap of the boom.

The expression for the eccentricity e is given by

$$e = \rho\, \frac{\cos\frac{\psi}{2} - \frac{\sin\frac{\psi}{2}}{2}}{\pi + \frac{\psi}{2} - \frac{1}{2}\sin\psi} \qquad \text{(II-7-8)}$$

For the Hingelock boom $e = 0$; for the Edgelock boom $e = 2r$.

As can be seen from the torque equation, an understanding of the temperature distribution is necessary. The temperature distribution for the Hingelock and Edgelock TEEs was obtained through a nodal analysis. This nodal analysis agrees very well with the temperature equations given below. These non-dimensional equations were used to evaluate the thermal torque.

The temperature distribution for a double seam Hingelock TEE is:

$$\frac{T}{\Theta} = -f_1(\theta_s)\cosh\sqrt{B}(\pi - \beta) + f_2(\theta_s)\cosh\sqrt{B}\,\beta +$$

$$+ \frac{(\alpha_o - \chi\alpha_i)}{2(B+1)}\cos(\beta - \theta_s) - \frac{(\alpha_o + \chi\alpha_i)}{8\pi}\sum_{n=1}^{\infty}\frac{(-1)^n\cos 2n(\beta - \theta_s)}{\left(n^2 - \frac{1}{4}\right)\left(n^2 + \frac{B}{4}\right)}$$

$$+ \frac{4(\alpha_o + \chi\cdot\alpha_i)}{\pi B} \qquad o \le \beta \le \pi$$

$$\frac{T}{\Theta} = f_1(\theta_s)\cosh\sqrt{B}(\pi - \beta) - f_2(\theta_s)\cosh\sqrt{B}(2\pi - \beta) + \text{(continued next page)}$$

$$+ \frac{(\alpha_o - \chi \alpha_i)}{2(B+1)} \cos(\beta - \theta_s) - \frac{(\alpha_o + \chi\alpha_i)}{8\pi} \sum_{1}^{\infty} \frac{(-1)^n \cos 2n(\beta - \theta_s)}{n^2 - \frac{1}{4}\ n^2 + \frac{B}{4}}$$

$$+ \frac{4\alpha_o + \chi \alpha_i}{\pi B} \qquad o \leq \beta \leq \pi \qquad \text{(II-7-9)}$$

where

χ = % perforation by area

$\Theta = \dfrac{S\ r^2}{K\ t\ T_{avg}}$

$B = \dfrac{4 \epsilon_o r^2 \sigma T_{avg}^4}{K\ t\ T_{avg}}$

$\sigma\ T_{AV}^4 = \dfrac{(\alpha_o + \chi \alpha_i)\ S}{\pi \epsilon_o}$

$$f_1(\theta_s) = \frac{\left[\dfrac{(\alpha_o + \chi \alpha_i)}{4\pi} \sum_{n=1}^{\infty} \dfrac{(-1)^n\ n \sin 2\ n\ \theta_s}{\left(n^2 - \frac{1}{4}\right)\left(n^2 + \frac{B}{4}\right)} - \dfrac{(\alpha_o - \chi\ \alpha_i)}{2(B+1)} \sin \theta_s\right]}{\sqrt{B}\ \sinh\ \sqrt{B\pi}}$$

$$f_2(\theta_s) = \frac{\left[\dfrac{(\alpha_o + \chi \alpha_i)}{4\pi} \sum_{n=1}^{\infty} \dfrac{(-1)^n n \sin 2\ n\ \theta_s}{\left(n^2 - \frac{1}{4}\right)\left(n^2 + \frac{B}{4}\right)} + \dfrac{(\alpha_o - \chi\ \alpha_i)}{2(B+1)} 2\varphi\right]}{\sqrt{B} \sinh \sqrt{B\pi}}$$

The temperature distribution for a single seam Edgelock is

$$\frac{T}{\Theta} = f_1(\theta_s)\left[\cosh\sqrt{B}\beta - \cosh\sqrt{B}(2\pi - \beta)\right] + \frac{(\alpha_o - \chi\alpha_i)}{2(B+1)}\cos(B - \theta_s) - \frac{(\alpha_o + \chi\alpha_i)}{8\pi}\sum_{n=1}^{\infty}\frac{(-1)^n\cos 2n(\beta - \theta_s)}{\left(n^2 - \frac{1}{4}\right)\left(n^2 + \frac{B}{4}\right)} + \frac{4(\alpha_o + \chi\alpha_i)}{\pi B} \qquad \text{(II-7-10)}$$

Without loss of generality, we equate φ and θ_s, where θ_s is the angle of incidence of the sun relative to a slit location. Also, we perforate the booms 11.1 percent by area, and silver plate the outer surface and "blacken" the inner surface as discussed previously.

Performing the necessary integrations in the torque equation given above and collecting terms, yields the following equations for the thermal torque:

a. 1.0 in. Hingelock

$$T_{sc(z)} = \left[0.21\sin 2\varphi - 0.137\cos 2\varphi\right]\frac{d\varphi}{dz} \qquad \text{(II-7-11a)}$$

b. 0.5 in. Edgelock

$$T_{sc(z)} = \left[0.0129\cos 2\varphi\right]\frac{d\varphi}{dz} \qquad \text{(II-7-11b)}$$

In general, twist due to torque is given by

$$T_{sc} = C\frac{d\varphi}{dz} - C_1\frac{d^3\varphi}{dz^3} \qquad \text{(II-7-12)}$$

with the boundary condition

$$\varphi(0) = \frac{d\varphi}{dz}(0) = \frac{d\varphi}{dz}(L_o) = 0 \ .$$

The last boundary condition assumes that the tip is not free to twist. Substituting the torque Equation II-7-10 into the twist Equation II-7-12 yields, for the Hinge-lock TEE

$$\frac{d\varphi}{dz} = 2\left[A\varphi + \frac{C}{2C_1}\varphi^2 + \frac{0.21}{4C_1}\sin 2\varphi + \frac{0.137}{4C_1}\left(1 - \cos 2\varphi\right)\right]^{1/2} \quad \text{(II-7-13)}$$

where

$$C = 0.4691 \text{ lb in.}^2$$

$$C_1 = 8.25 \times 10^5 \text{ lb. in.}^4$$

By stating that $\frac{d\varphi}{dz}(L_o) = 0$, A in equation II-7-13 can be found for various values of assumed twist at the tip of the boom. Then, by performing an analog simulation of Equation II-7-13 using the values of A derived, values of φ (L) could be determined. For twist to exist, the assumed values of twist at the tip (boundary condition) and the numerically derived values of twist at the tip must intersect at some value of A. Figure II-7-6 shows these two relations. The intersection occurs at $A = 1.27 \times 10^{-7}$, $\varphi\ L_o = 0$. It was concluded, therefore, that thermal twisting will not occur.

For the Edgelock TEE, the twisting equation becomes

$$\frac{d\varphi}{dz}\left[C - 0]0129 \cos t\ 2\ \varphi\right] = 0. \quad \text{(II-7-14)}$$

The third derivative does not appear in this equation since the twist is independent of the length for the Edgelock. This is verified by tests done at Fairchild Hiller and by Harold P. Frisch in which the value of C = 30 was found for a single seam boom. This equation has two solutions: either

$$\cos{-2\varphi} = \frac{C}{0.0129}$$

which is impossible for C = 30 lb in.^{2} or

$$\frac{d\varphi}{dz} = 0$$

which implies no twist existing anywhere.

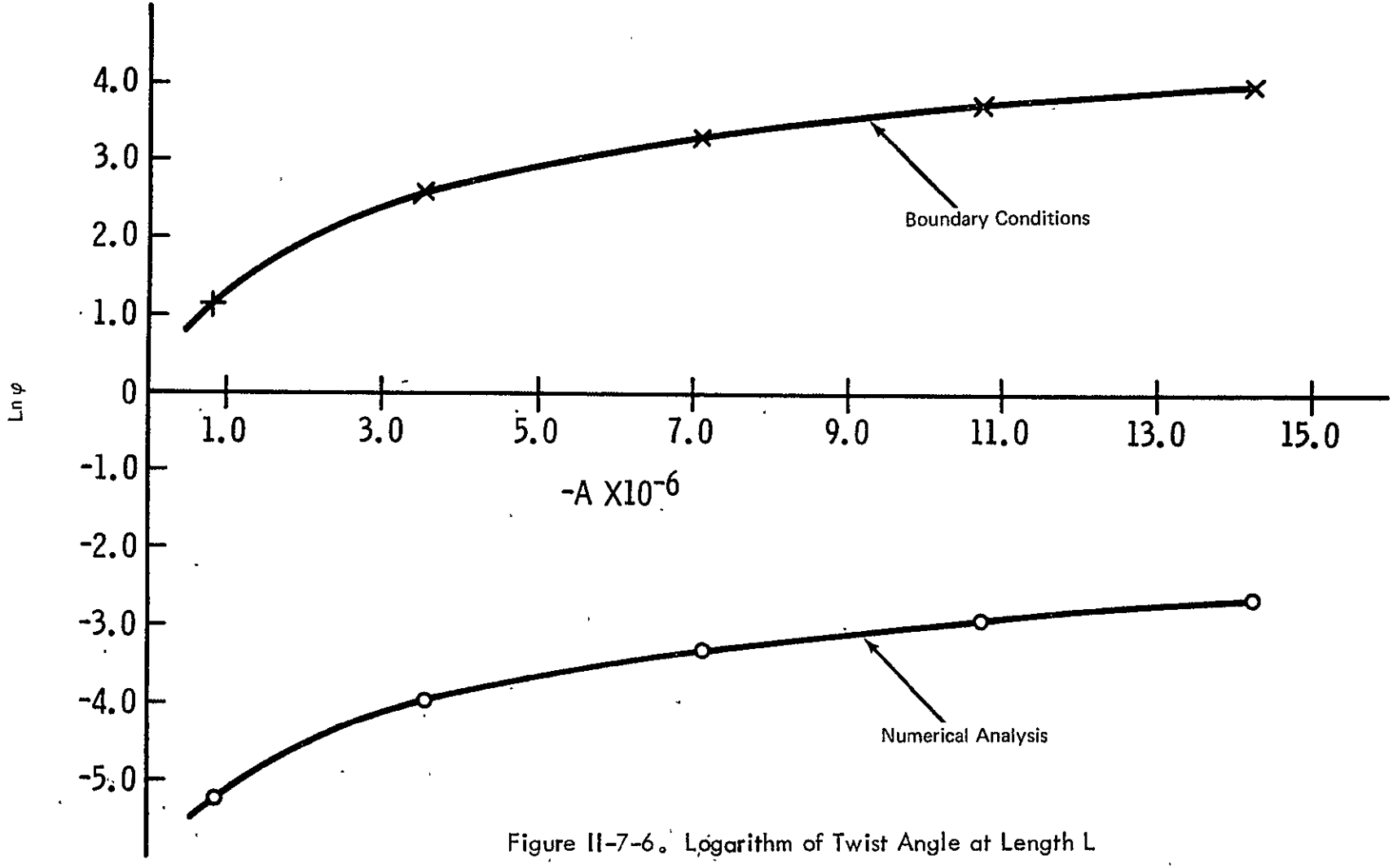

Figure II-7-6. Logarithm of Twist Angle at Length L

II-7.4 SYSTEM FREQUENCY

The system frequencies and amplitude will indicate how rapidly the baseline and satellite hub are moving. Tip weights of 0, 5, 10, and 15 lbs and boom lengths of 50, 75, ..., and 200 ft were used to calculate the system's frequencies. The system's symmetric frequencies were calculated from the well known formula for a cantiliver beam with a tip mass as follows:

$$\omega_n = \sqrt{\frac{k}{M + 0.23\ m}} \qquad \text{(II-7-15)}$$

$$k = \frac{3EI}{L_o^3} \qquad \text{(II-7-16)}$$

The antisymmetric frequencies were calculated using a method derived by Frisch.[34] With this method, the system frequencies can be predicted with slide-rule accuracy.

Although a parametric study was desired, some reasonable assumptions had to be made to do a realistic study. These included:

a. Mass moment of inertia of the satellite; 100 slug $ft^2 = I_S$
b. Desired moment of inertia about the pitch axis to be 1.2 times the mass moment of inertia about the yaw axis (done to size the gravity gradient boom)
c. Satellite radius; 2 ft.

The frequency equation of the reference is a complex, nonlinear equation in λL_o where[34]

$$\lambda^4 = \frac{m\omega_n^2}{EI}$$

and L_o is the boom length.

Solution of this equation then allows the system frequency to be found from

$$\omega_n = \frac{(\lambda L_o)^2}{L_o^2} \sqrt{\frac{EI}{m}} \qquad \text{(II-7-17)}$$

The symmetric frequency calculations for the TEEs are found in Figures II-7-7 and II-7-8 while antisymmetric natural frequencies are included in Figures II-7-9 and II-7-10. Notice that, in all cases, increasing the stiffness increased the frequency while increasing the boom length and tip weight decreased the system frequency, as was expected. For a 100 ft, 0.5 in. Edgelock, the period is expected to be about 77 s. For the 100 ft, 1.0 in. Hingelock, the period is expected to be about 27 s. (The assumption here is of an infinite tip weight, antisymmetric mode.) These values were also found in the simulation discussed in subsection II-7.5.

To alleviate the ACS requirements, a gravity-gradient subsystem was considered. As an approximation, and for investigative purposes only, the mass moment of inertia about the pitch axis of the satellite was arbitrarily made 20 percent greater than the mass moment of inertia about the yaw axis. Thus, taking mass moments about these axis, yields

a. pitch: $\frac{2}{3} m L_o^3 + 2L_o^2 M + I_s + \frac{2}{3} mL_g^3 + 2L_g^3 M_g = I_2$ (II-7-18)

b. yaw: $\frac{4}{3} mL_o^3 + I_s + 4 L_o^2 M = I_1$ (II-7-19)

c. $I_2 = 1.2 I_1$. (11-7-20)

With the above three equations, the gravity-gradient rod length was determined for known values of gradient tip mass, main boom length, mass per unit length, etc. The effect of gradient tip mass on the length of the gravity-gradient rod is shown in Figure II-7-11.

Finally, the effect of the gravity gradient on the system antisymmetric frequency was calculated using Reference (34). The system antisymmetric frequencies increased as expected. The results of these calculations are shown in Figures II-7-12 to II-7-13 for a 0.5 in. Edgelock and a 1.0 in. Hingelock, respectively.

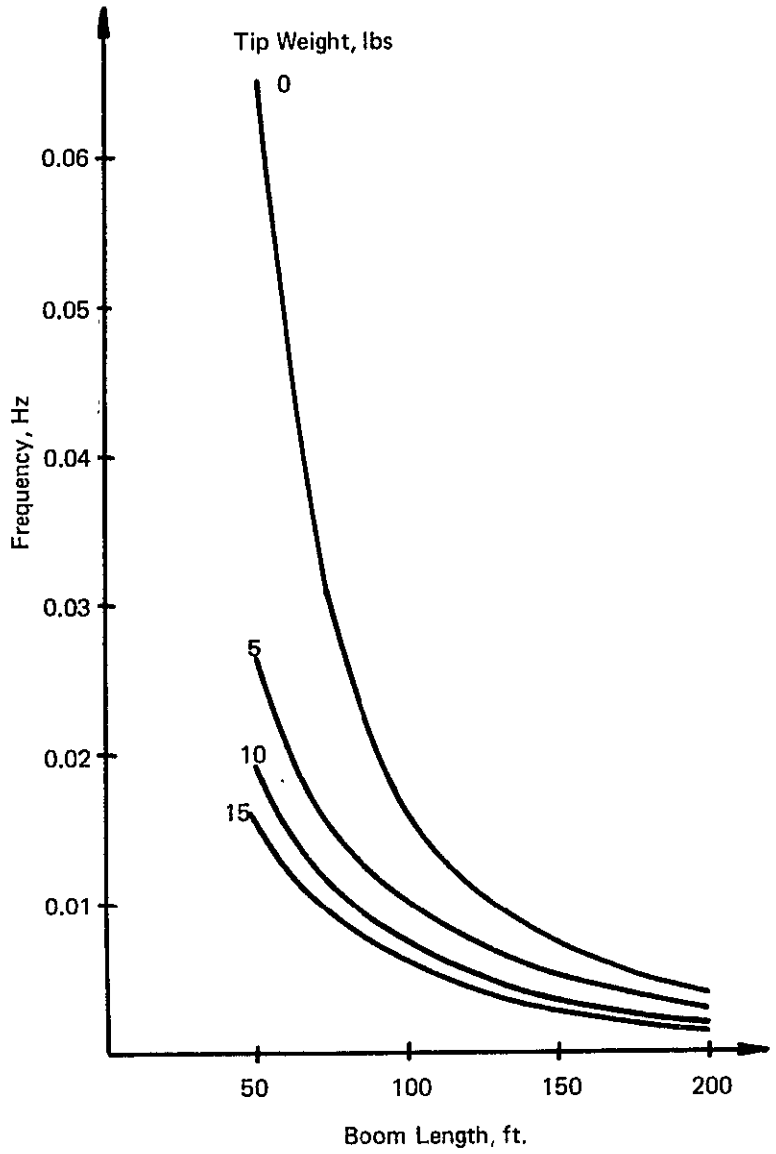

Figure II-7-7. Cantilever Frequency for 1.0 in. diam Hingelock TEE

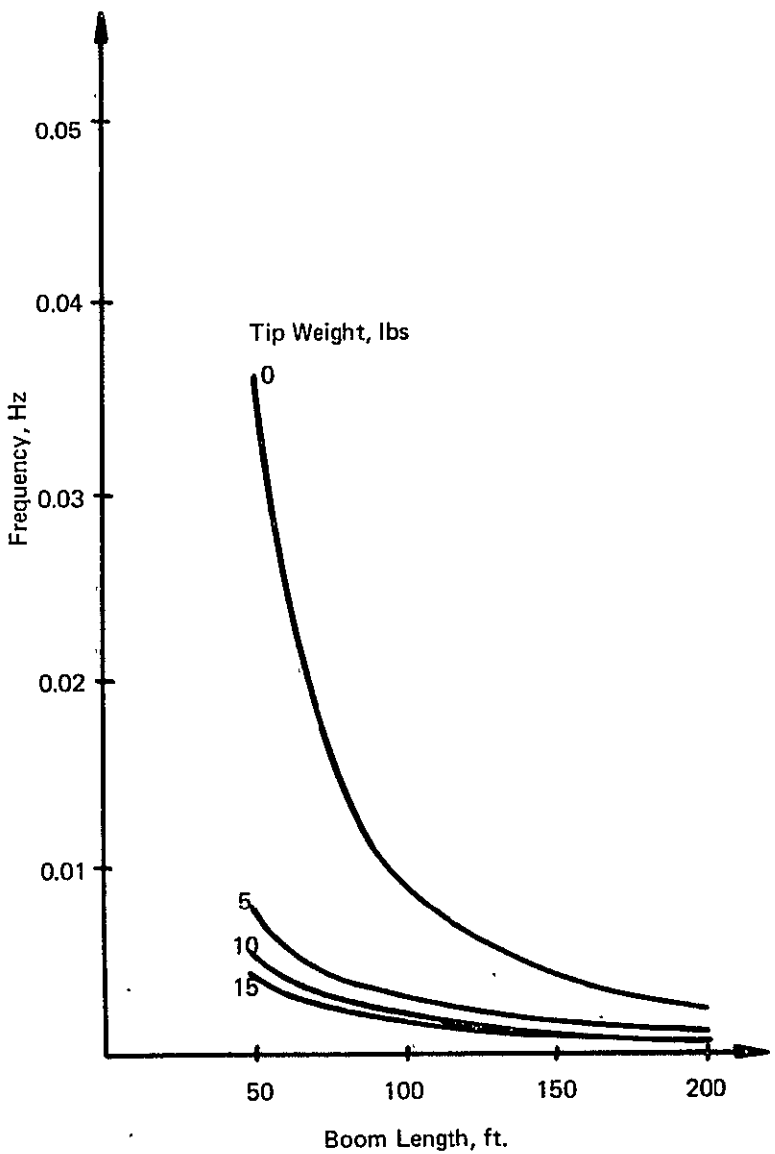

Figure II-7-8. Cantilever Frequency for 0.5 in. diam Edgelock TEE

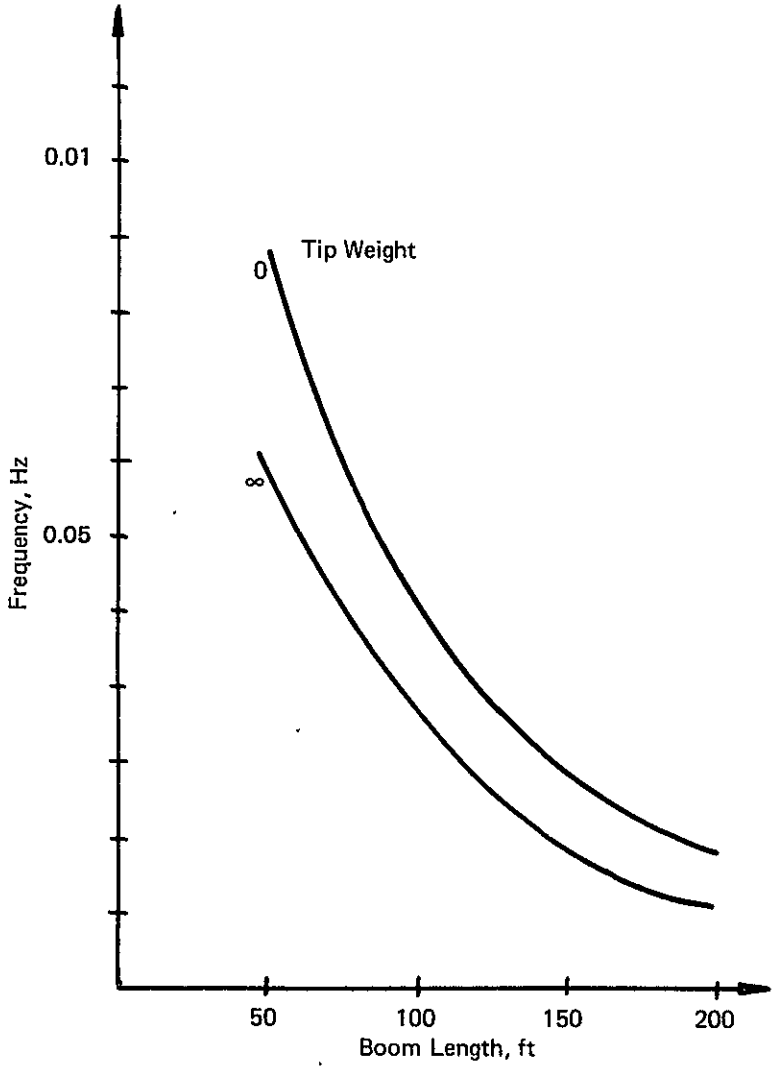

Figure II-7-9. Antisymmetric System Natural Frequency for 1.0 in. diam TEE

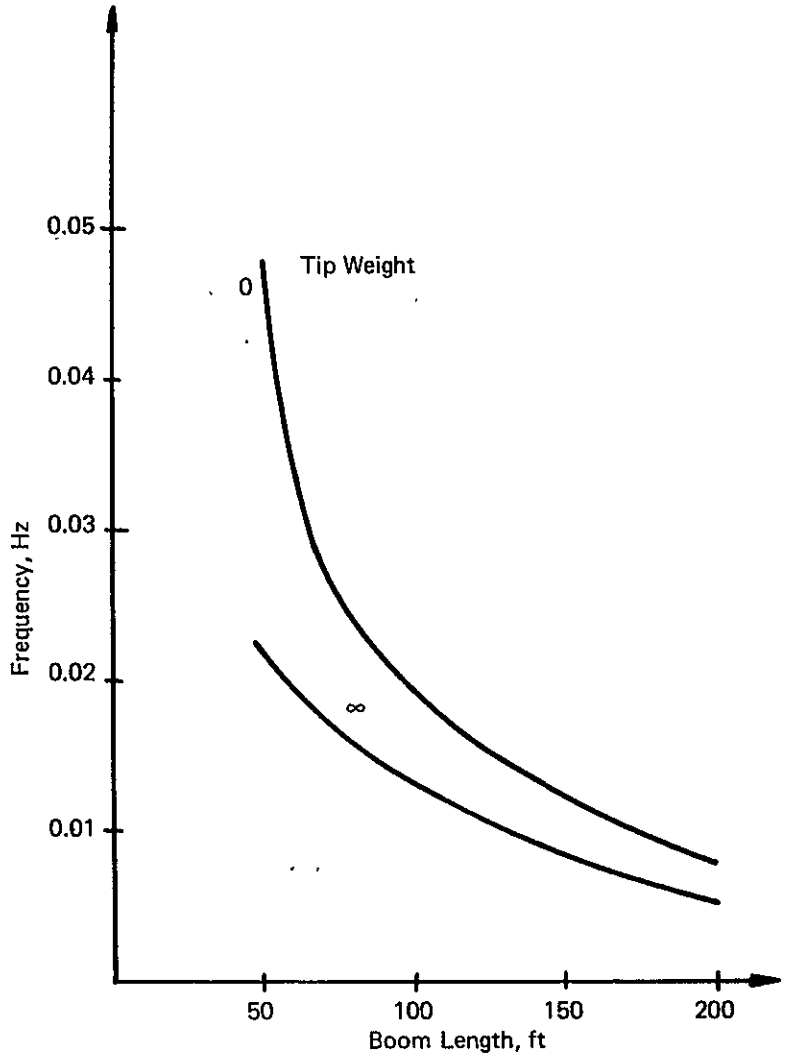

Figure II-7-10. Antisymmetric System Natural Frequency for 0.5 in. diam TEE

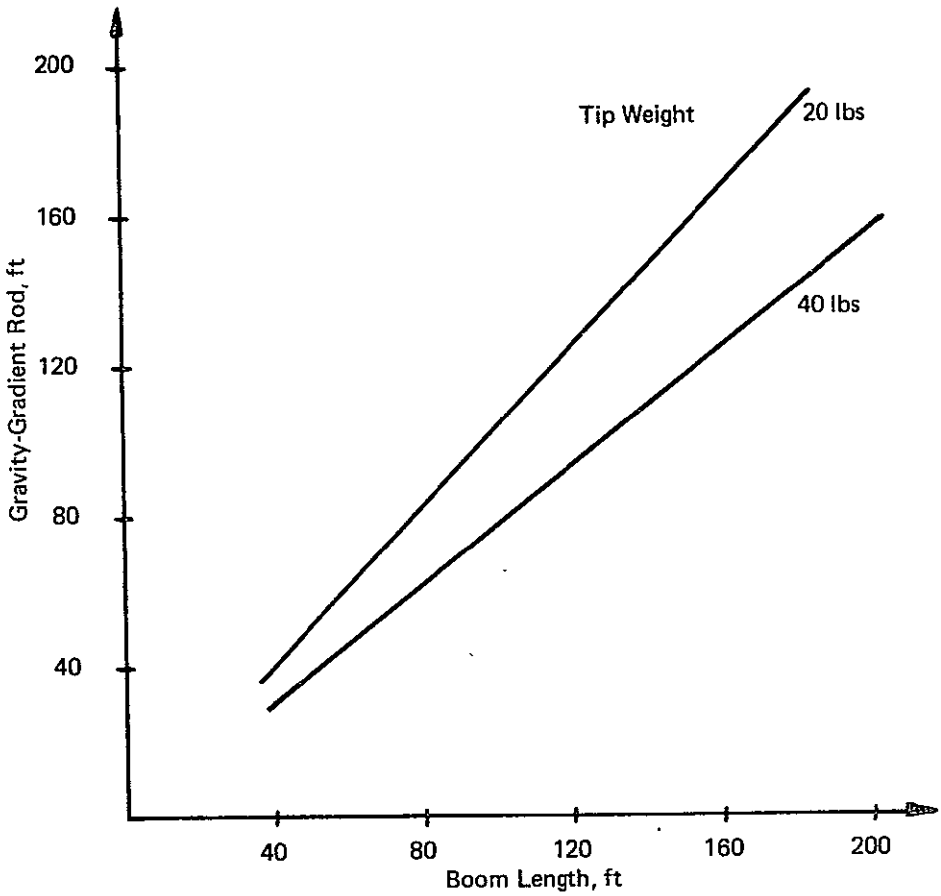

Figure II-7-11. Gravity-Gradient Rod as Function of Boom Length

II-7.5 DYNAMIC SIMULATION

To obtain an approximation of the motion of the baseline as it is affected by the thrusting during stationkeeping, by other ACS perturbations, and by various boom types and tip weights, a simulation with two degrees of freedom was formulated using the Lagrange energy technique. The coordinates of the problem are the rigid body rotation of the hub and booms and a time dependent mode shape normalized such that η is associated with the tip of the boom and is relative to a fixed body axis. The first cantilever mode shape was selected since this would provide the system with the lowest natural frequency. The simulation model is shown as Figure II-7-14.

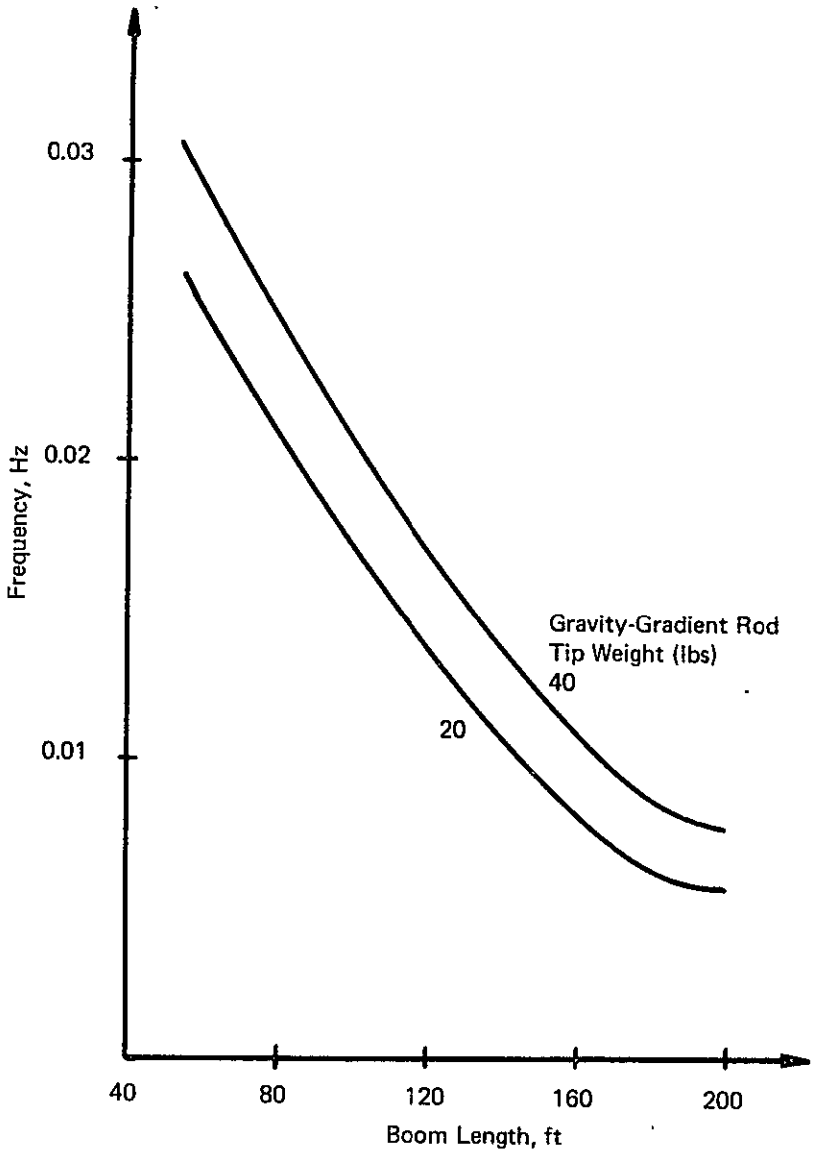

Figure II-7-12. Antisymmetric Natural Frequency with Gravity-Gradient Rod, 0.5 in. TEE

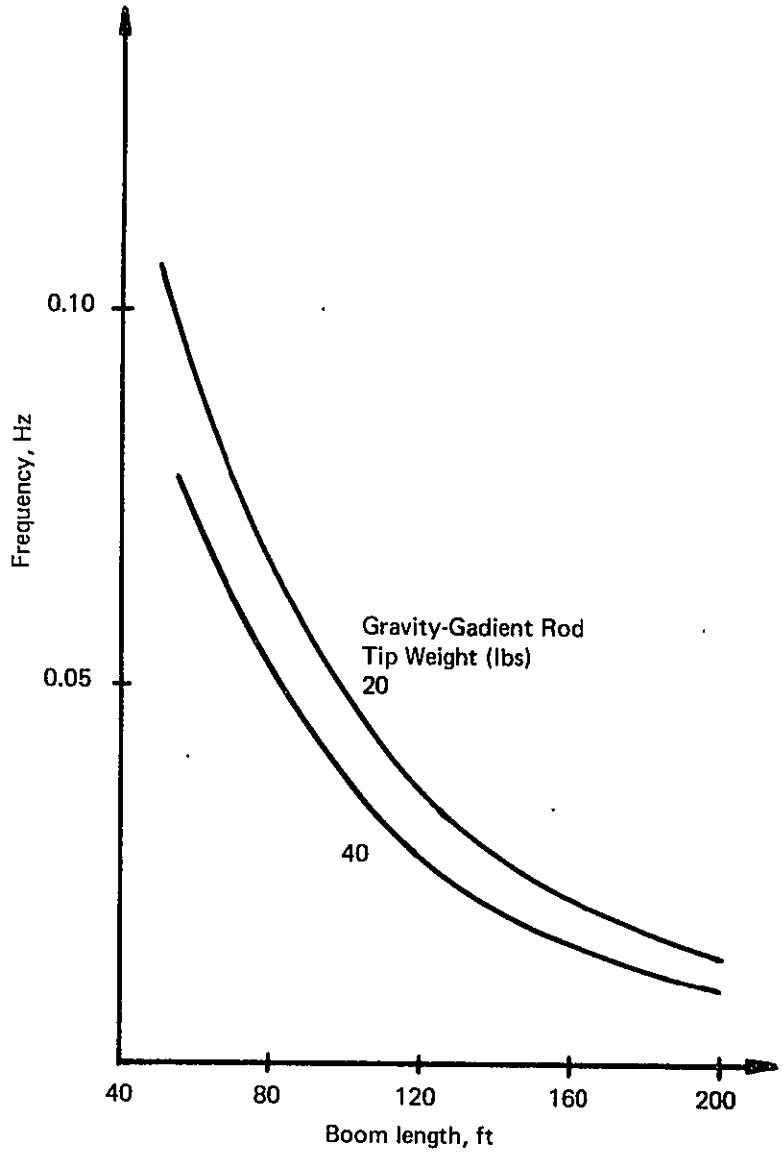

Figure II-7-13. Antisymmetric Natural Frequency with Gravity-Gradient Rod, 1.0 in. TEE

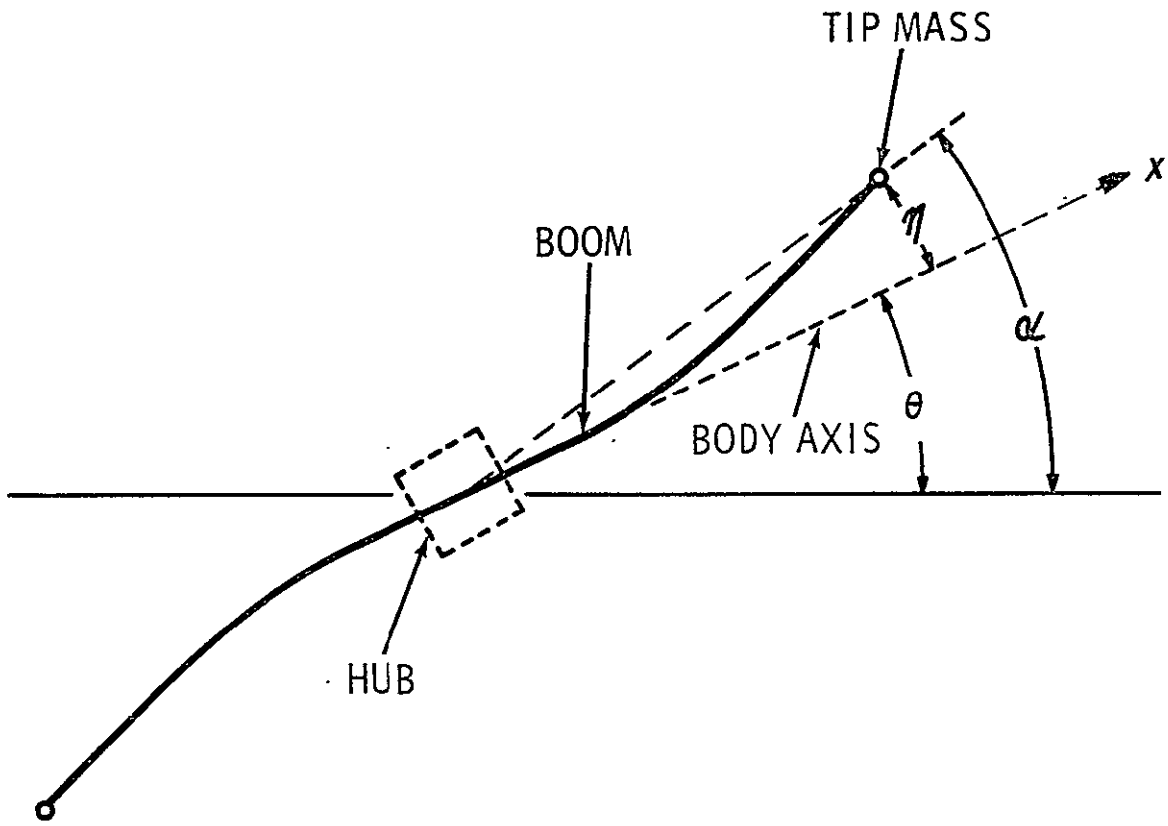

Figure II-7-14. Simulation Model

In the analysis, it was considered advantageous to consider the relative motion of the satellite with respect to a rotating axis system. Higdon and Stiles gives a complete description of this aspect of the problem.[35] The coordinate system is shown in Figure II-7-15 for ease of discussion.

Letting 0 concide with 0' yields the following position vector:

$$\vec{r} = \begin{Bmatrix} x \\ y \\ z \end{Bmatrix} + \eta \Phi \qquad \text{(II-7-21)}$$

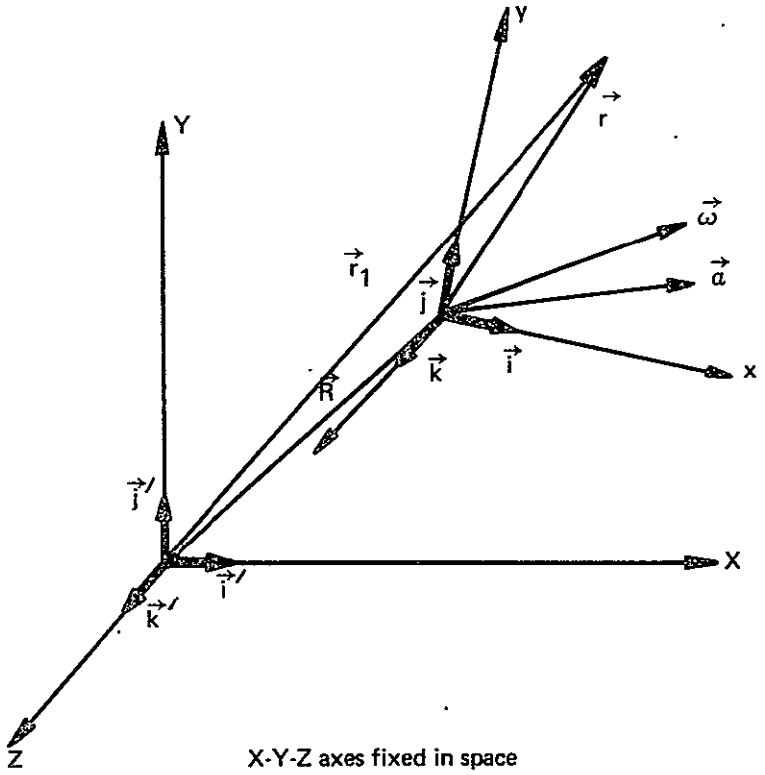

X-Y-Z axes fixed in space

x-y-z rotating axis system

$\vec{\omega}$ angular velocity

$\vec{a}$ angular acceleration

$\vec{r}$ position rector in rotating system

$$\vec{V}_p = \dot{\vec{r}} = \dot{\vec{R}} + \dot{\vec{r}}$$

$$\vec{v}_p = \dot{\vec{R}} + \vec{v}_p\Big/_{x,y,z} + \vec{\omega} \times \vec{r}$$

Figure II-7-15. Coordinate Frame for Dynamic Simulation

where $\eta\Phi$ is the first cantilever mode shape normalized to η at the boom tip and the velocity vector

$$\vec{V}_p = \begin{Bmatrix} -\omega & (y + \eta\Phi) \\ \dot{\eta}\,\Phi & +\omega x \\ 0 \end{Bmatrix} \qquad \text{(II-7-22)}$$

from which

$$v^2 = \omega^2\left(y^2 + 2y\eta\Phi + \eta^2\Phi^2\right) + \dot{\eta}^2\Phi^2 + 2\dot{\eta}\Phi\omega x + \omega^2 x^2 . \qquad \text{(II-7-23)}$$

The Lagrange equations for a system of N_o degrees of freedom capable of being defined by N_o independent coordinates and having been defined at the beginning by N_o such independent coordinates are:

$$\frac{d}{dt}\left(\frac{\partial L}{\partial q_j}\right) - \frac{\partial L}{\partial q_j} = Q_j \quad j = 1, 2, \ldots, N_o \qquad \text{(II-7-24)}$$

L = $T - V_j$ (assuming no damping)

T = Total Kinetic energy of the system

V = Total potential energy of the system.

For this problem,

N_o = 2

q_1 = θ

q_2 = η

$$T = 1/2 \int_{\text{Body}} v^2\, dm .$$

Inserting from Equation II-7-23 one obtains

$$T = 1/2 \int_{\text{Body}} \left[\omega^2\left(y^2 + x^2\right) + \left(\omega^2\eta^2 + \dot{\eta}^2\right)\Phi^2 + 2\dot{\eta}\omega x\Phi\right] dm .$$

This can be written as

$$T = 1/2\, I_T \omega^2 + \left(\omega^2 \eta^2 + \dot{\eta}^2\right) \frac{H_1}{2} + \dot{\eta}\,\omega H_2 \qquad \text{(II-7-25)}$$

where

$$H_1 = \int_{\text{Body}} \Phi^2\, dm; \quad H_2 \int_{\text{Body}} x\,\Phi\, dm$$

I_T = total mass moment of inertia of the system

Φ = first cantilever mode shape normalized to one at the boom tip.

Since only local dynamics are considered, we have

$$V = \frac{EI}{2} \int_{\text{Body}} \eta^2 \left(\Phi''\right)^2 dx = \frac{EI}{Z} H_3 \eta^2 ; \quad \Phi' = \frac{d\Phi}{dx} . \qquad \text{(II-7-26)}$$

Combining Equations II-7-25 and II-7-26 yields

$$L = \frac{1}{2} I_T \omega^2 + \left(\omega^2 \eta^2 + \dot{\eta}^2\right)\frac{H_1}{2} + \dot{\eta}\,\omega H_2 - \frac{EI}{2} H_2 \eta^2 . \qquad \text{(II-7-27)}$$

Taking the necessary derivatives, adding, rearranging terms, and separating the variables yields the two equations of motion, namely:

$$\dot{\eta}^{\cdot} = \frac{-L_o}{I_s + \eta^2 H_1} \left\{ T_Q - \eta \left(2\omega\eta H_1 + \omega^2 H_1 - \frac{8EI}{L_o^2}\right)\right\}^{\cdot} +$$

$$+ \left(\omega^2 - \frac{8EI}{H_2 L_o^2}\right) \eta \qquad \text{(II-7-28)}$$

and

$$\dot{\theta}^{\cdot} = \dot{\omega} = \frac{1}{I_s + \eta^2 H_1} \left\{ T_Q - \eta \left(2\omega\dot{\eta}\ H_1 + \omega^2 H_z - \frac{8EI}{L_o^2}\right)\right\}^{\cdot} \qquad \text{(II-7-29)}$$

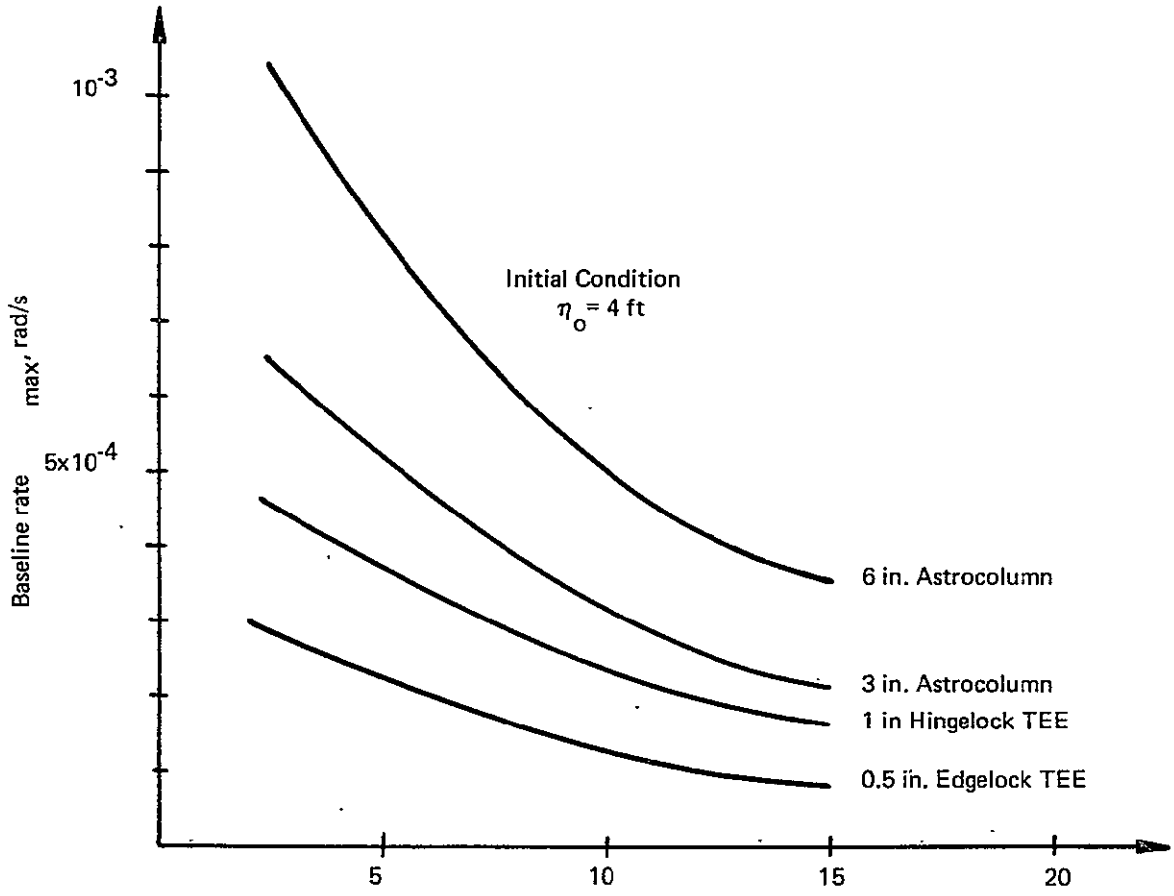

Figure II-7-16. Absolute Maximum Baseline Rate

where

I_s = mass moment of inertia of the hub.

These coupled, nonlinear equations did not yield a closed form solution. The simulation was, therefore, carried out by means of an analog simulation program.

A simple ACS logic was devised. It consisted of an on-off system in which a restoring mechanism, e.g., control jets or inertia wheels, would "fire" when the baseline angle exceeded 1 deg and return the system to the nominal position. The base angle α was calculated as

$$\alpha = \theta + \frac{\eta}{L_o} . \qquad \text{(II-7-30)}$$

The first initial condition chosen was a tip deflection of 4 ft, i.e., $\eta_o = 4.0$ ft. This was artibrarily chosen to guarantee that the restoring torque would be engaged. The program was run for the various configurations with different tip weights; altogether about 15 cases. Figure II-7-16 shows the variations in the baseline angular rate for the configurations. The conclusions that can be drawn from this analysis are the following. First, as the stiffness increases, so does the frequency. The period goes down correspondingly, which is undesirable since the baseline will be rotating faster. Second, as the tip mass is increased on a particular boom, the uncertainty in the baseline rate decreased.

After different cases had been studied, it was realized that for the stiffer systems, i.e., Astrocolumn and 1.0 in Hingelock, the 4 ft tip deflection was an unfair basis for comparison. A more realistic initial condition was taken to be a hub rotation of 1 deg, hub angular velocity of 10^{-5} rad/s. This simulates drift; for example, due to the gravity gradient. With this set of initial conditions, all the systems had comparable baseline performances.

The results of a typical run is shown in Figures II-7-17 to II-7-20. Figure II-7-17 shows that the hub has moved through 1 deg which has caused the restoring torque to "fire." The booms, since they are flexible, continue to move through the initial path. At about 40 s, the central body begins to "feel" the effect of the boom motion. At 75 s, the torque shuts down with the motion of the hub affected by the oscillating booms as the hub drifts towards the nominal position.

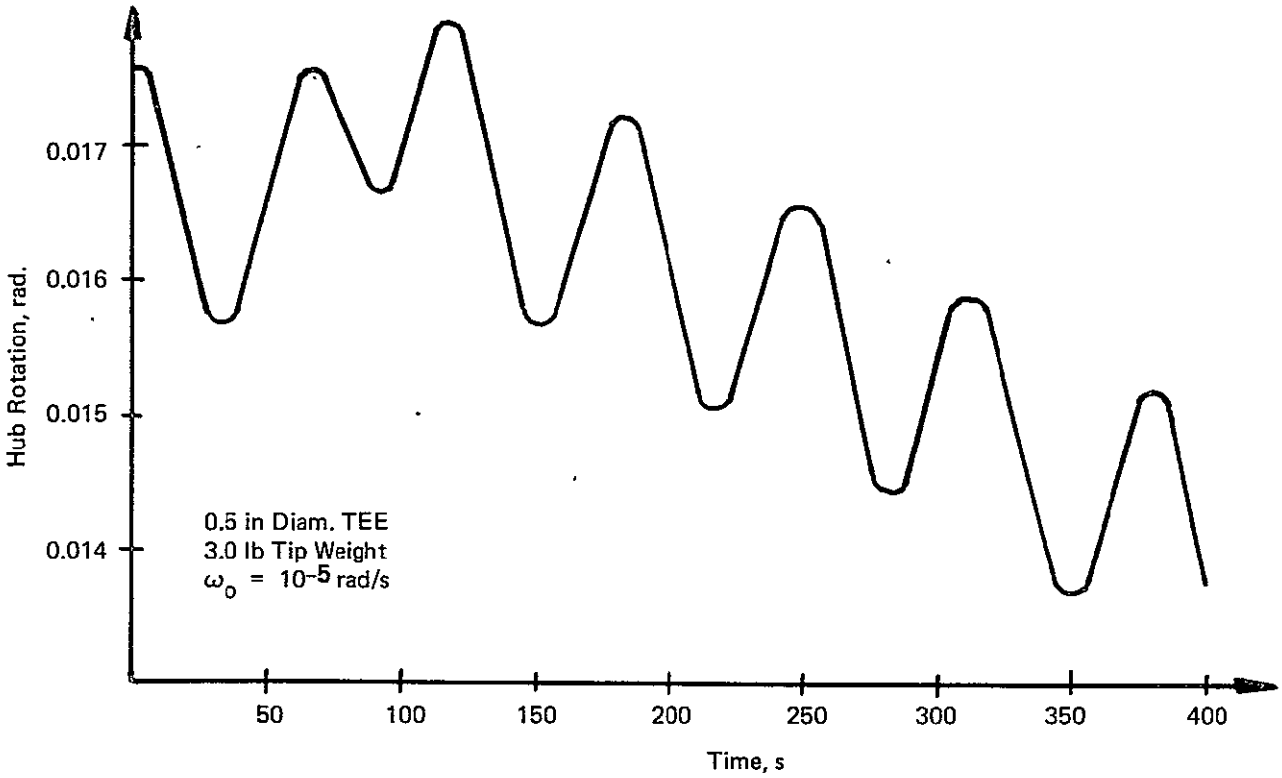

Figure II-7-17. Hub Rotation (Φ)

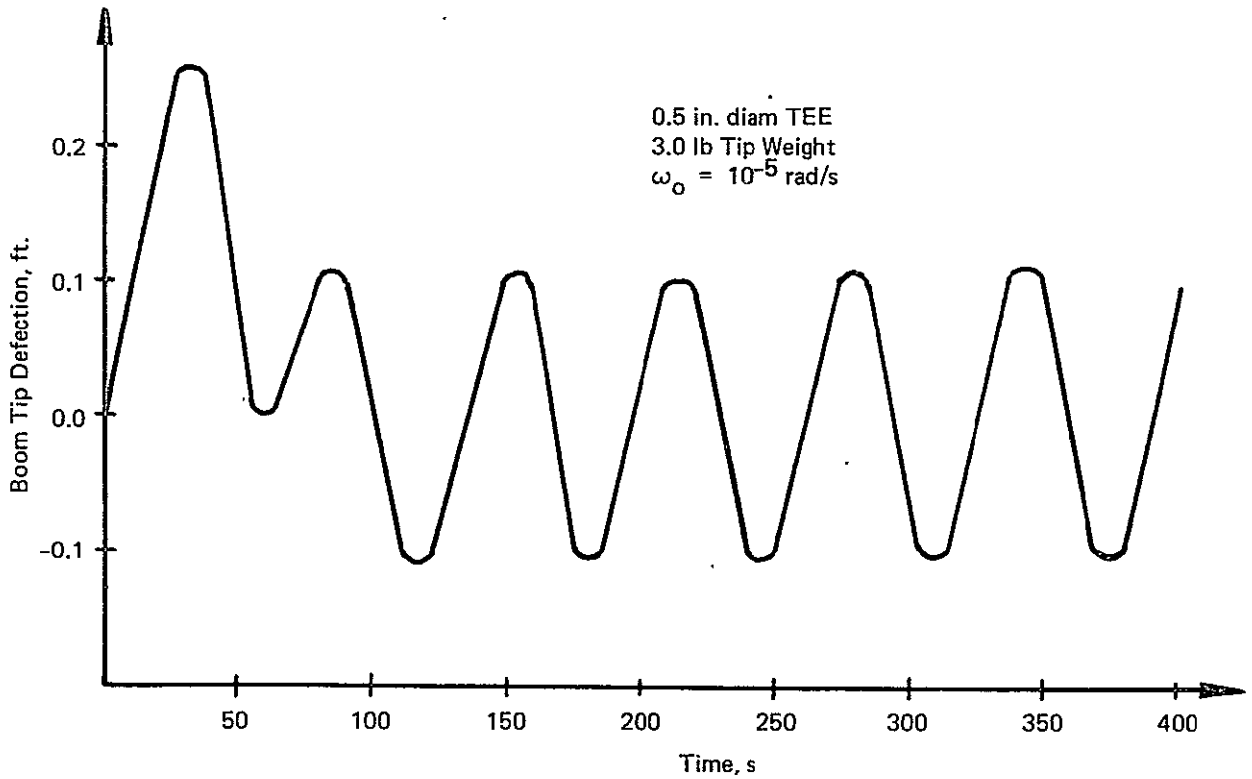

Figure II-7-18. Tip Deflection Relative to Body Axis (η)

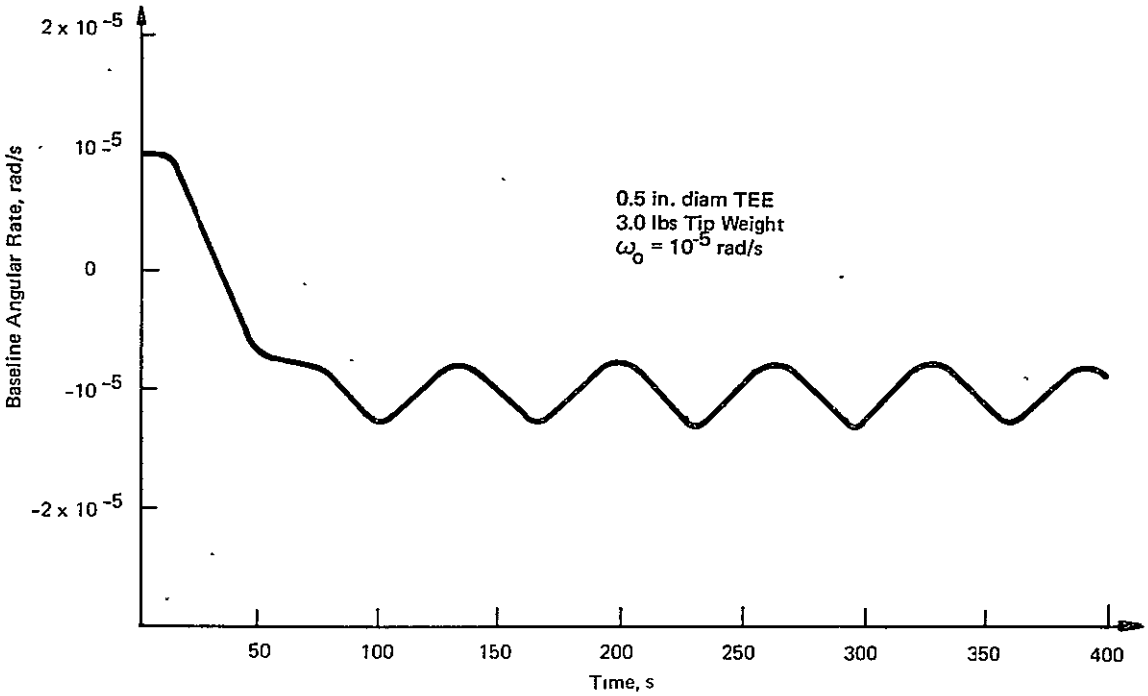

Figure II-7-19. Baseline Rate of Motion

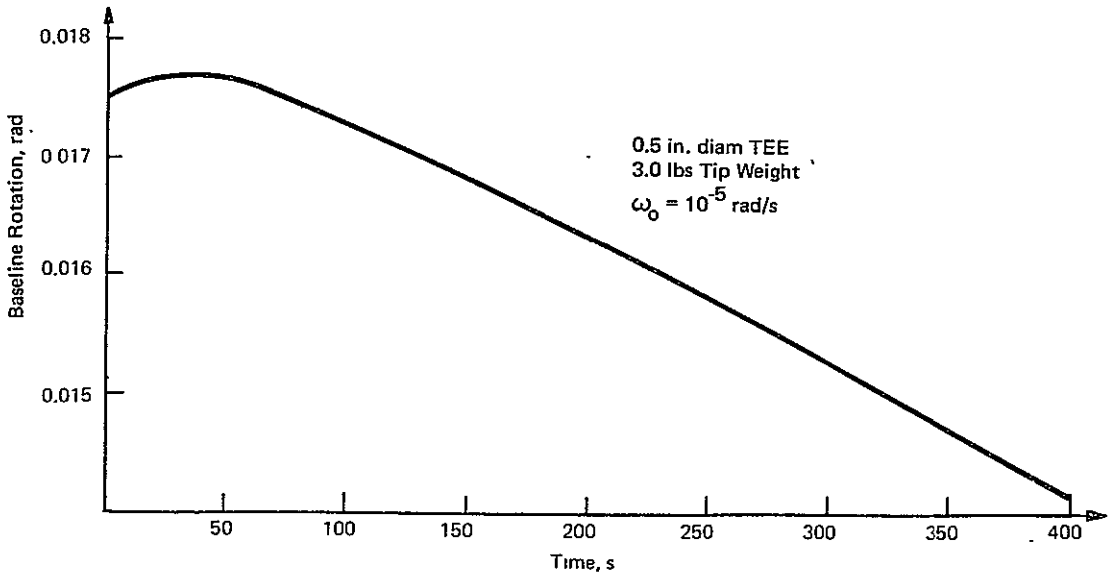

Figure II-7-20. Angular Baseline Position (α)

In Figure II-7-18, the booms start out having no deflection. As the hub rotates, the booms deflect, causing the pattern of oscillation shown in the figure. The pattern, not precisely sinusoidal, shows the dynamic effect of the hub rotation on the booms.

Figure II-7-19 shows the angular rate of the baseline. This parameter was programmed to vary as

$$\dot{\alpha} = \dot{\theta} + \frac{\dot{\eta}}{L_o} \qquad \text{(II-7-31)}$$

The first 50 s show the satellite being brought back to the nominal position by the torquer. As the torquer cuts off at 75 s the pattern again indicates the dynamic coupling between the spacecraft and booms.

Superimposing Figure II-7-17 onto Figure II-7-18 shows that the hub rotation and the boom tip deflection are 180 deg out of phase, as they should be for this model. Note in Figure II-7-20 that the angular position of the baseline(α) versus time appears as a smooth curve. The curve is actually irregular so that it has "wiggles"; however, they are very small. The curve can therefore be considered the "average" of the actual phenomena.

As mentioned in the formulation, damping was neglected; the oscillations, therefore, do not appear to be "dying out." Further, no appreciable difference was found in the magnitude of the baseline angular rates regardless of the boom parameters.

II-7.6 ATTITUDE CONTROL SYSTEM AND GRAVITY-GRADIENT CONTROL

The principal performance criteria are dictated by the special needs and capabilities of the interferometer system. Orientation of the satellite to the local vertical is required to maintain adequate coverage and signal strength of the antenna pattern. A relatively loose yaw orientation is acceptable, since the principal objective is to avoid the requirements for spherical coverage by the solar power array.

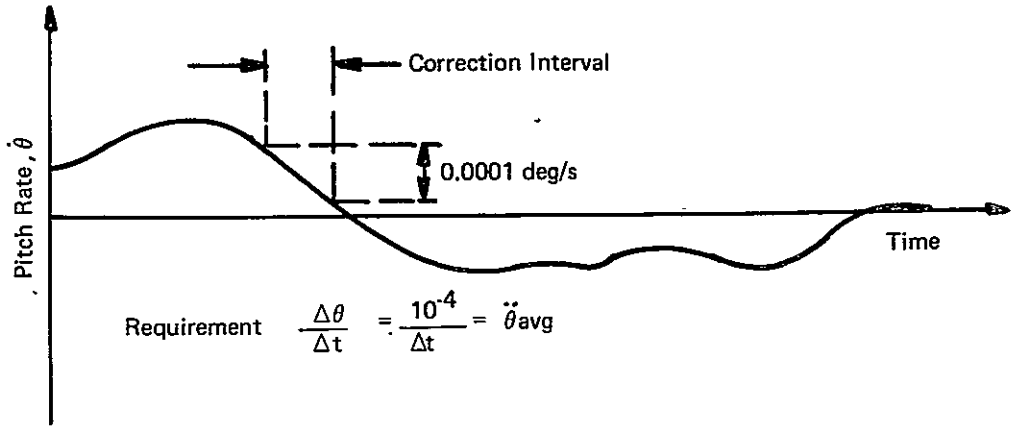

Figure II-7-21. Attitude Rate Uncertainty

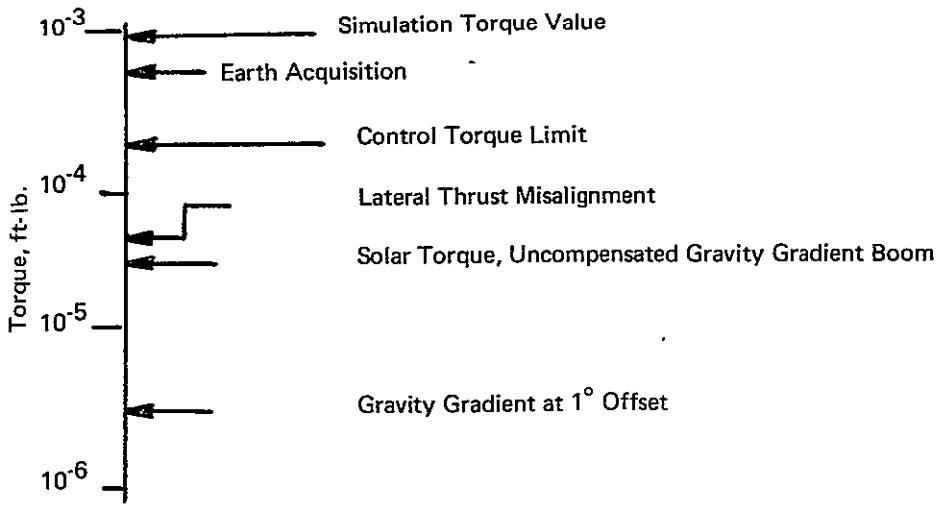

Figure II-7-22. Disturbance and Correction Torques

The principal parameter affecting interferometer position location accuracy is that of pitch and roll attitude rates. It is desired that the attitudes not change during a measurement interval, which may be in the range of 1 to 10 s, by more than the specified 0.001 deg. However, if the rates are known, the position location computation may be corrected for these known rates, so that the criteria is expressed as an uncertainty in the rate. Logically, the attitudes and rates are derived from the interferometer rather than from body-mounted earth sensors. The satellite control system will be simplified by making maximum use of the ground computer for generating specific control functions and commands.

To keep angular accelerations low, the control torque must be limited. Figure I-7-21 illustrates how the interval between corrections may be related to the satellite and control system parameters. Here an arbitrary pitch rate history is plotted as a function of time. Assuming a 10-s tracking interval, it is desired that the rate change by no more than 0.001 deg/s between corrections to the position location computation. This simply means that the average angular acceleration imparted to the antenna must be less than $0.001/\Delta t$. Knowing this, the control torque is found. Torque levels needed for compensation due to the other environmental pertrubations are shown in Figure II-7-22.

The satellite attitude can also be controlled by an on-off system. Such a system exercises no control until the error rate exceeds a given limit. Such a system can operate in different modes. Figure II-7-23 depicts the system behavior.

The first line shown is a torque-limited system, where the limit is established by the acceleration limit, which was previously derived. The constant torque is applied to first accelerate the system, then reversed to decelerate it. The duration of the control maneuver is relatively long, with a smooth motion of the boom.

An on-off system could also be operated at torque limits established by boom deflection. In the example shown, torque is set by a boom deflection of 1 deg. A comparatively short correction time is required, but balloon position location

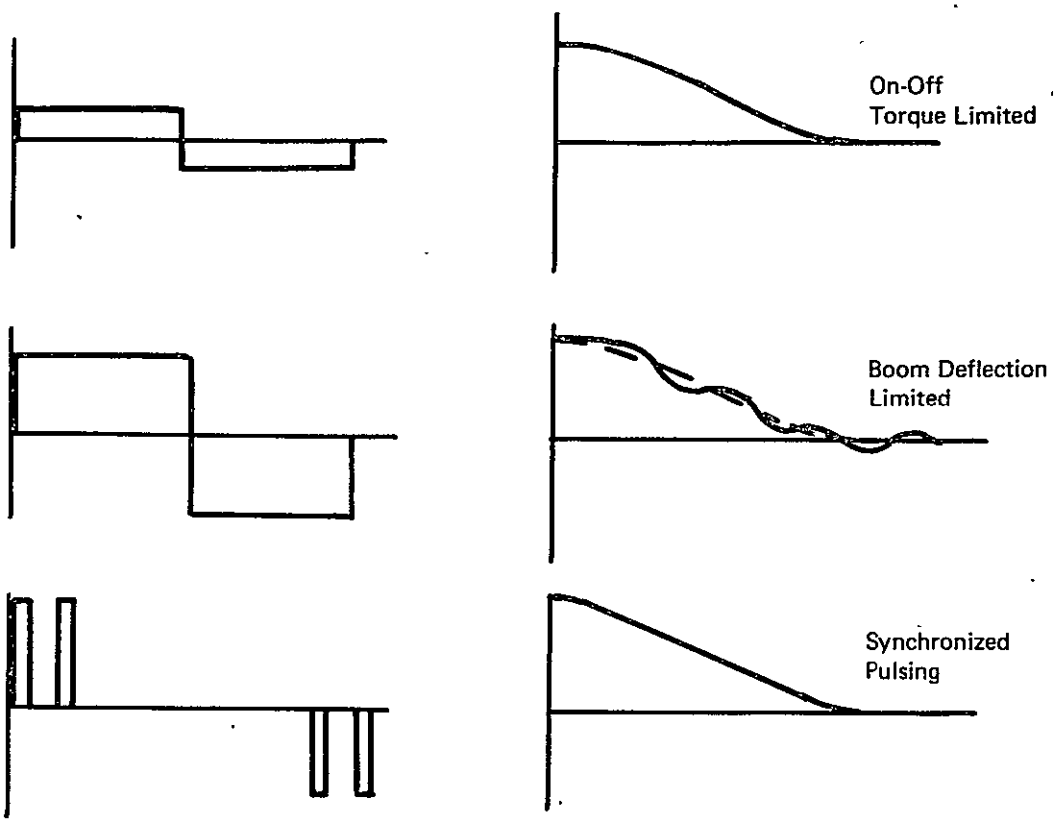

Figure II-7-23. System Behavior

will be degraded by the oscillations of the booms. This oscillation will tend to continue unless the torque periods are timed so as to cancel the oscillation at the end of the control period.

Finally, the system may be operated by relatively short high torque pulsing. If pairs of torque impulses are timed to be exactly one-half of the natural period apart, the succeeding motion will be constant and within the desired limit of rate uncertainty, so that tracking accuracy will not be degraded during the 20 min (typical) attitude correction.

This linear analysis of the control torque limitation was improved upon by varying the magnitude of the torque in the analysis of subsection II-7.5. It was found that torques up to 10^{-3} ft-lbs resulted in acceptably small deflections and rates of deflection.

Torque levels of 10^{-2} ft-lbs resulted in unreasonably large deflections. Beyond this, a reasonance condition was found to exist. However, as can be seen from Figure II-7-23, a torque level of 10^{-3} ft-lbs is more than sufficient to overcome the estimated disturbance torques. Further, a gravity-gradient subsystem would not be required for this application.

Section II-8

SATELLITE AND GROUND ELECTRONICS

The phase measurements and subsequent calculations are performed at a central ground station. The function of the satellite electronics then becomes one of relaying the emitter transmissions from the various interferometer antennas to this central ground station via an X-band downlink. To maintain the time relationship between the signals, frequency multiplexing is used within the satellite repeater so that all signals can be transmitted simultaneously. Figure II-8-1 shows a simplified version of the interferometer receiving system, including both satellite repeater and ground receiver functions, for only one pair of antennas. This diagram is presented to convey the concept of frequency multiplexing of the received signals by offset local oscillator frequencies, recovering the reference or offset frequency and performing the phase measurements after the signals are converted to 2 kHz.

II-8.1 SATTELLITE REPEATER

Figure II-8-2 illustrates the suggested implementation of the multiplexing repeater, where the frequency offsets are achieved with offset local oscillator frequencies. These local oscillator frequencies must be coherently related to each other in order to maintain the phase relationships in the downconverted signals. Figure II-8-3 shows one method of generating these local oscillator signals.

The phases of a pair of signals from a particular baseline are to be compared and, of course, this must be done at equal frequencies. For this reason, the local oscillator synthesizer reference frequency, which is used to produce the precise local oscillator frequency offsets, is continuously transmitted to the ground stations. In Figure II-8-2, this reference modulates a subcarrier, which is then added to the received signal just prior to upconversion to X-band.

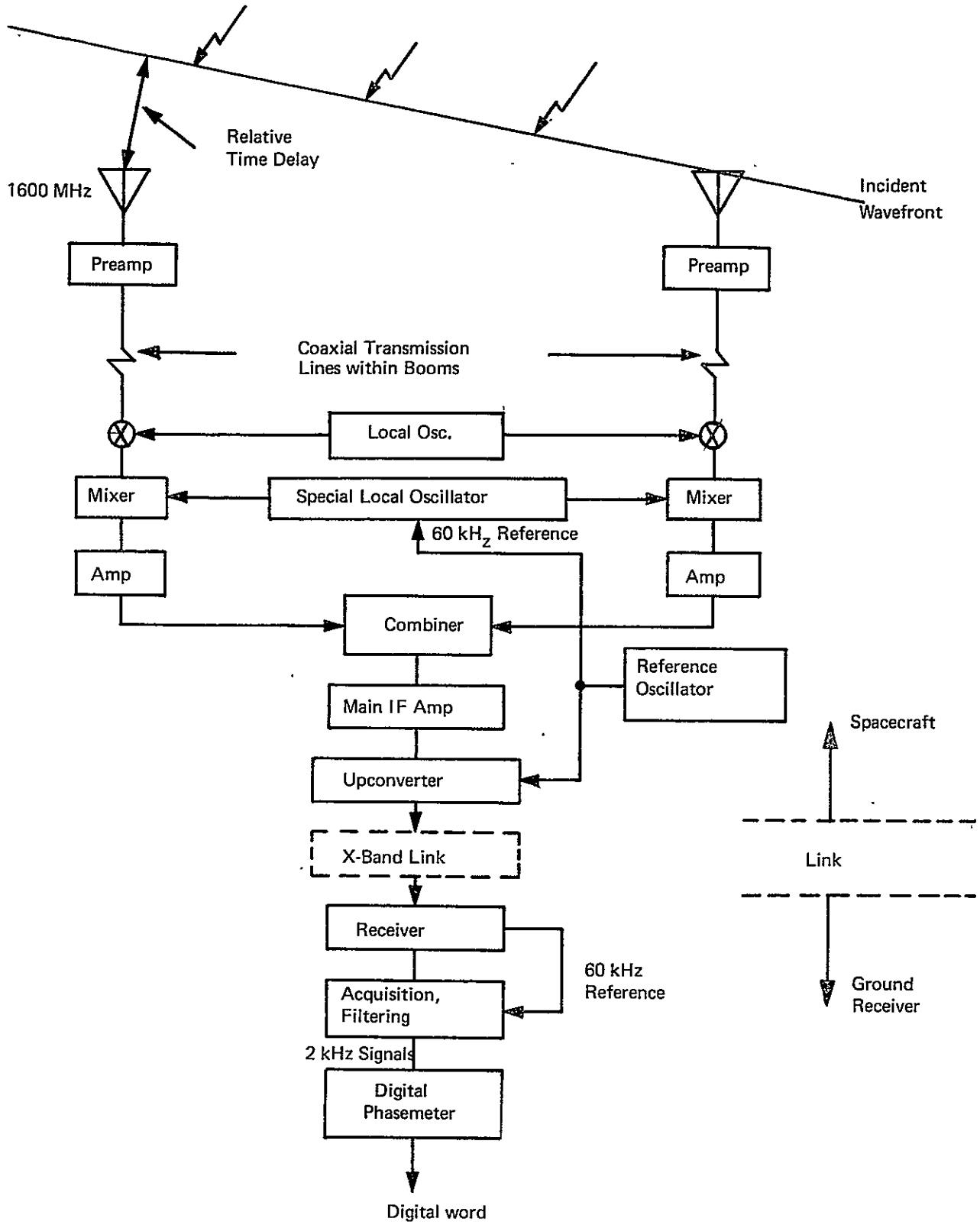

Figure II-8-1. Essential Elements for a Simplified Interferometer Receiver System

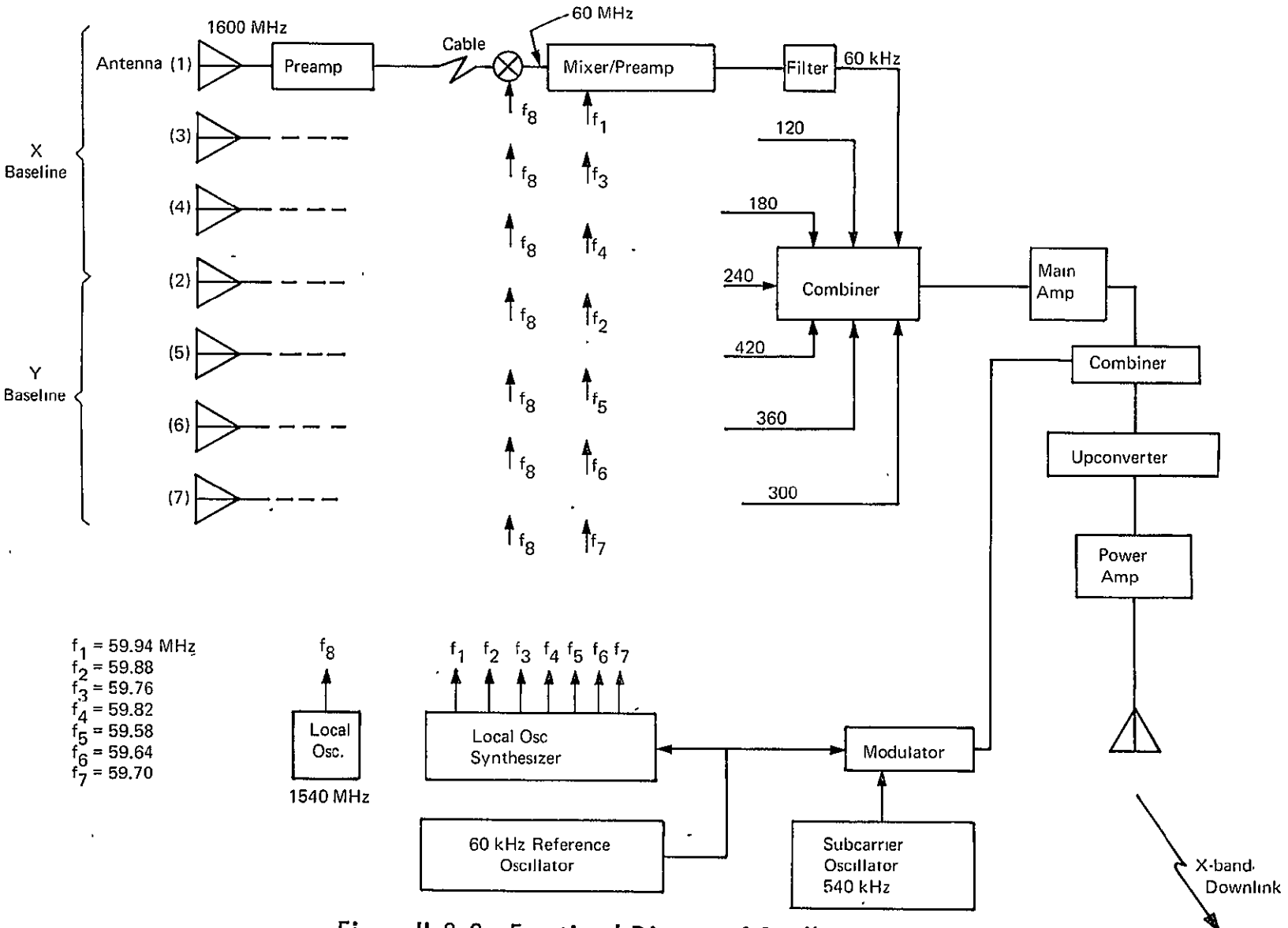

Figure II-8-2. Functional Diagram of Satellite Repeater

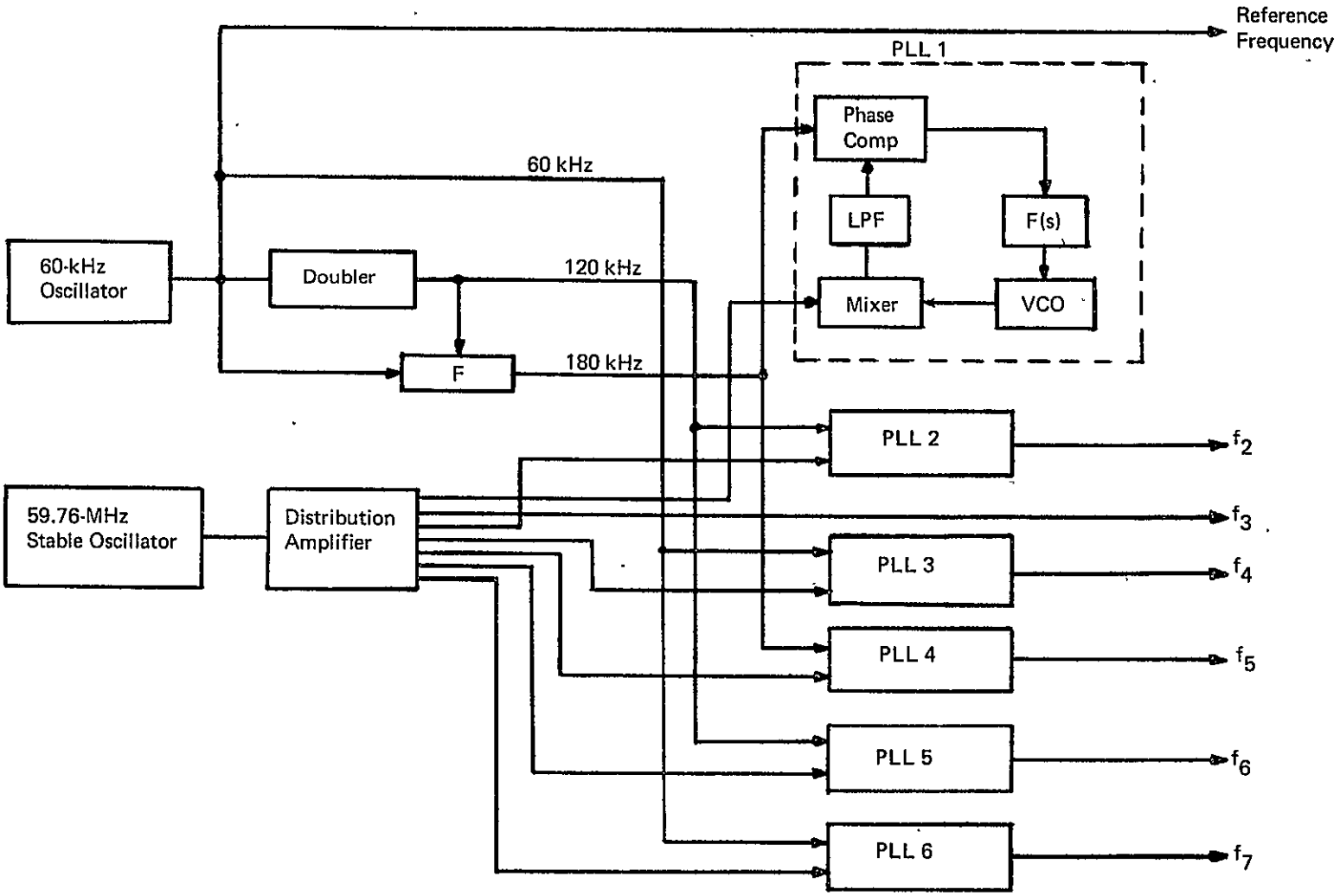

Figure II-8-3. Local Oscillator Synthesizer

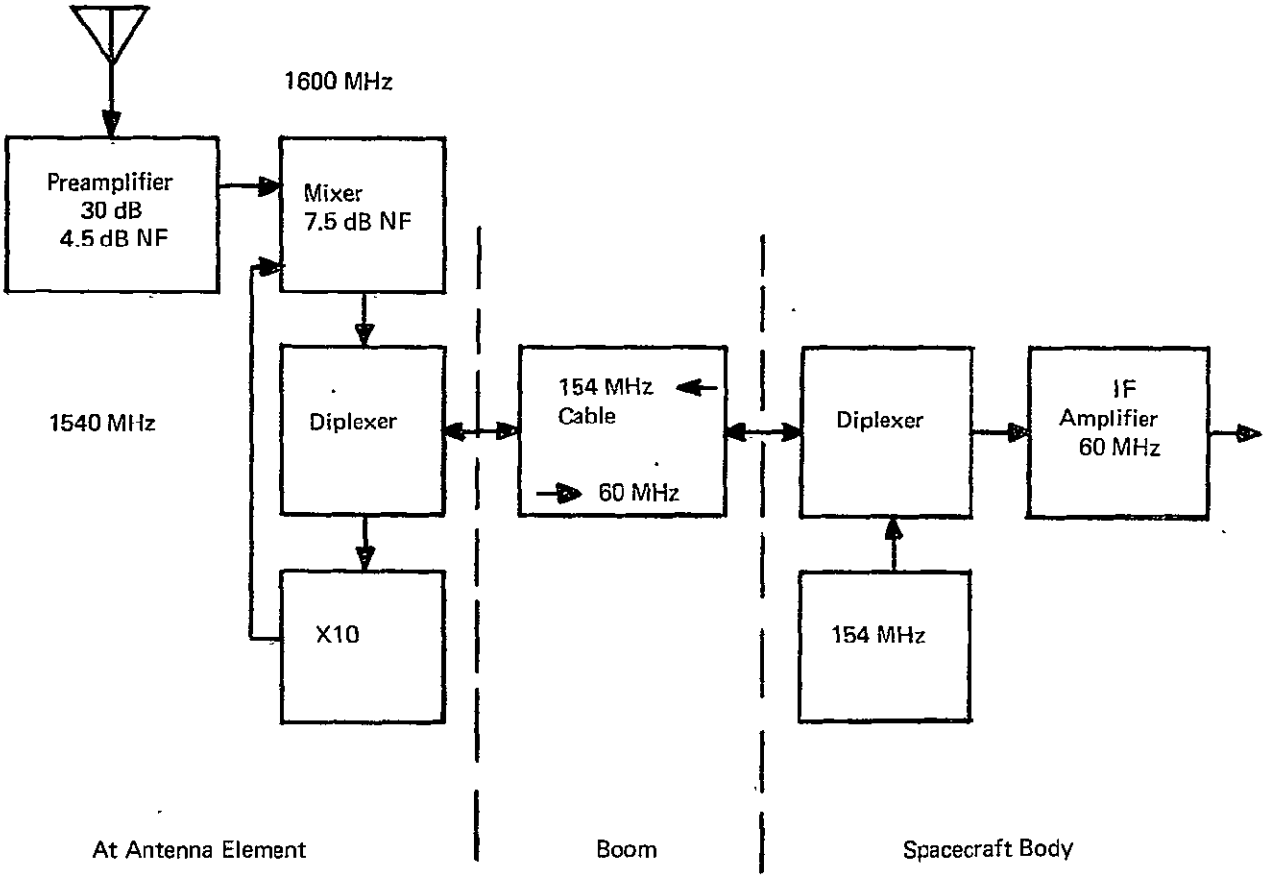

Figure II-8-4. Alternate Method of Signal Transmission from Antenna to Spacecraft

Figure II-8-2 shows each antenna element connected directly to an RF preamplifier, which then feeds the coaxial cable which carries the signals along the 120 ft boom. This signal transfer from antenna to spacecraft body could also be performed at IF, as shown in Figure II-8-4. This alternate method has the advantage of reducing the cable loss by transmitting the received signals through the cable at the intermediate frequency (IF) rather than at the radio frequency (RF). However, the method shown in Figure II-8-2 is preferable because of its relative simplicity and because its required preamplifier gain of 35 to 40 dB to offset the cable loss (about 27 dB) can be obtained with a transistor amplifier.

The effect of the repeater frequency multiplexing is shown in Figure II-8-5, which is a typical spectrum format at the repeater upconverter input. The signals appearing at each antenna are represented as blocks about 30 kHz wide along the frequency axis, where the antenna signals within a particular baseline have been grouped together and the reference frequency transmission has been represented as narrowband modulation of the subcarrier. Within the expanded view of a signal block (see Figure II-8-5), it is seen that each antenna will receive the balloon transmissions (average of seven at any given time), which occur randomly within a 16-kHz band, plus the ground illuminator (CT) signals. Notice that, in Figure II-8-5, the balloon signals are shown separately as CW carriers; but it should be noted that, at any given instant of time, some of the signals will be phase-shift keyed (PSK) modulated by data, with an RF bandwidth of about 20 Hz. Note also that CT signals (from ground illuminators) have been positioned on both sides of the balloon emission spectrum to enable calibration across the band.

The upconverter can be either a crystal diode balanced mixer or a varactor (parametric) upconverter. The output of the mixer or varactor upconverter is connected to a chain of a driver amplifier and power amplifier to reach the required output power of 1 W.

Linear operation of the mixer or varactor is important to ensure a minimum level of unwanted inband spectral components (intermodulation products) which

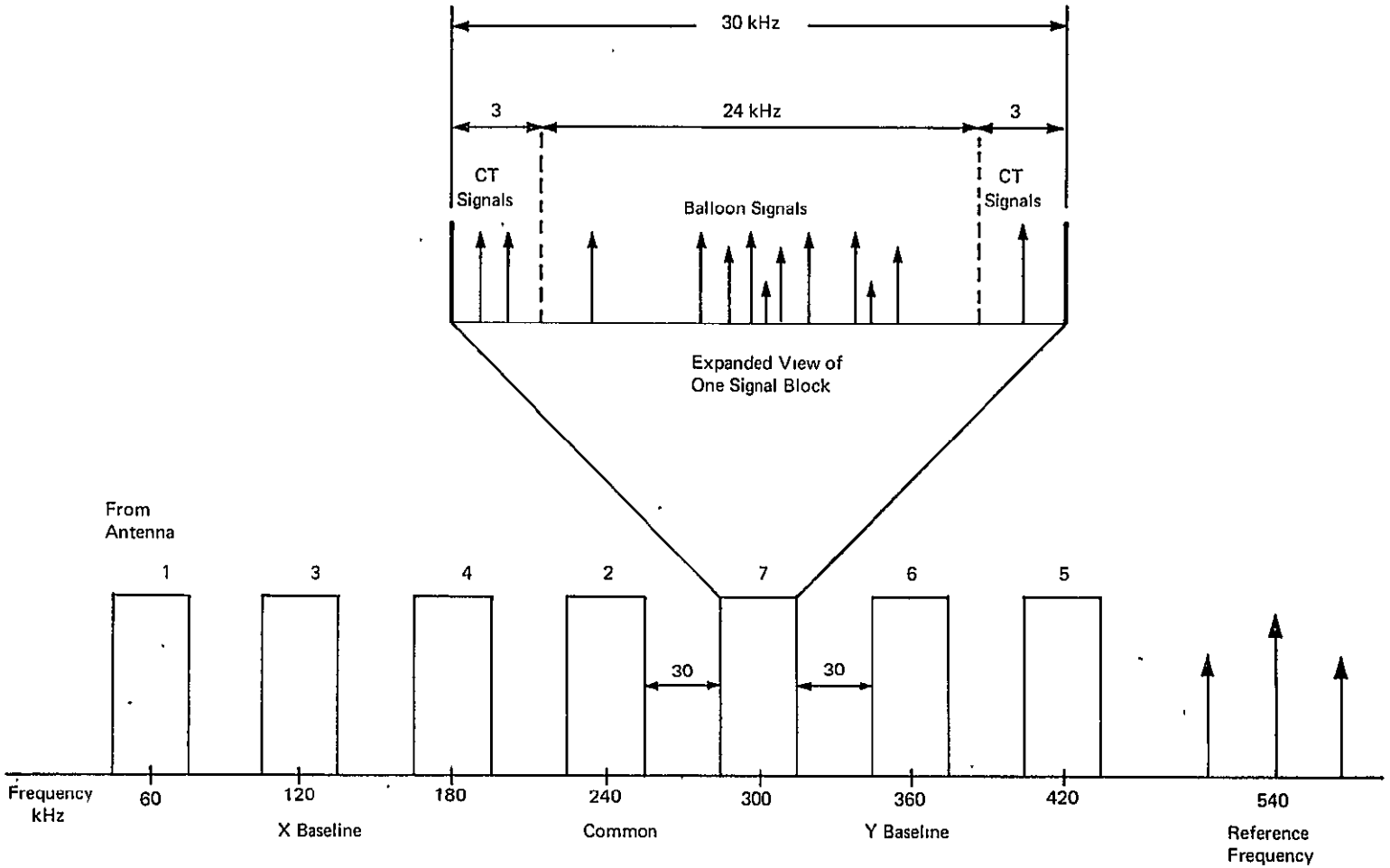

Figure II-8-5. Typical Spectrum Format at Input to Repeater Upconverter

would contaminate the final phase measurement. The fourth-order terms $f_L + (2f_i - f_j)$, for example, fall into the signal passband about $(f_L + f_i)$, where f_L is the local oscillator or pump frequency, and f_i and f_j are input signal frequencies.

The choice between a diode balanced mixer and the varactor upconverter is not clear cut. While both devices can be operated to have equivalent linearity, the output power will differ by several orders of magnitude for the devices. Therefore, the X-band gain of both configurations is examined.

As shown in Figure II-8-6, the upconverter/power amplifier combination must provide 1 W output power (P_o) to the transmitting antenna. The requisite X-band gain to attain the 1W is given by the ratio $\frac{P_o}{P_m}$, where P_m is the output power of the frequency translating device. P_m must be set at some maximum value for each device to limit the level of the undesirable fourth-order intermodulation to -60dB relative to the desired upconverter output. Available literature[36, 37] shows that the theoretical output power capability of the diode mixer and varactor upconverter is about -25dBm and -15dBm, respectively, such that the subject intermodulation is -60dB relative in both cases. However, laboratory testing of a commercial X-band diode balanced mixer (AEL, Inc. model 3072-3A) indicated that the mixer output level must be kept below -37 dBm to achieve 60 dB intermodulation rejection. Thus evaluation of the $\frac{P_o}{P_m}$ ratio shows that the required X-band gain is from 55 dB to 67 dB for use of the diode mixer and 45 dB for use of a varactor upconverter.

It can be seen that use of the simple diode mixer requires implementation of a higher gain at X-band; the spacecraft power and weight penalty resulting from this requirement has not been assessed. Alternately, use of the X-band varactor upconverter has inherent problems of matching and pump amplitude and frequency stability, while still requiring 45 dB gain at X-band and more pump power. This tradeoff will have to be resolved by a thorough study of the state-of-the-art at the time of implementation.

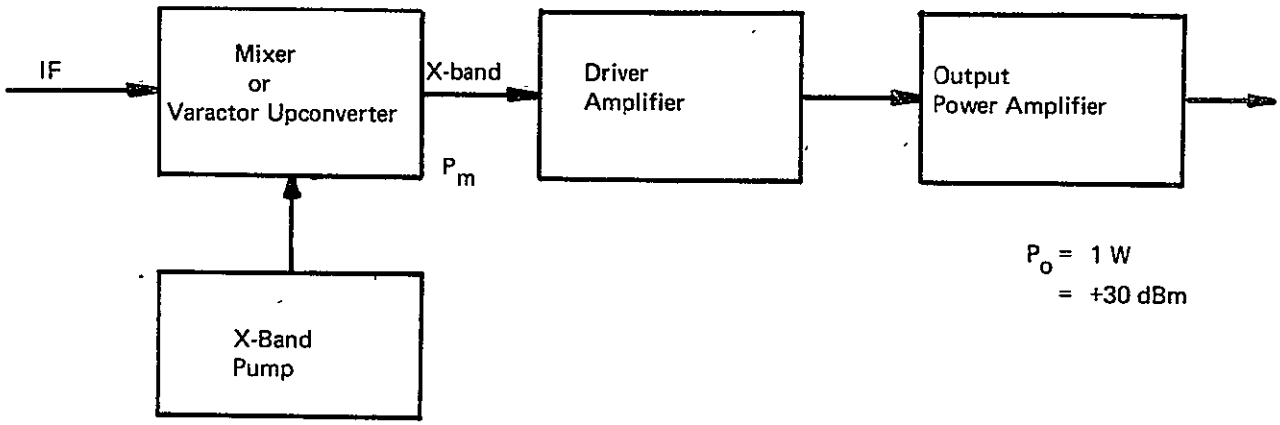

Figure II-8-6. Upconverter Output Power Amplifier Configuration

Nonlinearities in the TWT output power amplifier have also been considered, since this device produces third-order intermodulation products which could fall into the passband. Operation of an amplifying tube far below its maximum power will effectively reduce nonlinearity.[38] For example, the third-order intermodulation products will be down almost 60 dB in relative power for an input power 20 dB below that required for tube saturation. A tapered-velocity circuit will result in even lower level intermodulation products. Thus a TWT amplifier operated well below saturation (at the expense of dc-to-RF efficiency) will produce satisfactory linear operation.

II-8-2 GROUND STATION RECEIVER

The ground station receiver primary functions are to measure the phases between appropriate signals received at the interferometer antennas and to demodulate the data sent from the balloons. As discussed, the signals received by a particular interferometer antenna occupy a predetermined portion of the received spectrum. The first function of the ground receiver, after the base-band signal is recovered is to filter the incoming signal spectrum into those portions corresponding to particular antennas and the reference frequency subcarrier.

Next, due to large uncertainties in balloon transmission frequencies, a technique for acquisition and narrowband filtering is required. Figure II-8-7 illustrates the essence of this acquisition and filtering technique. A bank of narrowband filters and detectors is used for acquisition. Each filter will have a bandwidth of about 50 Hz, so that about 480 filters are required to cover the 24 kHz within which balloon transmissions will occur. These filters are used solely to make the initial settings of the voltage-controlled oscillators of the phase-locked loops for acquisition.

In the steady state, the output of the filter due to the signal input at antenna 1 will be at the frequency ω_0, which is the frequency of a fixed stable offset oscillator used as part of the phase-locked loop. The output of the filter due to the signal input at antenna 2 will be at the frequency $\omega_0 + \omega_r$, where ω_r is

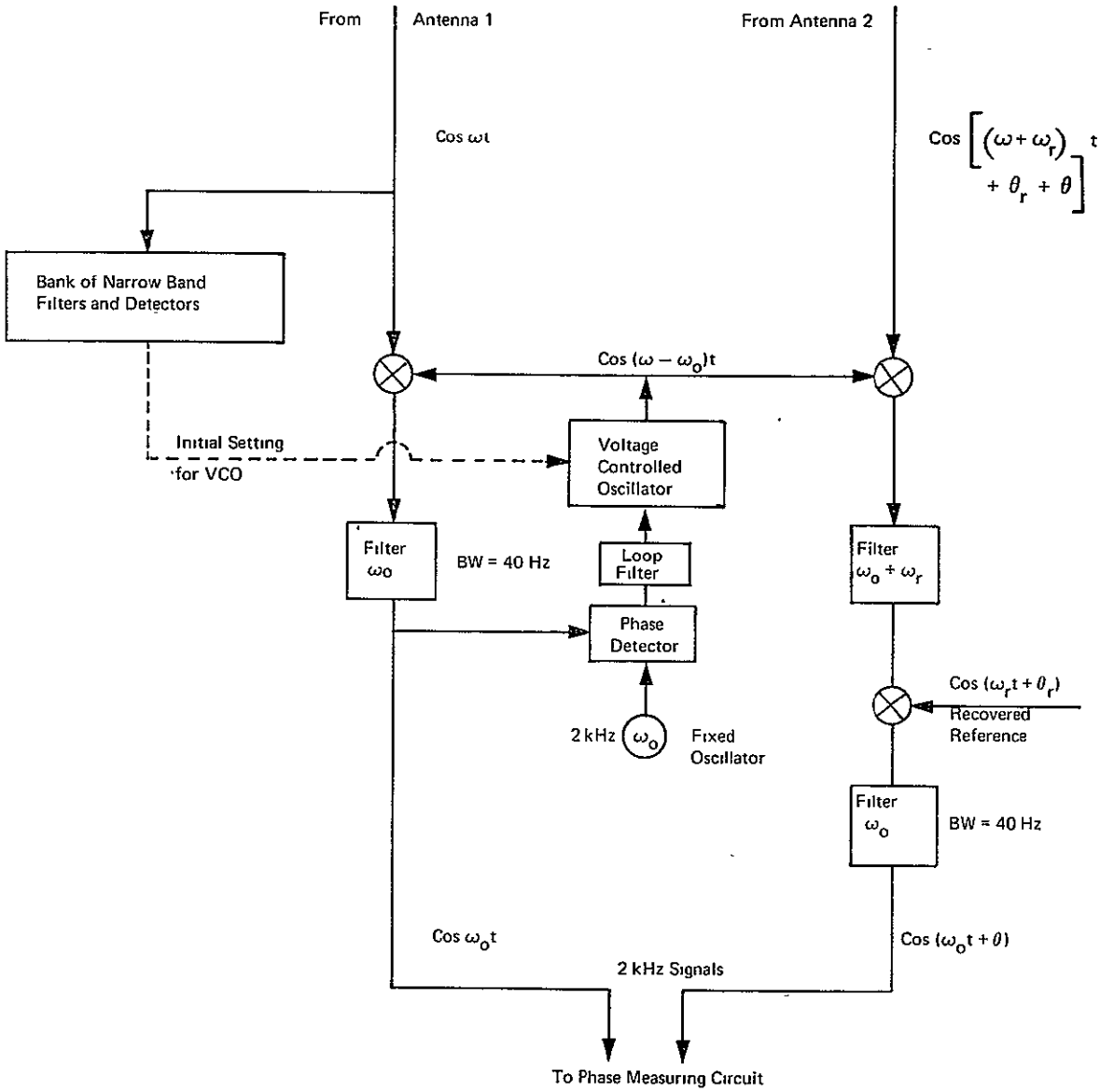

Figure II-8-7. Signal Acquisition and Filtering

the reference oscillator frequency in the satellite. This signal will be at phase $\theta_r + \theta$ with respect to that signal from antenna 1. When the signal from antenna 2 is mixed with the recovered reference and filtered, the output will be at the offset oscillator frequency ω_o. The 2 signals at frequency ω_o are introduced to a phase measuring circuit to obtain the desired phase θ.

It should be noted that, while it is necessary for the phase-locked loop to reach frequency lock so that there is no cycle slippage, it is not necessary that complete phase lock occur before phase is measured. Any residual phase error of the loop is transferred to both signals and will cancel out when the phase is measured.

Figure II-8-8 is a diagram of the essential parts of the ground receiver configuration. The bank of filters across the top of the diagram accomplishes the separation of signal blocks, after which the acquisition and filtering of Figure II-8-7 is implemented with a bank of phase-locked loops and mixers. Each phase-locked loop is designed to be capable of being set to track a signal anywhere in the 24-kHz band where the presence of a signal is detected.

II-8-3 ACQUISITION TIME

The bandwidth of the phase-locked loops will be approximately 25 Hz. This will give a loop SNR of about 12 dB for the balloons at elevation angles of 20 deg. This gives an adequate margin for the loop to be able to acquire the signal. Since the filters used to locate the signals are 50 Hz apart, the initial setting of the VCOs will be within 25 Hz of the correct value.

The time for a second-order loop to pull into lock for an initial offset $\Delta\omega$ is given by

$$\text{pull in time} \doteq \frac{(\Delta\omega)^2}{2\zeta\,\omega_n^3} \qquad \text{II-8-1}$$

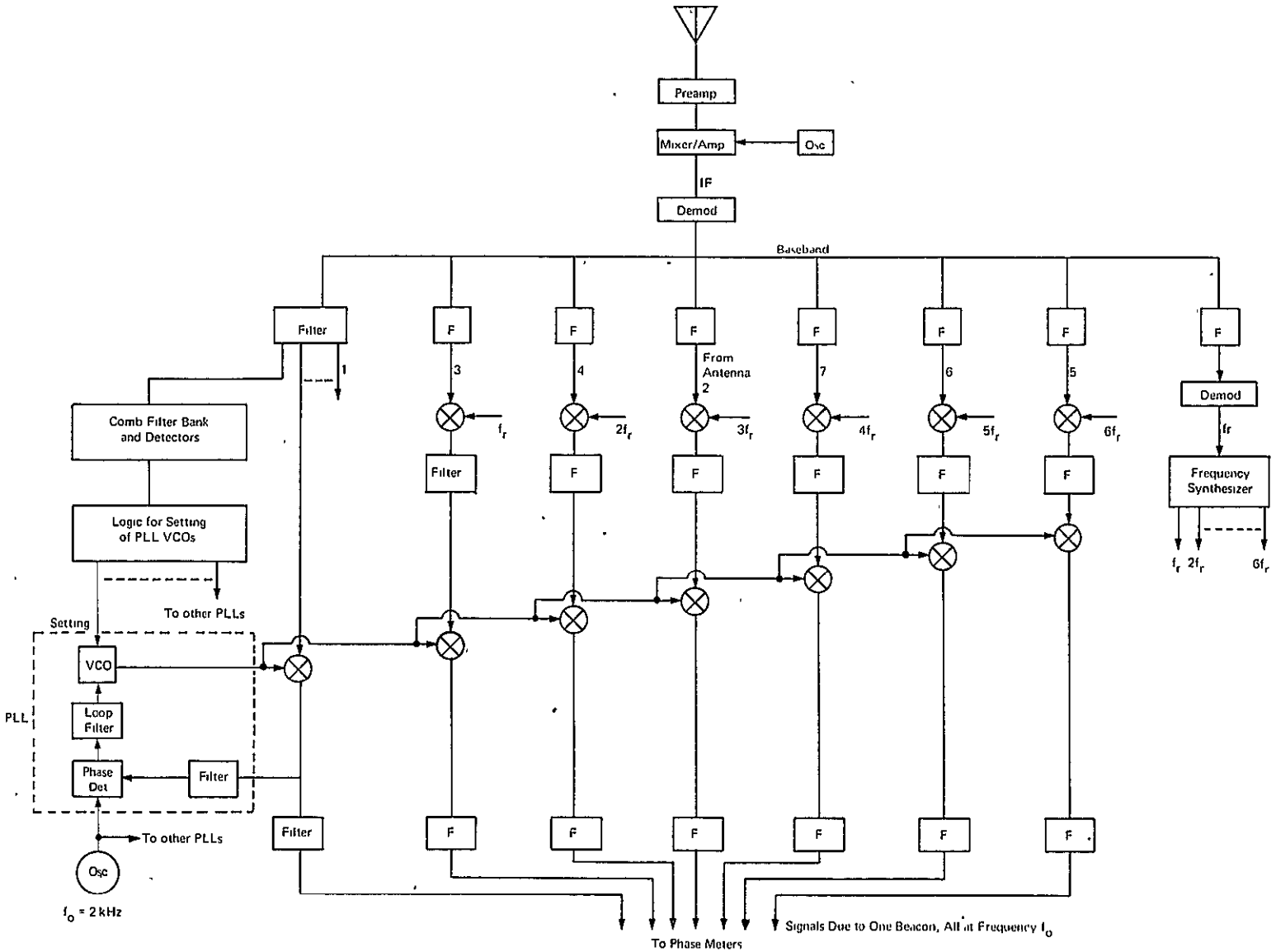

Figure II-8-8. Ground Station Receiver Configuration

where

$\Delta\omega$ = initial frequency offset

ζ = damping constant

ω_n = loop natural frequency.

For a critically damped loop with a loop bandwidth of 25 Hz, $\omega_n \doteq 50$ and since $\zeta = 0.707$, the pull in time will be about 0.1 s. Allowing 0.3 s for signal detection and acquisition, 9.7s of the 10-s transmission time is available for phase measurements.

II-8.4 PHASE MEASUREMENT

The actual phase measurement can be made using a digital phase meter as illustrated in Figure II-8-9. The two antenna signals drive zero crossing detectors. One signal sets a flip-flop, and the other resets it. The number of clock generator pulses counted in this time interval is proportional to the phase difference of the two signals. With a clock speed of 4.096 MHz, 2048 pulses correspond to 360 deg at the 2 kHz signal frequency. Thus the quantization step of the measurement will be 0.18 deg. The 1σ error due to quantization will be 0.05 deg.

To decrease the standard deviation of the phase measurements, many phase measurements are made during the 10-s transmission time, so that effectively an average over the 10 s is obtained. This gives an equivalent filtering of the noise of a 0.1-Hz bandwidth system.

If the actual bandwidth of the signals into the phase meter is 40 Hz, independent samples occur approximately every 0.025 s. Thus a total of 400 measurements is required.

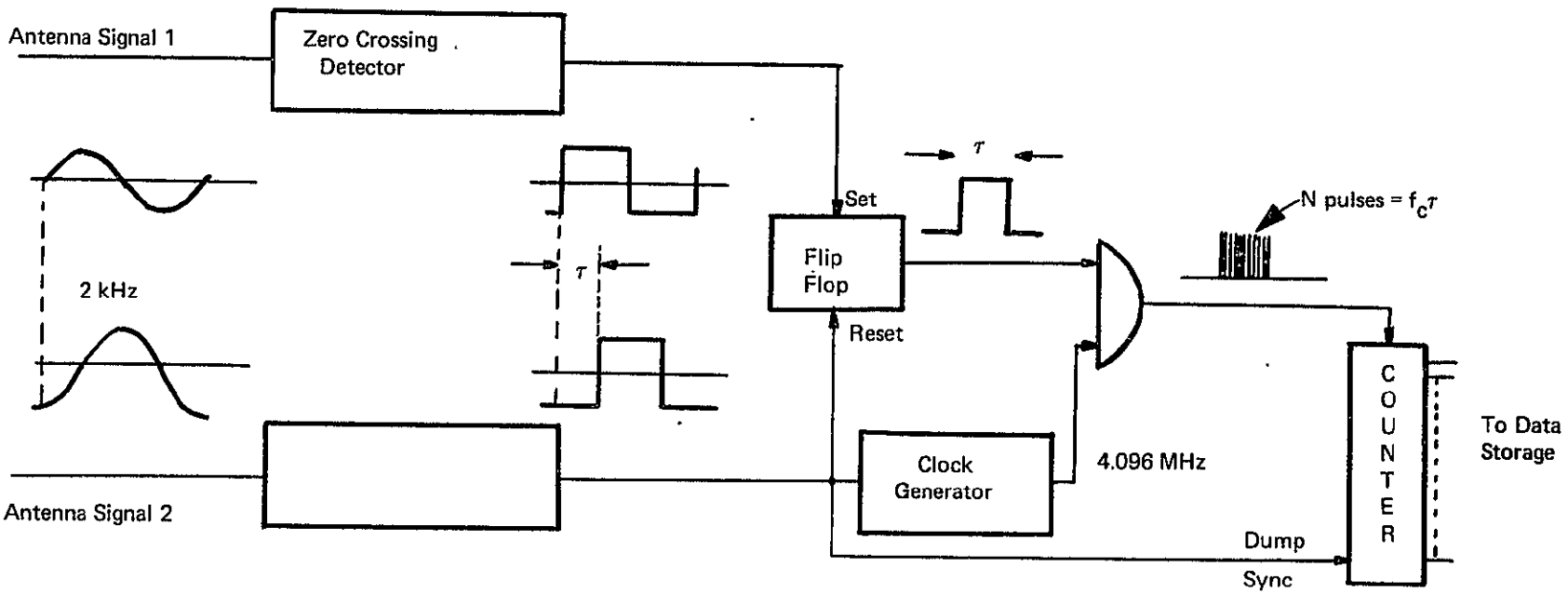

Figure II-8-9. Digital Phase Meter

Section II-9

BALLOON BEACON

Considerable research and experimentation have been devoted to developing constant pressure balloons. Results to date indicate that the reliabilities and lifetimes necessary for an operational system are attainable. Table II-9-1 shows the basic balloon platform electronic package requirements.

Several methods for implementation of the electronics exist. The prime requirements are low cost, frangibility, and low weight. The electronics package must either be attached to the balloon or suspended below the balloon in a manner that provides the requisite attitude stability (±5 deg desired) for antenna directivity. Suspension beneath the balloon also provides a more desirable location for an optional temperature sensor whose accuracy would otherwise be affected by boundary layers near the balloon surface.[39]

Development of frangible packaging technologies has mainly concentrated on the 2-dimensional printed circuit thin film/hybrid technique using flexible multilaminates of Mylar* or Kapton*. This technique has been used by the Advanced Programs Division of the G. T. Schjeldahl Company, Northfield, Minnesota, in balloon electronics packages for both the U. S. Weather Bureau-sponsored GHOST program and the French EOLE program. The primary requirements of low cost, light weight, and frangibility appear to be achievable with this flexible substrate technique, since no heavy structural elements are required and the printed circuit technique is amenable to low-cost production.

---

*Dupont Trademarks.

Table II-9-1

BALLOON PLATFORM REQUIREMENTS

Quantity (fully implemented)	15,000
Power Source	Solar cells
Transmitter RF Power	1 W
Transmitter Frequency	Approximately 1600 MHz
Transmitter Frequency Stability	10^{-5}
Transmission Time	10 s
Time Between Transmissions	2 h
Transmission	PCM/PSK
Antenna Polarization	Circular
Antenna Gain	+2 dB at zenith
Antenna Beamwidth	160°
Data Measurements	2 parameters
Data Measurement Accuracy	1%
Operating Temperature Range	-80°C to + 30°C

Active elements (including integrated circuits) in the form of chips can readily be attached to the flexible substrate for the necessary analog or digital circuit functions.

The primary components of the balloon electronic package are the timer, the encoder (data formatter and identification word generator), the transmitter, the antenna, and the power system. Figure II-9-1 is a diagram of the balloon electronics package.

II-9.1 BALLOON ANTENNA

Balloon antenna characteristics of prime interest are the polarization circularity over the hemisphere and the power radiation pattern both over the hemisphere and in the multipath direction.

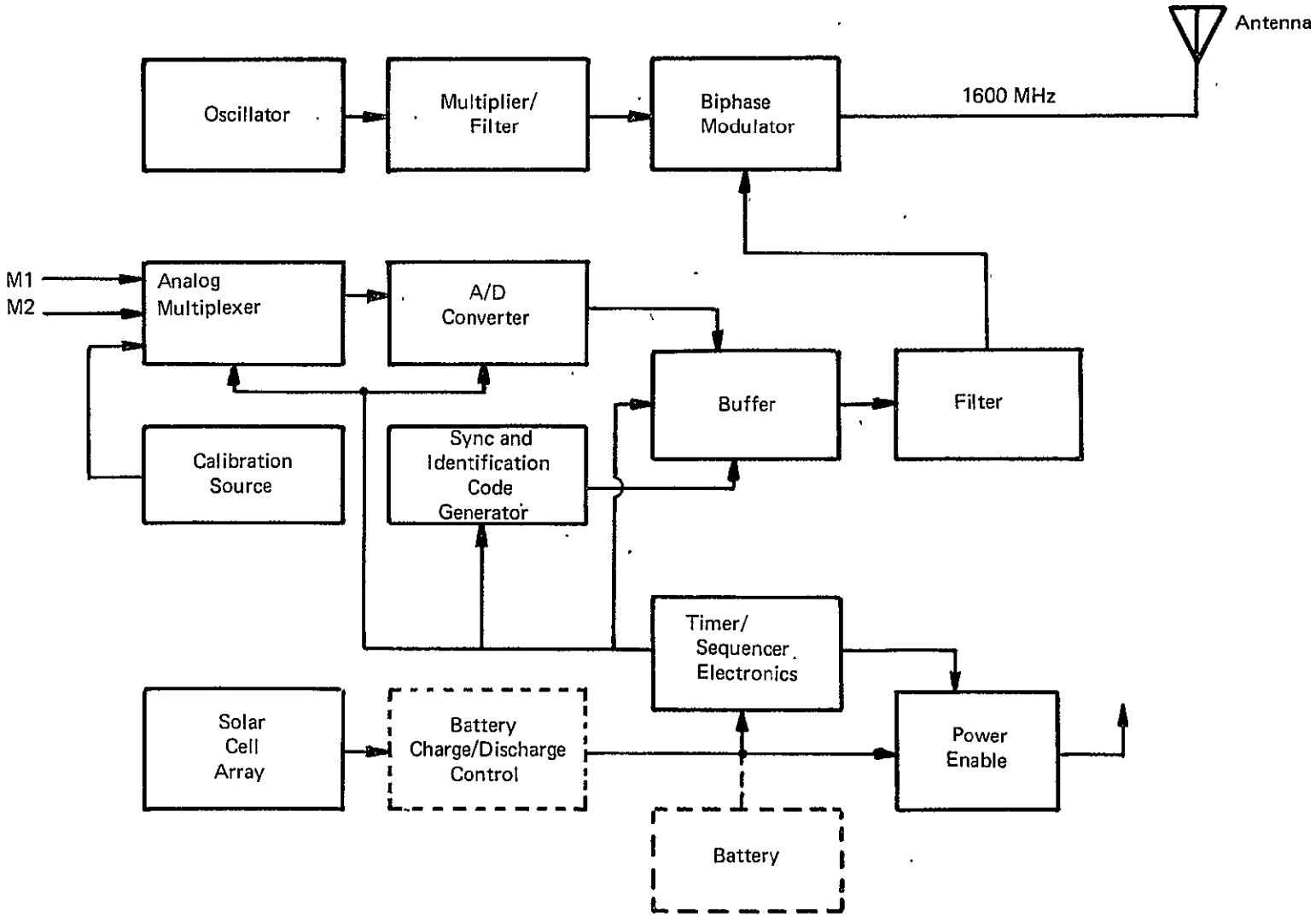

Figure II-9-1. Functional Diagram, Balloon Electronics

Two of the most obvious candidates for the balloon antenna are the crossed dipoles and the planar spiral, because they are both circularly polarized and relatively simple, flat constructions. The axial ratio of the crossed dipoles, however, degrades very quickly (to greater than 4 dB) at elevation angles below 40 deg, which is a severe disadvantage. The planar spiral (Ref. 28, pp. 188-192), on the other hand, exhibits an axial ratio less than 3.5 dB over a range of elevation angles from 20 deg to 90 deg. For this reason, the planar spiral has been chosen as the most desirable antenna for the balloon emitter.

A variety of radiation patterns[41] can be obtained by varying the spacing between the spiral and the ground plane. Since path attenuation, multipath, and geometrical dilution become worse at low elevation angles, it is desirable to choose a balloon antenna radiation pattern which provides an equitable distribution of gain at the lower elevation angles near 20 deg, even at the expense of lowering the gain at 90 deg elevation (zenith) where the abovementioned sources of error are much less troublesome. Using the technique (Ref. 18, p. 519) of graphically determining the field pattern of two isotropic point sources (which is valid for an isotropic point source mounted above ground plane), the field distribution was investigated for several values of antenna-to-ground spacing. A spacing of 0.35λ was found to provide a desirable distribution of gain, as shown in Figure II-9-2. An acceptable pattern will be obtained if the actual spacing is within 10 percent of the design. The maximum gain of the spiral antenna would be approximately +4 dBI. The FR-2 study report[41] stated that the gains of two particular spiral antennas were 6 dBI and 2.5 dBI, with spacings of 0.25λ and 0.48λ, respectively. Measured efficiencies were about 70 percent at the optimum frequency. A gain of +4 dB for the spiral antenna is consistent with information on commercially available cavity-backed spiral antennas.

In Section II-3 of this report, an antenna gain in the direction of the satellite of 10 dB with respect to the gain in the multipath direction was assumed. Measured radiation patterns[41] indicate that this gain is readily achieved with a spiral antenna mounted above a ground plane.

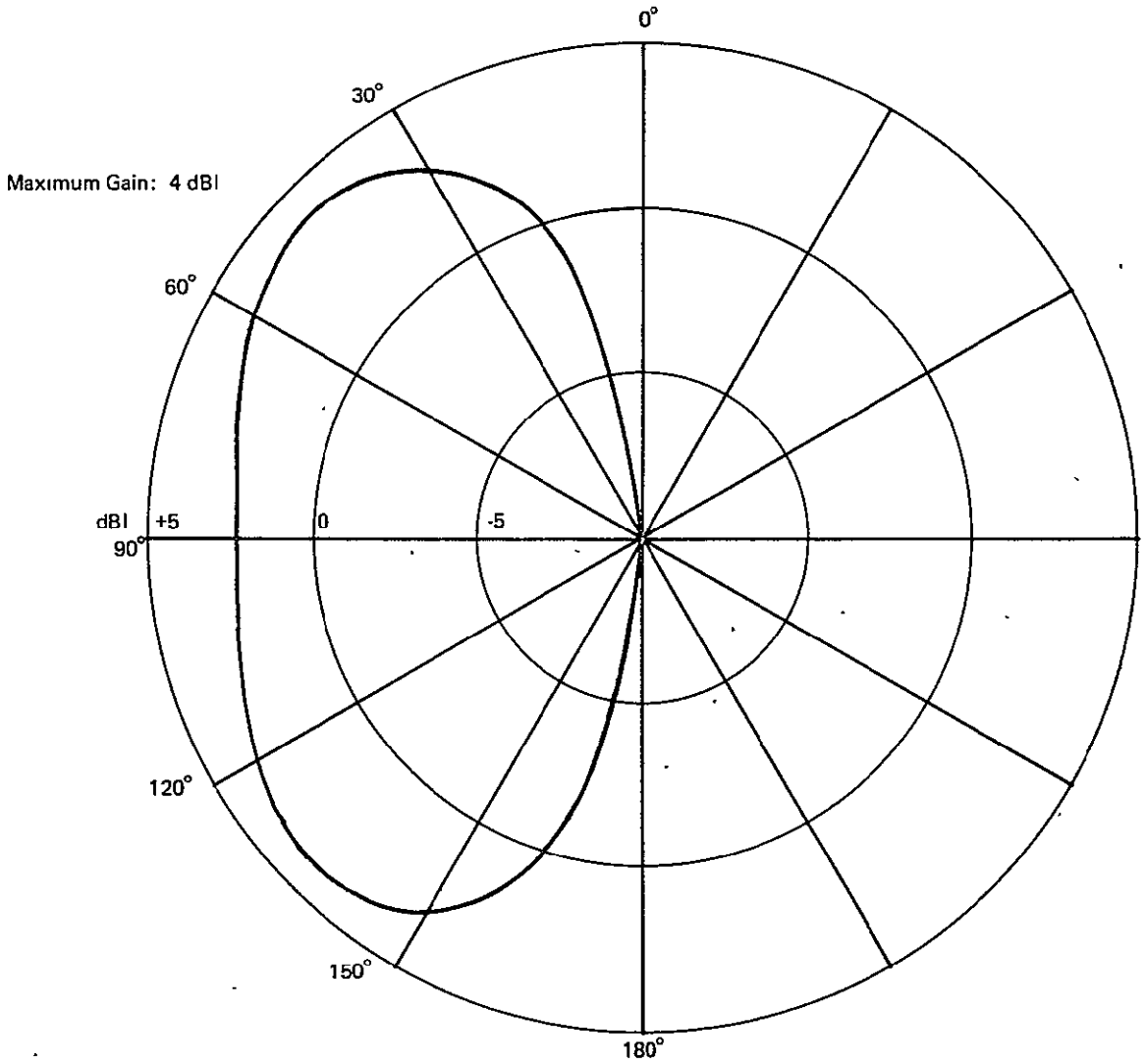

Figure II-9-2. Radiation Pattern of Planar Spiral Mounted 0.35 λ above a Ground Plane

II-9.2 BALLOON TRANSMITTER

The transmitter consists of a crystal controlled oscillator, multiplier/filter combination and a modulator for PCM/PSK (phaseshift keyed) modulation of the carrier. An alternate configuration is to use a VCXO (voltage controlled crystal oscillator) modulator, a low level frequency multiplier, a power oscillator phase locked to the modulator output and a frequency doubler.

This latter method is used in a unit designed and built by TRF, Inc.[42] This unit, operating at a frequency of 1700 MHz with a power output of 2W and a frequency stability of 0.001%, had an overall efficiency of 20.5%. Package size was 2.8 x 2.6 x 1.4 or 20.2 cubic inches. Data indicated that an efficiency of 25% can be achieved with a somewhat larger package size.

II-9.3 IDENTIFICATION

During the 10-s balloon transmission, a binary word of sufficient length (number of bits) must be modulated onto the carrier to identify the source of the transmission. For 15,000 possible balloons, a 14-bit word length is sufficient for this purpose, since $2^{14} = 16,384$.

As shown in sub-section II-9.4.2, for the data rate required (8.9 bps), a bit error probability of 10^{-6} should be easily obtained with PSK modulation. Thus errors in decoding the identification word will be few, and it is suggested that merely one bit be added to the identification for parity check. This enables the detection of single errors, which will be virtually the only existing errors. The identification word is shown as 16 bits in length to allow more expansion of the system.

II-9.4 DATA MEASUREMENT AND TRANSMISSION

II-9.4.1 Encoder for Data Measurement

The addition of two meteorologic data measurements, such as temperature and relative humidity, will greatly aid the meteorologist in making accurate

forecasts. A third data point for barometric pressure would also aid in tracking the balloon and would confirm superpressure status and balloon altitude.

The meteorological data points would appear as analog voltages across some nominal impedance (see Figure II-9-1). These data points are sampled sequentially under timer control along with some additional fixed voltages for calibration which will be required to attain the requisite accuracy of 1 percent. These calibration voltages could be derived from a voltage reference and a resistive divider. Temperature stability will be a problem and may further complicate the calibration process. The analog voltage would then be converted to a digital representation in an A/D converter. A 9-bit word, including a bit for parity check, is more than adequate from an accuracy point-of-view.

Although there are a number of methods for making analog-to-digital conversions, size, accuracy, power consumption, and stability requirements severely limit the number of techniques which are actually applicable. In the successive-approximation technique, the digital output is determined one bit at a time, starting with the most significant bit. This process is controlled by a timing register which is part of the A/D converter logic shown in Figure II-9-3. The unknown analog input is compared with one-half of the full-scale voltage by setting the most significant bit in the register to logical 1. If the input is greater than half scale, the second most significant bit in the register is set to 1. On the other hand, if the analog input is less than the first approximation, the first register is reset while the second is set to logical 1. As this process continues, successively better approximations are determined. A useful feature of this technique is that a serial output is available at the comparator output.

An examination of circuit technology to be used in the implementation of a successive approximation A/D converter reveals advantages for MOSFET (Metal Oxide Silicon Field Effect Transitor) intergrated in chip form or substrates. The attainable accuracy of a 9-bit A/D converter using this technology has been studied by IBM. Of specific interest was theperformance of the voltage comparator, reference voltage supply, ladder, and ladder switches. The temperature range of interest in this study was -55°C to +40°C. Worst-case effects (-55°C)

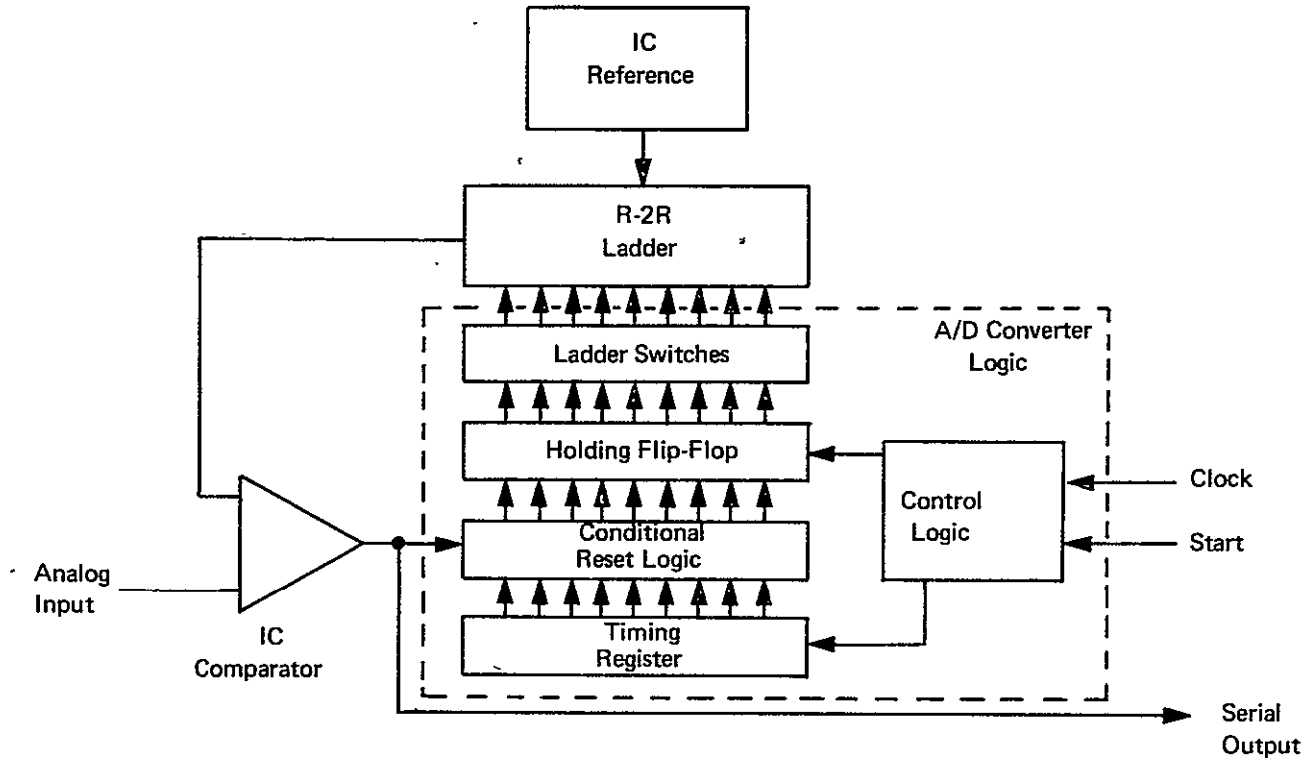

Figure II-9-3. Successive Approximation, A/D Converter.

of a 3σ error due to comparator offset, source drift, and ladder-ladder switch variations were 0.056 percent, 0.060 percent, and 0.0188 percent, respectively, relative to a 5.12-V reference. The RSS total is 0.15 percent, including the 0.098 percent quantization error for a 9-bit converter. This is considerably better than the 1 percent accuracy specified for this application, although the anticipated temperature range will degrade the expected performance to some extent. A reduction to 8-bit A/D conversion, while maintaining the 1 percent or better accuracy, may possibly reduce size and power requirements. The A/D converter can also be implemented using low power transistor-transistor logic (TTL) integrated circuits, except ladder switches, with only a modest increase in size and power requirements.

II-9.4.2 Data Transmission

As previously indicated, the digital data will be modulated onto the balloon beacon carrier by PSK, because this technique affords good immunity to noise, its bandwidth is small, and angle modulation does not interfere with the phase measurement needed for balloon position location.

Thus the format within the 10-s interval of transmission from each balloon will be 2 s of CW to facilitate acquisition at the ground receiver, followed by the necessary digital information. The digital format will consist of the sequential transmission of the following blocks of bits:

- 10 bits for bit timing*.
- 18 bits for frame synchronization*
- 16 bits for ID word (including 1-bit parity check)
- 9 bits for sensor calibration
- 18 bits for meteorological data samples (2).

A time diagram of the transmission is given in Figure II-9-4.

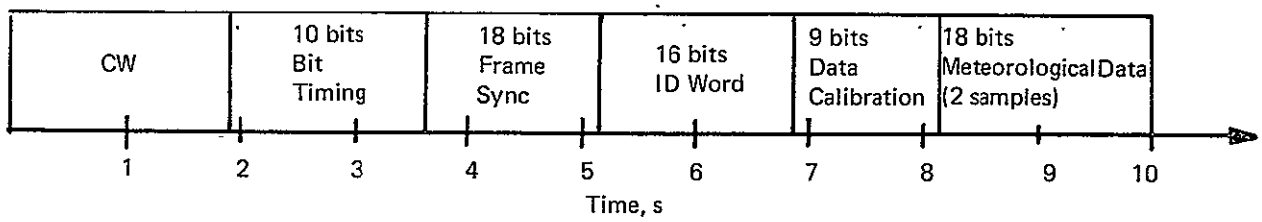

Figure II-9-4. Balloon Transmission Format

*Approximate requirements.

Transmission of the 71 bits during 8 s gives a bit rate of 8.9 bps. With a carrier-to-noise-density ratio of +26 dB-Hz, the bit-energy-to-noise-density ratio will be +16.5 dB. Allowing 3 dB for degredation in the system, the bit energy-to-noise-density ratio will be +13.5 dB, which will provide a bit error probability of less than 10^{-6} for coherent PSK data transmission.

II-9.5 TIMER REQUIREMENTS

The function of the timer is to periodically activate the balloon electronics for a certain period during which the balloon transmits. The turn-on period will be 2 h; during the 10-s active interval, the timer must provide for timing of the identification coder and the data encoder. The timing structure of the transmitted signal was described earlier.

The timer, consisting of an oscillator and divider circuits operates continually, enables the transmitter circuitry at the preset intervals, and controls transmission of the identification code (gating and bit timing). The timer operates as a free running clock during the lifetime of the system. The transmitter oscillator may possibly be used for the timer circuit also.

The bit timing pattern, synchronizing pattern, and identification code are generated in a preset register under control of the timer. This register could be implemented by using a special-purpose integrated circuit chip.

A high degree of precision of the timing period is neither practical nor desirable. A staggering of the time between transmissions will cause randomizing of the balloon package timing when considering the system of 15,000 balloons.

II-9.6 BALLOON (dc) POWER REQUIREMENTS

Table II-9-2 tabulates the estimated power requirements. If it is assumed that a solar cell array provides the power, the necessary size of the array can be computed from available information.[43] The solar radiant power density at sea level is about 100 mW/cm^2. With a solar cell efficiency of 8%, a collecting area

of 700 cm^2 is required to generate 5.5W. If the cells are spaced over the balloon surface so that the same area is exposed regardless of the sun angle, 4 times this area or 2800 cm^2 would be required. The array would weigh about 1 lb.

Table II-9-2

BALLOON PACKAGE POWER REQUIREMENTS

	Mode 1 (ON) (in W)	Mode 2 (STANDBY) (in W)
Transmitter	4.0	0.0
Transducer Bias Circuits	0.3	0.0
A/D Converter	0.5	0.0
Code Generator	0.2	0.0
Timer Circuits	0.5	0.1
TOTALS	5.5	0.1

The preceding calculation assumed that the power input to the balloon electronics is supplied totally by the solar cell array, with no battery storage provided. This situation implies operation during daylight hours only.

Naturally a system design calling for operation during night hours would require a rechargeable battery supply capable of meeting both frangibility and low temperature operation specifications. Night time operation would add significantly to the cost of the balloon package.

GLOSSARY*

G.1 Abbreviations
G.2 Mathematical English Symbols
G.3 Mathematical Greek Symbols
G.4 Subscripts
G.5 Superscripts

*In general, the abbreviations used are consistent with the recommendations of the IEEE in the IEEE Spectrum, August 1965, pp. 111-115. This glossary lists additional abbreviations used in this report.

G.1 ABBREVIATIONS

ACS	Attitude Control System
CT	calibration transmitter
CEP	circular error probable
CP	circular polarization
dBI	decibel gain, referred to an isotropic antenna
dBW	decibel referred to 1 W
ERP	effective radiated power
LOS	line-of-sight
LP	linear polarization
m x n	m by n matrix
MSR	multipath-to-signal ratio
PLL	phase-locked loop
SMR	signal-to-multipath ratio

G.2 MATHEMATICAL ENGLISH SYMBOLS

A	direct ray signal amplitude; constant of integration for twist; boom configuration cross-sectional area
[A]	row matrix of unit vector along the direction $\vec{\rho}_s$ (defined in Equation (2.1-11b))
A_1	Astrocolumn longeron cross-sectional area
A_m	amplitude of sinosuidal component of baseline rotation
A_s	boom configuration surface area
B	multipath ray signal amplitude
B_1, B_2	angle of orientation of polarization ellipse
B_j	a matrix defined by Equation (II-2-37)
B_M	bandwidth used to filter against multipath
B_n	noise bandwidth
C	mutual coupling factor between antennas; torsional rigidity
C( )	correlation function
C, C_1	integration constants (see Equation II-7-13)

C_D	drag coefficient
C_p	specific heat of the material
D	spherical divergence factor; Astrocolumn folded diameter
[D]; $[D_B]$	matrices defined by equations II-2-30 and II-2-26
E	elevation angle; Young's modulus of elasticity
E ( )	expected value of
$\vec{E}$	electrical field vector
$[E_{L1}]$ $[E_{L2}]$	matrices defined by Equation II-24b
E_{Tx}, E_{Ty}, E_{Ry}, E_{Ry}	electrical field vector components for transmitter and receiver antenna
EI	boom configuration stiffness
F	scalar factor (see Equation II-2-21)
G	antenna gain
G_{dm}	beacon antenna front-to-back ratio
H	normalized balloon altitude
$H_1 H_2$	function of boom mode shape, defined by Equation (II-7-25)
I	configuration area or mass moment of inertia
[I]	unit matrix
I_1	total mass moment of inertia about satellite yaw axis
I_2	total mass moment of inertia about satellite pitch axis
I_s	satellite mass moment of inertia
I_T	total mass moment of inertia of the system
K	conductivity (thermal)
$\vec{K}_1$, $\vec{K}_2$	unit vectors along the incoming and reflected rays, respectively (see multipath analysis)
K_{gg}	gravity-gradient torque coefficient, $\frac{3}{2}$ go $\frac{Ro^2}{3}$
$[K_j]$	matrix indicating total number of wavelengths in calibration analysis
L	length of baseline
L_g	gravity-gradient rod length
L_o	length of one boom; original boom length

$\vec{L}_j$	vector of j^{th} interferometer baseline
$[L^*_j]$	augmented j^{th} baseline vector, including differential phase bias
Lo_j, La_j	longitude and latitude of j^{th} calibration transmitter
L_p	path loss
M	number of phase-locked loops in the system; tip mass
M_g	gravity-gradient tip mass
$[M_j]$	matrix mapping calibration station survey errors from earth-fixed spherical frame into earth-fixed Cartesian frame
N	number related to the index of refraction
N_B	number of balloons in the system
N_E	number of electrons per unit volume
$[N_k]$	sensitivity matrix relating three beacon position errors to k^{th} error set
N_o	noise density
P	power; probability; pressure, aerodynamic and solar; perimeter of boom configuration cross-section (boom twist analysis)
$\vec{P}$	vector position of beacon
$[P_B]$	beacon position in matrix notation
P_d	power in the direct ray
P_o	power in the reflected ray (multipath analysis)
Q	function of geometry used in multipath analysis (defined by Equation II-3-38a)
R	axial ratio of polarized signal; Fresnel reflection coefficient
S	solar flux, approximately 460 $\frac{BTU}{ft^2\ hr}$
S_1, S_2	electrical signal arriving at interferometer antennas
S_j	covariance matrix of parameter j
T	time interval between measurements; surface correlation interval; temperature, °Rankine
T_f	final temperature

T_i	initial temperature
T_m	mean temperature
T_Q	ACS torque magnitude
U	signal voltage induced in an antenna
V_1, V_2	velocity of antenna 1 and antenna 2, respectively
$\vec{V}_P$	absolute velocity vector
W	abbreviation used in multipath analysis; bandwidth over which transmission frequencies are spread
[W]	a matrix defined by Equation II-2-24a
X	(1-dimensional) balloon position (length); a measurement sample
Z	measure of bandspread used in multipath analysis (defined by Equation II-3-38b)
Z_o	exponential constant measuring the decay of old data in data estimation
a_j	component of interferometer baseline vector
$\vec{a}_x$ $\vec{a}_y$	unit vectors along x- and y-axes (used where complex vector notation is needed to avoid confusion of $\vec{j}$ and j $=\sqrt{-1}$)
b	movement of a balloon in the time interval τ
b_j	component of interferometer baseline vector
c	velocity of light
c_j	component of interferometer baseline vector
d	length of ray travel from wavefront to second interferometer antenna; differential
dx, dy, dz	Cartesian components of line-of-sight vector
e	eccentricity of boom configuration; shear centergeocenter separation
e_c	thermal conductivity of boom material
f	frequency (dimension Hz)
g_o	gravitational constant on earth
h	altitude
$\vec{i}$	unit vector, x direction

j	$\sqrt{-1}$
$\vec{j}$	unit vector, y direction
k	wave number; number of balloons transmitting simultaneously in field-of-view
$\vec{k}$	unit vector, z direction
l	length of a Yagi array antenna
m	constant; mass per unit boom length
n	index of refraction; constant; number of times a balloon transmits in T hours; number of turns of a helix antenna; summation index
p	electrical angle difference corresponding to length of travel from wavefront to second interferometer antenna (Equation II-3-8); constant; abbreviation for $\Delta t/10800$ T
q	electrical angle difference of multipath ray (Equation II-3-8)
r	coordinate ($r \phi \theta$ system); range from beacon to satellite; with subscripts other ranges
$\vec{r}$	vector distance between beacon and satellite
s	distance measured along boom configuration circumference from a boom slit
s_{max}	maximum bump dimension of a reflecting rough surface
t	configuration wall thickness; time
v	balloon velocity
x, y, z	coordinates
$x_{u_j}, y_{u_j}, z_{u_j}$	components of calibration transmitter in earth-centered coordinates
z	longitudinal boom parameter

G.3 MATHEMATICAL GREEK SYMBOLS

α	multipath-to-signal amplitude ratio; angle between reference line and line through antenna phase center (baseline angle of rotation); angular inclination of a helix antenna
α_1	internal absorptance
α_o	external absorptance

β	angle between the normal to the reflection element and z-axis of local multipath scattering frame; angle between ray and local normal; also angle between beacon line-of-sight vector and satellite position vector; angle measured within boom configuration cross-section, referenced from a slit position describing any point on the cross-section's circumference (boom twist analysis)
β_o	tan β_o used in multipath analysis; it is the mean square value of the slope of surface irregularities; $\tan \beta_o = \frac{2\sigma}{T}$
γ	electrical angle (phase difference)
γ_j	electrical phase difference across j^{th} baseline
δ	electrical angle error resulting from multipath
$\delta( )$	variation of ( )
δ_{max}	maximum or tip deflection
δ_{pol}	electrical angle error resulting from polarization mismatch
∂	partial derivative
ϵ	space angle between direct and multipath ray; permittivity
ϵ_o	emissivity
ϵ_r	relative dielectric constant
ζ	angular orientation of ray arriving at interferometer out of x-y plane; damping constant of PLL
η	angular orientation between ray arriving at interferometer and x-z plane; angle between body x-axis and line through boom tip mass (boom tip deflection)
θ	multipath reflection angle; coordinate of r $\not\theta$ θ system; angle between local horizon and nominal boom position; satellite hub angle of rotation
θ_{3dB}	3-dB antenna beamwidth
θ_s	sun angle
θ_t, θ_R	phase of the electrical transmission signal received at the interferometer
k_1, k_2	filter gain function

λ	wavelength; Lagrangian multiplier
μ	Doppler shift frequency, multipath (defined by Equation II-3-38c)
ξ	earth central angle (satellite-balloon-earth center)
π	3.14159 . . .
ρ	radius; material weight per unit length
ρ_a	atmospheric density
ρ_e	earth's radius
ρ_s	radius of the satellite location (absolute value)
$\vec{\rho}_s$	satellite radius vector
ρ_{uj}	geocentric of the radius of j^{th} calibration transmitter
σ	surface bump height; Stefan-Baltzmann constant
σ_e	electrical conductivity
σ_k	standard deviation of k^{th} error
σ_x	standard deviation of the variable
τ	time interval
ϕ	space angle r ϕ θ system; angle of twist for boom deformation
φ	space angle (angle between wavefront and baseline)
χ	electrical angle, corresponding to the space angle, used in multipath analysis; percentage of perforation
ψ	arbitrary angle difference between direct and multipath signal; overlap angle (boom twist analysis)
ω	radian frequency (dimension s^{-1}); satellite angular velocity ($\dot{\theta}$)
ω_n	natural frequency of boom-satellite system; phase-locked loop natural frequency
ω_r	reference frequency
Γ	angle used in multipath analysis (see Equation II-3-29)
Γ_j	column vector, formed by phase differences across baseline j by different calibration signals
Δ	accuracy interval (used with other symbol such as Δx); increment in general (examples: Δf; Δt)

Δ_B	$\Delta B = B_2 - B_1$, difference between the angle orientation of polarization ellipses
$\Delta\gamma_m$	maximum phase error resulting from antenna element mutual coupling
$[\Delta D_j]$	matrix of errors in the LOS to the j^{th} calibration transmitter
Δp_{u_j}	column matrix of CT survey errors in earth-centered spherical frame
Δf	frequency band within which one transmission would interfere with another
Δt	transmission duration (pulse length)
ΔT	difference between final and initial temperature
ΔV	vector velocity error
Θ	temperature normalization factor
Λ	factor used in boom twist equation
$\Phi( )$	power spectrum, multipath analysis; mode shape of boom
Ψ	angle of the balloon velocity vector with respect to the plane in which multipath reflection takes place
Ω	angle used in multipath analysis (see Equation II-3-33)

G.4 SUBSCRIPTS

B	beacon; balloon
BB	phase bias
e	earth
E	electron
L_j	baseline j
M	multipath
R	receiver
s	satellite
T	transmitter
u_j	j^{th} calibration transmitter site

G.5 SUPERSCRIPTS

-1	matrix inversion
P	predicted value
r	estimate of
T	matrix transportation

REFERENCES

1. Navigation Satellite System. Contract NASW-785. Westinghouse Defense and Space Center, Baltimore, Maryland, 1964 and Navigation/Traffic Control Techniques Experiment Study. Contract NASW-01387. Westinghouse Defense and Space Center, Baltimore, Md., 1966.

2. Perry I. Klein. "Analysis of a Short-Baseline Radiation Interferometer Navigation Satellite Concept Incorporating Methods to Eliminate Systematic Navigation Errors." Grant #NGR-39-010-087. University of Pennsylvania, Philadelphia, Pa., 1968.

3. G.H. Millman. "An Analysis of Tropospheric, Ionospheric and Extra Terrestrial Effects on U.H.F. and V.H.F. Propagation." G.E. Report #R56EMH 31. General Electric Company, Electronics Division, Syracuse, N.Y., Oct. 6, 1956.

4. Interferometer Subsystem. Book 1, Doc. No. ATS990-35, EP69-503. Fairchild-Hiller Corporation, Sept. 17, 1969. (A proposal for ATSF&G (Phase D) prepared by Fairchild-Hiller Corporation for Goddard Space Flight Center. Contract NAS511509. Vol. IK.)

5. M.I. Skolnik, Introduction to Radar Systems. McGraw-Hill, New York, San Francisco, Toronto, London, 1962, Sect. 10.

6. J.W. Duncan. "The Effects of Ground Reflections and Scattering on an Interferometer Direction Finder." IEEE Trans. AES, Vol. 6, No. 3. November 1967, p. 922.

7. J. Foley, et al., "L-Band Satellite Communication Surveillance Terminal Study," Vol. 3. Contract NAS12-621. Boeing Aircraft Company, Renton, Washington, N69-21095, Nov., 1968

8. P. Beckman and A. Spizzichino. The Scattering of Electromagnetic Waves From Rough Surfaces. MacMillan, N.Y., 1963, Sect. 12.4.

9. S.H. Durrani and H. Staras. "Multipath Problems in Communication Between Low Altitude Spacecraft and Stationary Satellites." RCA Rev. March 1968, pp. 77-105.

10. "Orbiting Data Relay Network." Final Report AEDR-3152. RCA, Astro Elecs. Division, Princeton, N.J., March 22, 1967. (Prepared for NASA, Washington, D.C., under Contract No. NASW-1447.)

11. K.L. Faute, J. Lozow and R. Bonaccorso. "Effect of Multipath on A Satellite-Balloon Communication Link," Vol. I. Avco Missile System Division, Wilmington, Mass. (Submitted to NASA/GSFC, Greenbelt, Md. under Contract No. NAS-5-9461.)

12. R.W. Hartop. "Power Loss Between Arbitrarily Polarized Antennas." JPL Tech. Report No. 32-457. Jet Propulsion Laboratory, Pasadena, Calif., Sept. 1964.

13. H.W. Ehrenspeck. "A Family of Novel Antennas: The Backfire Antenna." N68-16382.

14. F.J. Zucker. "The Backfire Antenna: A Qualitative Approach to Its Design." Proc. IEEE, Vol. 53. July 1965, pp. 746-747.

15. O. Woodward. "Circularly Polarized Corner Reflector Antenna." IRE Transactions, Antennas and Propagation; Vol. AP-7. July 1957, pp. 290-297.

16. R.W. Klopfenstein, "Corner Reflector Antennas With Arbitrary Dipole Orientation and Apex Angle." IRE Transactions, Antennas and Propagation, Vol. AP-7. July 1957, P297.

17. R.W.P. King. Theory of Linear Antennas. Harvard University, University Press, 1965.

18. J.D. Kraus. Antennas. McGraw-Hill Book Co., New York, N.Y., 1950.

19. S. Schelkunoff and H. Friis. Antennas, Theory and Practice. Wiley, 1952, p. 600.

20. B.L. Diamond. "Mutual Coupling Effects in Hybrid-Fed Crossed-Dipole-Pair Arrays." Digest IEEE Symposium on Antennas and Propagation. 1965, pp. 157-163.

21. J.D. Dyson. "Equiangular Spiral Antenna." IEEE Transactions, Antennas and Propagation, Vol. AP-7. Apr. 1959, pp. 181-187.

22. M.S. Wheeler. "Phase Characteristics of Spiral Antennas for Interferometer Applications." IRE Int. Conv. Record, Part 2. March 1964, pp. 143-152.

23. Conical Log Spiral Antennas. Alto Systems Engineers, Inc.

24. J.D. Dyson. "Unidirectional Equiangular Spiral Antenna." IRE Transactions, Antennas and Propagation, Vol. AP-7. Oct. 1959, pp. 329-334.

25. J.D. Dyson. "Determination of Phase Center and Phase Patterns of Antennas." (In Radio Antennas for Aircraft and Aerospace Vehicles), AGARD Conf. Proc., No. 15. Technivision Services, Maidenhead, England, Apr. 1968.

26. E.F. Harris. "Helical Antennas." in Antenna Engineering Handbook, H. Josik, ed. McGraw-Hill, 1961.

27. D.J. Angelakos and D. Kajfez. "Modifications on the Axial Mode Helical Antenna." Proc. IEEE, Vol. 55. Apr. 1967, pp. 558-559.

28. T.S. Chu and R.G. Kovyoumijian. "An Analysis of Polarization Variation and Its Application to Circularly Polarized Radiators." IRE Transactions on Antennas and Propagation, Vol. AP-12, March 1962.

29. S. Sander and D.K. Cheng. "Phase Center of Helical Beam Antennas." IRE National Convention Record, Part 1, 1958, pp. 152-158.

30. K.R. Carver. Private Communication, Dec. 1969.

31. E. Wolff. Antenna Analysis. J. Wiley, 1966, pp. 405-409.

32. Lattice Column Applications. Astro Research Corp., Santa Barbara, Calif.

33. H.P. Frisch. "Thermal Bending Plus Twist of a Thin-Walled Cylinder of Open Section with Application to Gravity Gradient Booms." NASA TND-4069. Goddard Space Flight Center, Greenbelt, Md.

34. H.P. Frisch, "The Dynamic Characteristics of a Satellite Being Long Elastic Members." NASA TND-4576, Goddard Space Flight Center, Greenbelt, Md.

35. A Higdon and W.B. Stiles. Engineering Mechanics, Vector Edition, Vol. II: Dynamics. Prentice Hall, Englewood Cliffs, N.J., 1962, p. 449.

36. D.G. Tucker. "Intermodulation Distortion in Rectifier Modulators." Wireless, Engineer, June 1954.

37. C.W. Broderick, A.W. Cuilwik, and P.T. Hutchison. "Varactor Upconverters for Satellite Use." Microwave Journal, June 1967, pp. 57-61.

38. John Putz. "Predicting Nonlinear Effects in TWTs." Microwaves, June 1965.

39. R.D. Reynolds and R.L. Lamberth. "Ambient Temperature Measurements from Radiosondes Flown on Constant-Level Balloons." Journal of Applied Meteorology, Vol. 5, No. 3. June 1966, p. 304.

40. The Microwave Engineers' Handbook and Buyer's Guide. Horizon House-Microwave, Inc., 1968, p. 134.

41. FR-2 Antenna Study. Final Report. NASA Contract No. NAS5-9453. Keltec, Aug. 31, 1967.

42. Solid-State S-Band Transmitter. Final Report. Contract No. NAS5-11607. TRF, Inc., Apr. 1969. (A report prepared by TRF, Inc. for NASA, Greenbelt, Md.)

43. Handbook of Telemetry and Remote Control. E.L. Gruenberg, Ed. McGraw-Hill Book Co., New York, N.Y., 1967, pp. 10-94.

BIBLIOGRAPHY

1. Bellenger, M., "Experimental Verification of the Prediction of an Interferometer for Satellite Tracking," Proc. 16th International Astron. Congress, Vol. 3, Support Equipment for Space Vehicles, ppg. 259-272, Also: Tech Info. Service, Am. Institute of Aeron. and Astron., Doc. #A67-30681.

2. Calvit, T.O., "Feasibility of Satellites for Range Instrumentation," Final Report, Contract AF-19-(628)-4200, General Electrical Co. for Directorate of Aerospace Instrumentation, E.S.C., L.G. Hanscom Field, Bedford, Mass., ESD TR 65-416, September 1965.

3. Cubic Corporation, "Feasibility Study for a Vehicle Attitude Determining System" Final Report No. RADC-TDR-64-318 (Vol. I and II) for USAF Contract No. AF 30 (602)-3135, November, 1964

4. D'Antonio, R.A., and Gaffney, J.E., Jr., "Pseudo-Noise Interferometer, Trans." AES, 4, #5, September 1968, ppg. 728-732.

5. Easton, R.L. and Fleming, J.J., The Navy Space Surveillance System, Proc. IRE, pp. 663-669; April 1960.

6. Easton, R.L. and Downey, F.X., "A Primer on Phase Comparison Telemetry for the Navy Space Surveillance System, " National Telemetry Conference Proceedings, 1966, pp. 205-210.

7. Fairchild Hiller/IBM "ATS-4 Interferometer Experiment Study," Contract NASW-1411, 1966.

8. Fairchild Hiller/IBM ATS-F Phase B and C Study, Contract NAS5-11609, 1968.

9. General Dynamics, Large Space Structure Experiments for AAP-Crossed-H Interferometer for Long Wave Radio Astronomy, Contract NAS 8-18118, 1967.

10. Hrusovsky, R.A., "Reducing Multipath Error in an Angle-Measuring Navigation Satellite System", Interim Technical Report, University of Pennsylvania, Moore School Report No. 70-07, Grant NGR-39-010-087 from NASA, September 1969.

11. Jankovich, J.L., "Phase Locked Interferometer", Proc. 16th Int'l. Astron. Congress, Vol. 3, Support Equipment for Space Vehicles, ppg. 213-240.

12. Nachszunow, G., "Localization des Satellites Basée sur le Principle de L'Interferometere Radioelectrique", Vol. 1, published by Mme W. Nachszunow, 8, Allee du Dr. Dupeyroux, 94- Chréteil, France

13. Simas, V., "A System for Re-Entry Tracking of the Apollo Spacecraft", Publications of GSFC, 1963: II, Space Technology

14. Quigley, W.W., "Gemini Rendezvous Radar", AIAA Guidance and Control Cong., August 12-14, 1963, MIT, Cambridge, Mass.